Al-Rubaiee, Mohanad (2026) *Monolithic 1.55-µm passively semiconductor mode-locked laser diodes for optical clock and multi-wavelength / frequency-comb microwave photonics.* PhD thesis.

# Monolithic 1.55-µm Passively Semiconductor Mode-Locked  Laser Diodes for Optical Clock and Multi-Wavelength / Frequency-Comb Microwave Photonics


**Mohanad Al-Rubaiee**


A thesis submitted in fulfilment of the requirements
for the degree of
**Doctor of Philosophy (PhD)**


James Watt School of Engineering
College of Science and Engineering
University of Glasgow


May 2026

# Abstract

Semiconductor mode-locked lasers are attractive sources for compact and low-cost microwave photonics because they can generate stable optical pulse trains, low-noise RF signals, and multi-line optical spectra from a monolithic chip. This thesis investigates the design, modelling, and experimental demonstration of several passively mode-locked laser platforms operating near 1.55 μm, targeting optical clock generation, multi-/dual-wavelength operation for mmWave and low microwave photonic signal generation, and broadband optical frequency comb sources.

The work begins with the development of an ultrastable 10 GHz passively mode-locked laser fabricated on a semi-insulating InP substrate. Fundamental and subharmonic RF injection locking, as well as optical injection locking, are investigated to stabilise the repetition rate and strongly suppress timing jitter. Sub-Hertz RF linewidths and sub-100-fs timing jitter are demonstrated, highlighting the potential of this device as a compact optical clock source.

Next, two monolithic multi-wavelength mode-locked DFB laser platforms are presented, both based on cavity and grating engineering to control the number of wavelengths and their spacing within a single chip. The first platform employs chirped conventional and four-phase-shifted sampled Bragg gratings to realise stable four- and six-wavelength mode-locked operation with uniform channel spacing and high spectral purity. The second platform uses waveguide Bragg grating microcavities to demonstrate controllable tri-, four-, six-wavelength, and dual-wavelength operation, enabling compact single-cavity sources suitable for multiple optical carriers and mmWave photonic beating, while maintaining a fabrication-friendly process flow.

Finally, a broadband, high-repetition-rate frequency-comb source is demonstrated using an asymmetric multiple-quantum-well (AMQW) passively mode-locked laser diode. The device produces a 100 GHz comb with 14 optical lines within a 10.14 nm (−3 dB) bandwidth centred near 1525 nm, and sub-picosecond pulses with a deconvolved pulse duration down to 0.52 ps.

Overall, the results of this thesis establish practical monolithic semiconductor mode-locked laser platforms that combine stabilisation techniques, multi-/dual-wavelength spectral control, and broadband comb generation, supporting future integrated microwave-photonic systems for clocking, communication, and signal-processing applications.

# Publications

### First Author journal articles

1. **M. Al-Rubaiee**, X. Sun, Y. Sun, S. Zhu, Z. Wang, J. H. Marsh, S. J. Sweeney, and L. Hou, “Dual-wavelength distributed feedback laser based on waveguide Bragg grating microcavities,” *Optics Letters*, vol. 50, no. 23, pp. 7219–7222, 2025. doi: 10.1364/OL.575610.
2. **M. Al-Rubaiee**, B. Qiu, S. Zhu, X. Sun, A. S. Hezarfen, Z. Wang, J. H. Marsh, S. J. Sweeney, and L. Hou, “Broadband 100 GHz frequency comb from an asymmetric MQW passively mode-locked laser,” *IEEE Photonics Technology Letters*, vol. 37, no. 23, pp. 1365–1368, 2025. doi: 10.1109/LPT.2025.3604691.
3. **M. Al-Rubaiee**, Y. Fan, B. Yuan, Y. Sun, S. Zhu, A. S. Hezarfen, Z. Wang, X. Sun, J. H. Marsh, S. J. Sweeney, and L. Hou, “Monolithic multi-wavelength mode-locked DFB laser using chirped conventional and four-phase-shifted sampled Bragg gratings,” *IEEE Journal of Quantum Electronics*, early online publication, Oct. 1, 2025. doi: 10.1109/JQE.2025.3616281.
4. **M. Al-Rubaiee**, X. Sun, B. Yuan, Y. Fan, S. Zhu, Y. Sun, J. H. Marsh, S. J. Sweeney, and L. Hou, “Simultaneous multi-wavelength mode-locked DFB laser based on waveguide Bragg grating microcavities,” *Optics Express*, vol. 33, no. 11, pp. 22222–22234, 2025. doi: 10.1364/OE.563242.
5. **M. Al-Rubaiee**, B. Yuan, Y. Fan, S. Zhu, J. Marsh, and L. Hou, “Ultrastable 10 GHz mode-locked laser on semi-insulating substrate through RF injection locking,” *IEEE Photonics Technology Letters*, vol. 36, no. 19, pp. 1189–1192, 2024. doi: 10.1109/LPT.2024.3451690.

### First author Conferences

1. **M. Al-Rubaiee**, X. Sun, J. Wang, S. Zhu, A. S. Hezarfen, Z. Wang, J. H. Marsh, A. E. Kelly, S. J. Sweeney, and L. Hou, “Compact monolithic dual-wavelength DFB laser based on a waveguide Bragg grating microcavity,” in *Conference on Lasers and Electro-Optics (CLEO 2026)*, Charlotte, NC, USA, May 17–21, 2026, accepted for publication.
2. **M. Al-Rubaiee**, S. Ye, X. Sun, A. S. Hezarfen, S. Zhu, Z. Wang, J. H. Marsh, S. J. Sweeney, and L. Hou, “Passively mode-locked 10 GHz laser with three quantum wells on semi-insulating InP substrate,” in *SPIE Photonics West*, San Francisco, CA, USA, Jan. 17–22, 2026.
3. **M. Al-Rubaiee**, B. Qiu, S. Zhu, X. Sun, A. S. Hezarfen, Z. Wang, J. H. Marsh, S. J. Sweeney, and L. Hou, “Asymmetric MQW passively mode-locked laser for broadband 100 GHz frequency comb generation,” in *European Semiconductor Laser Workshop (ESLW 2025)*, Kongens Lyngby, Denmark, Oct. 3–4, 2025.
4. **M. Al-Rubaiee**, X. Sun, Y. Fan, S. Zhu, Y. Sun, A. Seckin, J. H. Marsh, S. J. Sweeney, and L. Hou, “Monolithic multi-wavelength mode-locked DFB laser based on waveguide Bragg grating microcavities,” in *51st European Conference on Optical Communication (ECOC 2025)*, Copenhagen, Denmark, Sept. 28–Oct. 2, 2025. doi: 10.1109/ECOC66593.2025.11263341.
5. **M. Al-Rubaiee**, B. Yuan, Y. Fan, S. Zhu, Y. Sun, X. Sun, J. H. Marsh, S. J. Sweeney, and L. Hou, “Four-wavelength mode-locked DFB laser using chirped sampled Bragg grating,” in *CLEO/Europe–EQEC 2025 (Technical Digest Series)*, Munich, Germany, Jun. 23–27, 2025, paper cb_3_6.

6. **M. Al-Rubaiee**, Y. Fan, B. Yuan, S. Zhu, Y. Sun, A. S. Hezarfen, J. H. Marsh, S. J. Sweeney, and L. Hou, "Four-wavelength mode-locked DFB laser with four phase-shifted chirped sampled Bragg grating," in *Conference on Lasers and Electro-Optics (CLEO 2025) (Technical Digest Series)*, Long Beach, CA, USA, May 4–9, 2025, paper SS130_7. doi: 10.1364/CLEO_SI.2025.SS130_7.
7. **M. Al-Rubaiee**, S. Ye, B. Yuan, Y. Fan, J. H. Marsh, and L. Hou, "10 GHz low divergence angle mode-locked lasers with ultralow timing jitter through injection-locking techniques," in *CLEO 2024 (Technical Digest Series)*, Charlotte, NC, USA, May 5–10, 2024, paper JTu2A.31.
8. **M. Al-Rubaiee**, S. Ye, B. Yuan, Y. Fan, J. H. Marsh, and L. Hou, "Ultra-stable 10 GHz optical clocks based on injection mode-locked semiconductor lasers," in *46th European Semiconductor Laser Workshop (ESLW 2023)*, University of Glasgow, Glasgow, UK, Sept. 30, 2023.

**Journal articles (co-authored)**

1. Z. Wang, Y. Sun, **M. Al-Rubaiee**, A. S. Hezarfen, Y. Fan, S. Zhu, B. Yuan, W. Huang, X. Sun, J. H. Marsh, A. E. Kelly, and L. Hou, "Dual-wavelength DFB lasers based on continuous-phase-shift gratings for MMW/THz photomixing," *Optics Letters*, vol. 51, no. 10, pp. 2876–2879, 2026. doi: 10.1364/OL.593301.

2. X. Sun, **M. Al-Rubaiee**, Z. Li, J. H. Marsh, A. E. Kelly, S. J. Sweeney, and L. Hou, "Bifunctional operation semiconductor laser with mode-locking and single-longitudinal modes," *Optics and Laser Technology*, vol. 193, Part B, Art. no. 114285, 2026. doi: 10.1016/j.optlastec.2025.114285.

3. A. S. Hezarfen, Z. Li, **M. Al-Rubaiee**, S. Zhu, Z. Wang, J. H. Marsh, and L. Hou, "Energy-efficient all-optical control of optomechanical photonic crystal nanobeam cavities," *Optics Letters*, vol. 50, no. 21, pp. 6598–6601, 2025. doi: 10.1364/OL.572114.

4. S. Zhu, B. Yuan, Y. Fan, **M. Al-Rubaiee**, X. Sun, Z. Li, A. S. Hezarfen, A. E. Kelly, J. H. Marsh, and L. Hou, "A reconfigurable multi-channel on-chip photonic filter for programmable optical frequency division," *Nanophotonics*, vol. 14, no. 15, pp. 2619–2631, 2025. doi: 10.1515/nanoph-2025-0119.

5. Y. Fan, **M. Al-Rubaiee**, S. Zhu, B. Yuan, X. Sun, Y. Sun, A. E. Kelly, J. H. Marsh, and L. Hou, "Mode-locked DBR and DFB lasers with multiple phase-shifted gratings for THz generation," *Journal of Lightwave Technology*, vol. 43, no. 16, pp. 7752–7760, 2025. doi: 10.1109/JLT.2025.3576202.

6. A. S. Hezarfen, S. Zhu, **M. Al-Rubaiee**, J. H. Marsh, and L. Hou, "All-optical reconfigurable photonic crystal-microring hybrid cavities with high-efficiency tuning via the mechanical Kerr effect," *Optics Express*, vol. 33, no. 10, pp. 20722–20735, 2025. doi: 10.1364/OE.561749.

7. S. Zhu, B. Yuan, **M. Al-Rubaiee**, Y. Sun, Y. Fan, A. S. Hezarfen, S. J. Sweeney, J. H. Marsh, and L. Hou, "Widely tunable photonic filter based on equivalent chirped four-phase-shifted sampled Bragg gratings," *ACS Photonics*, vol. 12, no. 2, pp. 899–907, 2025. doi: 10.1021/acsphotonics.4c01899.

8. X. Sun, Z. Li, Y. Fan, **M. Al-Rubaiee**, J. H. Marsh, A. E. Kelly, S. J. Sweeney, and L. Hou, "Multi-wavelength DFB laser based on a sidewall third-order four phase-shifted sampled Bragg grating with uniform wavelength spacing," *Optics Letters*, vol. 50, no. 3, pp. 714–717, 2025. doi: 10.1364/OL.542734.

9. Y. Sun, S. Zhu, B. Yuan, Y. Fan, **M. Al-Rubaiee**, X. Sun, J. H. Marsh, S. J. Sweeney, and L. Hou, "Continuous phase modulation technology based on grating period interval for high grating coupling coefficient and precise wavelength control," *Optics Letters*, vol. 50, no. 30, pp. 750–753, 2025. doi: 10.1364/OL.543872.

10. S. Zhu, B. Yuan, W. Cheng, Y. Fan, Y. Sun, **M. Al-Rubaiee**, J. Akbar, J. H. Marsh, and L. Hou, "Dual-band photonic filters with wide tunable range using chirped sampled gratings," *IEEE Photonics Technology Letters*, vol. 37, no. 3, pp. 169–172, 2025. doi: 10.1109/LPT.2025.3525549.

11. Y. Sun, B. Yuan, X. Sun, S. Zhu, Y. Fan, **M. Al-Rubaiee**, J. H. Marsh, S. J. Sweeney, and L. Hou, "Narrow linewidth distributed feedback lasers utilizing distributed phase shift," *Optics Letters*, vol. 50, no. 2, pp. 471–474, 2025. doi: 10.1364/OL.541027.

12. Y. Fan, B. Yuan, **M. Al-Rubaiee**, Y. Sun, S. Zhu, J. H. Marsh, and L. Hou, "Dual-wavelength distributed feedback laser array based on four-phase-shifted sampled Bragg grating for terahertz generation," *Optics Letters*, vol. 49, no. 12, pp. 3472–3475, 2024. doi: 10.1364/OL.524107.

13. Y. Fan, B. Yuan, **M. Al-Rubaiee**, Y. Sun, S. Zhu, J. Akbar, J. H. Marsh, and L. Hou, "Millimeter-wave generation based on four phase-shifted sampled Moiré grating dual-wavelength DFB laser," *IEEE Photonics Technology Letters*, vol. 36, no. 4, pp. 282–285, 2024. doi: 10.1109/LPT.2024.3351531.

**Conferences (co-authored)**

1. A. S. Hezarfen, **M. Al-Rubaiee**, Z. Wang, X. Sun, A. E. Kelly, J. H. Marsh, and L. Hou, "Functional wavelength routing in optomechanically coupled hybrid photonic crystal–microring resonators," in *Conference on Lasers and Electro-Optics (CLEO 2026)*, Charlotte, NC, USA, May 17–21, 2026, accepted for publication.

2. Z. Wang, **M. Al-Rubaiee**, Y. Sun, A. S. Hezarfen, Y. Fan, B. Yuan, J. H. Marsh, A. E. Kelly, and L. Hou, "Dual-wavelength DFB laser with 0.64 THz frequency spacing based on continuous phase modulation technology," in *Conference on Lasers and Electro-Optics (CLEO 2026)*, Charlotte, NC, USA, May 17–21, 2026, accepted for publication.

3. X. Sun, Y. Sun, Z. Li, Y. Wang, J. Wang, **M. Al-Rubaiee**, J. H. Marsh, S. J. Sweeney, A. E. Kelly, and L. Hou, "Semiconductor laser with mode-locking and single-longitudinal bifunctional operation," in *51st European Conference on Optical Communication (ECOC 2025)*, Copenhagen, Denmark, Sept. 28–Oct. 2, 2025. doi: 10.1109/ECOC66593.2025.11263392.

4. S. Zhu, **M. Al-Rubaiee**, Y. Fan, X. Sun, Y. Sun, J. H. Marsh, and L. Hou, "A programmable and reconfigurable on-chip photonic filter for next-generation multi-

channel DWDM," in *51st European Conference on Optical Communication (ECOC 2025)*, Copenhagen, Denmark, Sept. 28–Oct. 2, 2025. doi: 10.1109/ECOC66593.2025.11263250.

5. A. S. Hezarfen, S. Zhu, **M. Al-Rubaiee**, Z. Wang, J. H. Marsh, and L. Hou, "Highly efficient all-optical control of optomechanical photonic crystal nanobeam cavities via the mechanical Kerr effect," in *51st European Conference on Optical Communication (ECOC 2025)*, Copenhagen, Denmark, Sept. 28–Oct. 2, 2025. doi: 10.1109/ECOC66593.2025.11262990.

6. Z. Wang, Y. Fan, X. Sun, B. Yuan, Y. Sun, **M. Al-Rubaiee**, A. S. Hezarfen, S. Zhu, J. H. Marsh, A. E. Kelly, and L. Hou, "Linewidth-reduced optical injection-locked laser utilizing four-phase-shifted sampled Bragg gratings," in *Conference on Lasers and Electro-Optics (CLEO 2025)* (Technical Digest Series), Long Beach, CA, USA, May 4–9, 2025, paper JPS200_65. doi: 10.1364/CLEO_AT.2025.JPS200_65.

7. Y. Sun, **M. Al-Rubaiee**, B. Yuan, A. S. Hezarfen, X. Sun, S. Zhu, Y. Fan, J. H. Marsh, and L. Hou, "DWDM source utilizing a 4PS-SBG DFB laser array with monolithic ATG technology," in *Conference on Lasers and Electro-Optics (CLEO 2025)* (Technical Digest Series), Long Beach, CA, USA, May 4–9, 2025, paper AA125_3, accepted for publication.

8. S. Zhu, **M. Al-Rubaiee**, B. Yuan, Y. Fan, Y. Sun, J. H. Marsh, and L. Hou, "Broadband tunable photonic filter utilizing equivalent chirped sampled Bragg gratings for optical frequency division," in *Optical Fiber Communications Conference and Exhibition (OFC 2025)*, San Francisco, CA, USA, Mar. 30–Apr. 3, 2025. doi: 10.1364/OFC.2025.Tu2G.5.

9. S. Zhu, **M. Al-Rubaiee**, B. Yuan, Y. Fan, Y. Sun, J. H. Marsh, and L. Hou, "Dual-band microwave photonic filter utilizing equivalent chirped four-phase-shifted sampled Bragg grating for 52.1 GHz–439.5 GHz range," in *Proc. SPIE 13362, Silicon Photonics XX*, San Francisco, CA, USA, Jan. 28–30, 2025, paper 133620F. doi: 10.1117/12.3038893.

10. Y. Fan, B. Yuan, **M. Al-Rubaiee**, J. H. Marsh, and L. Hou, "Dual-wavelength DFB laser based on four phase-shifted sampled Moiré grating for MMW generation," in *CLEO 2024*, Charlotte, NC, USA, May 5–10, 2024, paper STh1O.4. doi: 10.1364/CLEO_SI.2024.STh1O.4.

11. B. Yuan, Y. Fan, W. Cheng, **M. Al-Rubaiee**, Y. Zhan, X. Chen, J. H. Marsh, and L. Hou, "Monolithic dual-wavelength laser array based on four phase-shifted grating and equivalent chirp technology," in *2023 European Conference on Optical Communications (ECOC 2023)*, Glasgow, Scotland, Oct. 1–5, 2023. doi: 10.1049/icp.2023.2270.

# List of Contents

# List of Figures

# List of Tables

# Acronyms

| | |
|---|---|
| 5G | Fifth-generation |
| 6G | Sixth-generation |
| WDM | Wavelength-division multiplexing |
| CMOS | Complementary metal–oxide–semiconductor |
| HML | Hybrid mode locking |
| RF | Radio frequency |
| UOC | Ultrafast Optical Clock |
| DBR | Distributed Bragg reflector |
| III-V | III–V compound semiconductor |
| DFB | Distributed feedback |
| DWDM | Dense wavelength-division multiplexing |
| ML-DFB | Mode-locked distributed feedback |
| MMI | Multimode interference |
| MQW | Multiple-quantum-well |
| SLM | Single-longitudinal-mode |
| SA | Saturable absorber |
| AMQW | Asymmetric multiple-quantum-well |
| QW | Quantum well |
| SMSR | Side-mode suppression ratio |
| CW | Continuous-wave |
| SMLLD | Semiconductor mode-locked laser diode |
| TMM | Transfer matrix method |
| TWM | Travelling-wave model |
| SI | Semi-insulating |
| DI | Deionised water |
| IPA | Isopropanol |
| PMMA | Polymethyl methacrylate |
| HSQ | Hydrogen silsesquioxane |
| MIBK | Methyl isobutyl ketone |
| TMAH | Tetramethylammonium hydroxide |
| BOE | Buffered oxide etch |
| RIE | Reactive ion etching |
| PECVD | Plasma-enhanced chemical vapour deposition |
| NiCr | Nickel–chromium (adhesion layer) |

| | |
|---|---|
| SCH | Separate confinement heterostructure |
| SSB | Single-sideband |
| RMS | Root-mean-square |
| FRL | Far-field reduction layer |
| SMF | Single-mode fibre |
| SPM | Self-phase modulation |
| RC | Resistance–capacitance |
| CPW | Coplanar waveguide |
| ICP | Inductively coupled plasma |
| FWHM | Full width at half maximum |
| GSG | Ground–signal–ground |
| DC | Direct current |
| SBG | Sampled Bragg grating |
| REC | Reconstruction-equivalent chirp |
| C-SBG | Conventional sampled Bragg grating |
| 4PS | Four phase-shifted |
| 4PS-SBG | Four-phase-shifted sampled Bragg grating |
| WBG | Waveguide Bragg grating |
| MOVPE | Metal-organic vapour phase epitaxy |
| FSR | Free spectral range |
| AC | Autocorrelation |
| SEM | Scanning electron microscope |
| PC | Polarisation controller |
| EDFA | Erbium-doped fibre amplifier |
| OSA | Optical spectrum analyser |
| RBW | Resolution bandwidth |
| PD | Photodiode |
| ESA | Electrical spectrum analyser |
| TBP | Time–bandwidth product |
| VOA | Variable optical attenuator |
| SOA | Semiconductor optical amplifier |
| TEC | Thermoelectric cooler/controller |
| FWM | Four-wave mixing |
| 2D | Two-dimensional |
| AR | Anti-reflection coating |
| VBW | Video bandwidth |

| | |
|---|---|
| PDM | Power difference between modes |
| QD | Quantum dot |

# Acknowledgments

I would like to sincerely thank everyone who supported me throughout my PhD. This work reflects not only my own effort, but also the guidance, patience, and kindness I received from many people during the journey.

First, I would like to express my deep appreciation to my supervisor, **Prof. Lianping Hou**, for his continuous guidance, encouragement, and trust. His support helped me grow both technically and academically, and his feedback consistently pushed me to improve the quality of my work. I am especially grateful for the balance he maintained between giving me independence and offering direction whenever I needed it.

I would also like to thank **Prof. John H. Marsh** for his invaluable advice and thoughtful discussions throughout my PhD journey. Even after his official retirement, he generously continued to share his insights, feedback, and support, and I truly appreciate the care and commitment he showed during the rest of my studies.

I would also like to express my sincere gratitude to **Prof. Stephen Sweeney**, who supported the later stage of my PhD, for his insightful guidance on my publications and for his help at times when I lacked access to essential experimental equipment.

I would also like to give special thanks to **Dr. Xiao Sun**, not only as a colleague and friend, for the valuable ideas, design feedback, and practical suggestions he shared with me throughout the project. His input was consistently thoughtful and had a real positive impact on my work during this journey.

My sincere thanks go to the **Centre for Doctoral Training (CDT) in Applied Photonics**, including the administrators and management team, for their support throughout my studies. I would also like to acknowledge **Prof. Martin Lavery** for his helpful comments and suggestions during annual reviews, which often gave me new direction and helped me see clearer ways forward.

I am grateful to **Dr. Shengwei Ye** for his mentorship in nanofabrication. His practical guidance and willingness to share his experience made a huge difference in my confidence and skills in the cleanroom. I also thank the staff at **JWNC** for their training, support, and patience in helping me use the facilities and understand the tools properly.

I would like to thank my colleagues and friends, **Yizhe Fan, Simeng Zhu, Ahmet Seckin Hezarfen, Zhefan Wang, and Yiming Sun**, for their support and friendship during my time in Scotland. Sharing the daily ups and downs together made the PhD experience less stressful and much more memorable. I would also like to give a special thanks to **Bocheng Yuan**, not only for his great help throughout my PhD, but also for introducing me to Chinese food and culture, which became a small but meaningful part of my life here.

Finally, I want to thank my family: **my father and mother**, and **my brother and sister**. Your love, encouragement, and sacrifices have been the foundation behind everything I achieved. Even from far away, your support never felt distant, and it gave me the strength to keep going during the hardest moments. I also want to thank **my wife**, **my daughter**, and **my son** for being with me throughout this journey. Your patience, love, and presence made everything easier, and I could not have done this without you.

Lastly, I would like to thank **all my friends**, especially those back home. During my PhD, I often missed the time we spent together, and those memories and moments always kept me going.

With sincere thanks,
*Mohanad Al-Rubaiee*

# Author Declaration

I hereby declare that the submitted PhD thesis, titled **Monolithic 1.55-µm Passively Mode-Locked Semiconductor Lasers for Optical Clock and Multi-Wavelength / Frequency-Comb Microwave Photonics**, is the result of my independent and original research conducted at the James Watt School of Engineering, University of Glasgow. All sources of information and materials used in the thesis have been clearly cited and acknowledged within the text. Where the work of others has been included, it has been properly referenced following academic conventions.

I solemnly declare that this thesis does not contain any instances of academic misconduct, such as plagiarism, fabrication, or falsification of data. This work has not been submitted, either in whole or in part, for any other degree or qualification. I assume full responsibility for the legitimacy and authenticity of the findings presented in this thesis.

*Mohanad Al-Rubaiee*

# Chapter 1: Introduction and Literature Review

This chapter introduces the background, motivation, and key literature relevant to this thesis. It first outlines the growing demand for compact and integrable optical sources driven by high-capacity communication networks, optical clocking, and microwave photonic systems. The chapter then reviews semiconductor mode-locked laser diodes as promising platforms for generating low-jitter optical clocks, multi- and dual-wavelength emission, and optical frequency combs. Particular attention is given to the challenges of timing jitter, limited comb bandwidth, mode competition, temperature sensitivity, and fabrication complexity in existing devices. Finally, the chapter highlights the need for monolithic InP-based laser platforms that combine stable optical performance with simple fabrication, and defines the main aims of the thesis in addressing these limitations through four novel device concepts.

## 1.1 General background and motivation

Over the past few decades, the rapid growth of global data traffic has been driven by cloud computing, high-capacity data centres, 5G and emerging 6G networks, and bandwidth-hungry applications such as ultra-high-definition video, virtual reality, and industrial automation. To sustain this growth, modern communication systems increasingly rely on optical technologies to provide very large bandwidth, low loss over long distances, and immunity to electromagnetic interference [1]. At the same time, many electronic subsystems still operate at microwave and millimetre-wave frequencies, creating a strong demand for compact and efficient interfaces between the optical and electrical domains [2]. In this context, optical clock generation, optical frequency combs, and photonic generation of microwave signals have emerged as key enabling technologies [2,3]. Optical clock sources with high repetition rates and low timing jitter are essential for high-speed serial communication links, coherent transmission, and precise sampling systems. Optical frequency combs, consisting of many phase-locked spectral lines, can simultaneously provide multiple wavelength channels for wavelength-division multiplexing (WDM), coherent LiDAR, and advanced sensing schemes [3,4]. Likewise, converting optical signals into spectrally pure microwave and millimetre-wave tones enables microwave photonic links, radio-over-fibre distribution, and high-resolution radar and instrumentation [2]. In all of these applications, there is a strong motivation to realise compact, low-cost, and integrable light sources that can deliver multiple stable wavelengths or tightly controlled mode spacings on a single chip [4]. Among the various platforms available, semiconductor mode-locked laser diodes (SMLLDs) play a central role. Compared with bulk solid-state or fibre lasers, semiconductor devices are inherently compact, can be directly electrically pumped, and are naturally compatible with photonic integration. Two-section SMLLDs, in which a gain section is combined with a saturable absorber (SA), can generate picosecond and sub-picosecond pulse trains at repetition rates ranging from a few gigahertz up to beyond 100 GHz [5,6]. These devices, therefore, offer an attractive route to integrated optical clock sources and on-chip optical frequency combs [4,6]. Furthermore, by engineering the cavity and feedback structures, semiconductor lasers can be designed to support multi-wavelength or dual-wavelength operation, enabling direct generation of multiple optical carriers or stable microwave beat signals from a single device [7,8]. However, achieving the required performance in a practical and scalable form is far from trivial. For example, conventional approaches to multi-wavelength operation often rely on arrays of single-wavelength lasers combined by passive optical couplers, or on external modulators and filters to carve out multiple lines from a single source [7]. These architectures tend to be bulky, lossy, and fabrication-intensive, which limits their suitability for large-scale integration and cost-sensitive applications. At the same time, purely passive SMLLDs can suffer from relatively high timing jitter and sensitivity to temperature and fabrication tolerances [6]. For dual-wavelength and multi-wavelength devices intended for microwave photonics, it is particularly challenging to maintain stable frequency spacing and good spectral purity while keeping the design simple and manufacturable.

These considerations have motivated extensive research into novel cavity and grating concepts, advanced active-region designs, and hybrid locking schemes to improve stability, broaden the usable optical bandwidth, and reduce system complexity. Within this broad landscape, there is a clear need for monolithic semiconductor lasers that can provide well-controlled multi-wavelength or dual-wavelength operation, generate broadband low-jitter pulse trains, and remain compatible with practical fabrication and integration. Addressing this need is the main motivation for the work presented in this thesis.

## 1.2 Optical clock generation with semiconductor mode-locked laser diodes

High-speed digital systems and advanced Complementary metal–oxide–semiconductor (CMOS) technologies require clock signals with both high repetition rates and excellent timing stability. Optical clock generation based on mode-locked lasers has therefore become an important route to improving overall system performance. In particular, passively SMLLDs are attractive because they can generate high repetition rate pulse trains in a compact, fully integrated format [9–11]. However, purely passive SMLLDs typically exhibit higher timing jitter than actively or hybrid mode-locked lasers. Fig. 1.1 shows how timing jitter shifts the clock sampling edge and can degrade reliable data sampling in high-speed systems. This is mainly due to spontaneous-emission noise, which induces fluctuations in the optical gain, refractive index, and photon density, and consequently leads to variations in pulse timing and degraded timing resolution.

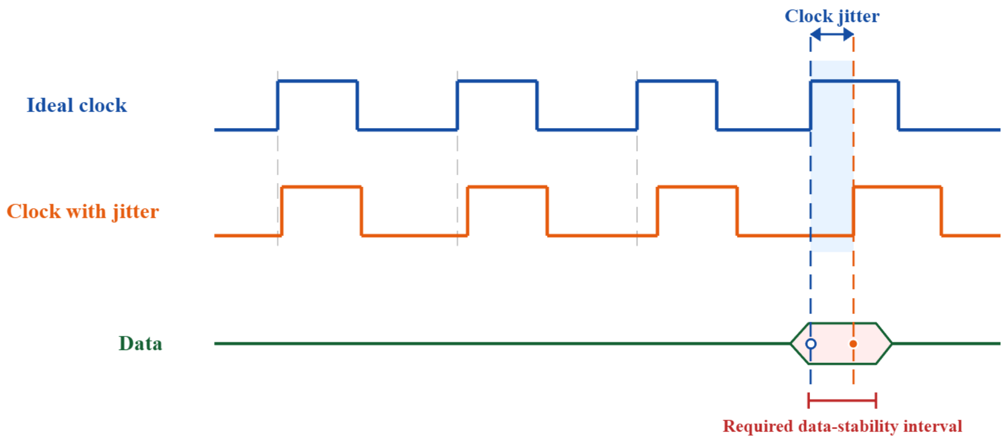


**Fig. 1.1. Illustration of how clock jitter can shift the sampling instant and lead to hold-time violations in high-speed digital systems.**

To suppress this timing noise, hybrid mode locking (HML) can be employed, in which a passively mode-locked laser is injection-locked to an external electrical signal at the fundamental mode-locking frequency or one of its subharmonics [12,13]. RF injection locking of SMLLDs has been widely investigated as an effective technique to stabilise the repetition rate and reduce phase noise. In the InGaAsP/InP material system with n-doped InP substrates, RF powers as high as 26 dBm have been reported for second subharmonic HML of a colliding-pulse SMLLD operating at 28 GHz [14], and around 20 dBm for second- and third-subharmonic HML of a DBR SMLLD at 33 GHz [15]. On a III–V-on-silicon platform, fundamental HML of a 1.009 GHz SMLLD has been demonstrated with approximately 8 dBm of injected RF power [16]. These results highlight both the effectiveness of RF injection locking and the relatively high RF power that is often required, especially for subharmonic operation at tens of gigahertz. Subharmonic injection locking is particularly attractive because it allows a high-repetition-rate laser to be stabilised using a lower-frequency electrical signal [17,18]. This simplifies the electronic circuitry, reduces cost, and makes it easier to drive very high repetition rate SMLLDs using more accessible RF sources. As a result, subharmonic HML has become a key technique for realising compact, low-noise optical clock sources for high-speed digital and microwave photonic systems.

## 1.3 Multi-wavelength mode-locked DFB lasers for DWDM and integrated photonics

Multi-wavelength distributed feedback (DFB) semiconductor lasers have attracted significant attention in both research and industry, particularly for applications in optical communications, dense wavelength division multiplexing (DWDM) sources, and spectroscopic sensing [19–21]. By generating multiple coherent wavelengths within a single compact device, these lasers offer reduced footprint, cost, and complexity compared to discrete single-wavelength sources [22,23]. Passively mode-locked DFB (ML-DFB) lasers, capable of producing stable short pulses at multiple wavelengths simultaneously, are especially promising for high-speed optical interconnects, coherent LiDAR, and advanced photonic integration. Traditionally, multi-wavelength lasing is realised using monolithically integrated multi-wavelength DFB laser arrays (MLAs) arranged in a parallel configuration [24]. To deliver a single optical output, these arrays often incorporate multimode interference (MMI) combiners or funnel combiners [25,26]. While effective, such combiners introduce optical power losses, increase the overall chip footprint, and typically require complex heterogeneous integration techniques such as butt-joint integration, selective area growth (SAG), or quantum well intermixing (QWI) [27–29]. To avoid these issues, series-configured MLAs have been proposed, in which multiple DFB sections are arranged in a cascade without optical combiners [30]. However, in both parallel and series configurations, achieving stable multi-wavelength operation and, in particular, simultaneous mode-locking across all wavelengths remains challenging due to mode competition and temperature sensitivity. These array-based architectures, therefore, remain relatively bulky and lossy, and they require complex integration steps such as on-chip combiners or cascaded sections. Fig. 1.3 conceptually compares such traditional multi-wavelength DFB arrays with the single-cavity multi-wavelength DFB strategy pursued in this work, where all wavelengths are generated within one compact grating cavity. Interactions between coexisting modes, through shared gain and carrier dynamics, can give rise to mode competition, leading to spectral instability and degraded pulse quality if not carefully controlled [31]. Temperature fluctuations further complicate stable operation by modifying the effective refractive index and, hence, the Bragg condition, causing wavelength shifts and disrupting phase coherence [6].

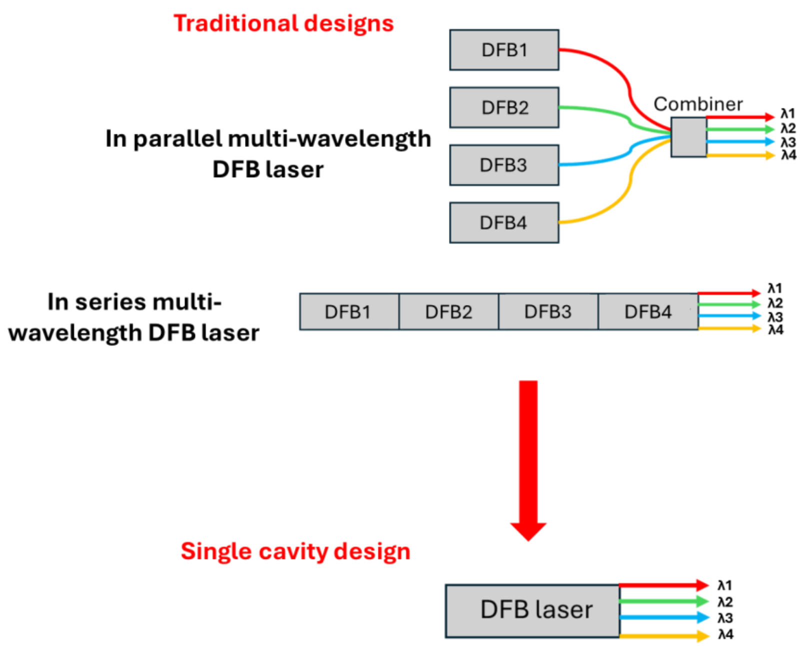


**Fig. 1.2. Conceptual comparison of traditional multi-wavelength DFB arrays with a single-cavity multi-wavelength DFB laser, where all wavelengths are generated in one compact device.**

A variety of approaches have been explored to realise multi-wavelength mode-locking in semiconductor lasers, including ring lasers, external-cavity injection locking, arrayed waveguide gratings (AWGs), and hybrid mode-locking schemes [32–35]. These techniques can provide multi-wavelength output, but they often rely on long fibre-based external cavities, additional reflectors and filters, external modulators, or complex heterogeneous integration, which increases system complexity, insertion loss, and limits the potential for compact monolithic integration. Consequently, there is a strong motivation to develop more compact and scalable solutions that enable stable multi-wavelength mode-locked operation within a fully integrated semiconductor platform. Compared with Fabry–Perot-based multi-wavelength lasers, the multi-wavelength DFB configuration offers relaxed cleaving tolerance and improved reproducibility, since the lasing wavelengths are determined by the grating and cavity design rather than facet positions. Moreover, because the optical cavity is fully defined within the waveguide, DFB lasers are naturally compatible with monolithic integration of additional components such as semiconductor optical amplifiers (SOAs), electroabsorption modulators (EAMs), and on-chip filters, which is much more difficult in multi-wavelength Fabry–Perot lasers that rely on facet reflectivity. While quantum-dot (QD) mode-locked lasers can generate broad optical combs, most reported devices operate near 1.3 µm, and QD devices at 1.55 µm generally exhibit broader pulses and lower modal gain compared to mature multiple-quantum-well (MQW) designs [36–38]. As a result, MQW-based multi-wavelength DFB lasers remain a highly attractive solution for compact, integrable, and spectrally stable sources in the C-band.

Beyond multi-wavelength operation, dual-wavelength semiconductor lasers form a particularly important special case for photonic microwave generation. A conventional optical approach is to generate a microwave signal by beating two discrete single-longitudinal-mode (SLM) lasers on a high-speed photodetector. The heterodyne signal corresponds to the optical frequency spacing between the two lasers. However, such dual-laser systems are prone to phase and frequency instability because each laser experiences independent thermal and mechanical fluctuations, so additional stabilisation circuits or phase-locking mechanisms are often required [39,40]. Another widely used method employs external modulation of a single laser to generate sidebands, from which two lines are selected using optical filters. Although this technique can generate microwave and even millimetre-wave frequencies, it relies on bulky and expensive modulators, high-speed drivers, and precise optical filtering and alignment [41,42]. Monolithic dual-wavelength semiconductor lasers (MDSLs) address many of these limitations by generating two optical longitudinal modes within the same physical cavity. Because both modes share identical environmental and thermal conditions, the frequency spacing between them is intrinsically more stable, and a microwave signal can be obtained simply by optical heterodyning at a fast photodetector, without external modulators or complex filtering. Recent reviews have highlighted robustness, reproducibility, and fabrication tolerance as key challenges for multi-wavelength and dual-wavelength lasers, especially when targeting narrow and controllable frequency spacings [7]. Several DFB-based strategies have been proposed to realise dual-wavelength lasing, including the introduction of two phase shifts along the cavity [43–45]. While this approach can produce dual-mode operation, the achievable frequency spacing is fundamentally constrained by the physical length and arrangement of the phase-shifted sections, making it difficult to reach arbitrary or widely tunable spacings, particularly below 100 GHz. Sidewall grating structures offer another route to dual-mode operation with potentially wider separations, but they often require precise lateral asymmetry or complex modulation of the grating coupling coefficient, which increases fabrication complexity and can compromise device stability [46,47]. Alternative designs based on distributed Bragg reflector (DBR) lasers suffer from issues such as front scattering loss, thermal cross-talk between sections, and the need for buried gratings, all of which complicate the realisation of robust dual-mode lasing [48]. Patterned-index Fabry–Perot lasers, which rely on post-growth index patterning and precise facet definition to select two modes, are also sensitive to cleaving tolerances and are less compatible with dense photonic integration [49]. In many of these multi- and dual-wavelength semiconductor laser architectures, stable pulsed or comb-like operation can be achieved by incorporating a monolithically integrated SA section, forming a two-section mode-locked laser. In this configuration, the gain section is forward-biased to provide amplification, while the reverse-biased SA introduces an intensity-dependent loss: low-intensity light is absorbed, whereas high-intensity spikes saturate the absorber and are transmitted, enabling pulse formation and passive mode-locking. This mechanism has been analysed in detail using delay-differential equation models [50], and sub-5 ps recovery times have been experimentally demonstrated in Al-quaternary MQW absorbers, making them suitable for high-repetition-rate operation [51]. Previous experimental studies on dual-wavelength DFB lasers have confirmed that this SA-based mode-locking mechanism can support stable dual-mode operation and coherent microwave beat-note generation in compact, monolithic devices [46,52]. Such results highlight the potential of carefully engineered Bragg-grating structures based on MQW to realise robust multi-wavelength and dual-wavelength semiconductor lasers that are well suited to integrated optical communications and microwave photonic systems.

## 1.4 Optical frequency comb generation with semiconductor mode-locked laser diodes

SMLLDs are key components for generating optical frequency combs in integrated photonic systems. Their compactness and stable operation make them ideal for applications where size, cost, and robustness are critical [4,16]. SMLLDs can operate at repetition rates from a few gigahertz to beyond 100 GHz, supporting both high-speed and dense optical communications [53,54]. Their combs have been deployed in long-haul coherent transmission, direct-detection access networks, and passive optical systems [55,56]. By delivering multiple stable wavelengths from a single chip, SMLLDs can replace arrays of discrete lasers, simplifying system design and reducing overall cost. Figure 1.3 illustrates the basic concept of an optical frequency comb, where the optical spectrum consists of many discrete lines separated by a fixed frequency spacing $\Delta f$. In SMLLDs, this spacing is set primarily by the cavity round-trip frequency (i.e., the repetition rate), while the overall spectral width determines how many usable comb lines are available. From a communications perspective, a wider comb is particularly valuable because it can provide a larger number of wavelength channels for WDM or multi-carrier coherent transmission, enabling higher aggregate data throughput from a single compact source. More broadly, increasing the comb bandwidth expands the usable optical frequency range for system design, allowing greater flexibility in channel allocation and improving the practicality of chip-scale comb sources for high-capacity links.

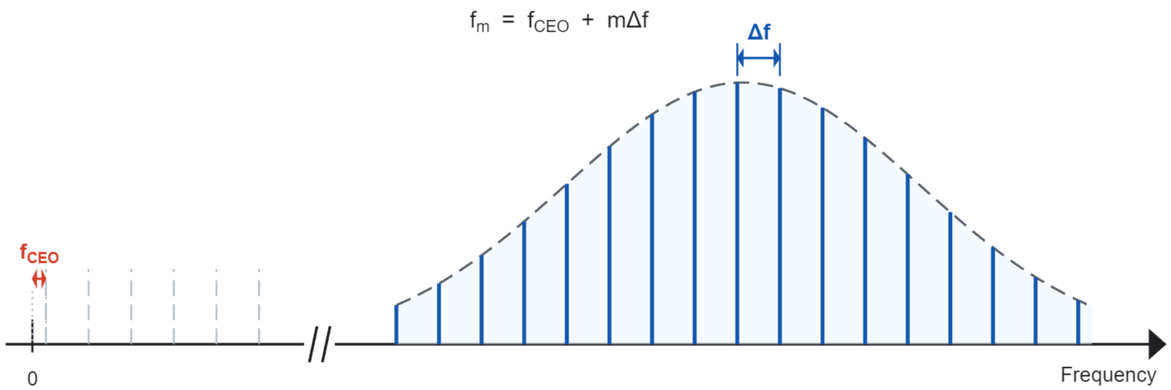


**Fig. 1.3. Conceptual frequency-domain representation of an optical frequency comb, showing discrete lines with uniform spacing $\Delta f$ and an offset frequency $f_{CEO}$.**

In the pursuit of wider optical frequency combs, quantum-dot and quantum-dash mode-locked lasers have been extensively investigated, particularly for their potential to deliver broad optical spectra [57,58]. For example, a record-high flat-top optical comb with a −3 dB bandwidth of 11.5 nm (corresponding to 20 comb lines) at 25 °C was reported using a 100 GHz, 1.3 μm InAs/GaAs quantum-dot conventional colliding-pulse mode-locked laser [58]. However, the performance of two-section quantum-dot and quantum-dash SMLLDs operating around 1.5 μm remains relatively underdeveloped, often limited by lower modal gain and broader pulse durations [37,59,60]. In contrast, MQW-based designs have proven more reliable in this wavelength range and typically offer superior gain characteristics. A notable example is a 40 GHz AlGaInAs/InP device that incorporated quantum well intermixing to suppress nonlinear broadening effects and achieved sub-picosecond pulses [61]. Nevertheless, many reported MQW structures still exhibit limited gain flatness, and their optical bandwidth often falls short of what is required for truly wide comb applications. This creates a clear need for MQW-based designs that explicitly prioritise spectral width as a primary performance metric. Previous efforts to broaden the optical spectrum of MQW-based comb sources have often relied on ring laser geometries combined with additional spectral-shaping elements. In one approach, a Mach–Zehnder interferometer was integrated with a passively mode-locked MQW ring laser to enhance spectral flatness; however, the resulting system delivered relatively low output power (around 2 mW), pulse durations longer than 20 ps, and a −10 dB bandwidth of only 8.7 nm [62]. In another demonstration using a similar ring-laser configuration, a −20 dB bandwidth of 40 nm was achieved, but the spectrum exhibited large power non-uniformity (up to 20 dB), the −3 dB bandwidth remained narrow at about 6 nm, and the average coupled power was limited to approximately 1 mW [63]. One effective strategy to extend the gain spectrum in MQW lasers is to employ asymmetric multiple quantum well (AMQW) structures, in which the active region comprises wells of varying thicknesses or compositions. Because each quantum well provides gain at a slightly different wavelength, their superposition yields a broader and potentially flatter overall spectral profile [64]. This concept was experimentally demonstrated by Hou et al. [65], who reported a passively mode-locked AMQW laser generating a 100 GHz-spaced optical frequency comb with an 8.05 nm −3 dB bandwidth. These results highlight AMQW engineering as a promising route to broadband MQW-based comb sources, and motivate further optimisation of quantum-well configurations to enhance spectral overlap, improve modal gain distribution, and support sub-picosecond pulse generation in compact SMLLDs.

## 1.5 Aim of this research

The aim of this research is to develop and experimentally demonstrate a set of compact monolithic AlGaInAs/InP-based SMLLDs around 1.55 μm that overcome key practical limitations in timing jitter, optical bandwidth, and multi-/dual-wavelength stability for optical clocking and microwave photonic applications. Specifically, the work targets four novel devices:

1)A semi-insulating-substrate mode-locked laser enabling low-jitter hybrid RF injection locking with reduced RF power.
2)A chirped sampled-grating DFB laser that realises intrinsically stable multi-wavelength mode-locked operation within a single cavity.
3)A waveguide Bragg grating microcavity platform demonstrated in multi-wavelength lasers and readily adapted to dual-wavelength devices, providing compact and thermally stable sources through a simple single-growth, single-etch fabrication process.
4)An AMQW mode-locked laser that broadens the gain spectrum to generate a wide optical frequency comb.

## 1.6 Thesis outline

The overall structure of this thesis is as follows,

Chapter 1 provides a brief introduction to optical clock generation using SMLLDs and reviews the key literature on injection locking, multi- and dual-wavelength DFB structures, and optical frequency comb generation, leading to the motivation and objectives of this thesis.

Chapter 2 presents the theory and design framework used in this work. It reviews the operation of SMLLDs, introduces the numerical tools for cavity and grating modelling, and describes the stabilisation schemes and multi-wavelength DFB designs based on chirped sampled Bragg gratings, waveguide Bragg grating microcavities, and an AMQW structure for broadband 100 GHz comb generation.

Chapter 3 presents details of each stage in the device fabrication process. The grown III-V epitaxial wafers are transformed into laser bars through a sequence of steps, including etching, metal deposition, insulation layer deposition, thinning, annealing, and cleaving.

Chapter 4 presents the results and discussion for a 10-GHz passively SMLLD on a semi-insulating(SI) InP substrate. It investigates fundamental and subharmonic RF injection locking and optical injection locking, demonstrating sub-Hertz RF linewidths and sub-100-fs timing jitter for optical clock applications.

Chapter 5 presents the results and discussion for compact multi-wavelength passively mode-locked DFB lasers based on chirped conventional and four-phase-shifted sampled Bragg gratings. It demonstrates stable four- and six-wavelength operation around 1.55 μm with uniform channel spacing, high SMSR, near–transform-limited pulses, and discusses the thermal stability and device reproducibility of the proposed grating design.

Chapter 6 presents the results and discussion for multi-wavelength mode-locked and dual-wavelength DFB lasers based on waveguide Bragg grating microcavities, demonstrating controllable tri-, four-, six-wavelength and dual-mode operation with stable wavelength spacing and different beat frequencies for compact mmWave photonic signal generation.

Chapter 7 presents the results and discussion for a broadband 100-GHz optical frequency comb source based on an AMQW passively mode-locked AlGaInAs/InP laser, demonstrating a 14-line comb with a 10.14-nm −3 dB bandwidth around 1525 nm, sub-picosecond pulses.

Chapter 8 discusses the future directions of the thesis, including possible ways to further develop and improve the proposed laser platforms for practical photonic applications, while also considering the main challenges that may arise in design, fabrication, and device performance.

# Chapter 2: Theory and Design

This chapter introduces the theoretical background and design concepts that underpin the semiconductor laser devices investigated in this thesis. It reviews the operating principles of semiconductor mode-locked lasers, including passive, active, and hybrid mode locking, and outlines the main material systems, device structures, and performance metrics relevant to their operation, particularly for the injection-locking studies presented later in Chapter 4. The chapter also presents the numerical tools used for device analysis and design, including transfer matrix and travelling-wave modelling, and introduces the key design concepts employed later in the thesis, such as sampled Bragg gratings for the devices in Chapter 5, waveguide Bragg grating microcavities for the devices in Chapter 6, and asymmetric multiple-quantum-well active regions for the device in Chapter 7. Together, these foundations support the design, simulation, and interpretation of the devices studied in the following chapters.

## 2.1 Semiconductor mode-locked laser diodes

SMLLDs are compact sources of periodic trains of short optical pulses, obtained by locking the phases of many longitudinal cavity modes. In contrast to continuous-wave (CW) operation, where the modes oscillate with random relative phases and the output power is nearly constant in time, an SMLLD emits a sequence of pulses with a repetition rate determined by the cavity round-trip time. Such devices are key building blocks in high-speed optical communication, microwave photonics, optical sampling and integrated frequency-comb systems [5,66,67].

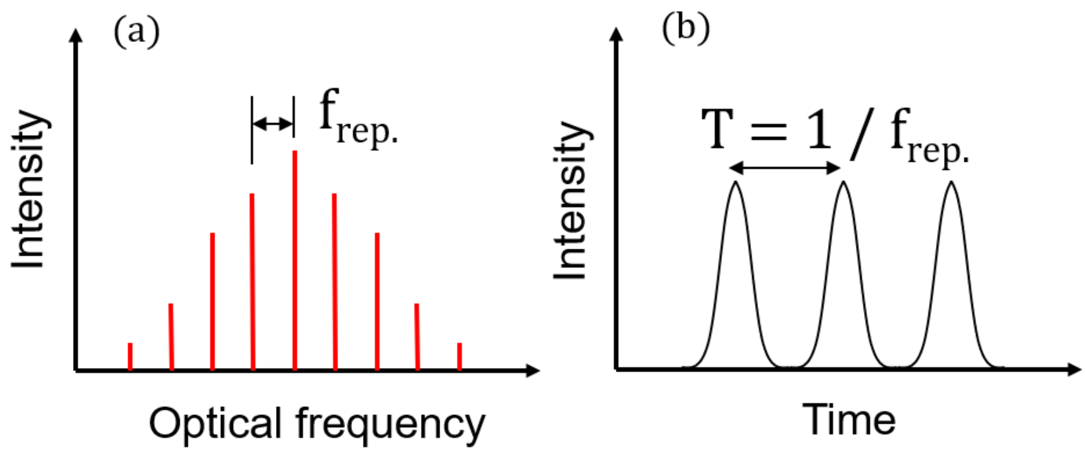


**Fig. 2.1. (a) Optical spectrum with equally spaced comb lines, (b) Corresponding train of pulses in the time domain, with period $T_{rep} = 1/f_{rep}$.**

In the frequency domain, an ideal SMLLD generates an optical frequency comb: a set of evenly spaced, phase-coherent lines with spacing equal to the pulse repetition frequency, as shown in Fig. 2 .1 (a) and (b), respectively. These combs combine the advantages of ultrafast pulse generation with a discrete multi-wavelength spectrum that is directly compatible with wavelength-division multiplexed systems [6,67,68].

### 2.1.1 Principle of mode locking in semiconductor cavities

A linear semiconductor Fabry–Pérot cavity of length $L_{cav}$ and group index $n_g$ supports a set of longitudinal modes with angular frequencies:

$$\omega_m \approx \omega_0 + m \cdot \frac{2\pi c}{2 n_g L_{cav}} \tag{2.1}$$

Where $\omega_0$ is the angular frequency of the reference central longitudinal mode corresponding to $m = 0,\ m$ is an integer and $c$ is the speed of light in vacuum. When these modes oscillate independently with random phases, their interference produces quasi-CW emission with only small temporal fluctuations, as shown in Fig. 2.2(a, b). Mode locking is achieved when a mechanism enforces a fixed phase relationship between the longitudinal modes. When many modes are locked with nearly equal spacing, their interference leads to constructive addition at specific times during the round trip and destructive interference elsewhere, forming a periodic pulse as shown in Fig. 2.2(c,d). The fundamental repetition frequency is approximately:

$$f_{rep} = \frac{c}{2 n_g L_{cav}} \tag{2.2}$$

so that the RF signal observed on a fast photodiode (PD) directly reflects the cavity length and group refractive index [66,68]. The minimum achievable pulse duration is determined by the available gain bandwidth, group-velocity dispersion and nonlinear phase modulation in the cavity. For a transform-limited pulse with a $\text{sech}^2$ temporal profile, the time–bandwidth product (TBP) is $\Delta\nu\, \tau_{FWHM} \approx 0.315$, while for a Gaussian it is $\approx 0.44$. Broad optical bandwidth and controlled dispersion are therefore required to obtain sub-picosecond pulses from SMLLDs [69].

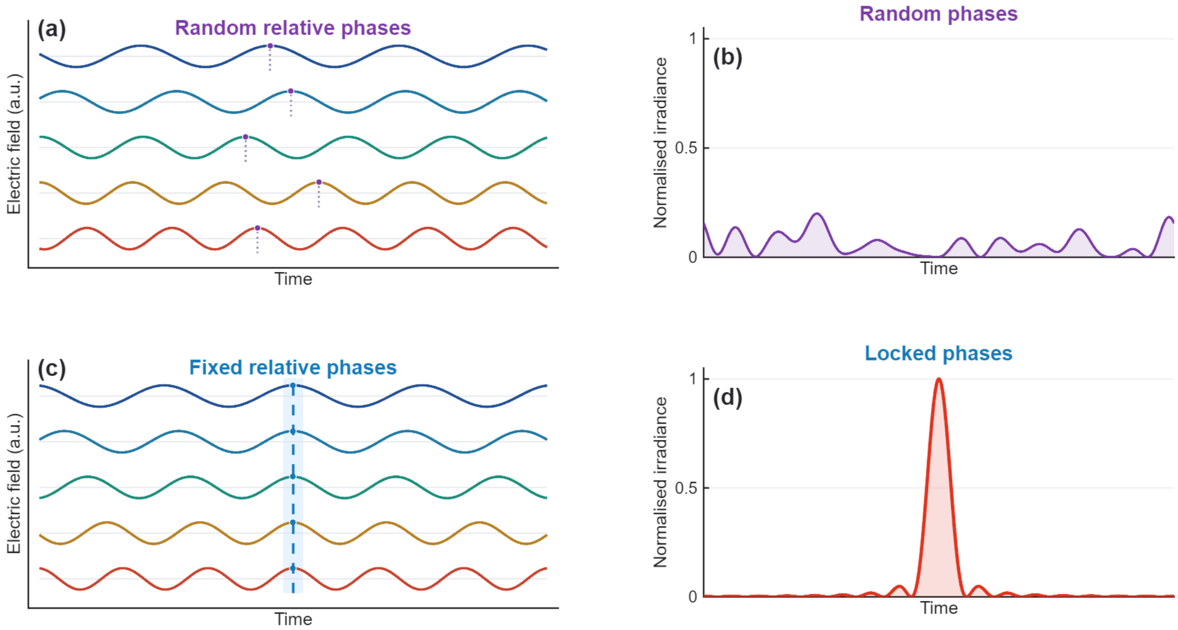


**Fig. 2.2. (a) Several cavity modes with random phases, (b) their corresponding sum showing no clear pulse formation, (c) the same modes with fixed relative phases, and (d) their corresponding sum forming a pulse.**

Theoretical descriptions of mode locking often start from the Haus master equation, which models the evolution of the slowly varying pulse envelope over successive round trips, including gain, loss, dispersion and nonlinear phase [70]. For semiconductor lasers, this framework is extended to include carrier dynamics, linewidth enhancement factors and SA effects, resulting in models such as the delay-differential or travelling-wave equations tailored for SMLLDs [50,66,71].

## 2.1.2 Passive mode locking with semiconductor saturable absorbers

In passive mode locking, the laser cavity contains an intensity-dependent loss element—typically a semiconductor SA—that favours high optical intensities and discriminates against low-intensity noise. The basic idea is to “insert something into the cavity that favours high intensities”: strong maxima grow stronger at the expense of weaker ones, so that after many round trips the optical energy is concentrated into short pulses [69,70,72]. A semiconductor SA is characterised by an absorption coefficient that decreases with increasing optical intensity. A simple model for the intensity-dependent absorption is:

$$\alpha(I) = \frac{\alpha_0}{1+I/I_{sat}} + \alpha_{ns} \quad (2.3)$$

where $\alpha_0$ is the unsaturated (modulatable) absorption, $I_{sat}$ is the saturation intensity and $\alpha_{ns}$ is the non-saturable loss. Here $I$ is the optical intensity inside the absorber and $\alpha(I)$ is the total absorption coefficient at that intensity. This intensity-dependent bleaching behaviour is sketched in Fig. 2.3. At low intensity, the absorber introduces high loss; at high intensity, the absorption saturates, and the loss decreases, so that intense parts of the intracavity field experience lower attenuation. A useful qualitative picture is to regard the SA as a “sponge”: low-intensity light is efficiently absorbed, while high-intensity spikes “burn through” the absorber and experience less loss. On each round trip, intensity fluctuations in the cavity are filtered by this nonlinear loss. Relatively strong spikes experience less loss and become even stronger, while weak parts of the field suffer higher loss and are suppressed. Over many round trips, this positive feedback leads to the formation of a short pulse that is localised in time [69,70,72].

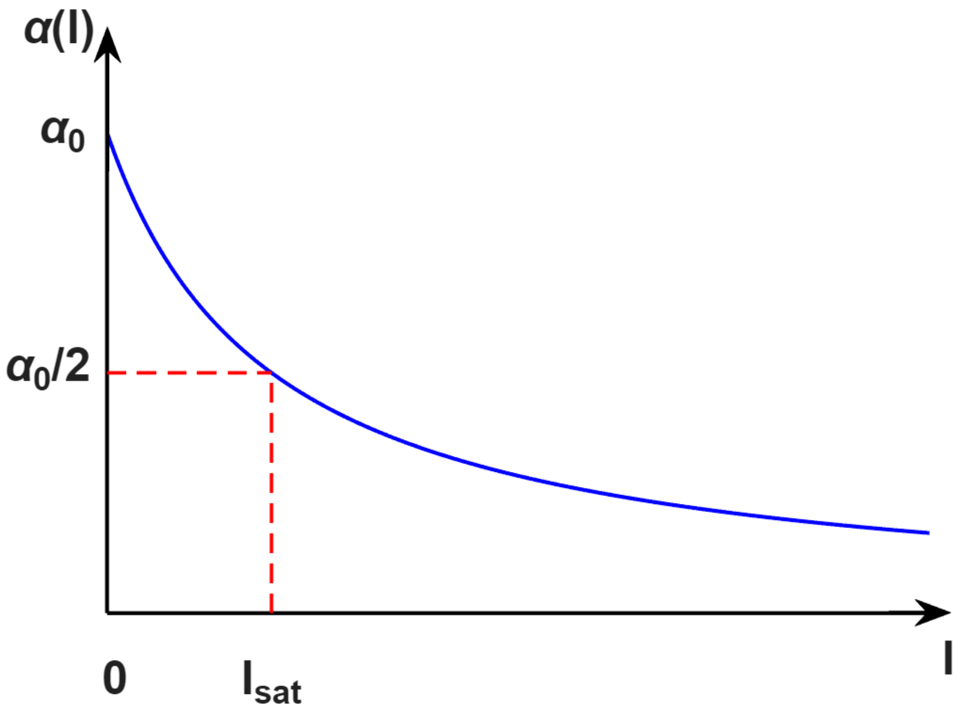


**Fig. 2.3. Intensity-dependent transmission curve of the SA (low transmission at low intensity, high transmission at high intensity).**

In semiconductor lasers, the dynamics are governed not only by the static saturation curve, but also by the carrier recovery times in the gain and absorber sections. For efficient passive mode locking, the absorber recovery time should be comparable to or shorter than the cavity round-trip time and shorter than the gain recovery time [50,66,72]. This condition ensures that the net cavity loss quickly returns to a high value outside the pulse, so that only a narrow temporal window satisfies the net-gain condition, gain > loss.

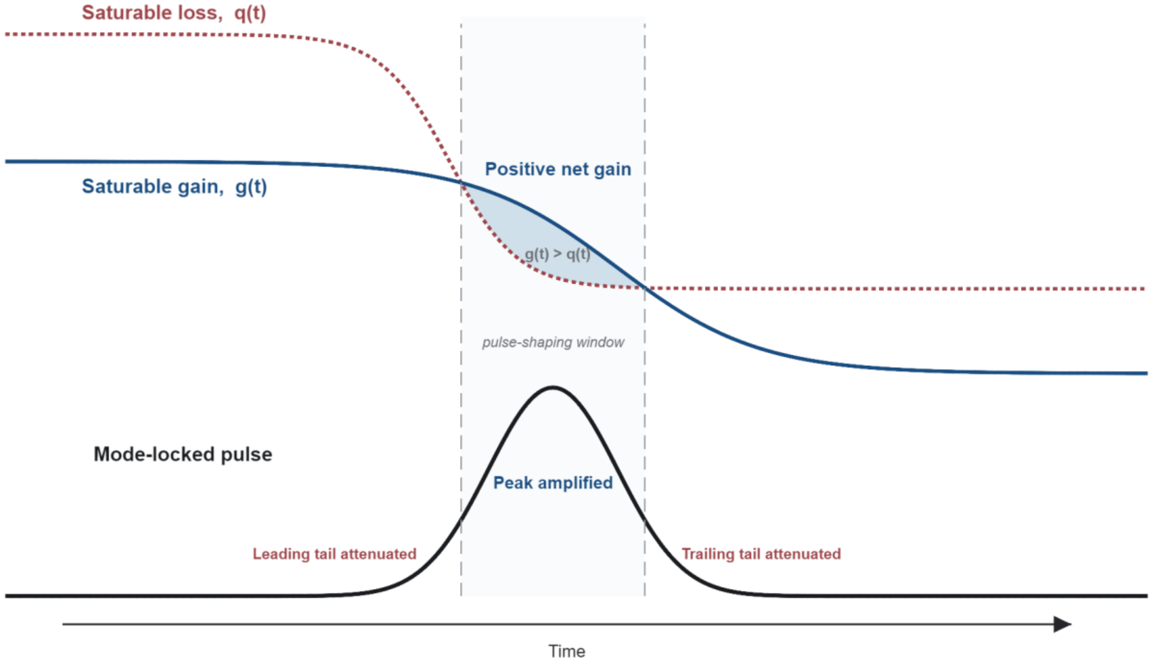


**Fig. 2.4. Gain and loss vs. time during one pulse: low net gain outside the pulse, a narrow temporal window with net gain during the pulse peak, and pulse shortening of the leading and trailing edges.**

This net-gain window is qualitatively depicted in Fig. 2.4. During this window, the central portion of the pulse experiences net gain, whereas the leading and trailing edges are clipped by the combined action of saturable absorption and gain saturation. On the trailing edge, the gain is depleted while the absorber begins to recover, so the net gain becomes negative and the pulse is shortened. This dynamic balance naturally shapes and stabilises the pulse envelope [50,70,72].

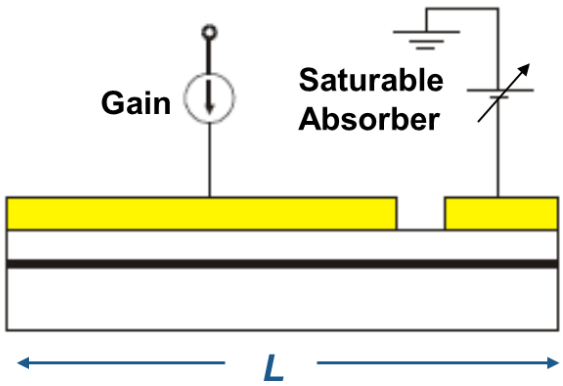


**Fig. 2.5. Schematic of a linear cavity with a gain section and the reverse-biased SA section at one end.**

The corresponding evolution of gain and loss for a single pulse is also shown in Fig. 2.4. In practical SMLLDs, the SA is implemented as a short reverse-biased section of the same waveguide that forms the gain cavity (see Fig. 2.5). By appropriate design of the epitaxial structure, bandgap and quantum-well composition, the SA can be engineered to have a low saturation energy, high modulation depth and sub-picosecond recovery time. For instance, AlGaInAs/InP multiple quantum wells (MQWs) have been shown to provide faster recovery and stronger saturation than conventional InGaAsP/InP MQWs, leading to shorter pulses and higher repetition-rate operation [51,72,73].

### 2.1.3 Active and hybrid mode locking in semiconductor lasers

In active mode locking (see Figure 2.6(b)), the intracavity loss or phase is modulated periodically at the cavity round-trip frequency (or a harmonic thereof) using an externally driven electro-optic or electro-absorption modulator. Only during the peak of the modulation cycle is the net gain positive, so that the cavity preferentially supports pulses synchronised to the modulation signal. In semiconductor lasers, active mode locking has been extensively studied using segmented cavities in which one section is driven with an RF signal [5,66,74]. Active mode locking simplifies synchronisation to electronic clocks but typically produces longer pulses than passive schemes due to the finite modulation bandwidth and weaker nonlinear discrimination.

HML combines an SA with external RF modulation of either the gain or absorber section [66,72,74] (see Figure 2.6 (c)). Here, the passive SA provides fast, intensity-dependent loss, enabling short pulses, while the RF drive serves to stabilise the repetition rate and reduce timing jitter and RF phase noise. This combination is particularly attractive when low-jitter microwave outputs are required, or when the cavity design alone does not guarantee sufficient stability. In practice, hybrid mode-locking schemes are often employed in high-repetition-rate InP-based SMLLDs where both electrical and optical control knobs are available [5,66,74].

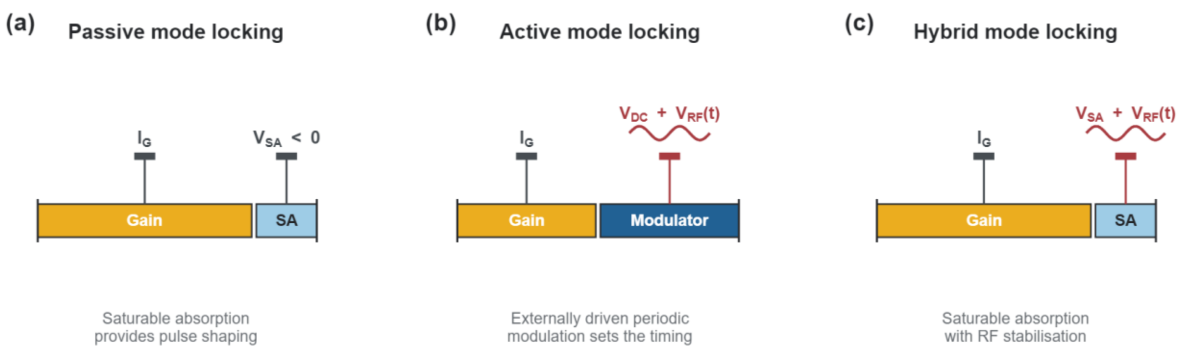


**Fig.2.6. (a) passively mode-locked SMLLD with gain and SA sections, (b) actively mode-locked device with an RF-driven electro-absorption or phase-modulator section, (c) hybrid device including both SA and RF modulation.**

### 2.1.4 Device structures and material systems for SMLLDs

Most monolithic SMLLDs for the 1.3–1.55 μm telecom bands are based on InGaAsP/InP or AlGaInAs/InP material systems [6,66,72]. InGaAsP/InP technology is mature and widely used in standard DFB and DBR lasers. However, AlGaInAs/InP quaternary quantum wells provide improved electron confinement, higher conduction-band offset and reduced hole pile-up, which translate into higher differential gain, higher characteristic temperature and more favourable SA dynamics for passive mode locking [51,72,73]. A typical example of the resulting fast absorber recovery time ($\tau$) as a function of reverse bias is shown in Fig. 2.7. For the AlGaInAs/InP structure, the active region consisted of five 6-nm-thick quantum wells separated by six 10-nm-thick barriers. Both the wells and barriers were formed from Al-quaternary materials. Compressive strain (1.2%) in the quantum wells and tensile strain (−0.5%) in the barriers ensured that the radiative transition was predominantly TE-polarised. Measured absorption recovery times as short as 2.5 ps were obtained at a bias of −4 V, while recovery times below 5 ps were consistently observed for reverse biases greater than 3 V. In comparison, higher bias voltages are required to achieve the same recovery time in InGaAsP MQW structures [51]. The simplest SMLLD geometry is the two-section Fabry–Pérot laser, consisting of a long gain section and a short SA section separated by an isolation region as shown in Fig. 2.5. Both sections share the same optical cavity but are biased independently: the gain section is forward-biased, while the SA is reverse-biased to widen the depletion region and accelerate carrier extraction. More complex structures include colliding-pulse configurations (with an SA located near the cavity centre so that counter-propagating pulses interact), extended cavity and ring geometries [5,6,66], and heterogeneous III–V-on-silicon or III–V-on-SiN platforms with low-loss passive waveguides [75,76]. In all these designs, the cavity length sets the fundamental repetition rate through the relation for $f_{rep}$, while the waveguide dispersion, facet or mirror reflectivities and integrated Bragg gratings determine the modal structure and spectral filtering. By combining tailored gain and absorber sections with DFB, DBR or sampled-grating structures, it is possible to engineer multi-wavelength or harmonically mode-locked operation, which is directly relevant to the devices studied later in this thesis [6,66,77].

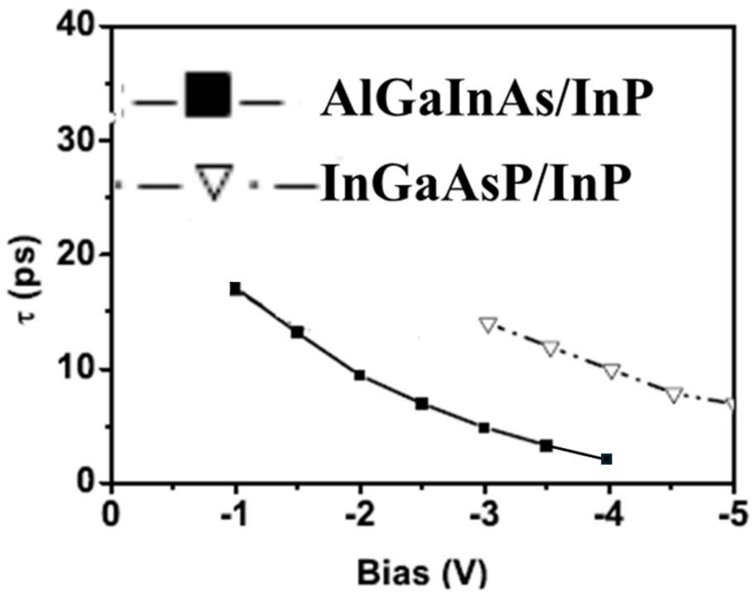


**Fig. 2.7. SA recovery time ($\tau$) versus reverse bias for AlGaInAs/InP and InGaAsP/InP material systems [51].**

### 2.1.5 Performance metrics for semiconductor mode-locked lasers

Several figures of merit are commonly used to characterise SMLLDs and will be referenced throughout this thesis:

- Pulse duration and optical bandwidth. SMLLDs using quantum-dash or quantum-dot gain media can generate sub-picosecond pulses with tens of nanometres optical bandwidth [6,57]. The achievable pulse width is governed by the gain bandwidth, cavity dispersion, absorption/gain recovery times, self-phase modulation effects and saturation properties of the SA and gain.
- Repetition frequency $f_{rep}$. The fundamental repetition rate is set primarily by the cavity length and group refractive index. Monolithic SMLLDs cover a broad range from ~1 GHz (long extended cavities) to beyond 100 GHz (short cavities, colliding-pulse and DFB/DBR-based designs) [5,66,77]. Harmonic mode locking, where multiple pulses circulate in the cavity, can further increase the effective repetition rate without reducing the physical length.
- Timing jitter and RF linewidth. The RF linewidth of the fundamental repetition tone is a direct measure of timing jitter. SMLLDs historically exhibit higher jitter than fibre lasers [5], but progress in cavity design, HML and material engineering has reduced RF linewidths to the Hz–kHz range in integrated platforms [6,67,75,76].
- Optical linewidth of individual comb lines. For coherent communications or microwave photonics, narrow comb-line linewidths (down to hundreds of kHz) are

desirable [5,6]. Extended cavities, low-loss waveguides and reduced carrier-induced index noise are critical to achieving such performance [75,76].

- Average and peak power. The average output power must be sufficient for system applications [5,66], while high peak power enables nonlinear functions such as wavelength conversion or supercontinuum generation [6,72]. Device optimisation often balances power handling (via wider waveguides or external amplification) with thermal management and reliability.

These metrics will be used later to compare and analyse the performance of the mode-locked structures investigated in this work.

## 2.2 Numerical simulation tools

Besides analytical models, this thesis makes use of numerical simulations to support the design and interpretation of Bragg-grating semiconductor lasers. Two complementary tools are employed:

- A frequency-domain transfer matrix method (TMM), based on coupled-mode theory, to calculate the reflection and transmission spectra of uniform, chirped, phase-shifted and sampled Bragg gratings [78–80].

- A time-domain travelling-wave model (TWM), implemented in the FreeTWM software package, to simulate the longitudinal dynamics of multisection semiconductor lasers, including gain and SA sections and distributed Bragg gratings [81–83].

The goal of these simulations in this thesis is modest: they are used to check that the designed grating structures provide the expected spectral response, and that realistic device parameters can support the type of multiple-wavelength or passively mode-locked operation discussed later.

### 2.2.1 Transfer matrix method for Bragg gratings

The design of DFB/DBR and sampled-grating structures is supported by a one-dimensional model based on coupled-mode theory and the TMM [78–80]. For a Bragg grating with period $\Lambda_0$, the free-space Bragg wavelength $\lambda_B$satisfies the Bragg condition

$$\lambda_B = \frac{2n_{eff}\Lambda_0}{m} \tag{2.4}$$

where $n_{\text{eff}}$ is the effective index of the guided mode and $m$is the diffraction order (for semiconductor DFB/DBR lasers, usually $m = 1$) [78,79]. The refractive index along the propagation direction $z$ is written as a weak modulation around an average value,

$$n(z) = n_{eff} + \Delta n(z) \tag{2.5}$$

where $\Delta n(z)$represents the grating-induced refractive index modulation. Under the slowly varying envelope approximation, the electric field can be expressed as a superposition of forward and backward waves,

$$E(z) = R(z)e^{-j\beta_0 z} + S(z)e^{+j\beta_0 z} \tag{2.6}$$

with propagation constant $\beta_0 = n_{eff}k_0$and $k_0 = 2\pi/\lambda_B$ [78–80]. The amplitudes $R(z)$and $S(z)$ satisfy the coupled-wave equations

$$\frac{dR}{dz} + j\Delta\beta\, R = -j\kappa\, S \tag{2.7}$$

$$\frac{dS}{dz} - j\Delta\beta\, S = j\kappa\, R \tag{2.8}$$

where $\Delta\beta$ is the detuning from the Bragg condition and $\kappa$ is the coupling coefficient that describes the strength of scattering between the forward and backward waves [78–80]. For wavelength sweeps, the detuning is typically written as

$$\Delta\beta = \beta - \beta_B \tag{2.9}$$

Where $\beta = \frac{2\pi n_{eff}}{\lambda}$, and $\beta_B = \frac{\pi}{\Lambda_0}$ $(\text{m} = 1)$. For a rectangular grating with a duty cycle of 0.5, the coupling coefficient can be written approximately as [80]

$$\kappa = \frac{(n_2^2 - n_1^2)\,\Gamma_{x,y}}{2n_{eff}^2\,\Lambda_0} \tag{2.10}$$

where $n_1$ and $n_2$ are the refractive indices of the low- and high-index regions, $\Gamma_{x,y}$ is the optical confinement factor of the mode in the grating region, and $\Lambda_0$ is the grating period.

For a uniform grating section of length $L$, the coupled-wave equations have an analytical solution that can be written in matrix form

$$\begin{bmatrix} R(L) \\ S(L) \end{bmatrix} = \mathrm{T}_g \begin{bmatrix} R(0) \\ S(0) \end{bmatrix} \tag{2.11}$$

where $\mathrm{T}_g$ is a $2 \times 2$ transfer matrix that depends on $\kappa$, $\Delta\beta$ and $L$ [78–80]. A convenient closed-form expression is

$$\mathrm{T}_g = \begin{bmatrix} \cosh(\gamma L) - j\frac{\Delta\beta}{\gamma}\sinh(\gamma L) & -j\frac{\kappa}{\gamma}\sinh(\gamma L) \\ +j\frac{\kappa}{\gamma}\sinh(\gamma L) & \cosh(\gamma L) + j\frac{\Delta\beta}{\gamma}\sinh(\gamma L) \end{bmatrix} \tag{2.12}$$

Where $\gamma = \sqrt{\kappa^2 - \Delta\beta^2}$ . More complex gratings (phase-shifted, chirped, apodized or sampled) are treated by dividing the structure into many short, quasi-uniform sections (Fig. 2.8).

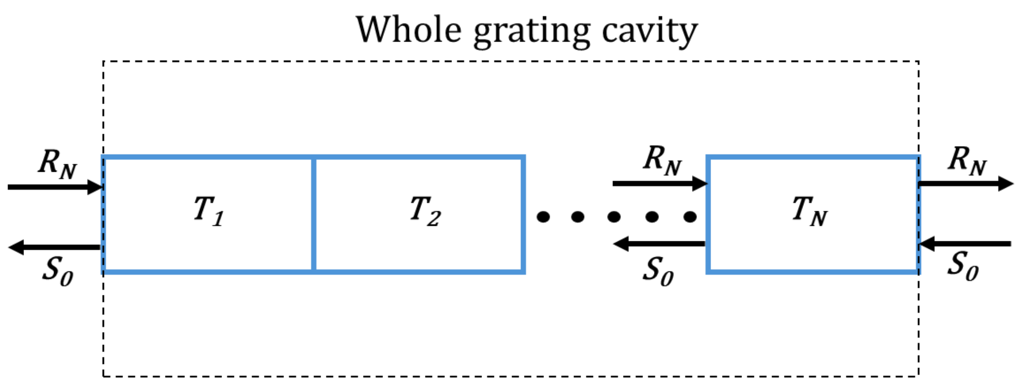


**Fig. 2.8. Schematic of TMM.**

Each section $i$ is assigned its own transfer matrix $\mathrm{T}_i$ based on the local coupling coefficient $\kappa_i$ and detuning $\Delta\beta_i$. Phase shifts, such as a $\pi$ phase shift, are represented by a simple diagonal matrix

$$\mathrm{T}_\phi = \begin{bmatrix} e^{-j\phi/2} & 0 \\ 0 & e^{+j\phi/2} \end{bmatrix} \ (\phi = \pi \text{ for a } \pi\text{-phase shift}). \tag{2.13}$$

The overall response of the grating is then obtained by cascading all matrices,

$$\begin{bmatrix} R_N \\ S_N \end{bmatrix} = T_N T_{N-1} \cdots T_1 \begin{bmatrix} R_0 \\ S_0 \end{bmatrix} = T \begin{bmatrix} R_0 \\ S_0 \end{bmatrix} \tag{2.14}$$

where $T$ is the net transfer matrix of the grating. From $T$, the complex reflection and transmission amplitudes can be obtained by assuming no backward incident wave from the output side ($S_N = 0$):

$$r(\lambda) = \frac{S_0}{R_0} = -\frac{T_{21}}{T_{22}}, t(\lambda) = \frac{R_N}{R_0} = T_{11} + T_{12}r(\lambda) \quad (2.15)$$

and the corresponding intensity spectra are $R(\lambda) = |r(\lambda)|^2$ and $T(\lambda) = |t(\lambda)|^2$. In this thesis, the TMM approach is used to simulate the spectral characteristics of the various grating structures used in the devices (uniform DFB/DBR gratings, phase-shifted gratings, chirped and sampled gratings). The key input parameters are the grating period $\Lambda_0$, effective index $n_{eff}$, index contrast, coupling coefficient $\kappa$, grating length, and any designed phase shifts or chirp profiles. In addition to the power spectra, the group delay can be calculated from the phase of the complex transmission coefficient $t(\lambda)$. Writing $t(\lambda) = |t(\lambda)| e^{j\phi(\lambda)}$, the group delay is obtained as

$$\tau_g(\lambda) = -\frac{d\phi(\lambda)}{d\omega} \quad \text{where} \quad \omega = \frac{2\pi c}{\lambda} \quad (2.16)$$

where $\phi(\lambda) = \arg\{t(\lambda)\}$, and $c$ is the speed of light. In practice, $\phi(\lambda)$ is phase-unwrapped, and the derivative is evaluated numerically over the wavelength grid. The photon-density (field localisation) profile along the grating at a selected wavelength (e.g. at a resonance peak) can be estimated from the internal forward and backward field amplitudes. Using the cascaded section matrices, the fields $R(z)$ and $S(z)$ are reconstructed along the structure, and a simple photon-density profile is taken proportional to the total local intensity,

$$N_{ph}(z) \propto |R(z)|^2 + |S(z)|^2 \quad (2.17)$$

which is typically plotted in normalised form to compare the spatial localisation of different resonances.

In this thesis, the TMM is used specifically for the grating-based device designs discussed later in Section 2.4, particularly Section 2.4.3 for the chirped C-SBG mode-locked DFB laser and Section 2.4.4 for the chirped 4PS-SBG mode-locked DFB laser, which correspond to the experimental devices presented in Chapter 5. It is also used in Section 2.5, particularly Section 2.5.1 for the multi-wavelength WBG microcavity DFB laser and Section 2.5.2 for the dual-wavelength WBG microcavity DFB laser, which correspond to the experimental devices presented in Chapter 6. In Section 2.4.3, the TMM is used to design the chirped conventional sampled Bragg grating by selecting the sampling pattern, chirp rate, and distributed $\pi$-phase-shift positions, and to predict the resulting transmission spectrum and longitudinal photon-density localisation of the four defect modes. In Section 2.4.4, the same TMM approach is used for the chirped 4PS-SBG structure to analyse the corresponding transmission spectrum and modal localisation. In Section 2.5.1, the TMM is used to calculate the stopband resonances, mode number, and group-delay response of the WBG microcavity as the central cavity length and $\pi$-phase-shift configuration are varied for multi-wavelength operation. In Section 2.5.2, the TMM is used to design the dual-wavelength WBG microcavity devices by determining the resonance spacing and confirming that only two modes are supported within the stopband for different central cavity lengths.

### 2.2.2 Time-domain travelling-wave model and FreeTWM

While the TMM provides a static, frequency-domain description of Bragg gratings, the time-domain travelling-wave model (TWM) is used to describe the dynamic behaviour of multisection semiconductor lasers. For this purpose, the open-source FreeTWM code is employed [81–83]. In the TWM, the slowly varying optical field in the waveguide is decomposed into forward and backward envelopes $E_+(z,t)$and $E_-(z,t)$. Under the slowly varying envelope approximation, these obey first-order coupled equations of the form

$$(\partial_t \pm \partial_z) E_\pm(z,t) = i\, P_\pm(z,t) - \lambda(z)\, E_\pm(z,t) - i\, \kappa_\pm(z)\, E_\mp(z,t) \tag{2.18}$$

where $P_\pm(z,t)$are the projections of the material Polarisation onto the forward and backward directions, $\lambda(z)$represents distributed internal loss, and $\kappa_\pm(z)$describes the local distributed coupling between counter-propagating waves (e.g. due to DFB/DBR sections or other index perturbations) [81]. The local complex gain and refractive index are obtained self-consistently from the ratio $P_\pm/E_\pm$, so that amplification, index changes and spatial hole burning are naturally included in the model [81,82]. The carrier dynamics are described by rate equations for a slowly varying average carrier density and a carrier grating that accounts for spatial hole burning. These equations include carrier injection through the local current density, non-radiative and radiative recombination, diffusion and stimulated emission/absorption terms coupled to the optical field [81,83]. In FreeTWM, the semiconductor material response is implemented via a fast convolution kernel derived from a microscopic quantum-well susceptibility model. This allows the same formalism to represent both broad gain sections and sharp, step-like SAs, which is important for modelling passively mode-locked devices [81,82]. To simulate a finite-length cavity, Eq. (2.18) is solved on a discretised space–time mesh, and is combined with facet boundary conditions. A convenient way to write the facet conditions is in matrix form, relating the incoming fields to the outgoing fields at the two ends,

$$\begin{bmatrix} E_+(0,t) \\ E_-(L,t) \end{bmatrix} = B \begin{bmatrix} E_-(0,t) \\ E_+(L,t) \end{bmatrix} \tag{2.19}$$

where $B$ represents the cavity terminations (facet reflectivities, or more general boundary coupling). For a simple Fabry–Pérot cavity with no external injection, $B$ is typically diagonal with elements $\sqrt{R_L}$and $\sqrt{R_R}$, corresponding to the left and right facet reflectivities. A device is then described by specifying, for each longitudinal section, its length and type (gain, SA, passive or grating), material parameters (gain/absorption coefficients, recombination parameters, group index, internal loss) and the facet reflectivity [81,83]. A configuration that is particularly relevant for this work is a simple two-section Fabry–Pérot laser consisting of a long gain section and a short SA section placed near one facet. In the model, most of the cavity length is treated as a gain region, whereas a short segment is assigned stronger unsaturated absorption, faster carrier recovery and no electrical pumping, representing a reverse-biased absorber. When the gain and absorber parameters fall in the passive mode-locking regime, the simulation shows that the field evolves from noise into a stable train of short pulses circulating in the cavity: the gain section provides net amplification, and the SA periodically bleaches during each pulse and recovers between pulses, supplying the intensity-dependent loss required for pulse shaping and stabilisation [50,83]. The main simulation outputs relevant for this thesis are time-domain intensity traces at the facets and the RF spectra of the intensity. The intensity is obtained directly from the facet fields as

$$I_\pm(t) = | E_\pm(t) |^2 \tag{2.20}$$

and the RF spectrum is then calculated from the Fourier transform of the intensity trace,

$$S_{RF}(f) = | \mathcal{F}\{I(t)\} |^2 \tag{2.21}$$

where $f$ is the RF frequency and $\mathcal{F}\{\cdot\}$ denotes the Fourier transform. In practice, the spectrum is evaluated after the transient has decayed, using a steady-state portion of the time trace. Two compact relations are helpful when reading the time traces and RF spectra produced by such simulations.

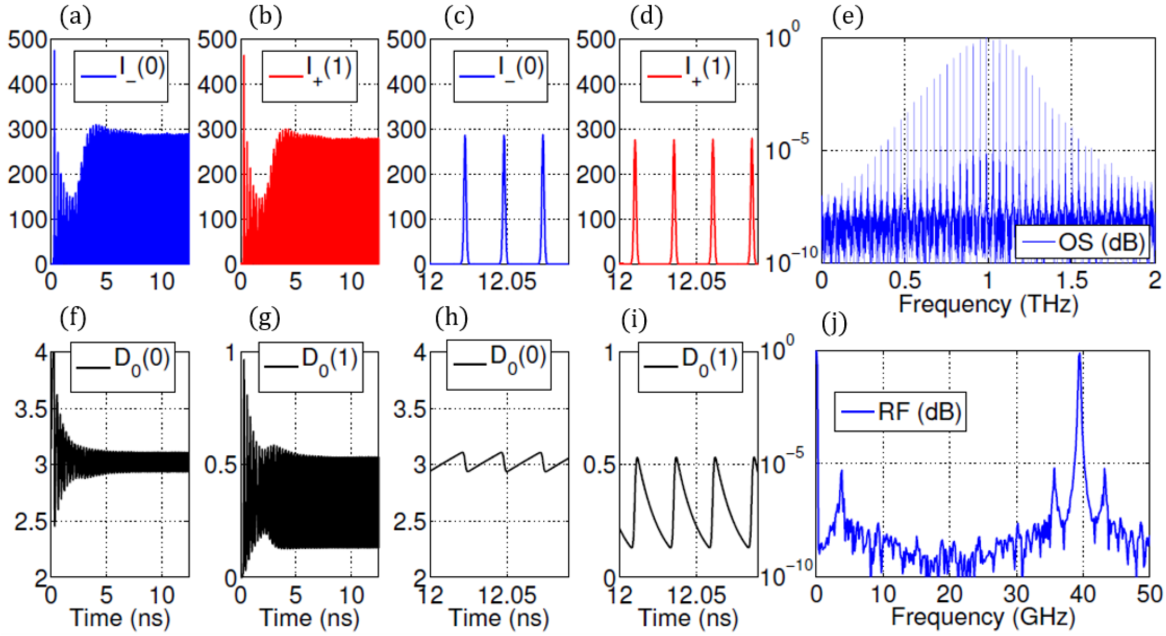


**Fig. 2.9. Representative FreeTWM output for a two-section Fabry–Pérot laser with a gain section and a short SA located at the right-hand end: (a, b) output intensities at the left gain-side facet, $I_-(0)$, and right SA-side facet, $I_+(1)$; (c, d) corresponding zoomed pulse trains; (e) optical spectrum; (f, g) carrier-density variables near the gain-side, $D_0(0)$, and SA-side, $D_0(1)$, ends; (h, i) corresponding zoomed carrier dynamics; and (j) RF spectrum [81].**

First, the pulse repetition period is mainly set by the cavity round-trip time $T_R$, i.e., the time required for light to complete one round trip in the cavity,

$$T_R \approx \frac{2n_g L}{c}, f_{\text{rep}} = \frac{1}{T_R} \approx \frac{c}{2n_g L} \tag{2.22}$$

where $L$ is the cavity length and $n_g$ is the group index. Second, a simple "background stability" condition is that the absorber can substantially recover between successive pulses [50],

$$\tau_{\text{SA}} < T_R, \tag{2.23}$$

where $\tau_{\text{SA}}$ is the effective recovery time of the SA. Fig. 2.9 gives a representative example of the typical outputs: time-domain intensity traces at the facets (showing a regular pulse train), carrier-density traces in the gain and absorber sections (showing pulse-induced bleaching and recovery), and the corresponding optical and RF spectra. In this example, the cavity length is 1.05 mm and the saturable absorber section is 3% of the cavity (about 31.5 μm), corresponding to a mode-locking frequency of about 40 GHz.

In this thesis, FreeTWM is used specifically in Section 2.6.2 for the two-section AMQW passively mode-locked laser, corresponding to the device studied experimentally in Chapter 7. It is used to simulate the passive mode-locking dynamics of the gain–SA cavity, including pulse formation, time-domain intensity traces, autocorrelation behaviour, pulse width, and the RF spectrum at the fundamental repetition frequency and its harmonics.

## 2.3 Stabilisation of the 10 GHz passively mode-locked laser

The theoretical background presented here is directly related to the device studied in Chapter 4. In particular, Section 4.2 discusses stabilisation through RF injection locking results, while Section 4.3 discusses stabilisation through optical injection locking results. Optical pulse trains generated from frequency-comb sources have been used for femtosecond-precision electronic clock distribution [84]. Passively mode-locked devices can generate high-repetition-rate pulse trains with relatively simple drive electronics and good energy efficiency, but their timing jitter is generally higher than in actively or hybrid mode-locked lasers because the pulse train is stabilised only by the intracavity SA dynamics and is continuously perturbed by spontaneous-emission noise [85–88]. In a typical two-section SMLLD, the repetition rate $f_{rep}$ is fixed by the cavity round-trip time $T_R \approx 1/f_{rep}$, while amplitude and phase noise are governed by carrier-density fluctuations in the gain and SA sections and by spontaneous emission [85,87,88]. The RF linewidth of the fundamental beat note scales inversely with the square of the cavity length $L$, so that longer cavities provide intrinsically narrower RF lines but still suffer from residual phase diffusion, which broadens the spectrum and limits timing precision. Timing jitter is commonly quantified using the single-sideband (SSB) phase-noise spectrum $L(f)$ of the RF beat note. For a mode-locked laser with a repetition rate $f_{\mathrm{rep}}$, the root-mean-square (RMS) timing jitter integrated over a frequency range $[f_1, f_2]$ is given by [87,88]

$$\sigma_t = \frac{1}{2\pi f_{rep}} \sqrt{2 \int_{f_1}^{f_2} L(f)\, df} \tag{2.24}$$

An illustration of the ideal oscillator, a real phase-noise–broadened oscillator, and the corresponding time-domain jitter is shown in Fig. 2.10(a-c). Achieving sub-hundred-femtosecond jitter, therefore, requires strong suppression of phase noise over several decades of offset frequency. Injection locking provides an efficient route to stabilise the SMLLD. When an external periodic signal at or near the cavity repetition frequency is applied—either as an RF modulation of the SA (RF injection locking / hybrid mode-locking) or as an optical pulse train injected into the cavity (optical injection locking)—the free-running oscillator can lock to the external reference. This suppresses phase diffusion, narrows the RF linewidth to sub-Hertz levels, and significantly reduces timing jitter. In the present work, we use a 10 GHz AlGaInAs/InP SMLLD on a semi-insulating (SI) InP substrate that is stabilised primarily by RF injection locking, with optical injection used as a complementary technique and for comparison with earlier studies.

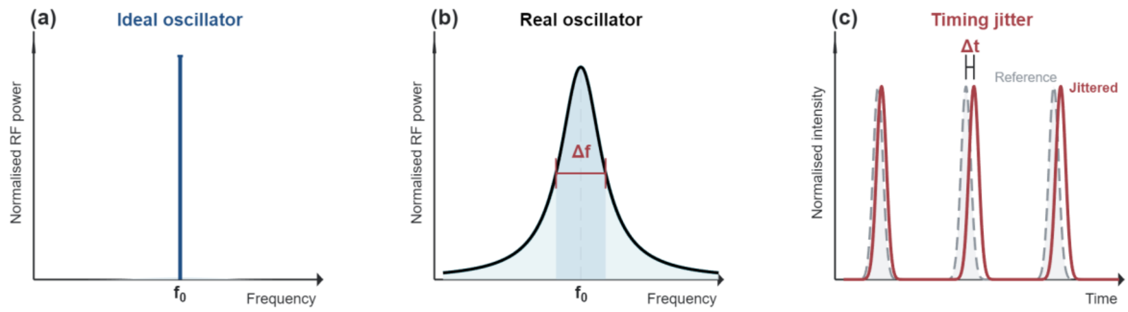


**Fig. 2.10. Conceptual illustration of phase noise and timing jitter. (a) Ideal oscillator, (b) Real oscillator with phase-noise–broadened spectrum, (c) Corresponding time-domain representation showing timing jitter.**

### 2.3.1 Device design on a semi-insulating substrate

The 10 GHz device is based on a two-section AlGaInAs/InP ridge-waveguide SMLLD with a long gain section and a short SA section. The active region comprises three compressively strained quantum wells (QWs). A schematic cross-section of the device, showing the ridge waveguide, three-QW active region, far-field reduction layer (FRL), InP spacer, and SI InP substrate, is presented in Fig. 2.11. The top ridge waveguide is 2.5 μm wide and 1.92 μm high. The second ridge waveguide, which contains the active layer with three QWs, is 14 μm wide and 608 nm high. To reduce optical overlap with the QWs and reduce the vertical divergence angle and improve coupling efficiency to a single-mode fibre (SMF), a 160 nm FRL is placed beneath the active layer and a 400 nm InP spacer layer. Compared with conventional MQW designs, the three-QW structure reduces the nonlinear phase shift accumulated per round trip while providing sufficient modal gain at 1.55 μm. This mitigates self-phase modulation (SPM)–induced spectral broadening and pulse distortion, which become significant in long gain sections [86,89–92]. SPM in semiconductor waveguides arises primarily from carrier-induced refractive-index changes. The nonlinear phase shift can be expressed as

$$\Delta\phi_{NL} \propto \int_0^{L_g} \Delta n_{car}(z)\, \Gamma(z)\, dz \tag{2.25}$$

where $\Delta n_{car}$ is the carrier-induced index change, $\Gamma$ is the local optical confinement factor in the QWs, and $L_g$ is the gain-section length [92,93]. By reducing $\Gamma$ through appropriate waveguide design and limiting the number of QWs to three, the device suppresses SPM while retaining adequate gain for stable passive mode-locking. In contrast to n-doped substrates, the SI wafer minimises parasitic capacitance between the RF electrodes and the underlying substrate, which substantially improves the RC bandwidth of the SA and coplanar waveguide (CPW) contacts [12]. The smaller capacitance allows efficient modulation of the SA at 10 GHz and above with relatively low RF drive power, enabling injection locking with RF powers on the order of –20 to –5 dBm instead of the tens of dBm typically required in devices on conducting substrates. This three-QW SI wafer platform forms the basis of the 10 GHz passively mode-locked laser investigated experimentally in Chapter 4.

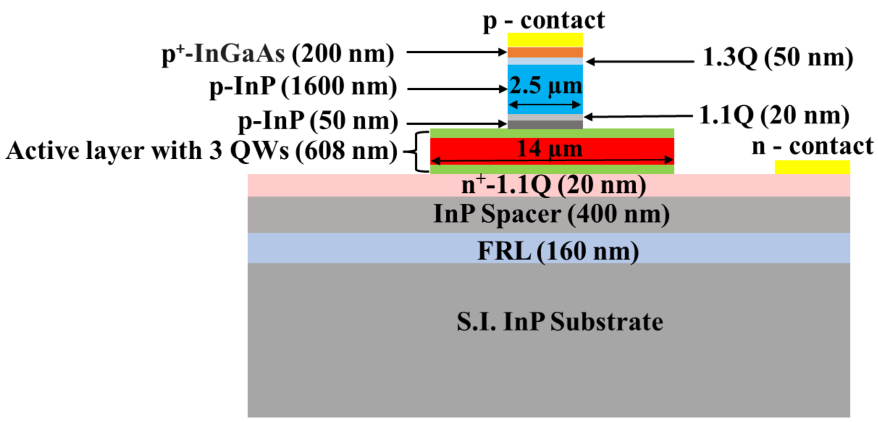


**Fig. 2.11. Schematic cross-section of the 10 GHz AlGaInAs/InP passively mode-locked laser on a SI InP substrate.**

Another key feature of the epitaxial design is the inclusion of an FRL beneath the active region. This thin layer reduces the refractive-index contrast seen by the optical mode, expanding the fundamental transverse mode in both the vertical and lateral directions [89,90]. The corresponding simulated horizontal and vertical far-field intensity profiles for this FRL design, with full width at half maximum (FWHM) angles of approximately 22.9° and 30.6°, respectively, are shown in Fig. 2.12. As a result, the horizontal and vertical far-field divergence angles are significantly reduced compared with standard ridge-waveguide SMLLDs, and the coupling efficiency with a SMF is enhanced. Assuming that both the waveguide mode and the fibre mode can be approximated as Gaussian beams with $1/e^2$ radii $w_x$ and $w_y$ in the horizontal and vertical directions for the SMLLD, and $w_{\mathrm{fb}}$ for the fibre, the coupling efficiency $\eta$ at optimum alignment is given by

$$\eta = \left| \int_{-\infty}^{+\infty} \int_{-\infty}^{+\infty} U_{fb}\,(x,y)\, U_{WG}^{*}(x,y)\, dx\, dy \right|^2 = \frac{4}{\left(\frac{w_x}{w_{fb}} + \frac{w_{fb}}{w_x}\right)\left(\frac{w_y}{w_{fb}} + \frac{w_{fb}}{w_y}\right)} \tag{2.26}$$

where $U_{fb}(x,y)$ is the normalised transverse electric-field distribution of the fibre mode, and $U_{WG}^{*}(x,y)$ is the complex conjugate of the normalised transverse electric-field distribution of the SMLLD waveguide mode. This expression follows from the overlap integral of two orthogonal Gaussian modes [94]. For conventional InP SMLLDs without an FRL, typical mode radii of $w_x \approx 2$ µm and $w_y \approx 1$ µm lead to fibre-coupling efficiencies of order 10 % for a standard SMF with $w_{fb} \approx 4$–5 µm. With the FRL, the simulated mode radii increase to approximately $w_x \approx 2.9$ µm and $w_y \approx 1.9$ µm, yielding coupling efficiencies around 20 % and far-field divergences reduced by nearly 10° in the vertical direction. The device facets are left uncoated, so the facet reflectivity is close to the Fresnel reflectivity of a semiconductor–air interface, typically around 30 % at 1.55 µm [95,96]. This moderate reflectivity keeps intracavity losses low while maintaining sufficient output coupling for efficient detection of the RF beat note.

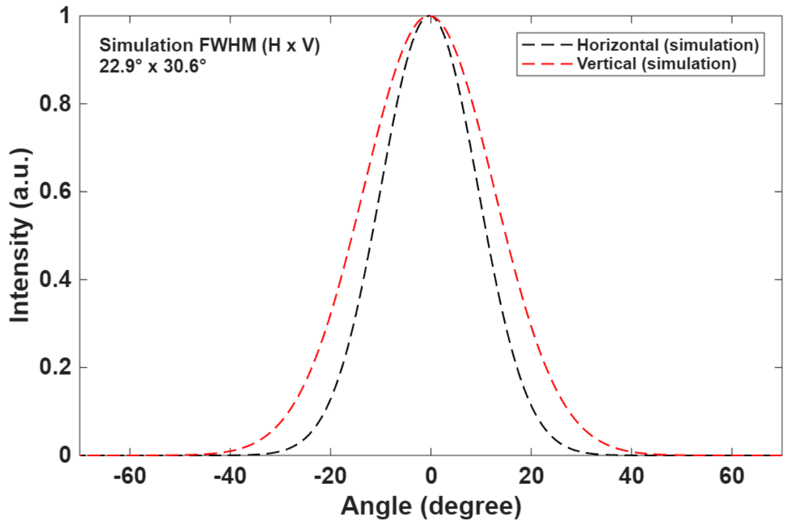


**Fig. 2.12. Simulated horizontal and vertical far-field intensity profiles of the 10 GHz SMLLD with the FRL.**

### 2.3.2 RF injection locking: fundamental and subharmonic operation

This subsection provides the theoretical basis for the RF stabilisation results presented in Section 4.2. In free-running operation, the SMLLD is passively mode-locked by the interplay between gain saturation in the long gain section and intensity-dependent losses in the reverse-biased SA section. Spontaneous-emission-induced fluctuations in the intracavity field cause random variations of the round-trip phase, leading to a finite RF linewidth and timing jitter as described in section 2.3 [85,88,89]. RF injection locking is implemented by applying a sinusoidal electrical signal at frequency $f_{RF}$ to the SA section through a broadband bias-T and an on-chip CPW contacted by a ground–signal–ground (GSG) probe. The DC (Direct current) port of the bias-T provides the reverse bias required for saturable absorption, while the RF port injects the modulation voltage. The SI substrate reduces the parasitic capacitance of the CPW and SA pads, so that the overall RC cut-off frequency, where $R_{SA}$ is the effective series resistance of the SA section and $C_{SA}$ is the associated parasitic capacitance of the SA pad and CPW structure, is given by

$$f_{RC} = \frac{1}{2\pi R_{SA} C_{SA}} \tag{2.27}$$

comfortably exceeds the 10 GHz repetition rate, ensuring that the SA transmission can follow the applied RF modulation without significant attenuation or phase lag. The dynamics of RF injection locking can be captured by treating the SMLLD as a self-sustained oscillator whose phase is driven by the external RF signal. For an RF frequency close to an integer multiple of the repetition rate,

$$f_{RF} \approx \frac{f_{rep}}{n}, n = 1,2, \dots \tag{2.28}$$

the phase difference $\phi$ between the oscillator and the injected signal can be described by an Adler-type equation [13,14,17,18,97]:

$$\frac{d\phi}{dt} = 2\pi(f_{rep} - n f_{RF}) - K_n \sin\phi \tag{2.29}$$

Here $K_n$ is an effective coupling coefficient that depends on the RF modulation depth at the SA, the modulation index of the intracavity loss, and the harmonic number $n$. In steady state, $d\phi/dt = 0$, and locking occurs when

$$| f_{rep} - n f_{RF} | \leq \Delta f_{L,n} = \frac{K_n}{2\pi} \tag{2.30}$$

Since the modulation depth scales approximately with the square root of injected RF power $P_{RF}$, the locking range $\Delta f_{L,n}$ increases with $\sqrt{P_{RF}}$ [13,14,17,97]. For fundamental RF injection locking, $n = 1$ and $f_{RF} \approx f_{rep}$. The SA transmission is modulated once per round trip, pulling the pulse train into synchronism with the external microwave source. Experimental studies of hybrid SMLLDs have shown that under optimal conditions, the RF linewidth can be reduced from tens of kilohertz to below the resolution bandwidth (RBW) of the spectrum analyser, with the integrated timing jitter improving by more than one order of magnitude [13,14,89]. Fig. 2.13 schematically illustrates the principle of RF injection locking: the free-running RF beat note of the SMLLD is slightly detuned from the external reference tone, and application of the RF clock pulls the laser peak onto the reference so that both coincide in frequency.

Subharmonic RF injection locking corresponds to $n > 1$, where the applied RF frequency is a fraction of the cavity repetition rate. In this case, the SA is modulated at a lower frequency $f_{RF} = f_{rep}/n$, but the nonlinear interaction between the pulse train and the SA generates harmonics of the RF modulation at integer multiples of $f_{RF}$. When one of these harmonics coincides with the fundamental repetition rate, the pulse train can lock to the lower-frequency drive signal. This mechanism has been widely exploited to stabilise high-repetition-rate SMLLDs using lower-frequency RF electronics [13,14,17,97]. However, as the subharmonic order $n$ increases, the strength of the relevant harmonic component decreases, so a higher RF power is required to achieve the same locking range. Under efficient RF injection locking—either fundamental or subharmonic—the SSB phase-noise spectrum $L(f)$ exhibits a pronounced reduction over a broad range of offset frequencies.

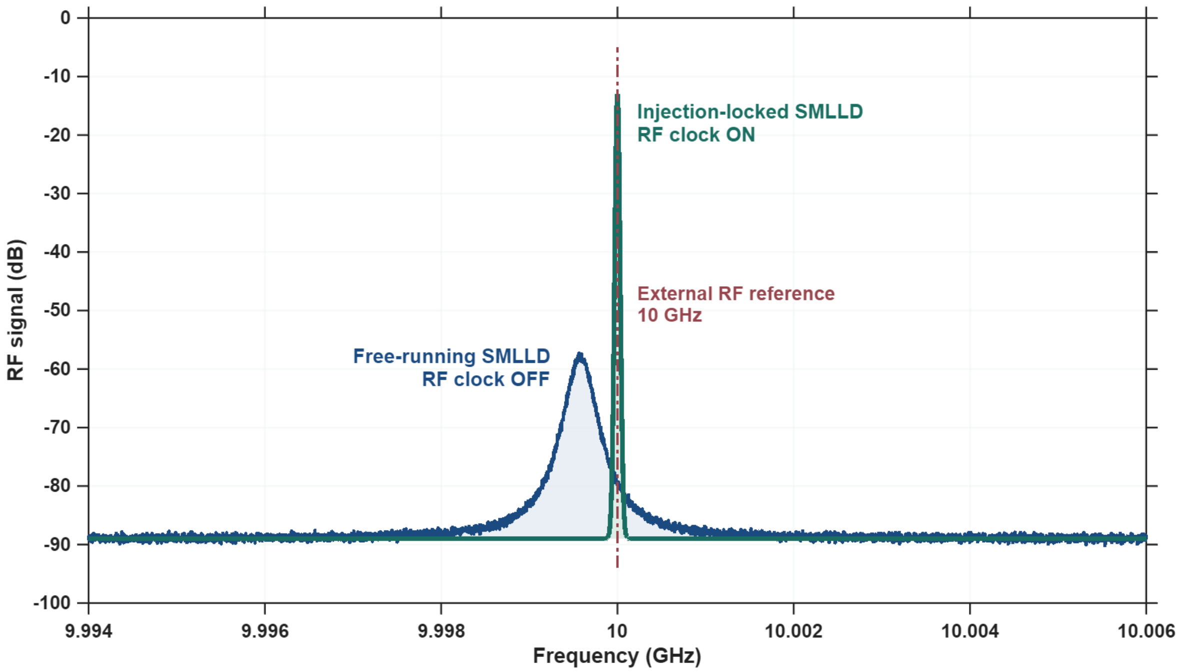


**Fig. 2.13. Schematic RF spectrum illustrating the principle of RF injection locking of the 10 GHz SMLLD.**

### 2.3.3 Optical injection locking

This subsection provides the theoretical basis for the RF stabilisation results presented in Section 4.3. In addition to RF injection, the 10 GHz SMLLD can be stabilised by optical injection from an external master laser that generates a low-noise pulse train at the same repetition rate. In this configuration, pulses from the master mode-locked laser are transmitted through an optical fibre link, attenuated and polarisation-controlled, and then coupled into the gain facet of the slave SMLLD via a lensed fibre and optical circulator. The slave laser can thus be remotely locked to a reference comb located at a different site, making the system suitable for remote optical-clock distribution [18,98,99]. The effect of optical injection on the slave laser can be described using standard injection-locking rate equations. In a simplified phase-only model, the evolution of the phase difference $\phi$ between the slave and master fields obeys an Adler-type equation [97,99]:

$$\frac{d\phi}{dt} = \Delta\omega - \kappa\sqrt{\frac{P_{in}}{P_s}}\sin\phi \tag{2.31}$$

where $\Delta\omega$ is the detuning between the free-running optical frequency of the slave and that of the master, $P_{in}$ is the injected optical power, $P_s$ is the intracavity power of the slave, and $\kappa$ is a coupling coefficient that depends on the cavity parameters and the linewidth-enhancement factor. The locking condition is

$$|\ \Delta\omega\ | \leq \Delta\omega_L = \kappa\sqrt{\frac{P_{in}}{P_s}} \tag{2.32}$$

Within this locking range, the slave repetition rate and optical carrier frequency are forced to follow those of the master, and phase fluctuations of the slave are strongly suppressed. The efficiency of optical injection locking depends on the coupling efficiency $\eta$ between the master laser and the slave cavity, as given in (2.3.1). The FRL-enhanced mode size and reduced divergence of the SMLLD therefore support both improved fibre coupling for output collection and efficient delivery of the injected master pulses [18,89]. As a result, only modest injected optical powers are required to reach the locking regime, making optical injection an attractive complementary stabilisation method for the 10 GHz SMLLD, even though the main stabilisation strategy in this work is RF injection locking.

## 2.4 DFB lasers based on sampled Bragg gratings

The theoretical background presented here is directly related to the devices studied in Chapter 5. In particular, Section 5.1 discusses Chirped C-SBG Mode-locked DFB laser results, while Section 5.2 discusses Chirped 4PS-SBG Mode-locked DFB laser results. Multi-wavelength distributed feedback (DFB) semiconductor lasers are key building blocks for DWDM, coherent optical communications, and photonic sensing, where several stable wavelengths are required on a compact integrated platform [19,20]. By generating multiple longitudinal modes in a single device, multi-wavelength DFB structures can reduce footprint and cost compared with arrays of discrete single-wavelength lasers. Traditionally, multi-wavelength operation has been realised using monolithically integrated DFB laser arrays arranged in parallel, with each channel defined by a different grating period and combined using MMI or funnel combiners [24,26,40]. These combiners introduce additional optical loss, increase chip area, and impose tighter fabrication tolerances. Furthermore, advanced heterogeneous or selective growth techniques, such as butt-joint regrowth, selective area growth, and quantum-well intermixing, are often required to integrate passive combiners and functional sections, complicating fabrication and reducing yield [27–29]. Series-arranged DFB arrays can eliminate the need for optical combiners but tend to suffer from enhanced mode competition and temperature sensitivity, degrading spectral stability and pulse quality [30,31]. Several alternative architectures have been explored for multi-wavelength mode-locked operation, including multi-wavelength mode-locked lasers based on semiconductor optical amplifiers, arrayed waveguide grating (AWG) cavities, and injection-locked comb lasers [34,35,100]. While these approaches can deliver wide combs and flexible wavelength allocation, they typically rely on external cavities, discrete filters, or additional reflectors, leading to increased system complexity, insertion loss, and alignment sensitivity. Sampled Bragg grating (SBG) DFB structures offer a compact, monolithic alternative. By engineering the sampling pattern of an underlying seed grating, reflection resonances with precise wavelength spacing can be realised [101,102]. Based on this concept, the idea is to design a single cavity capable of generating multiple wavelengths.

### 2.4.1 Sampled Bragg gratings (SBGs) and reconstruction-equivalent chirp (REC)

A conventional uniform Bragg grating consists of a periodic modulation of the effective refractive index with period $\Lambda_0$. In a waveguide with an effective index $n_{eff}$, the first-order Bragg wavelength is given by

$$\lambda_B = 2n_{eff}\Lambda_0 \tag{2.33}$$

and strong reflection occurs within a narrow stopband centred around $\lambda_B$ [19]. In a standard DFB laser, this uniform grating extends along the cavity and, with an appropriate phase-shift configuration, supports one longitudinal mode within the stopband. The spectral characteristics are governed by the coupling coefficient $\kappa$, grating length, as described by coupled-mode and transfer-matrix analyses [103]. An SBG is formed by multiplying the uniform seed grating with a periodic sampling function of period $P$, so that each sampling period contains a short "seed" grating section and a nominally unperturbed region [102]. In the spatial-frequency domain, this sampling process replicates the spectrum of the seed grating at integer multiples of the sampling spatial frequency. Near $\lambda_B$, this results in a comb of reflection peaks with an approximate wavelength spacing

$$\Delta\lambda_{\mathrm{SBG}} \approx \frac{\lambda_B^2}{2n_{eff}P} \tag{2.34}$$

where $P$ is the sampling period along the cavity. By choosing $P$ appropriately, the reflection peaks can be positioned to provide a desired channel spacing in the tens to hundreds of gigahertz range [101,102]. In a conventional sampled Bragg grating (C-SBG) with a 50% duty cycle, only half of each sampling period contains grating, as shown in Fig. 2.14(a), and the effective coupling coefficient of the strongest passband is significantly reduced compared with a uniform grating of the same index contrast [102,103]. The effective coupling coefficient of the C-SBG is only $1/\pi$ of that of a uniform grating. This reduction weakens feedback and limits the number of well-discriminated modes that can be supported within the stopband. To overcome this limitation, four-phase-shifted sampled Bragg gratings (4PS-SBGs) have been proposed, in which each sampling period is divided into four equal-length sections, and the grating in each section is phase-shifted by $0$, $\pi/2$, $\pi$, and $3\pi/2$ with respect to a reference as shown in Fig. 2 .14 (b). This fully periodic structure removes the non-grating regions present in C-SBGs and yields an effective coupling coefficient that can reach ~90% of that of a uniform grating. Reconstruction-equivalent-chirp (REC) generalises the sampled-grating concept by encoding the effective chirp entirely in the sampling pattern, while keeping the seed grating period uniform. REC technology has played a key role in easing the realisation of laser arrays with high-precision wavelength control. In REC, a Bragg seed grating with a uniform period is used for all devices in the array, and the operating wavelength of each laser is defined by the sampling period applied to this seed grating [101,102]. In our REC design, the sampling period is varied along the cavity so that each local region "selects" a different part of the replicated grating spectrum, allowing multiple reflection peaks to be positioned accurately without fabricating a genuinely chirped seed grating. As shown in the bandgap structure in Fig. 2.14 (c), the active region comprises five 6 nm thick compressively strained quantum wells, separated by six 10 nm thick tensile-strained barrier layers. The GRINSCH layers surrounding the active region provide carrier and optical confinement, while the tensile-strained barriers also contribute to strain compensation. The wafer is based on the AlGaInAs/InP material system and has a gain peak around 1550 nm. This five-quantum-well wafer forms the common active platform for both the chirped C-SBG and chirped 4PS-SBG mode-locked DFB lasers discussed in Sections 5.1 and 5.2.

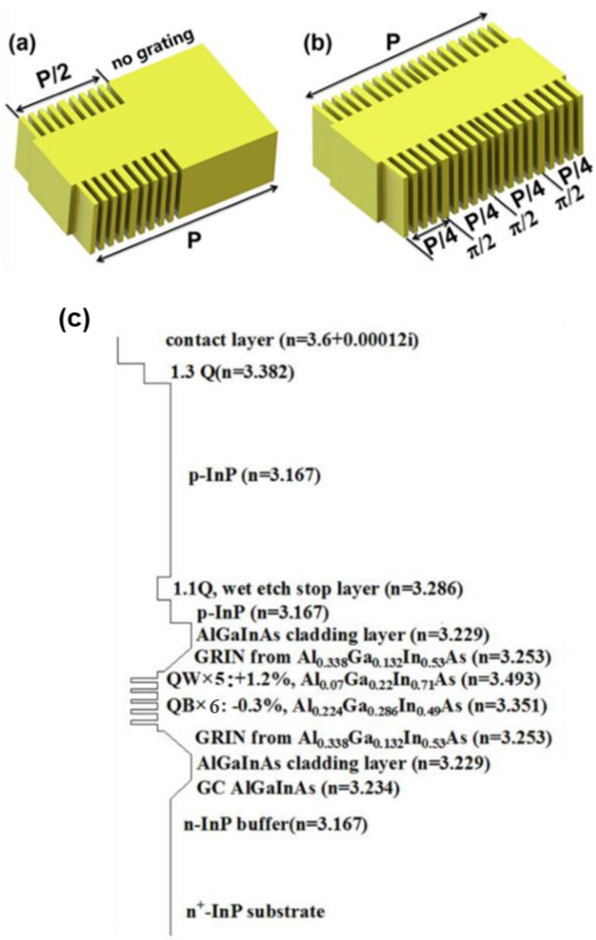


**Fig. 2.14. Grating structures of (a) C-SBG, (b) 4PS-SBG [101], (c) five quantum well wafer bandgap structure [102].**

## 2.4.2 Chirped sampled gratings with distributed $\pi$-phase shifts

Multi-wavelength operation is achieved by combining a linearly chirped SBG with multiple distributed $\pi$-phase shifts in a single DFB cavity. Chirp is introduced by allowing the sampling period $P(z)$ to vary along the cavity coordinate $z$:

$$P(z) = P_1 + Cz, 0 \leq z \leq L_{DFB} \quad (2.35)$$

where $P_1$ is the sampling period at the front facet, $L_{DFB}$ is the DFB cavity length, and $C$ is the chirp rate defined by the difference between the final and initial sampling periods divided by $L_{\mathrm{DFB}}$. For an SBG, the local sampling period determines the local Bragg wavelength $\lambda_B(z)$. A longitudinal mode at wavelength $\lambda_m$ experiences the strongest feedback in the region where $\lambda_m \approx \lambda_B(z)$, and the field decays away from this region. Because $P(z)$ is chirped, the condition $\lambda_m \approx \lambda_B(z)$ is satisfied at different positions for different modes, so each lasing wavelength is naturally localised in a different part of the cavity. Chirped sampled gratings therefore provide both multi-wavelength feedback and spatial separation of the modal photon densities, which is beneficial for reducing mode competition in multi-wavelength operation [30,102]. The linear chirp of the sampling period and the locations of the distributed π-phase shifts along the normalised DFB cavity are illustrated in Fig. 2.15(a). The chirp rate determines how rapidly the local Bragg condition changes along the cavity and therefore controls how strongly different wavelengths are separated in space. A small chirp produces only weak spatial separation, so the photon-density distributions of neighbouring modes remain close to each other and mode competition is not sufficiently reduced. A large chirp increases the longitudinal separation of the modes, but it also broadens the effective reflection response, increases the group-delay variation and dispersion, and weakens spectral selectivity. For this reason, the chirp rate must always be chosen as a compromise between mode separation and controlled feedback. In general, the 4PS-SBG requires a lower chirp rate than the conventional SBG because its fully periodic structure provides stronger and cleaner feedback in the working channel. Unlike the conventional SBG, it does not contain non-grating gaps, so its effective coupling coefficient is higher and the defect modes introduced by the distributed π-phase shifts are more strongly confined. As a result, less chirp is needed in the 4PS-SBG to separate the modal photon-density distributions, whereas the weaker conventional SBG requires a larger chirp to achieve a similar level of spatial mode separation. Distributed π-phase shifts are introduced by locally shifting the grating phase by π at selected positions $z_k$ along the cavity. A π-phase shift at $z_k$ can be viewed as a sudden sign change of the index modulation (or coupling), which breaks the periodicity of the grating and creates a localised defect mode inside the stopband, with its field centred around $z_k$ and decaying away from it [19,103]. When multiple π-phase shifts are distributed along the cavity, each phase shift behaves like a separate internal defect in the periodic grating. To first order, the regions between neighbouring π-phase shifts act as coupled sub-cavities, and the number of supported longitudinal modes is therefore approximately equal to the number of $\pi$-phase shifts. For a set of $N$ phase shifts placed at equal fractional positions along the cavity,

$$z_k \approx \frac{k\,L_{DFB}}{N+1} \qquad\qquad k = 1, \ldots, N \tag{2.36}$$

the corresponding defect modes form a set of wavelengths clustered around $\lambda_B$ with nearly uniform spacing [101,103]. Simulated photon-density distributions of the four longitudinal modes ($\lambda_1$–$\lambda_4$) for the C-SBG, obtained using the transfer-matrix method for the devices discussed in the next sections, are shown in Fig. 2.15(b); by comparison with Fig. 2.15(a), it can be seen that each mode is mainly localised near a different $\pi$-phase-shift position, confirming that the combination of chirp and distributed $\pi$-phase shifts separates the modal photon densities along the cavity.

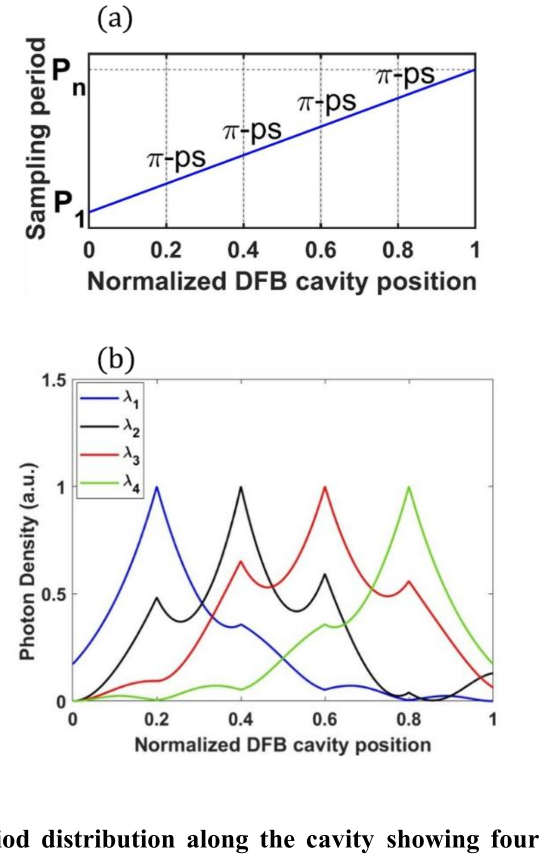


**Fig.2.15. (a) Sampling period distribution along the cavity showing four $\pi$-phase-shift positions. (b) Normalised photon-density profiles of the four lasing modes $\lambda_1$–$\lambda_4$ of C-SBG, each localised near a different $\pi$-phase-shift.**

Introducing additional $\pi$-phase shifts, however, also shortens the effective grating length available to each mode and reduces the product $\kappa L$. This weakens mode discrimination and can increase competition between neighbouring modes, particularly for outer channels whose photon-density distributions overlap more strongly with the cavity facets and any residual reflections. As a result, there is a trade-off between the desired number of wavelengths, the mode spacing, and the achievable side-mode suppression ratio (SMSR).

### 2.4.3 Multi-wavelength Chirped C-SBG

This subsection provides the theoretical basis for the chirped C-SBG mode-locked DFB laser results presented in Section 5.1. The chirped C-SBG considered in this work incorporates a sidewall grating with a uniform seed period $\Lambda_0 = 257$ nm and 50% duty cycle. The sampling periods $P_n$ are linearly modulated along the DFB cavity to implement a chirped C-SBG, following the general relation in equation (2.35), with an initial sampling period $P_1 = 4.42$ μm at the front facet and a chirp rate of 300 nm/mm. The relatively large chirp used in the C-SBG is required because the conventional sampled grating yields weaker effective feedback due to non-grating regions within each sampling period. A stronger chirp rate is therefore needed to produce sufficient longitudinal separation of the four defect modes and reduce overlap between their photon-density distributions. Four $\pi$-phase shifts are positioned at 1/5, 2/5, 3/5, and 4/5 of the DFB cavity length, as shown in Fig. 2.15(a), in line with the general scheme described in Section 2.4.2. Each phase shift is aligned to an integer multiple of the seed grating period $n\Lambda_0$, so that the placement tolerance is limited to within one seed period. A schematic top view of the grating is shown in Fig. 2.16.

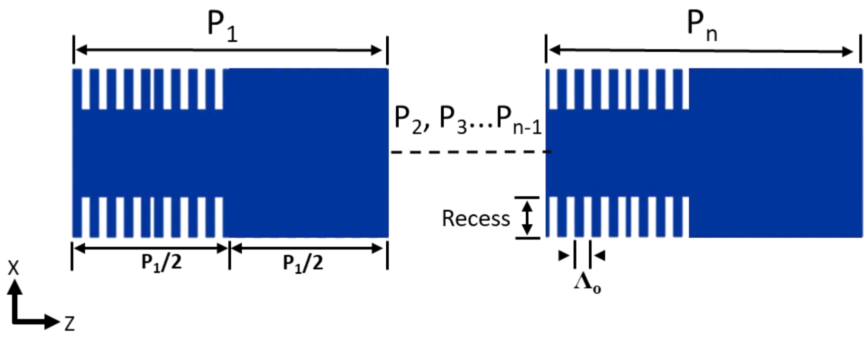


**Fig. 2.16. Top view of the chirped C-SBG schematic structure,**

Transfer-matrix method (TMM) simulations are used to design the chirped C-SBG and optimise the sampling pattern and phase-shift positions. The simulated transmission spectrum of the C-SBG structure (Fig.2.17) shows four narrow transmission peaks within the stopband, corresponding to the four defect modes supported by the distributed $\pi$-phase shifts.

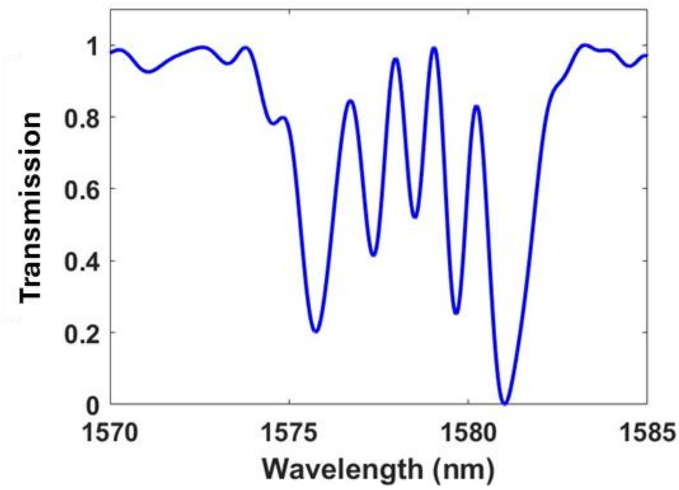


**Fig. 2.17. Simulated transmission spectrum of the chirped C-SBG.**

The linear chirp of the sampling period and the locations of the distributed π-phase shifts along the normalised DFB cavity are illustrated in Fig. 2.15(a), while the corresponding normalised photon-density distributions of the four longitudinal modes, obtained from the same TMM-based model, are shown in Fig. 2.15(b). The key simulation parameters used for the chirped C-SBG structure are summarised in Table 2.1

**Table 2.1. Key parameters for chirped C-SBG transmission simulation using TMM.**

| Parameter | Value |
|---|---|
| DFB cavity length ($L_{DFB}$) | 1500 μm |
| Effective refractive index ($n_{eff}$) | 3.2 |
| Seed grating period ($\Lambda_0$) | 257 nm |
| Initial sampling period ($P_1$) | 4.42 μm |
| Chirp rate ($C$) | 300 nm/mm |
| π-phase-shift positions ( $Z_k$) | 1/5, 2/5, 3/5, and 4/5 of $L_{DFB}$ |

## 2.4.4 Multi-wavelength Chirped 4PS-SBG

This subsection provides the theoretical basis for the chirped 4PS-SBG mode-locked DFB laser results presented in Section 5.2. The 4PS-SBG considered in this work replaces the conventional sampled grating with a fully periodic 4PS-SBG structure. Each sampling period is divided into four equal segments whose grating phases are offset by 0, $\pi/2$, $\pi$, and $3\pi/2$, respectively, eliminating the non-grating regions present in C-SBG designs as discussed in Section 2.4.1. A schematic top view of the grating is shown in Fig. 2.18.

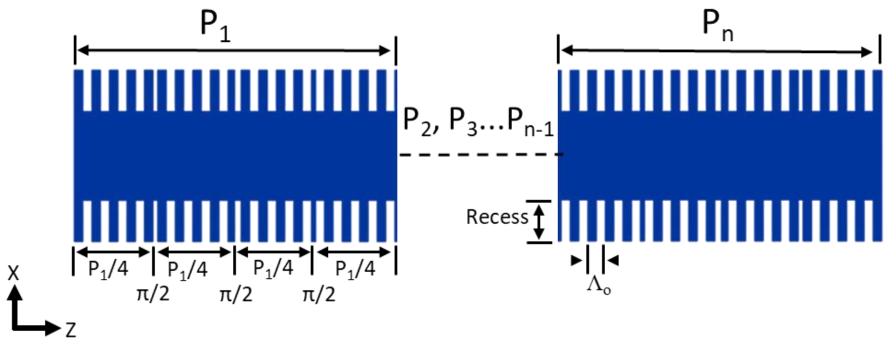


**Fig. 2.18. Top view of the chirped 4PS-SBG schematic structure.**

As in the C-SBG case, the sampling period of the 4PS-SBG is linearly chirped along the DFB cavity to broaden the −1st-order stopband and distribute the mode locations. The chirp follows the general relation in equation (2.35), with an initial sampling period $P_1 = 4.46$ and a chirp rate of approximately 80 nm/mm. In contrast to the C-SBG, the 4PS-SBG requires only a moderate chirp because its fully periodic structure provides stronger and cleaner feedback in the working channel. The higher effective coupling improves mode confinement and discrimination, so a smaller chirp is sufficient to separate the four modes spatially, while avoiding unnecessary broadening of the reflection response and excessive chirp-induced dispersion. Four $\pi$-phase shifts are again introduced at $1/5$, $2/5$, $3/5$, and $4/5$ of the DFB cavity length, defining four defect modes whose wavelengths and photon-density profiles are determined jointly by the 4PS-SBG sampling pattern and the phase-shift positions. TMM simulations of the chirped 4PS-SBG predict four narrow transmission peaks within the designed −1st-order stopband as shown in Fig.2.19. The linear chirp of the sampling period and the locations of the distributed $\pi$-phase shifts along the normalised DFB cavity are illustrated in Fig. 2.15(a), while the corresponding normalised photon-density distributions of the four longitudinal modes are shown in Fig. 2.19(b). The key simulation parameters used for the chirped 4PS-SBG structure are summarised in Table 2.2.

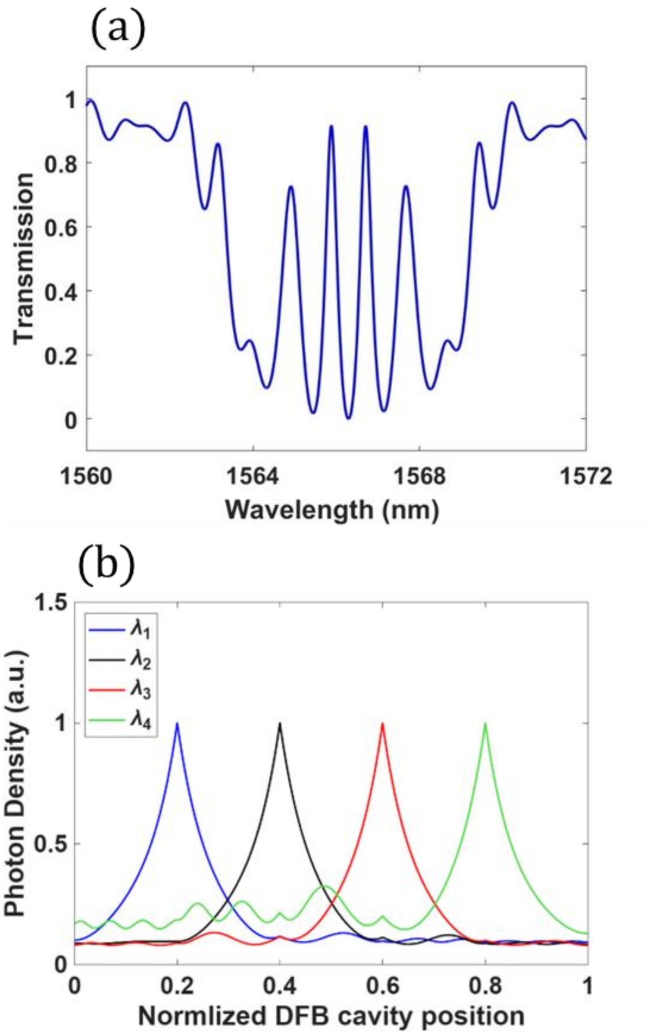


**Fig. 2.19. Simulated transmission spectrum of the chirped 4PS-SBG, (b) Normalised photon-density profiles of the four lasing modes $\lambda_1$–$\lambda_4$ of 4PS-SBG, each localised near a different π-phase-shift.**

**Table 2.2. Key parameters for chirped 4PS-SBG transmission simulation using TMM.**

| Parameter | Value |
|---|---|
| DFB cavity length ($L_{DFB}$) | 1600 µm |
| Effective refractive index ($n_{eff}$) | 3.2 |
| Seed grating period ($\Lambda_0$) | 257 nm |
| Initial sampling period ($P_1$) | 4.46 µm |
| Chirp rate ($c$) | 80 nm/mm |
| π-phase-shift positions ($Z_k$) | 1/5, 2/5, 3/5, and 4/5 of $L_{DFB}$ |

## 2.5 DFB lasers based on Waveguide Bragg Grating Microcavity

The theoretical background presented here is directly related to the devices based on waveguide Bragg grating (WBG) microcavities studied in Chapter 6. In particular, Section 6.1 discusses multi-wavelength DFB laser results, while Section 6.2 discusses dual-wavelength DFB laser results. In the previous section, chirped SBGs were discussed as a way to control the longitudinal mode structure of DFB lasers within a single cavity. In this section, we introduce the second design concept used in this thesis: the WBG microcavity. This structure underpins a monolithic multi-wavelength mode-locked DFB laser and also forms the basis of the dual-wavelength device presented later in this section. The WBG microcavity consists of a central ridge waveguide section embedded between two uniform Bragg gratings, forming a high-Q cavity whose effective length and resonance structure can be engineered with high precision. Unlike a simple Fabry–Perot cavity, where the resonance is set by cleaved facets, here the longitudinal modes are defined lithographically by the distributed Bragg gratings, which is advantageous for reproducible, on-chip multi-wavelength operation [79,104]. This structure can be viewed as a simple evolution of the conventional $\pi$-phase-shifted DFB laser. In a standard $\pi$-phase-shifted device, a short central ridge section of length $\Lambda_0$ (one grating period) without etched grating is introduced to create a single resonance inside the stopband [78,105].

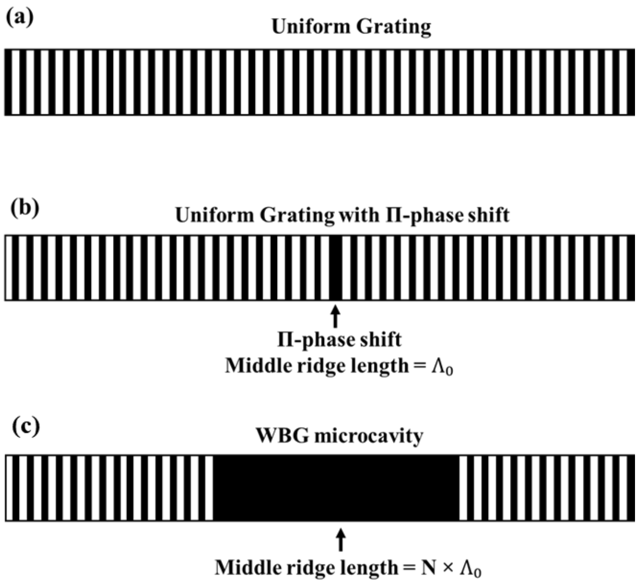


**Fig. 2.20. Schematic structures of: (a) uniform grating without phase shift, (b) uniform grating with a central $\pi$-phase shift section, and (c) Structure of the proposed WBG microcavity DFB laser with an elongated central ridge.**

In the proposed WBG microcavity DFB laser, this central section is extended to an integer multiple of the Bragg period, $N \times \Lambda_0$ with $N > 1$, while keeping the gratings uniform on both sides. This forms a compact microcavity embedded within a single DFB resonator, as illustrated schematically in Fig. 2.20(a–c). Using uniform sidewall gratings also allows the structure to be realised with a single metal-organic vapour phase epitaxy (MOVPE) growth and one dry-etch step, which keeps the design and fabrication flow straightforward and attractive for large-scale photonic integration [106,107]. The Chapter 6 WBG microcavity devices discussed in Sections 6.1 and 6.2 are fabricated on the asymmetric multiple-quantum-well (AMQW) wafer structure described later in Section 2.6, with its bandgap structure shown in Fig. 2.25.

### 2.5.1 Multi-wavelength WBG Microcavity

This subsection provides the theoretical basis for the WBG-based multi-wavelength DFB laser results presented in Section 6.1. Uniform Bragg gratings consist of a periodic modulation of the effective refractive index along the waveguide, providing wavelength-selective reflection around the Bragg wavelength [79,104]. When two such gratings are placed on either side of a central cavity, they act as distributed mirrors and form a WBG microcavity. Within the grating stopband, light penetrates the gratings before being reflected, so the standing-wave field extends beyond the physical central cavity. As a result, the cavity behaves as if it were longer than its lithographic length, and a discrete set of high-Q resonances appears inside the stopband. These resonances can be viewed as a set of equally spaced "comb lines" in wavelength (or frequency), with a free spectral range (FSR) that is primarily determined by the effective cavity length $L_{eff}$ rather than only the physical cavity length [78,106]. Because the standing wave penetrates the gratings, the effective cavity length $L_{eff}$ is longer than the lithographically defined central cavity length $L_{cc}$ as shown in the schematic structure in Fig.2.21. A common way to describe this effect is to write

$$L_{eff} = L_{cc} + 2\delta \tag{2.37}$$

where $\delta$ is the penetration depth of the optical field into each grating [78,104]. The penetration depth depends on both the grating coupling coefficient $\kappa$ and the grating length $L_g$. For uniform Bragg gratings operating near the Bragg wavelength, a good approximation for $\delta$ is

$$\delta = \frac{1}{2\kappa}\tanh(\kappa L_g) \tag{2.38}$$

larger $\kappa$ gives stronger reflection but shorter penetration depth [78,108]. The FSR $\Delta\lambda$ of the WBG microcavity is then determined by the usual relationship for a Fabry–Perot-like cavity, but with $L_{eff}$ instead of the physical cavity length:

$$\Delta\lambda \approx \frac{\lambda_0^2}{2n_g L_{eff}} \tag{2.39}$$

where $\lambda_0$ is the central wavelength and $n_g$ is the group index of the guided mode [78,104]. For a fixed material platform and wavelength, increasing $L_{eff}$ reduces the FSR, so doubling the effective length approximately halves the spacing between resonant modes. In our design, the central cavity length is chosen to be an integer multiple of the seed Bragg period $\Lambda_0$. By adjusting $L_{cc}$ while keeping the grating parameters fixed, we can systematically design devices that support multiple resonant modes within the stopband while maintaining a similar overall grating reflectivity [106,107].

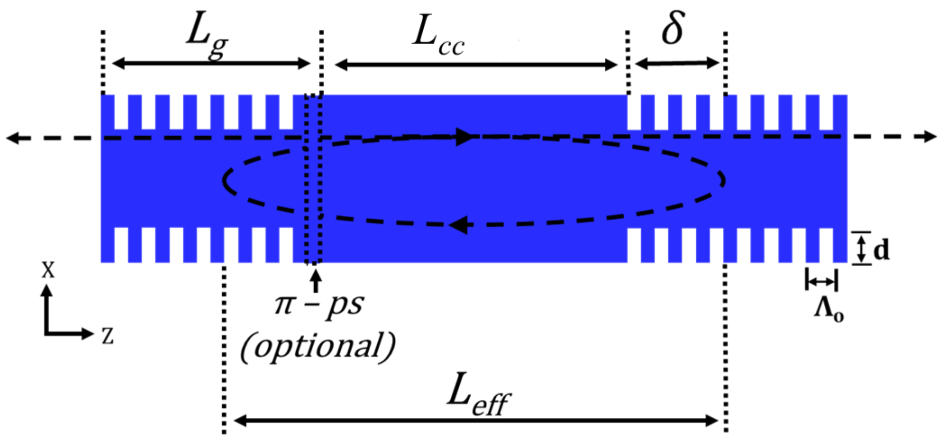


**Fig. 2.21. Top view of the WBG microcavity schematic structure.**

In the absence of any additional phase shift, the longitudinal resonance condition for a cavity of effective length $L_{eff}$ can be written as

$$m\frac{\lambda_m}{2} = n_{eff}L_{eff} \tag{2.40}$$

Where $m$ is an integer mode number, $\lambda_m$ is the resonance wavelength of the $m$-th mode, and $n_{eff}$ is the effective index of the guided mode. A $\pi$-phase shift can be introduced at one of the grating interfaces by displacing the grating pattern by half a period or, equivalently, by introducing a half-wavelength optical path difference at that position [78]. This additional phase changes the resonance condition to

$$\left(m+\frac{1}{2}\right)\frac{\lambda_m}{2} = n_{eff}L_{eff} \tag{2.41}$$

so that the entire set of resonances is shifted by half an FSR. Physically, the $\pi$-phase shift inverts the standing-wave pattern and toggles the set of allowed modes from "even" to "odd" modes (or vice versa). In practice, this means that for a given $L_{eff}$ one can choose whether the cavity supports an odd or an even number of modes inside the stopband [78,106,107]. The simulated transmission spectra of the designed uniform grating-based WBG microcavities are shown in Fig. 2.22. Three different central cavity lengths were used: half ( $L_{cc}/2$ ), standard ($L_{cc}$), and double ($2L_{cc}$), where $L_{cc}$ = 412.36 µm. The number of supported modes increases with cavity length, following the inverse relationship between the FSR and the $L_{eff}$. The simulations were performed using the TMM. Figs. 2.22(a–c) depict cavities with a π-phase shift, supporting an odd number of longitudinal modes (1, 3, and 5).

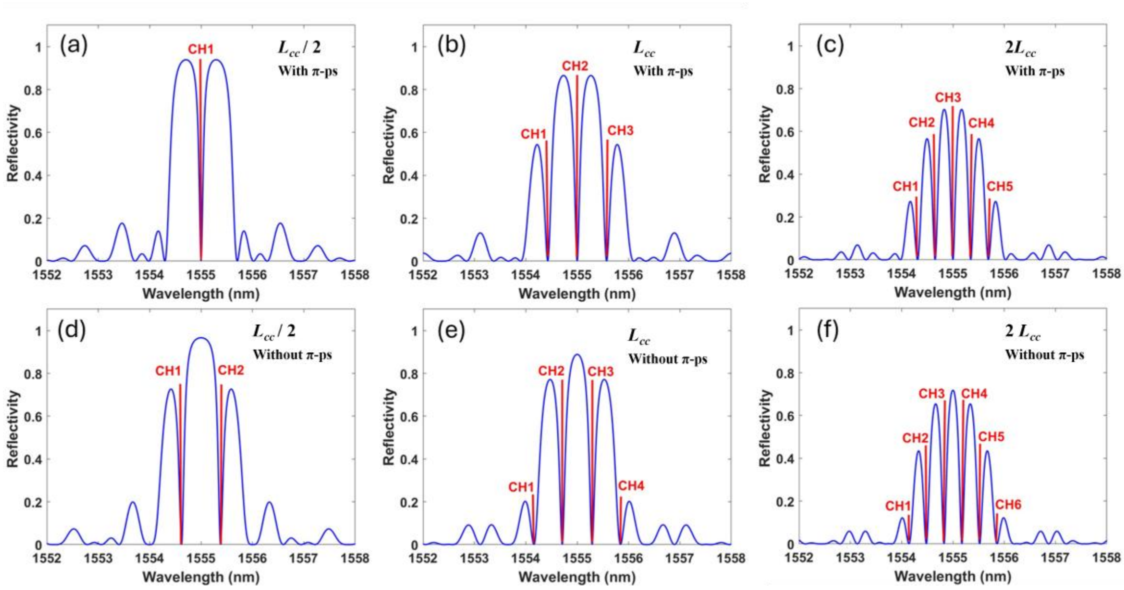


**Fig. 2.22. Simulated transmission spectra of the WBG microcavity with (a) $L_{cc}/2$ and a π phase shift, (b) $L_{cc}$ with a π phase shift, (c) $2L_{cc}$with a π phase shift, (d) $L_{cc}/2$ without a π phase shift, (e) $L_{cc}$ without a π phase shift, (f) $2L_{cc}$ without a π phase shift.**

In contrast, Figs. 2.22(d–f) show cavities without a π-phase shift, where the resonance condition shifts to even-numbered modes (2, 4, and 6). A π-phase shift effectively inverts the phase of the reflected optical field at that boundary, altering the standing wave conditions within the cavity. Physically, this is equivalent to introducing a half-wavelength optical path difference, which switches the resonance condition from even to odd modes (or vice versa).

As a result, the number of supported longitudinal modes can be toggled. To provide further insight into mode competition and resonance behaviour, we simulated the group delay response for the devices corresponding to our experimental configurations (dual, three, and six channels' devices) as shown in Figs. 2.23(a-c). Each peak in the delay curve corresponds to a longitudinal mode within the grating stopband, and its sharpness reflects the photon lifetime and modal selectivity at that wavelength. In the context of multi-wavelength mode-locking, these peaks indicate where energy is most strongly confined, helping to explain which modes dominate and how closely spaced modes interact.

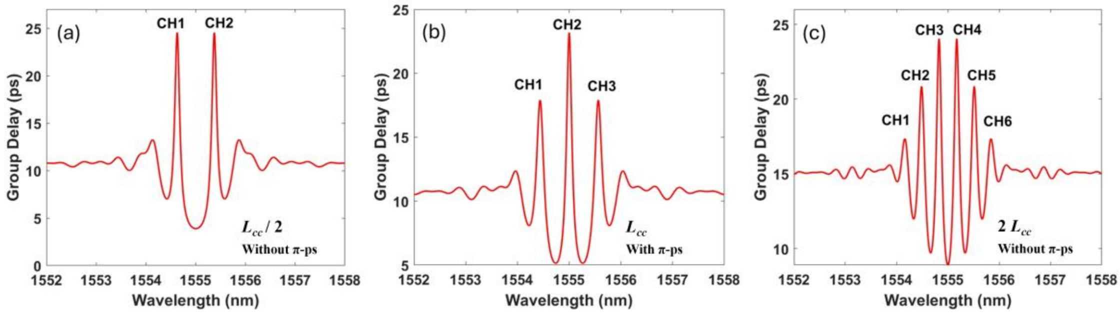


**Fig. 2.23. Simulated time delay spectrum (a) $L_{cc}/2$ without a $\pi$ phase shift, (b) $L_{cc}$ with a $\pi$ phase shift, (c) $2L_{cc}$ without a $\pi$ phase shift.**

### 2.5.2 Dual-wavelength WBG Microcavity

This subsection provides the theoretical basis for the WBG-based dual-wavelength DFB laser results presented in Section 6.2. Based on the same WBG microcavity concept described in the previous section, the cavity can also be engineered to support only two resonant modes inside the grating stopband, enabling stable dual-wavelength operation. The underlying physics is unchanged: the effective cavity length $L_{eff}$ is still defined by the central cavity length and the penetration of the field into the uniform sidewall gratings, and the FSR is governed by the Fabry–Perot-like relation in equation (2.37) [107]. In contrast to the multi-wavelength WBG devices, no additional $\pi$-phase-shift section is introduced in the gratings here. The central cavity is designed so that only two resonant modes fall inside the stopband, and varying $L_{cc}$ is used only to tune the spacing between these two modes, not to change their number. As discussed earlier, the FSR scales approximately as

$$\Delta\lambda \propto \frac{1}{L_{eff}} \tag{2.42}$$

so shorter cavities give larger FSR, and longer cavities give smaller FSR. For dual-wavelength operation, the WBG microcavity is designed so that the FSR is larger than roughly half of the grating stopband width. In this regime, only two resonant modes can fit inside the stopband, while all other potential modes fall outside the high-reflection region and are strongly suppressed. In the dual-wavelength design, we numerically investigate three WBG–DFB structures, each with a total cavity length of $L_{DFB}$ = 1000 µm. The WBG microcavity is formed by a central cavity of length $L_{cc}$ = 366 µm, 244 µm or 122 µm (DFB1, DFB2 and DFB3, respectively), bounded by uniform sidewall Bragg gratings with the same seed Bragg period $\Lambda_0$ = 244 nm as in the multi-wavelength design. The grating lengths on each side are chosen such that $L_{DFB} = L_{cc} + 2\ L_g$ = 1000 µm, giving $L_g$ = 317 µm, 378 µm and 439 µm for DFB1, DFB2 and DFB3, respectively. The simulated spectra, shown in Fig. 2.24, exhibit a single Bragg stopband with two narrow resonances for each structure, with FSR of approximately 0.42 nm, 0.50 nm and 0.62 nm. Because no $\pi$-phase shift is present, changing $L_{cc}$ only modifies the FSR and the spacing between the two resonances; the number of modes inside the stopband remains fixed at two.

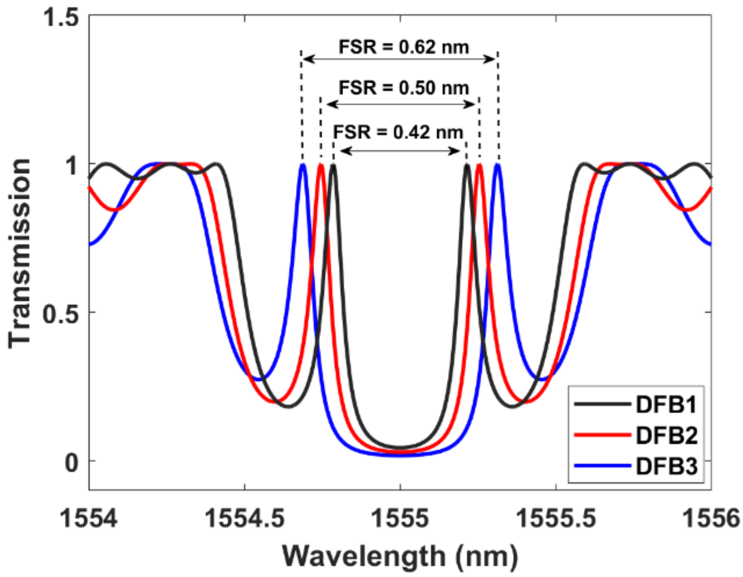


**Fig.2.24. Simulated transmission spectra for three different DFB structures.**

## 2.6 Asymmetric multiple-quantum-well passively mode-locked laser

The theoretical background presented here is directly related to the device results presented in Chapter 7, related to a broadband 100 GHz frequency comb from an asymmetric MQW passively mode-locked laser. SMLLDs are compact sources of optical frequency combs suitable for integrated photonic systems and short-reach optical communications [4,53]. Around 1.55 µm, two-section MQW passively mode-locked lasers have demonstrated stable operation at tens of gigahertz and sub-picosecond pulse durations [61,109]. However, conventional MQW structures typically provide a relatively narrow and non-flat gain spectrum, which limits the achievable comb bandwidth and spectral uniformity [62,63]. An effective strategy to extend and flatten the gain spectrum of MQW lasers is to employ AMQWs, in which the active region contains wells with different thicknesses and/or compositions [64]. Each quantum well provides gain at a slightly different transition energy, and the superposition of these contributions can produce a broader and more uniform modal gain profile than that of a conventional, identical-well MQW design [64,65]. In this work, we consider a two-section passively mode-locked AlGaInAs/InP laser whose gain section incorporates an AMQW active region specifically engineered for broadband comb generation at a repetition rate in the ≈100 GHz range. The general principles of passive mode-locking in two-section SMLLDs have been introduced in Section 2.1; here, we focus on the aspects that are specific to AMQW-based gain engineering and its impact on the comb spectrum.

### 2.6.1 AMQW gain engineering

In an AMQW structure, the active region consists of at least two groups of quantum wells with different effective bandgaps. For simplicity, we denote them as "type-A" and "type-B" wells. Type-A wells provide gain around a shorter wavelength $\lambda_A$, while type-B wells provide gain around a longer wavelength $\lambda_B$. The total modal gain spectrum is then the sum of the contributions from the different well types [64,65]:

$$g_{tot}(\omega, N) = \sum_j g_j(\omega, N) \tag{2.43}$$

where $g_j(\omega, N)$ is the modal gain contribution from the $j$-th type of quantum well, $\omega$ is the angular frequency and $N$ is the carrier density in the active region. The individual gain terms $g_j(\omega, N)$ are calculated using a multiband $\mathrm{k} \cdot \mathrm{p}$ model based on the Luttinger–Kohn Hamiltonian combined with many-body gain theory [110,111]. Each well type exhibits a gain spectrum peaked at its transition energy; the superposition of the spectra from the different wells leads to a broadened and potentially flattened total gain profile:

$$g_{tot}(\lambda, N) \approx g_A(\lambda, N) + g_B(\lambda, N) \tag{2.44}$$

where $g_A$ and $g_B$ correspond to the short- and long-wavelength wells, respectively. By choosing the energy separation and relative strength of these contributions appropriately, the combined gain can be engineered to be wide and relatively flat over the target spectral range [64,65].

In the present work, the AMQW design is chosen such that the two gain peaks partially overlap within the desired wavelength range around 1.5 µm. The wafer is based on the AlGaInAs/InP material system and follows standard SMLLD epitaxial and fabrication procedures similar to those reported for AlGaInAs/InP passively mode-locked lasers in [61,109]. This AMQW wafer forms the active platform of the broadband 100 GHz passively mode-locked laser investigated experimentally in Chapter 7.

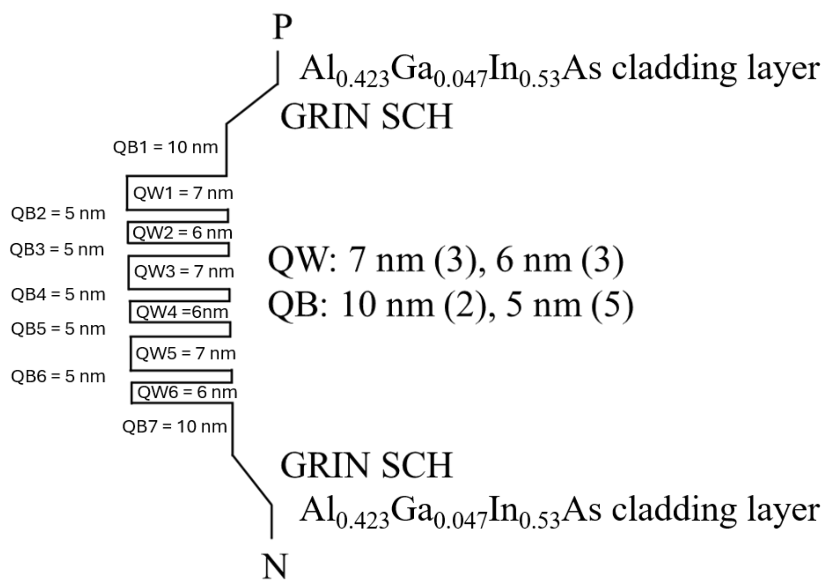


**Fig. 2.25 AMQW bandgap structure.**

The key difference is the active region, which uses a new AMQW design. As shown in the bandgap structure in Fig. 2.25, the active region comprises three 7 nm and three 6 nm thick 1.14 % compressively strained AlGaInAs QWs, separated by two 10 nm and five 5 nm 0.3 % tensile-strained quantum-barrier (QB) layers. The wells share the same material composition; the different thicknesses set two distinct transition energies, while the tensile-strained barriers provide strain compensation and suitable carrier/optical confinement. For InP-based MQW lasers, QW thicknesses in the range of about 4–8 nm are known to yield low threshold current density and good differential gain [64,65]. Within this range, the 6 nm/7 nm combination was chosen using modal-gain simulations and experience with similar AlGaInAs/InP devices [61,65,109]. In this structure, the 7 nm wells form the longer-wavelength gain peak (around 1540 nm), while the 6 nm wells form the shorter-wavelength peak (around 1515 nm). The simulated total AMQW modal gain at various carrier densities

($N$) using the Luttinger–Kohn Hamiltonian approach and many-body theory, representing the combined contributions from the 6 nm and 7 nm thick QWs, is shown in Fig. 2.26. The combination of 6 nm and 7 nm QWs was chosen to achieve an optimal balance between spectral separation and overlap, enabling a broader usable gain spectrum while mitigating issues such as excessive strain, carrier redistribution, and uneven threshold behaviour. This interplay produces an AMQW structure with a flatter and broader gain spectrum compared to that of a conventional MQW with identical QW thickness. The internal waveguide loss, obtained from Fabry–Pérot test lasers on the same wafer using the Hakki–Paoli method, is approximately 15 $cm^{-1}$ and is included in the analysis of the net modal gain [112].

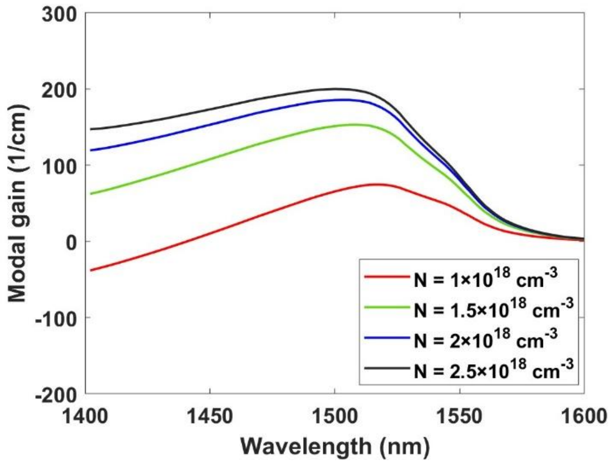


**Fig. 2.26. Simulated total modal gain spectra of the AMQW structure at different carrier densities.**

### 2.6.2 Two-section passive mode-locking based on AMQW

The AMQW device adopts the standard two-section Fabry–Pérot topology (forward-biased gain section and reverse-biased SA), in which passive mode-locking is enabled by the intensity-dependent loss of the SA [53, 61]. The fundamental repetition rate $f_{\text{rep}}$ is defined as in Section 2.1 (Eq. 2.2), and the travelling-wave time-domain model described in Section 2.2.2 is used to simulate the temporal and spectral behaviour [81].

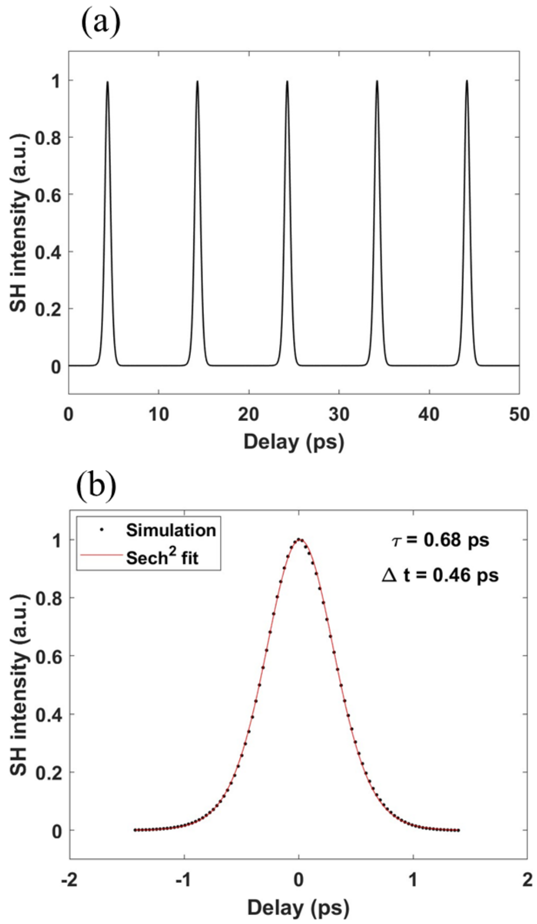


**Fig. 2.27. (a) Simulated full AC trace, (b) simulated isolated pulse fitted with a sech² profile.**

In this model, the forward and backward propagating field envelopes in the cavity are solved together with carrier dynamics in the gain and SA sections. A representative simulated intensity autocorrelation (AC) trace is shown in Fig. 2.27(a), together with an isolated AC peak fitted with a sech$^2$profile in Fig. 2.27(b). The simulated AC corresponds to an AC width of about 0.68 ps, which deconvolves to a pulse duration of approximately 0.46 ps assuming a sech$^2$ pulse shape. This demonstrates that the AMQW-based device can support sub-picosecond pulses at the designed high repetition rate. The corresponding simulated RF spectrum is shown in Fig. 2.28. The spectrum exhibits a fundamental peak at 100 GHz, consistent with equation (2.45), with higher-order harmonics visible at integer multiples of this frequency and a low noise floor over the full RF span, as shown in the inset of Fig.2.28. The key simulation parameters used in the FreeTWM simulation are shown in Table 2.3.

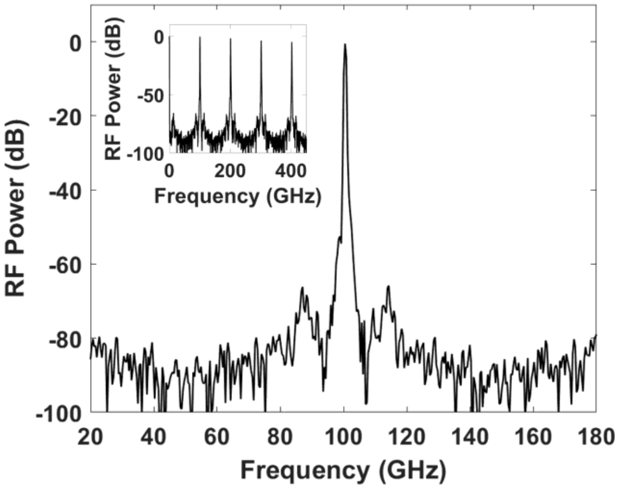


**Fig. 2.28. Simulated RF spectrum, with the full RF span shown in the inset.**

**Table 2.3. Key parameters for simulation using FreeTWM.**

| Parameter | Value |
|---|---|
| Cavity single-pass transit time ($\tau_c$) corresponding to 100 GHz | 4.915 ps |
| SA fraction of cavity length | 2% of $L$ |
| Facet power reflectivity (both facets) | 0.30 |
| Internal loss ($\alpha_i$) | 14.40 $cm^{-1}$ |
| Carrier density at transparency ($N_t$) | $1 \times 10^{18}$ $cm^{-3}$ |

# Chapter 3: Device Fabrication Process

Nanofabrication of semiconductor devices generally follows a two-step pattern transfer approach. The initial step defines the intended geometry in a resist mask through exposure and subsequent development. In the second step, this mask is used to replicate the pattern onto the sample, typically via etching or, in some cases, through thin-film deposition. In this chapter, the fabrication procedure for converting a 2-inch InP wafer into testable laser-bar strips is presented.

## 3.1 Sample preparation and marker definition

InP-based epitaxial wafers are typically supplied in a standard 2-inch format. Processing the full wafer in a single run can be less practical: if a process step goes wrong (or there is non-uniformity across the wafer), the material loss can be large. To reduce this risk and to keep the fabrication more controllable, the wafer is first cleaved into smaller pieces. In this work, the wafer was divided into multiple samples with a typical size of 11 × 12 mm, and fabrication was carried out on one sample at a time. This approach limits potential waste and makes it easier to adjust and optimise the process. Fig. 3.1(a–c) shows the wafer preparation and cleaving process, including the initial wafer, the cleaving setup, and the resulting samples prepared for further processing.

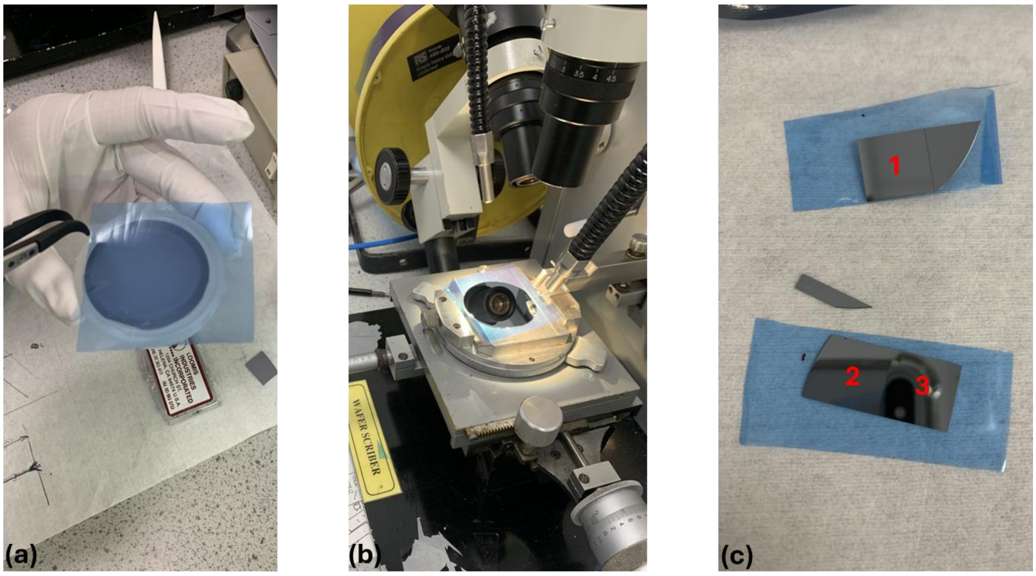


**Fig. 3.1. Example of wafer preparation and cleaving process: (a) 2-inch InP wafer prior to processing, (b) manual cleaving setup using a wafer scriber and microscope, (c) cleaved samples.**

After cleaving, each sample is cleaned sequentially using acetone, isopropanol (IPA), and deionised (DI) water, followed by drying with nitrogen ($N_2$) gas. Acetone is used first because it is a strong organic solvent and is effective at removing most organic contamination (e.g., photoresist residues and handling-related organics), while also evaporating quickly. IPA is then used because it is miscible with acetone and helps remove any remaining traces, including some more polar contaminants that may not be fully removed by acetone. In addition, IPA has relatively low surface tension, which helps it wet the surface and reduce residue formation. Finally, a DI water rinse removes any remaining solvent residues and leaves the surface free of ionic or organic impurities. The sample is then dried using nitrogen gas to minimise water marks and avoid spot formation on the surface.

Since the fabrication flow requires multiple electron-beam (e-beam) lithography steps, it is essential that every written layer is accurately aligned to the previous ones. For this reason, alignment markers are defined at an early stage and then used as reference points during all subsequent e-beam exposures to ensure reliable overlay between mask levels. Gold (Au) is selected as the marker material because it provides high contrast and remains stable throughout the processing sequence. To form the marker pattern, a bilayer PMMA (polymethyl methacrylate) resist stack is used. First, 15% 2010 PMMA is spin-coated onto the sample at 4000 rpm [113,114], followed by baking on a hotplate at 180°C for 5 minutes. PMMA is a positive-tone resist, meaning that the regions exposed to the e-beam become more soluble in the developer and are removed during development. The baking step improves film uniformity by driving off residual solvent, which helps achieve more consistent exposure and development. Under these spin conditions, the 15% PMMA layer produces a thickness of approximately 1.2 µm (layer1). A second layer of 4% 2010 PMMA is then spin-coated using the same procedure, forming a thinner top mask layer with a typical thickness of around 110 nm (layer2). The resist-coated sample is subsequently exposed using the e-beam according to the predefined marker layout and then developed to open the patterned regions. Development is carried out using a MIBK (methyl isobutyl ketone): IPA mixture with a 1:2.5 ratio. This developer selectively dissolves the exposed PMMA while leaving the unexposed regions intact. The sample is immersed in the developer for 30 s at 23°C, then immediately rinsed in pure IPA for 30 s to quench the development and remove any remaining developer. This controlled rinse step is important to avoid overdevelopment, which can lead to loss of critical dimensions or pattern deformation. The sample is then rinsed in DI water for 60 s to remove residual IPA, and finally dried using nitrogen gas.

A bilayer PMMA stack is particularly useful for lift-off because it tends to produce a natural undercut after development. In this work, the thicker 15% PMMA bottom layer is more sensitive to e-beam exposure than the thinner 4% PMMA top layer. As a result, the developed opening in the lower layer becomes slightly wider than the opening in the upper layer, which creates the desired undercut profile. This geometry is important during metal deposition because it prevents the metal deposited on the resist top surface from forming a continuous bridge to the metal deposited inside the patterned opening. In other words, the metal on the resist is "separated" from the metal on the substrate, which makes the subsequent lift-off cleaner and leads to a sharper, better-defined pattern.

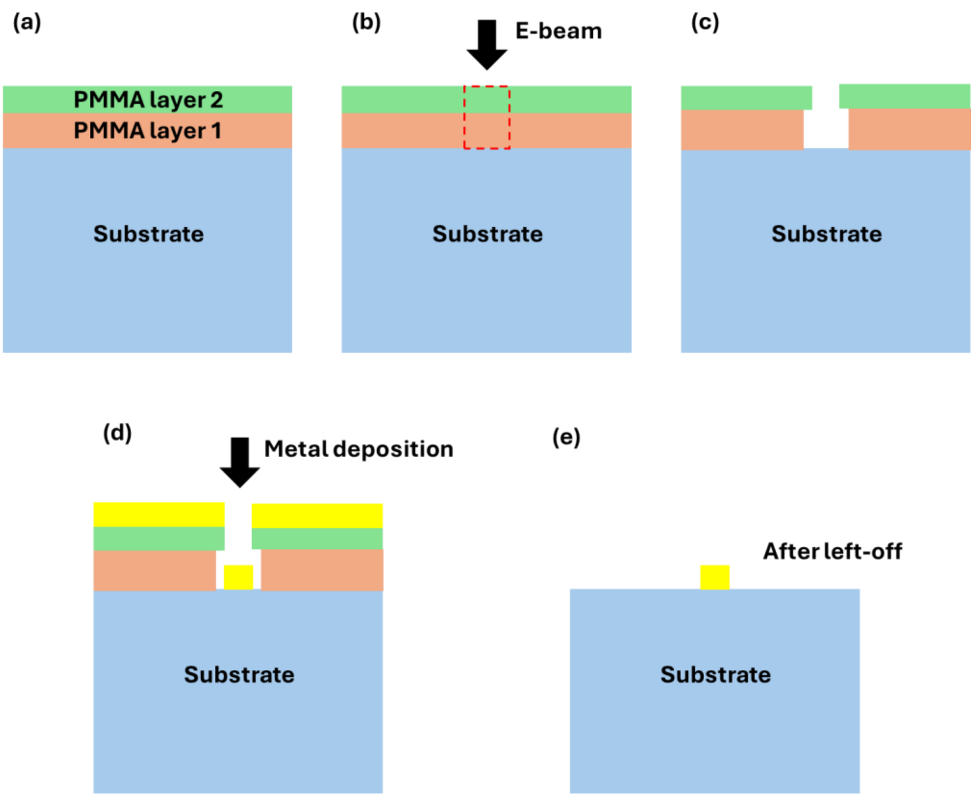


**Fig. 3.2. Schematic process sequence for metal deposition and lift-off for the marker: (a) spin-coating of a bilayer PMMA mask, (b) e-beam exposure, (c) developed resist pattern, (d) metal deposition, and (e) sample after lift-off.**

Fig. 3.2 illustrates the full process flow, starting from the bilayer PMMA coating and e-beam exposure, through development, metal deposition, and finally lift-off. After lift-off, small amounts of resist residue or other organic contamination can still remain on the surface. To remove these traces, the sample is cleaned using $O_2$ plasma ashing at 150 W RF power for 150 s. This step oxidises the remaining organic material and removes it effectively, leaving a cleaner patterned surface for later processing. For metal deposition, a thin NiCr (nickel–chromium) layer of 30 nm is first evaporated to act as an adhesion layer, improving the bonding between the metal stack and the InP surface. Afterwards, 100 nm of Au is deposited to form high-contrast alignment/identification markers that remain clearly visible during subsequent fabrication steps. After metal deposition, the sample is immersed in acetone in a 50°C water bath. In this lift-off step, the metal deposited outside the patterned regions is removed together with the dissolved PMMA, leaving only the metal that is directly attached to the sample surface within the exposed and developed areas. This completes the transfer of the mask pattern onto the sample surface. Fig. 3.3 presents the designed marker layout on the sample, together with an optical microscope image of the markers after the lift-off step. The long metal line located to the left of the three cross markers is included specifically to check rotational misalignment between the written marker pattern and the edge of the cleaved sample. This check is important because InP cleaves along crystallographic directions, meaning the cleaved edges are naturally parallel or perpendicular to the crystal lattice. If the marker pattern is rotated by more than 1° with respect to this crystallographic direction, the final devices can become noticeably misaligned when the sample is later cleaved into laser-bar strips. In practice, this may lead to partially cleaved (incomplete) devices and end facets that are not perpendicular to the ridge waveguide, which can degrade device quality. Therefore, if the rotational offset between the pattern and the sample edge is found to exceed 1° after development, the mask should be removed and the marker-definition step repeated to ensure correct rotational alignment.

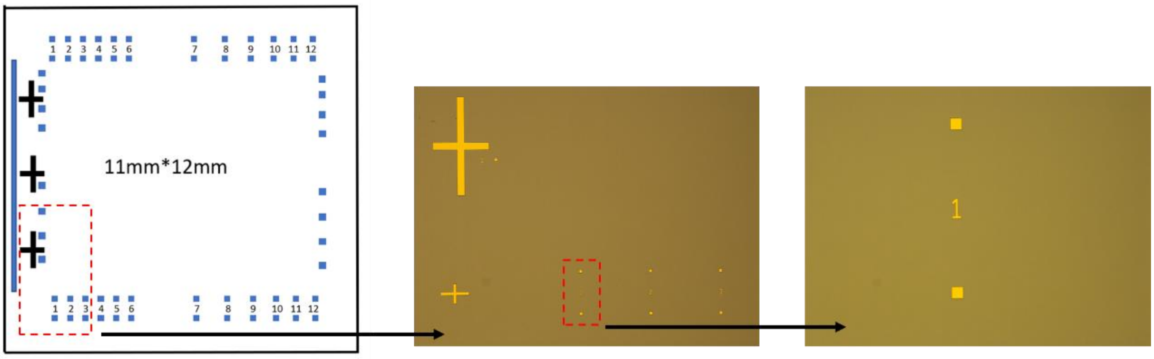


**Fig. 3.3. Optical microscope image showing the fabricated alignment marker pattern.**

The overall fabrication process used for the devices in this thesis is summarised in Fig. 3.4. Figure 3.4(a) shows the common initial fabrication steps, while Figs. 3.4(b) and 3.4(c) show the subsequent fabrication routes for devices on conductive n-InP and SI-InP substrates, respectively. The conductive-substrate route is used for the devices presented in Chapters 5–7, whereas the SI-InP route is used for the 10 GHz SMLLD presented in Chapter 4. Each fabrication stage shown in Fig. 3.4 is described in detail in the following sections.

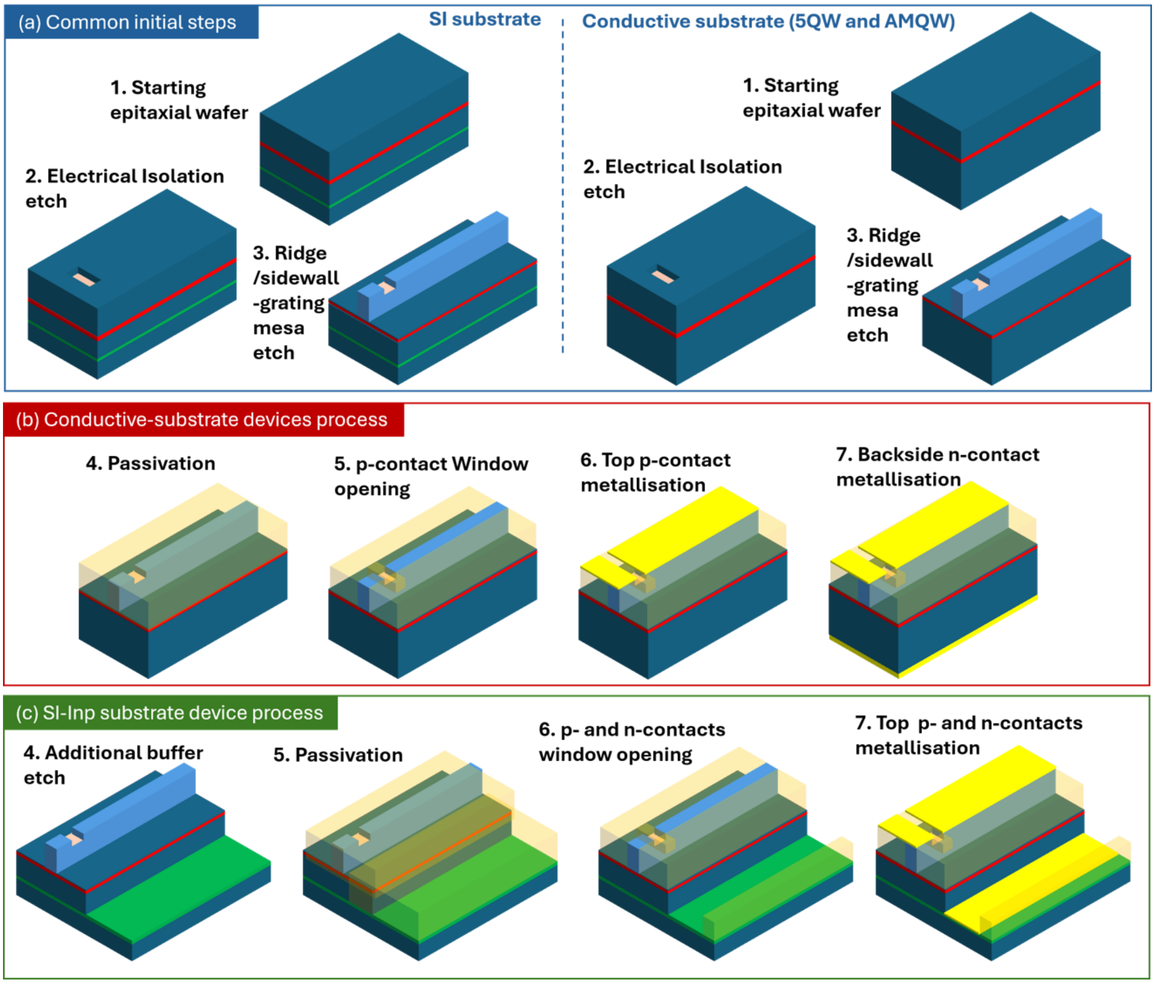


**Fig. 3.4. Schematic step-by-step fabrication process flow for the semiconductor laser devices presented in this thesis: (a) common initial fabrication steps; (b) fabrication route for devices on conductive n-InP substrates; (c) fabrication route for the SI-InP substrate device.**

The representative top-view mask layouts of the devices fabricated in this thesis are shown in Fig. 3.5. Figure 3.5(a) corresponds to the 10 GHz SMLLD discussed in Chapter 4. Figure 3.5(b) corresponds to the multi-wavelength SBG-based devices discussed in Chapter 5, namely the 4-channel C-SBG, 4-channel 4PS-SBG, and 6-channel 4PS-SBG devices; these share the same overall mask geometry, with differences only in the internal grating design. Figures 3.5(c) and 3.5(d) show the layouts of the multi-wavelength and dual-wavelength devices discussed in Chapter 6, respectively, and Fig. 3.5(e) shows the layout of the 100 GHz device discussed in Chapter 7.

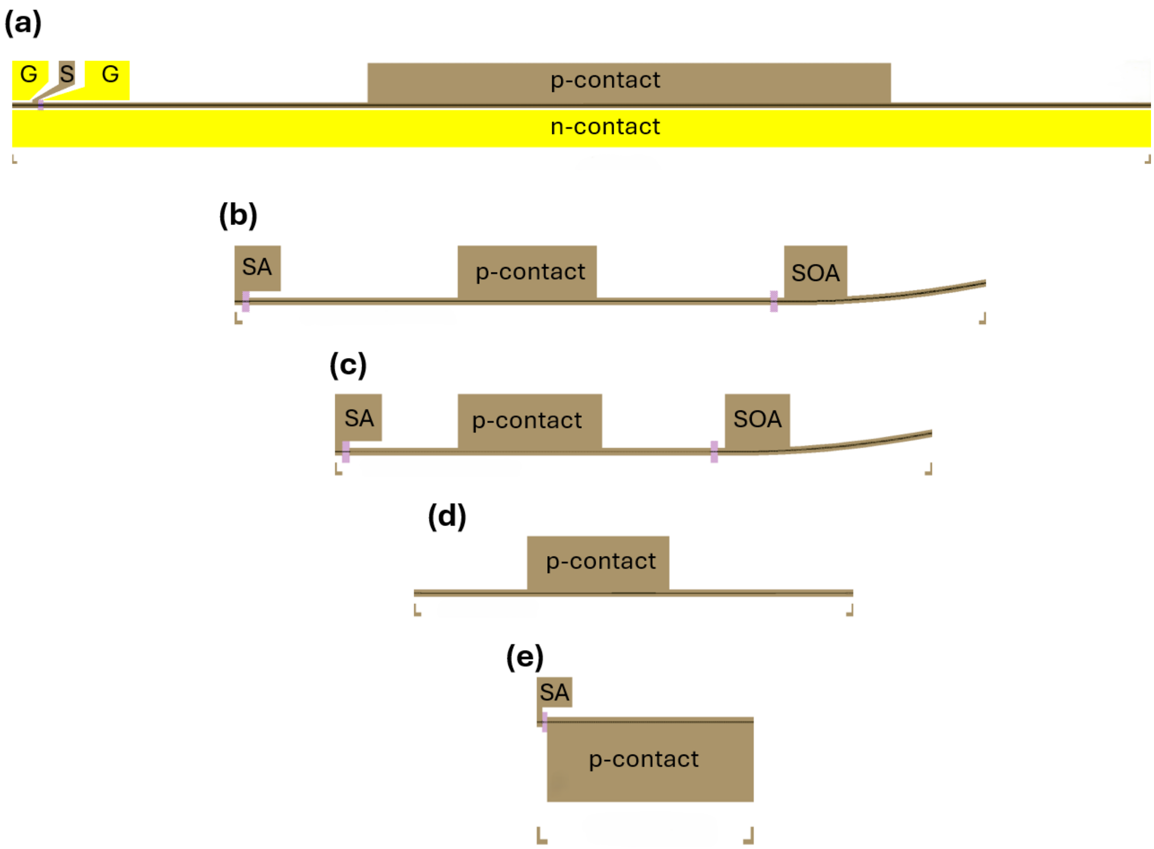


**Fig. 3.5. Representative top-view mask layouts of the devices fabricated in this thesis: (a) 10 GHz SMLLD presented in Chapter 4; (b) common layout used for the 4-channel C-SBG, 4-channel 4PS-SBG, and 6-channel 4PS-SBG devices presented in Chapter 5, which share the same overall device geometry but differ in their internal grating designs; (c) multi-wavelength WBG device presented in Chapter 6; (d) dual-wavelength WBG device presented in Chapter 6; and (e) 100 GHz AMQW SMLLD presented in Chapter 7.**

## 3.2 Electrical Isolation and Waveguide Etching

### 3.2.1 Inductively coupled plasma dry etch

Patterning of the electrical isolation regions and grating waveguides is carried out using inductively coupled plasma (ICP) etching [115–117]. ICP etching is a well-controlled semiconductor fabrication technique that enables accurate transfer of fine features into an epitaxial wafer by removing material using a plasma-based process. Fig. 3.6 shows the basic configuration of an ICP etching chamber. The etching gases are introduced through the etching gas inlet, and an RF-driven coupling coil (supplied by the ICP power) generates a high-density plasma by ionising the process gases. This high plasma density supports efficient etching with good anisotropy and improved profile control. The plasma consists of ions, electrons, and neutral species, and material removal occurs through a combination of chemical reactions and physical sputtering. The sample is positioned at the etching station on the lower electrode, where an additional RF power is applied to bias the substrate and control the ion energy reaching the surface, allowing the etch rate and sidewall profile to be tuned. During etching, helium piping is typically used to assist with backside cooling and temperature stabilisation of the sample. Finally, the etched by-products are removed through the vacuum channel, which maintains the required low-pressure environment for stable plasma operation.

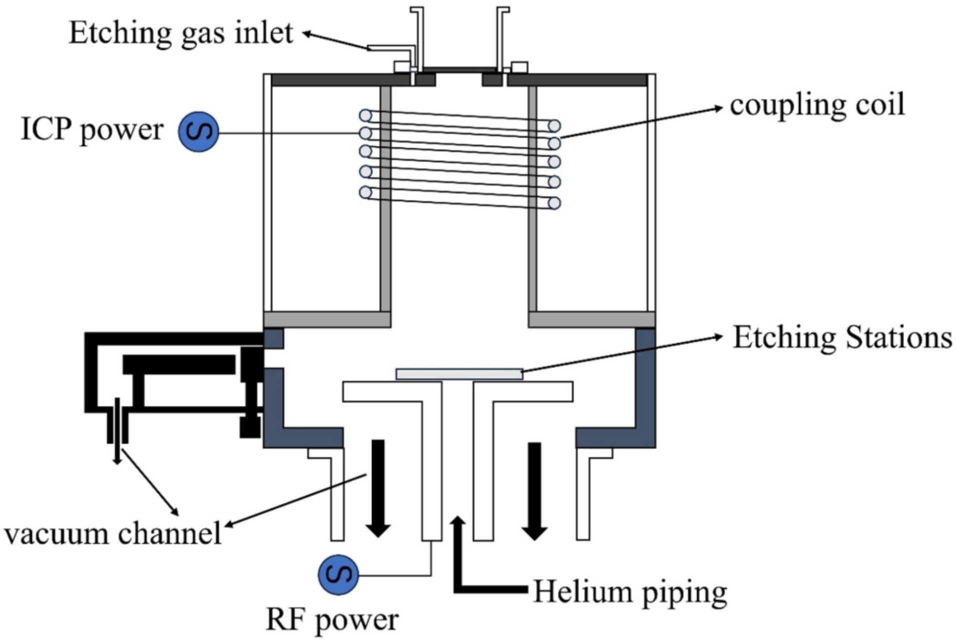


**Fig. 3.6. Schematic of ICP Chamber [118].**

In InP-based dry etching, a gas mixture of $Cl_2$ (chlorine), $H_2$ (hydrogen), $CH_4$ (methane), and Ar (argon) is commonly used. Chlorine provides the main chemical etch activity for InP [119]. It reacts with indium (In) and phosphorus (P) at the surface to form volatile chloride products (e.g., $InCl_3$ and $PCl_3$), which can then be removed from the chamber by the pumping system. $H_2$ is mainly included to assist with surface passivation and to help control the etch profile, which can improve etch anisotropy. $CH_4$ can contribute to producing volatile etch by-products when used with chlorine, and it can also help promote more anisotropic etching by forming a thin passivation layer on the sidewalls, supporting more vertical profiles. Ar is an inert species that does not chemically react with the sample, but it enhances the physical sputtering component of the etch by increasing ion bombardment energy. In addition, Ar can help stabilise the plasma and improve process repeatability under steady conditions [120–122].

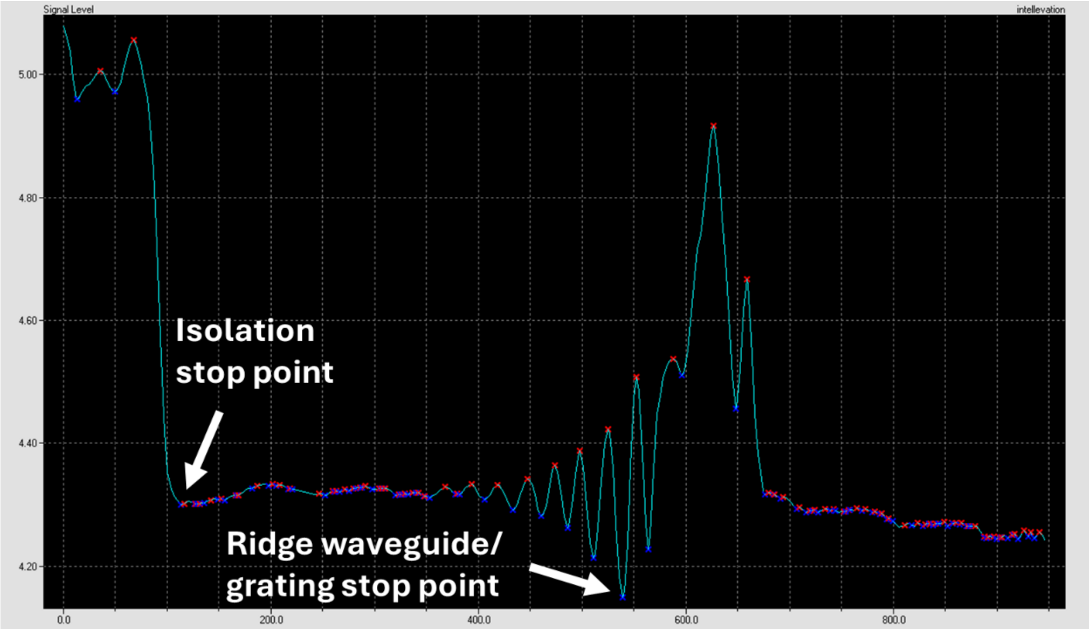


**Fig. 3.7. Reflectivity trace from the interferometer for isolation and ridge waveguide etch.**

An interferometer is used to monitor the etch depth in situ. In this method, a 670 nm wavelength probe beam is directed onto the sample surface, and the reflected intensity is tracked throughout the etch. Because the wafer contains multiple stacked epitaxial layers, the reflected signal changes as the etch proceeds, due to interference between reflections from different interfaces within the layer structure. Figure 3.7 shows a typical interference trace recorded during etching, starting from the wafer surface and continuing until completion of the ridge waveguide etch. The isolation stop point corresponds to the material removed for electrical isolation, which includes the 200 nm $p^+$-InGaAs contact layer and the 50 nm p-InGaAsP (1.3Q) layer. The ridge waveguide/grating stop point represents the etching of the upper p-InP layer, with a total thickness of 1.6 µm. Beyond this point, the etch has progressed into the upper separate confinement heterostructure (SCH) layer. The cross-sectional epitaxial structures of the wafers used in this thesis are shown in Fig. 3.8. Figure 3.8(a) shows the five-QW n-InP wafer used for the devices presented in Chapters 5 and 6, Fig. 3.8(b) shows the three-QW SI-InP wafer used for the 10 GHz SMLLD presented in Chapter 4, and Fig. 3.8(c) shows the AMQW wafer used for the 100 GHz SMLLD presented in Chapter 7. Their layer structures determine the subsequent fabrication steps, particularly the contact scheme and substrate-processing route.

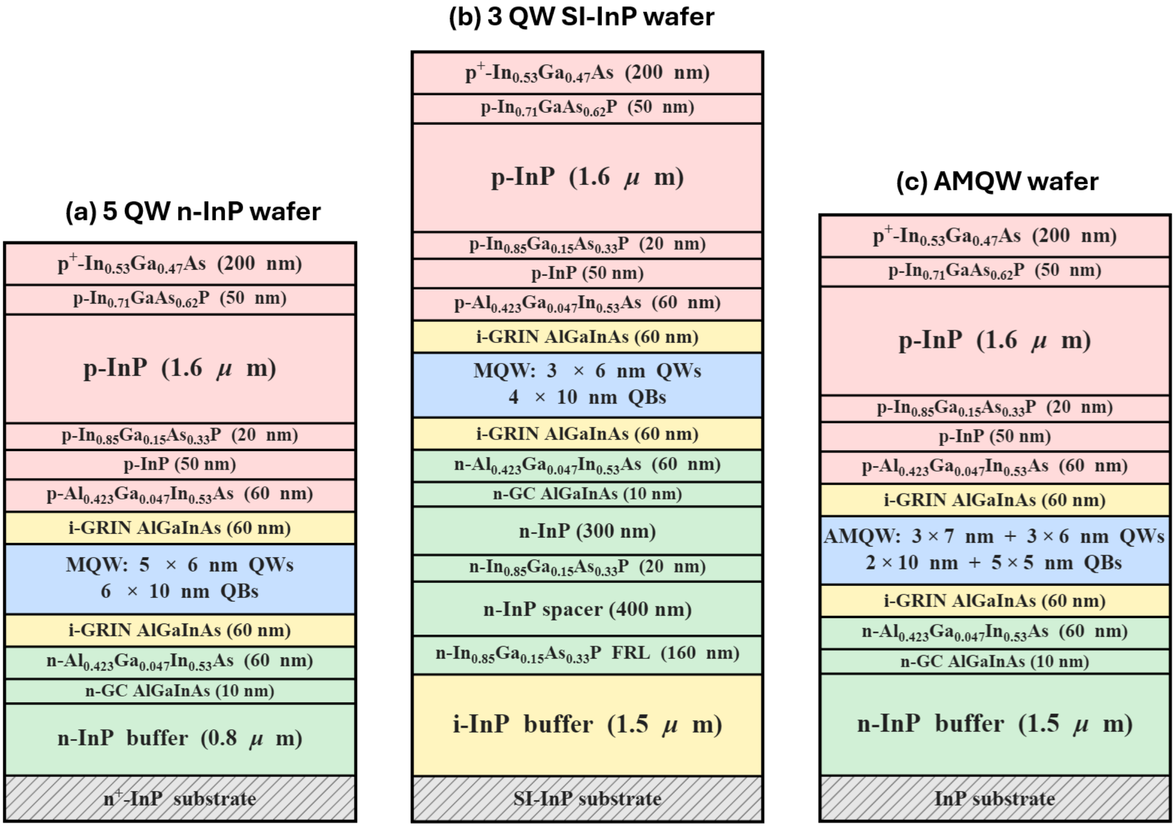


**Fig. 3.8. Cross-sectional epitaxial structures of the wafers used in this thesis: (a) five-QW n-InP wafer, (b) three-QW semi-insulating InP wafer, and (c) AMQW wafer used for the 100 GHz SMLLD. The structures are schematic and not to scale.**

### 3.2.2 Electrical isolation

Since the laser device is mostly divided into two functional sections, the gain section or the DFB cavity and the SA, each section requires an independent electrode. After completing the marker deposition, the next fabrication step is to define the electrical isolation region by dry etching across the ridge waveguide. This etch step electrically separates the two sections, which allows independent biasing and control of the gain or DFB cavity and the SA. This electrical-isolation step is required for all multisection devices with separately biased active sections, namely the 10 GHz SMLLD in Chapter 4, the chirped C-SBG and chirped 4PS-SBG devices in Sections 5.1 and 5.2, the multi-wavelength WBG microcavity devices in Section 6.1, and the AMQW SMLLD in Chapter 7. By contrast, it is not required for the single-contact dual-wavelength WBG devices in Section 6.2, where no separate SA section is used. To achieve effective isolation, the highly doped top layers, 200 nm InGaAs and 50 nm InGaAsP(1.3Q), must be removed in the isolation area. With proper etch depth and alignment, this typically provides an inter-section resistance of around 9 kΩ, which is sufficient to minimise electrical leakage between the two sections.

The mask for the electrical isolation pattern consists of two layers of 15% 2010 PMMA, spin-coated at 4000 rpm and baked at 180°C. Since the etch selectivity between PMMA and InP in chlorine-based ICP etching is typically greater than 1:1, using a double-layer PMMA stack provides a total resist thickness of approximately 2.4 μm. This helps ensure the mask is not fully consumed during the etch. The ICP gas recipe used for this step is described in Section 3.2.3. After the dry etch is completed, the remaining PMMA mask is removed by immersing the sample in acetone in a 50°C water bath for 30 minutes. Figure 3.7 shows a microscope image of the electrical isolation pattern after completion of the dry etch. The isolation width is set to 20 μm to provide sufficient separation between the electrodes. The longitudinal dimension is 80 μm to ensure the etched region fully covers the ridge waveguide. A slight scalloping, or wavy appearance, can be observed along the isolation sidewalls. This is likely caused by non-uniform erosion of the PMMA sidewalls during the plasma etch process.

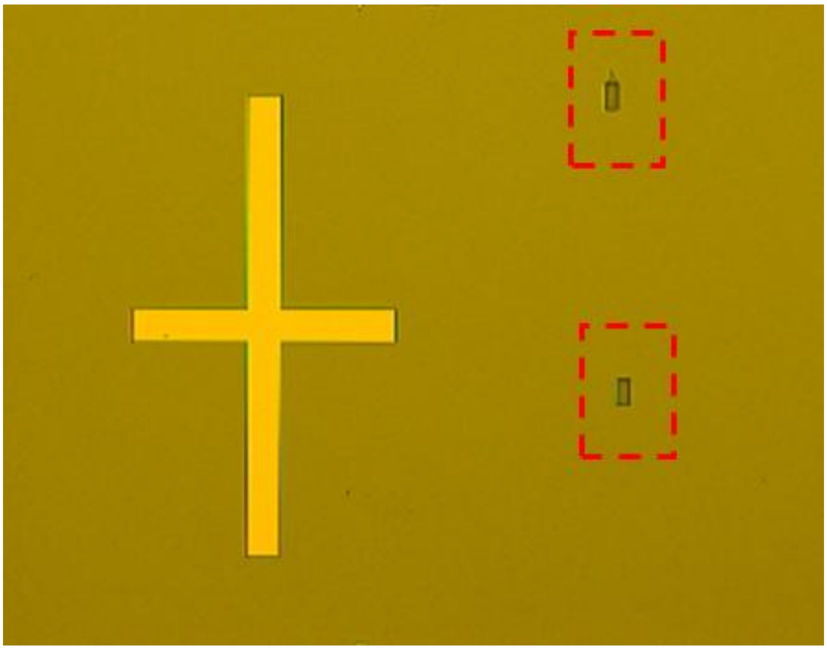

**Fig. 3.7. Optical microscope image of the electrical isolation region after etching and mask removal.**

### 3.2.3 Ridge waveguide and sidewall grating ridge waveguide

In this work, two waveguide structures are used. The first is a standard ridge waveguide with smooth sidewalls, which is used in sections that do not require distributed feedback, such as gain and SA sections. The second is a sidewall grating ridge waveguide, where a periodic corrugation is added to the ridge sidewalls to provide Bragg feedback. Importantly, both structures share the same waveguide width and height and are etched using the same ICP process. The difference is mainly in the lithography pattern that defines either a smooth ridge or a corrugated sidewall ridge. In the later device chapters, these two ridge variants are used for different purposes. The smooth ridge waveguide is used for the non-grating SMLLD devices in Chapters 4 and 7, and also for the non-grating sections of the multisection devices in Sections 5.1, 5.2, and 6.1, such as the SA and SOA regions. The sidewall grating ridge waveguide is used for the grating-defined DFB sections in Sections 5.1 and 5.2 for the chirped sampled-grating devices, and in Sections 6.1 and 6.2 for the WBG microcavity devices. Thus, this subsection provides the common ridge-etch platform for both the plain waveguide lasers and the grating-based DFB lasers studied later.

In current semiconductor DFB lasers, there are mainly two grating approaches, buried gratings (BG) and sidewall gratings [123–128]. In a BG design, the grating is typically etched into an InGaAsP layer positioned either above or below the quantum wells. Since the optical field is strongly confined near the quantum well region, a shallow grating etch depth of around 40 to 60 nm is often sufficient to achieve a coupling coefficient in the range of 200 to 300 $cm^{-1}$. In contrast, for a sidewall grating structure, the grating is formed by etching the ridge sidewalls together with the waveguide, so the etch depth is typically close to the full ridge depth, around 2 μm, to achieve comparable coupling. This approach can increase waveguide loss because the corrugation locally narrows the waveguide and introduces additional scattering. Despite this, sidewall gratings offer two practical advantages. First, they avoid a second epitaxial regrowth step, which simplifies fabrication and reduces process complexity. Second, the ridge and the grating are defined in the same exposure and etch step, so there is no alignment error between the waveguide and the grating. This is especially useful for complex grating layouts such as Moiré gratings and superimposed gratings, where small alignment offsets can significantly degrade performance. For defining both the ridge waveguide and the sidewall grating ridge patterns, HSQ (hydrogen silsesquioxane) is used as the hard mask material [129,130]. HSQ is a negative-tone e-beam resist, where exposed regions become insoluble in the developer. Compared with PMMA, HSQ provides higher resolution and improved resistance during InP etching. In a chlorine-based etching process, the selectivity between the etched material and HSQ can exceed 5:1, and HSQ is also less prone to lateral erosion, which helps reduce sidewall roughness in the etched ridge and grating structures.

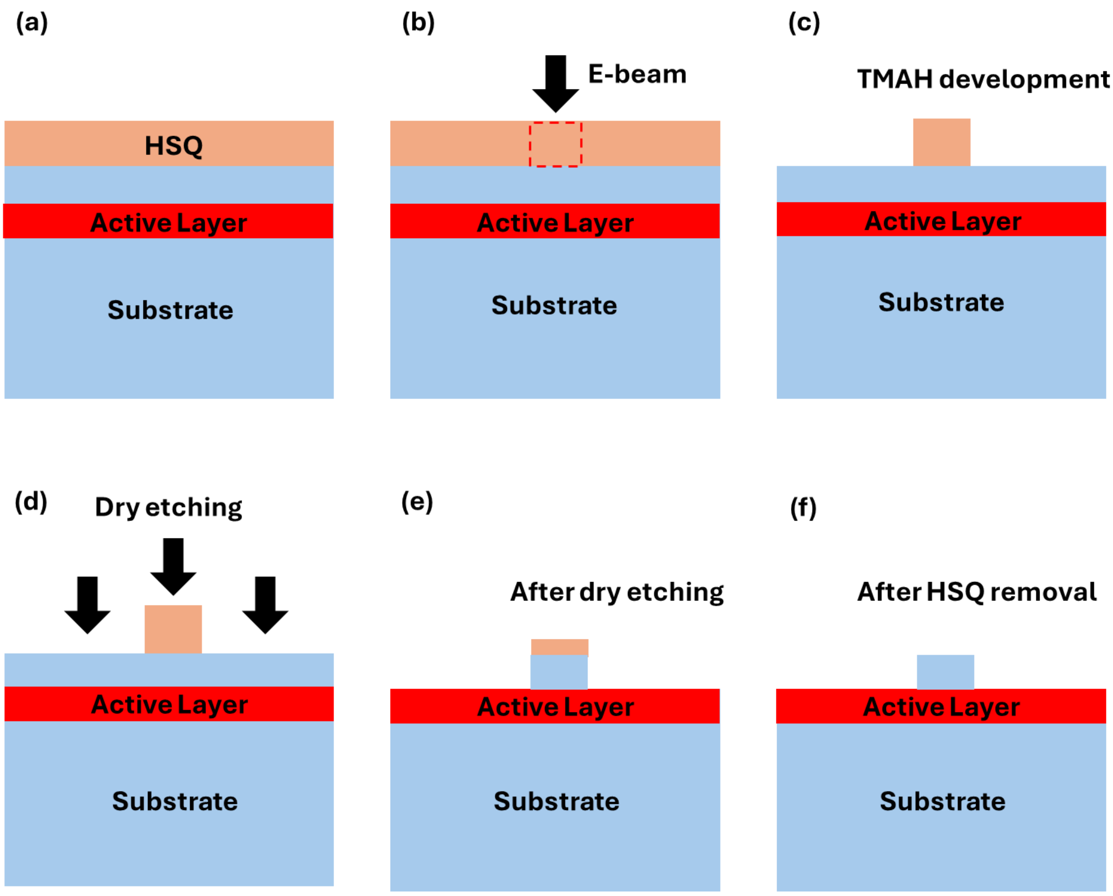


**Fig. 3.7. Ridge waveguide definition using an HSQ hard mask: (a) HSQ coating, (b) e-beam exposure, (c) developed HSQ mask, (d) ICP dry etching, (e) etched ridge waveguide, (f) after HSQ removal.**

Before coating HSQ, the sample is treated in a UV ozone cleaner for 5 minutes. This step helps remove residual organic contamination and improves the adhesion of HSQ to the surface. HSQ is then spin-coated at 2000 rpm, followed by baking on a hotplate at 90°C for 3 minutes to stabilise the film. Under these conditions, the HSQ thickness is typically around 600 nm. After e-beam exposure, the pattern is developed using 25% TMAH (tetramethylammonium hydroxide). The sample is immersed in 25% TMAH at 23°C for 30 seconds, then rinsed in DI water for 60 seconds to stop the development and dilute any remaining TMAH. The sample is then immersed in IPA for 30 seconds and dried with nitrogen gas. After development, the pattern is inspected using a scanning electron microscope (SEM) to confirm the feature integrity and to ensure there is no residual HSQ remaining within the grating openings. If incomplete development or residual HSQ is observed, the HSQ layer can be removed using an HF-based cleaning step, and the lithography process can be repeated.

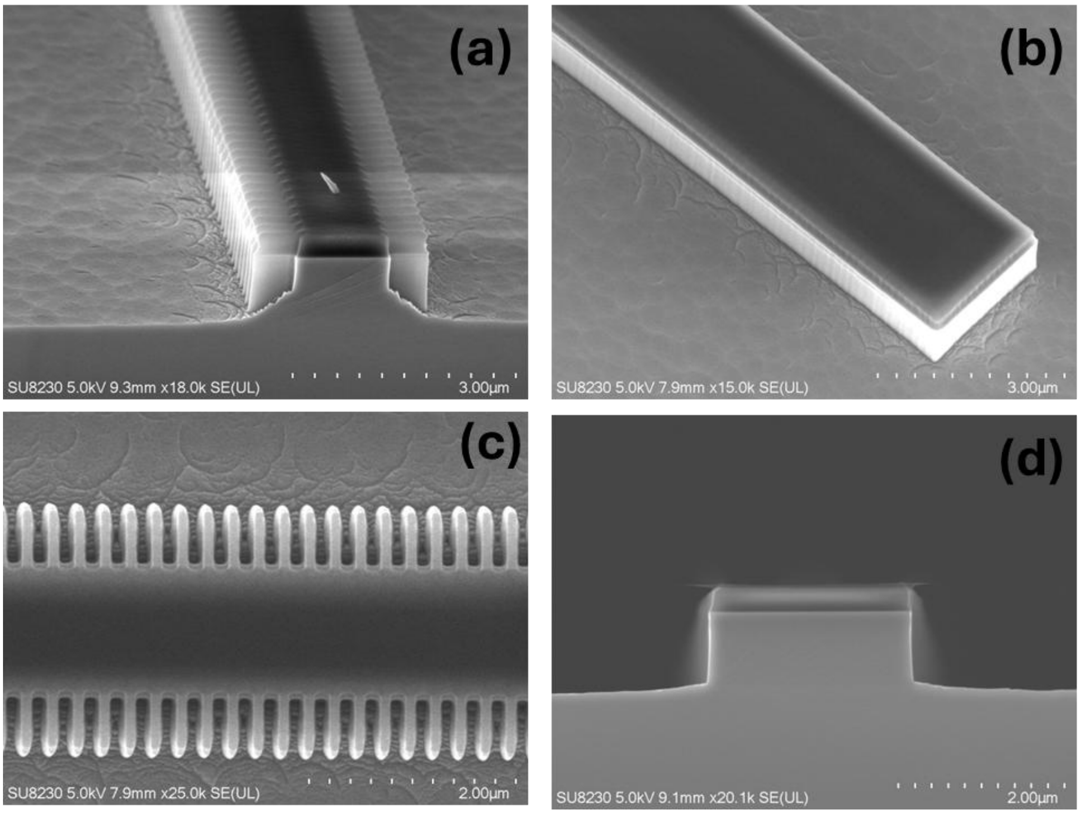


**Fig. 3.8. SEM images of etched waveguide structures: (a) Tilted view of the sidewall grating, (b) tilted view of the standard ridge waveguide, (c) close-up image showing the sidewall grating corrugations, and (d) cross-sectional image of the etched standard ridge waveguide profile.**

After preparing the HSQ mask, the sample is etched using the ICP process described earlier, with etch depth monitored by the interferometric signal shown in Fig. 3.7. The etch proceeds through the 1.6 µm p-InP layer and continues briefly to reach the target ridge etch depth of approximately 1.92 µm. A small etch depth variation across the sample can occur, with slightly faster etching near the edges, but the overall depth typically remains within a narrow range. After etching, the remaining HSQ mask is removed using a 6:1 buffered oxide etch (BOE) solution. An exception is made for samples processed on a SI substrate, where the HSQ is intentionally retained at this stage to support a subsequent patterning step, which is described in the following subsection. Fig. 3.7 summarises the ridge definition steps, including the HSQ mask after development, the etched ridge after ICP etching, and the structure after HSQ removal. Figure 3.8 shows representative SEM images of the etched standard ridge and sidewall grating ridge structures. The sidewall grating ridge shows clear periodic corrugations with good pattern fidelity, while the standard ridge waveguide shows smooth and well-defined sidewalls. These images confirm successful pattern transfer from the HSQ mask into the InP-based epitaxial structure.

For the HSQ patterning, the e-beam exposure dose followed the established process used in our group at JWNC, and a dose of 1000 $\mu C \cdot cm^{-2}$ was used for the ridge and sidewall grating layouts. The ICP dry etching was performed using the Oxford ICP 300 Cobra system at 60°C and 5 mTorr, with ICP power 750 W and platen RF power 100 W, using a $Cl_2/H_2/CH_4/Ar$ chemistry with flow rates of 10/15/10/10 sccm, respectively.

### 3.2.4 Buffer etching for Semi-insulation substrate

In the standard ridge waveguide process, the remaining HSQ hard mask shown in Fig. 3.7 (e) is removed after completing the ridge etch. However, for devices fabricated on an SI substrate, the substrate back side is not conductive, so the required electrical contact of the n-doped layer cannot be formed from the back side. For this reason, the fabrication flow includes an additional step to etch further from the top side, so that the etch reaches the $n^+$-doped layer for electrical contact. This additional buffer-etch step is specific to the semi-insulating-substrate device presented in Chapter 4. Because the substrate is semi-insulating, a conventional backside n-contact cannot be used, so the $n^+$-doped layer must be accessed from the top side. This is why the Chapter 4 device requires a second HSQ definition step and a deeper top-side etch. By contrast, the devices presented in Sections 5.1, 5.2, 6.1, 6.2, and Chapter 7 are fabricated on conductive substrates and therefore do not require this additional top-side access etch, since their n-contact is formed later from the backside after thinning.

Therefore, after completing the ridge waveguide etch, the HSQ mask is not removed for SI-substrate devices. Instead, a second HSQ layer is applied using the same coating conditions as the first HSQ layer, meaning the same spin and bake process, to obtain a similar HSQ thickness. This second HSQ layer is then patterned by e-beam lithography to define a protected buffer region around the original ridge waveguide, so that the ridge and the quantum wells beneath it are not exposed to the extended etch. The process flow for this additional HSQ patterning and the subsequent extended etch is summarised in Fig. 3.10. In this step, the HSQ mask is designed such that a 14 μm wide region centred on the ridge waveguide remains covered by HSQ and therefore remains unetched, while the surrounding areas are opened and etched further to reach the target layer. SEM image of the ridge waveguide with the buffer area after the second dry etch is shown in Fig. 3.11.

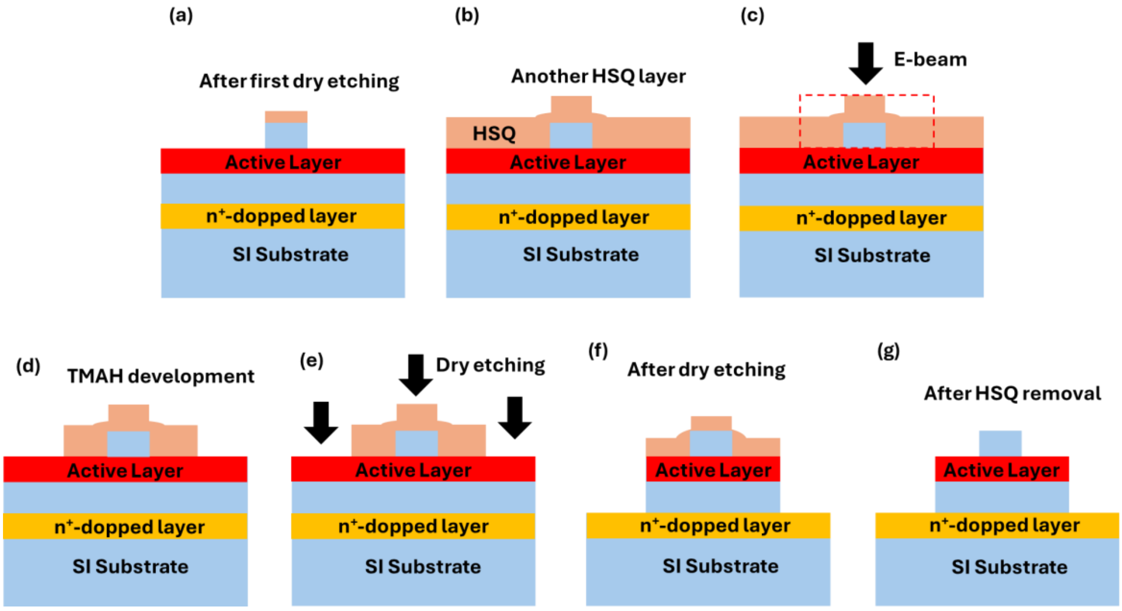


**Fig. 3.10. Extended etching process for SI-substrate: (a) ridge waveguide after the initial etch with thin remaining HSQ layer, (b) second HSQ coating, (c) e-beam exposure to define the protected buffer region, (d) developed second HSQ mask, (e) extended ICP dry etch to reach the n-doped layer while protecting the ridge region, (f) structure after removal of the second HSQ mask.**

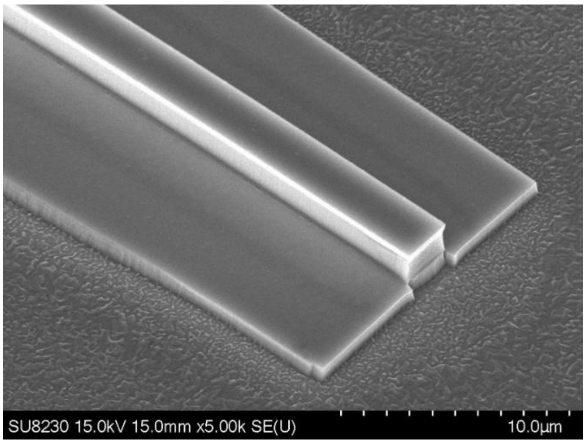


**Fig. 3.11. SEM image of the ridge waveguide with the buffer area after the second dry etch.**

After development of the second HSQ pattern using the same HSQ development procedure described earlier, the sample is returned to the ICP system, and the dry etch is continued using the same ICP etching approach. The etch was continued by an additional depth of 608 nm to reach the n-doped layer. The etch depth is monitored using the interferometer reflectivity signal, and the corresponding interferometer trace for this additional etching step is presented in Fig. 3.12. The etch is stopped once the target layer for the top-side contact is reached. After completing this extended etch, the HSQ mask is removed using an HF-based solution, as described previously.

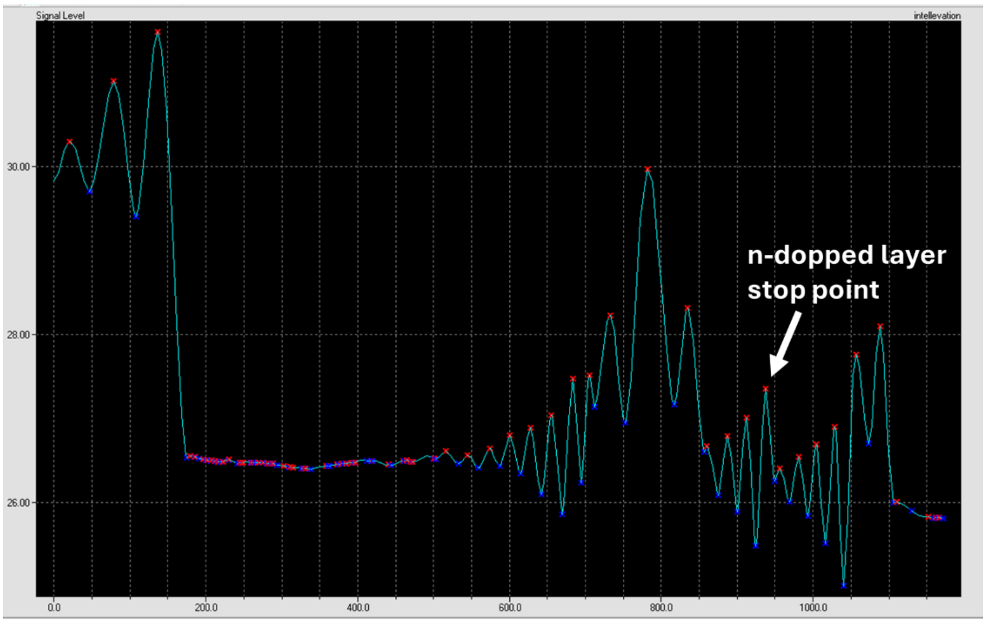


**Fig. 3.12. Reflectivity trace from the interferometer for n-dopped layer.**

## 3.3 Passivation layer deposition

After the grating and ridge waveguide etching is completed and any remaining HSQ mask is removed, a passivation insulating thin film is deposited on the sample surface. This insulating layer serves several purposes. First, it provides electrical isolation so that, after the contact windows are opened, current injection is confined to the ridge waveguide region, which improves injection efficiency. It also helps to reduce the parasitic capacitance of the device, which can support higher modulation speed. In addition, the insulating film protects the etched ridge and grating structures, improving mechanical stability and limiting surface degradation when the sample is exposed to air.

In this work, the insulating stack consists of silicon dioxide ($SiO_2$) together with a passivated HSQ layer. A 200 nm $SiO_2$ film is first deposited by PECVD (plasma-enhanced chemical vapour deposition) at 300°C [131,132]. PECVD is suitable here because it offers good conformal coverage and gap filling, which is particularly important for uniformly filling the grating trenches. Next, HSQ is spin-coated onto the sample at 4000 rpm, followed by curing in an oven at 180°C for 1 hour. Since HSQ is applied as a liquid, it reflows before curing and partially levels the ridge topography, converting the stepped ridge profile into a smoother surface. This smoothing step simplifies the subsequent metal deposition for the top electrode by reducing sharp topography changes. Finally, an additional 100 nm $SiO_2$ layer is deposited by PECVD to improve adhesion with the subsequently deposited metal contact layers and enhance the structural robustness of the device.

## 3.4 Contact window opening

After depositing the insulating stack on the sample surface, the next step is to open contact windows in the regions where current injection is required. This "window opening" step removes the insulating layers locally, exposing the ridge waveguide surface so that metal contacts can later be deposited. For devices fabricated on an SI substrate, the contact to the $n^+$-doped layer is also formed from the top side. This difference between the standard substrate and SI substrate window-opening schemes is illustrated in Fig. 3.14. Therefore, the opening for the n-contact access region is defined and etched during the same window-opening process used for the p-contact, with the mask layout including both regions. In relation to the later device chapters, the p-contact window-opening process described here is common to all devices presented in Chapters 4–7, since all of them use top-side p-metallisation. However, the top-side n-contact window is required only for the semi-insulating-substrate SMLLD in Chapter 4, where the $n^+$-layer must be reached from above. The devices presented in Sections 5.1, 5.2, 6.1, 6.2, and Chapter 7 follow the standard conductive-substrate route and therefore require only the top-side p-contact window at this stage, with the n-contact formed later from the backside after thinning. Similar to the electrical isolation step, a lithography mask is formed using two layers of 15% PMMA. The window regions are then exposed and developed to define where the insulating layers will be removed. The insulating stack is etched using a reactive ion etching (RIE) system [133]. In RIE, plasma is generated by applying RF power directly to the substrate electrode, which acts as the bottom electrode. While ICP systems can offer higher anisotropies and better performance for high aspect-ratio features, RIE is sufficient here because the window opening patterns are typically on the micron scale. The p-contact window width is designed to be slightly smaller than the ridge width to prevent the top metal electrode from spreading onto the regions beside the ridge. In this work, with a ridge width of 2.5 µm, the window opening width is set to 1.3 µm. Where the n-contact window is set to a width of 140 µm.

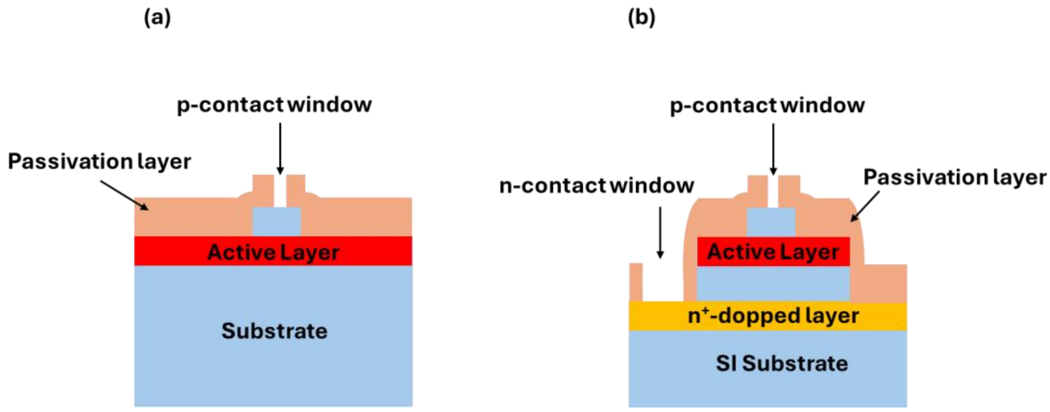


**Fig. 3.14. Contact window opening schemes for (a) standard substrate devices and (b) SI substrate devices with top-side access to the $n^+$-doped layer.**

For $SiO_2$ etching, $CHF_3$ (trifluoromethane) and Ar are used with flow rates of 25 sccm and 15 sccm, respectively. The chamber pressure is 30 mTorr, the substrate temperature is 20°C, and the RF power is 150 W. Under these conditions, the $SiO_2$ etch rate is approximately 22 nm/min, while cured HSQ etches slightly faster. The etch depth is monitored using an interferometer. Since this recipe has minimal reactivity with the top $p^+$-InGaAs layer, the monitoring curve shows little change once the $SiO_2$ removal is complete and the underlying semiconductor is reached. After etching, the residual PMMA mask is removed by an $O_2$ plasma clean in the same chamber using an $O_2$ flow rate of 50 sccm for 5 minutes. Microscope image of both p- and n-contacts windows on the SI substrate is shown in Fig. 3.15.

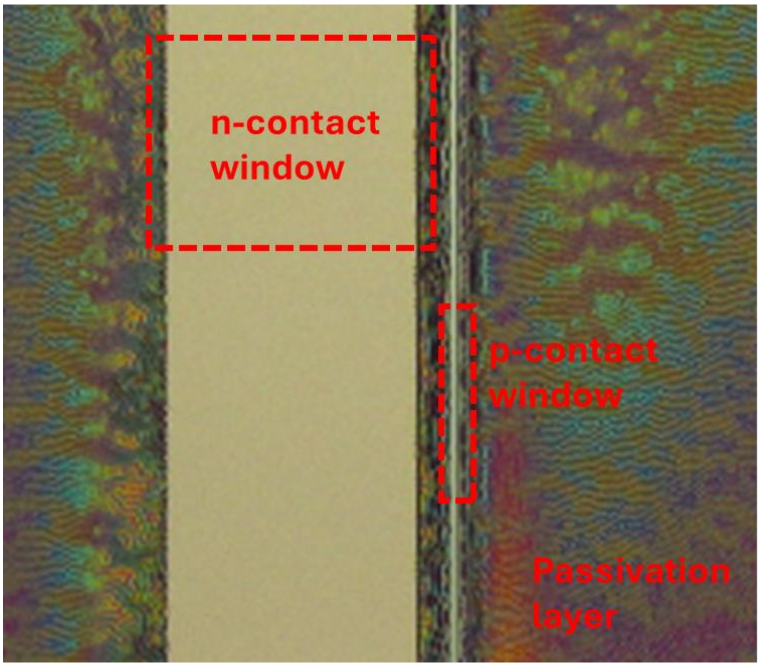


**Fig.3.15. Microscope image showing both p- and n-contact windows on the SI substrate.**

## 3.5 Contacts electrode deposition

After completion of the contact window opening process, the next step is the deposition of the metal electrodes. In all devices presented in this thesis, the p-contact is formed on the top side of the ridge waveguide. The implementation of the n-contact, however, depends on the substrate type and device configuration. For devices fabricated on a conductive substrate, the n-contact is formed later by backside metallisation after thinning. In contrast, for devices fabricated on a SI substrate, electrical access to the n-type region is provided from the top side, and no backside n-contact is required. These different approaches are reflected in the contact design but share the same top-side metallisation procedure described below. This distinction corresponds directly to the later device chapters. The simultaneous top-side p- and n-contact scheme is used for the SI-substrate 10 GHz SMLLD in Chapter 4, enabling RF access through the on-chip CPW and GSG probing arrangement. By contrast, the devices presented in Sections 5.1, 5.2, 6.1, 6.2, and Chapter 7 use the standard conductive-substrate scheme, in which only the top-side p-contact is defined at this stage and the n-contact is completed later by backside metallisation after thinning. To define the contact metal patterns, a multilayer PMMA resist stack is used to enable a reliable lift-off process. Three PMMA layers are spin-coated sequentially at 4000 rpm. The first two layers use a 15% PMMA solution, while the top layer uses a 4% PMMA solution. Each layer is baked individually to harden the resist, with baking times of 4 minutes for the first layer, 5 minutes for the second layer, and 6 minutes for the final layer. Compared with earlier metal deposition steps, an additional PMMA layer is required here due to the pronounced topography of the ridge waveguide. During spin-coating, the resist thickness above the ridge is reduced relative to the surrounding planar regions. The three-layer PMMA stack ensures sufficient resist thickness across the ridge and contact window regions, which is critical for achieving a clean and complete lift-off after metal deposition. After exposure and development of the contact patterns, the sample is treated in an $O_2$ plasma asher at 150 W for 2 minutes to remove any residual PMMA in the opened windows. Immediately before metal deposition, the sample is immersed in a diluted hydrochloric acid solution ($HCl$: $H_2O$ = 1:5) for 90 seconds. This step removes native oxides from the exposed semiconductor surfaces, improving metal–semiconductor adhesion and reducing contact resistance. The contact metal stack is then deposited using electron-beam evaporation [134,135]. The stack consists of 30 nm Ti, 30 nm Pt, and 240 nm Au. Titanium serves as an adhesion layer, ensuring good bonding between the metal and the semiconductor. Platinum acts as a diffusion barrier, preventing interdiffusion between titanium and gold, while gold provides low electrical resistivity and excellent chemical stability, forming the main conductive layer of the electrode. After metal deposition, the sample is immersed in acetone and placed in a 50°C water bath to complete the lift-off process. This removes the excess metal together with the PMMA resist, leaving well-defined top-side contact electrodes. Example microscope image of the fabricated sample with p-contacts is shown in Fig. 3.16.

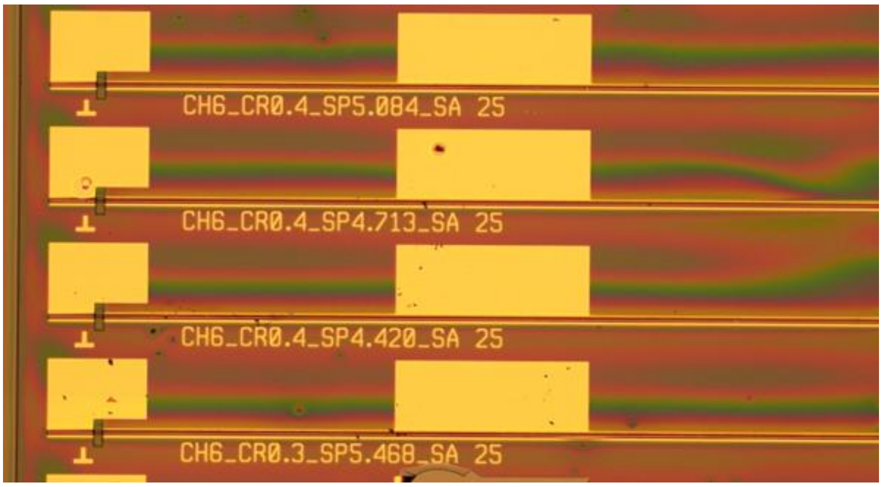


**Fig.3.16. Microscope image of the fabricated sample with p-contacts.**

For SI-substrate devices, this step completes both the p- and n-contact metallisation from the top side. For conductive-substrate devices, the n-contact is formed later, following substrate thinning, as described in the next section. For devices fabricated on a conductive substrate, the backside contact is formed after substrate thinning by directly evaporating a Ti (30 nm)/Pt (30 nm)/Au (240 nm) metal stack over the entire backside surface, without the use of a lithographic mask.

## 3.6 Thinning and cleaving

To reduce the device series resistance and improve thermal dissipation, the fabricated sample is mechanically thinned after completion of the top-side contact metallisation. Thinning is carried out manually using an alumina suspension on a frosted glass plate. Initially, a 9 µm alumina suspension is used as the abrasive medium to remove material efficiently. Starting from an initial wafer thickness of approximately 370 µm and targeting a final device thickness of around 200 µm, a total thickness reduction of about 170 µm is required. When the remaining thickness approaches the target value, the alumina suspension is replaced with a 3 µm suspension to polish the bottom surface, resulting in a smoother and more uniform finish.

For devices fabricated on a conductive substrate, the backside contact is formed immediately after thinning by depositing metal uniformly across the entire backside surface, without the use of any lithography mask. The metal stack and deposition conditions are identical to those used for the top-side contact. After metallisation, the sample undergoes an annealing process at 380°C for 1 minute, which improves the metal–semiconductor interface and reduces contact resistance [136,137]. For devices fabricated on an SI substrate, this backside contact step is not required, since electrical access to the n-type region is provided from the top side, as described in the previous section. Accordingly, the backside metallisation route described here applies to the conductive-substrate devices presented later in Sections 5.1, 5.2, 6.1, 6.2, and Chapter 7, whereas the Chapter 4 SI-substrate device follows the alternative top-side n-contact route described earlier and therefore does not require backside n-metallisation. The final thinning and cleaving step, however, is common to all device types, since it defines the laser-bar geometry and the cleaved end facets used in the measurements reported in the later chapters. Once the annealing process is completed, the sample is cleaved along the crystallographic cleavage planes and the designed cavity length to form individual laser bar strips. This cleaving step defines the end facets of the devices, preparing them for subsequent optical and electrical characterisation. This final thinning and cleaving workflow, and the resulting cleaved laser bars, are shown in Fig. 3.17.


**Fig. 3.17. Photographs of the final processing steps: (a) manual sample thinning, (b) sample cleaving setup, and (c) cleaved laser bar strips ready for testing.**

## 3.7 Chapter summary

This chapter described the main fabrication flow used to produce testable laser bar devices. The process includes sample preparation and alignment marker definition, electrical isolation etching, ridge waveguide and sidewall grating formation by ICP etching, deposition of the insulating stack, contact window opening, and metal contact deposition. For devices fabricated on SI substrates, an additional buffer etch step was included to enable top-side access to the n-contact. The fabrication sequence then continues with sample thinning and cleaving into laser bar strips for device characterisation. In this work, the fabrication recipes and processing conditions follow the established and optimised procedures used within our group, enabling reproducible ridge and grating profiles suitable for the devices presented in the following chapters.

# Chapter 4: Ultrastable 10 GHz Mode-Locked Laser on Semi-Insulating Substrate

This chapter presents an ultrastable 10 GHz passive SMLLD on a SI-InP substrate for optical clock applications. It introduces the device structure and fabrication, then outlines the free-running passive mode-locking operation. The chapter mainly focuses on stabilisation through RF injection locking applied to the SA via the on-chip CPW using a GSG probe, with emphasis on both fundamental and subharmonic operation to enable locking using lower-frequency RF signals. Finally, optical injection locking is briefly included as a secondary stabilisation approach for comparison[1]. This chapter builds directly on the theoretical background presented in Section 2.3 for the 10 GHz passively mode-locked laser and its stabilisation through RF and optical injection locking, as discussed in Sections 2.3.2 and 2.3.3, respectively.

## 4.1 Device overview

Fig. 4.1 shows a schematic of the 10 GHz passive SMLLD fabricated on SI-InP substrate. The wafer layer structure is described in Section 3.1 and shown in Fig. 2.11. The devices comprises a 4230 µm gain section and a 60 µm SA section, with a 10 µm electrically isolated region in between, which is formed by etching away the top p-type contact layer. The device has on-chip coplanar waveguide (CPW) contacts for ground–signal–ground (GSG) probe access. The top ridge waveguide is 2.5 µm wide and 1.92 µm high. The fabrication process follows the procedure described in Chapter 3 and can also be referenced in the SMLLD fabrication procedures reported in [89], except that the p- and n-contacts were defined simultaneously on the same side of the wafer. A microscope image of the fabricated SMLLD devices and an SEM image of the ridge waveguide cross-section are presented in Fig. 4.1(b) and (c), respectively. After fabrication, the devices were cleaved with uncoated facets and mounted onto a copper heat sink using indium solder for continuous-wave (CW) testing at 20 °C.

[1] Part of this chapter have been published previously in: M. Al-Rubaiee *et al.*, *IEEE Photonics Technology Letters*, **36**, 1189-1192 (2024).

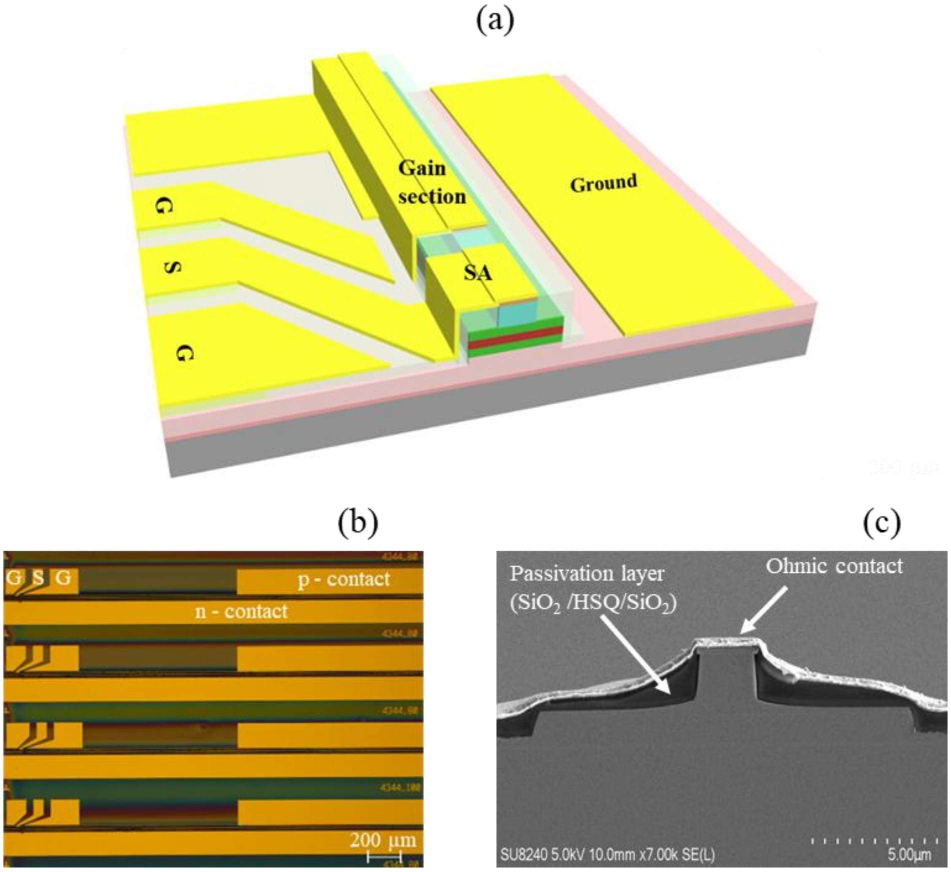


**Fig. 4.1. (a) Schematic of the passive SMLLD, (b) microscope image of the fabricated SMLLDs, (c) SEM image of the cross-section of the ridge waveguide.**

The output power of the device was measured from the SA side as a function of the gain currents ($I_{gain}$, from 0 mA to 500 mA) at different SA reverse voltages ($V_{SA}$, from 0 V to -3 V), as shown in Fig. 4.2. The measured threshold current ($I_{th}$) is 90 mA when the SA is floating. The device exhibited an output power of 8.6 mW at a gain injection current of 200 mA when the SA section voltage was 0 V. Passive mode-locking (ML) of the device was achieved by forward biasing the gain section and applying a reverse voltage to the SA section. We observed typical trends: pulses broaden with increasing gain current and shorten with increasing SA reverse voltage. When the gain section injection current was 200 mA and a reverse bias of 1.8 V was applied to the SA section, the device demonstrated free running ML with an average output power of 5 mW.

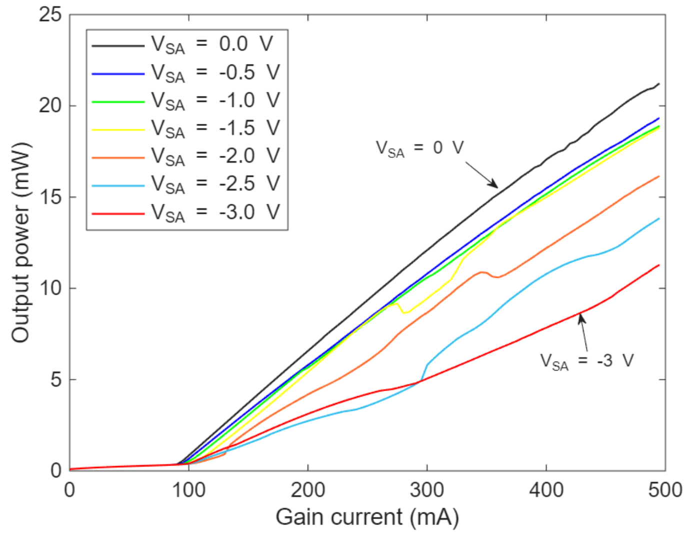


**Fig. 4.2. I-P curve characteristics for different $V_{SA}$.**

Notably, the measured divergence angles from the gain side in the horizontal and vertical directions were 18.3° and 31.1°, respectively. These values also compare well with the simulated divergence angles of 23° (horizontal) and 31° (vertical), as shown in Fig. 4.3 This is a clear reduction compared with the conventional SMLLD vertical divergence angle of ~40°, improving the coupling efficiency to a cleaved SMF to 20%, which is nearly twice that of a conventional QW laser without an FRL layer (~10%).

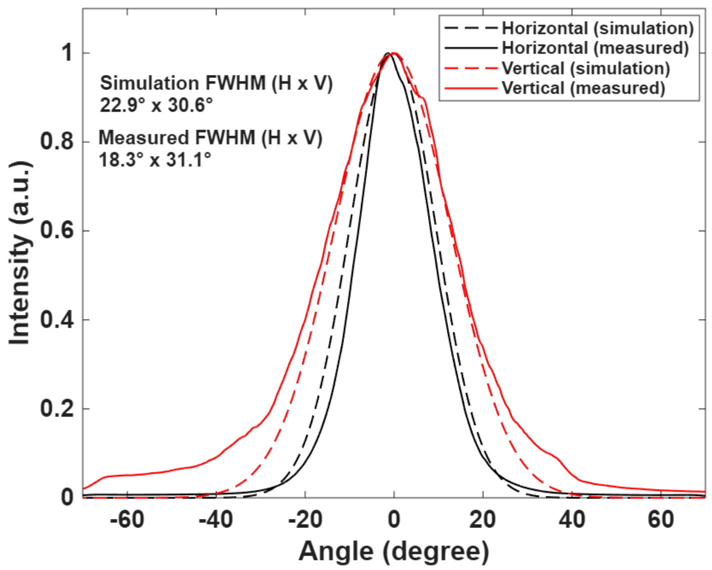


**Fig.4.3. Measured and simulated far field pattern under the condition of $I_{gain}$= 150 mA and SA floating.**

## 4.2 Stabilisation through RF injection locking

The experimental setup for the RF injection locking is shown in Fig. 4.4. A CW laser current source was used to forward bias the gain section of the SMLLD, while a DC voltage supply was applied to reverse bias the SA. RF signals together with a DC reverse bias were delivered to the SA through a bias-T and an on-chip CPW, using a GSG probe.

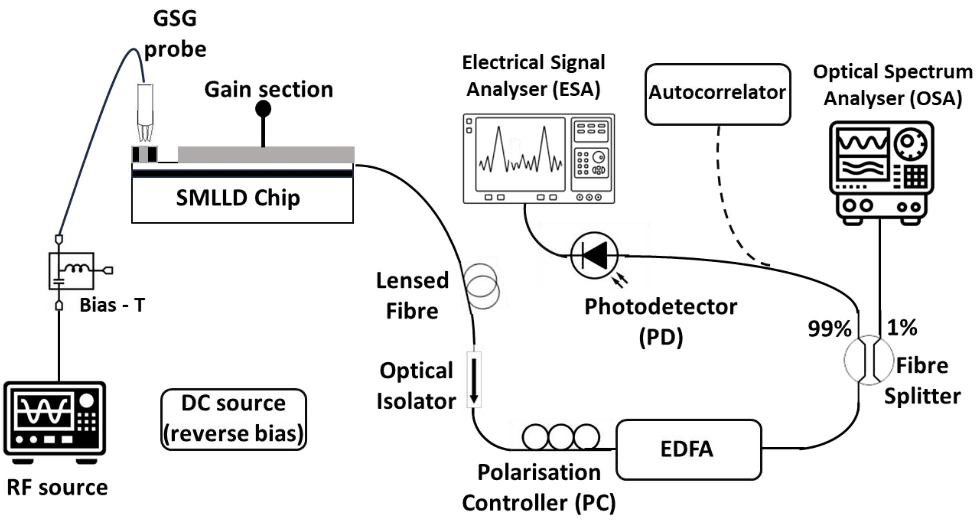


**Fig. 4.4. Experimental configuration of the injection locking.**

The optical output emitted from the gain-section facet of the laser was coupled into a lensed SMF, a Polarisation controller (PC), an erbium-doped fibre amplifier (EDFA), and a 99:1 fibre splitter. From the splitter, 1% of the light was sent to an optical spectrum analyser (OSA) with a 0.06 nm resolution bandwidth (RBW) for detailed spectral analysis. Simultaneously, 99% of the light from the fibre splitter was directed to a 50 GHz InGaAs PD and a 50 GHz electrical spectrum analyser (ESA) Keysight N9020B for comprehensive RF analysis. This 99% portion could also be connected to an autocorrelator for AC trace measurements. A PriTel SPFA-23-03-IO EDFA was used before the autocorrelator to provide sufficient optical power. Therefore, the measured autocorrelation traces represent the combined output of the SMLLD and EDFA. Manufacturer data for the SPFA-23 show pulse broadening from 150 fs to approximately 195 fs, with the optical spectrum largely preserved. Since the pulses measured here were several picoseconds wide, the EDFA-induced contribution is expected to be small relative to the measured pulse width. This consideration applies to all autocorrelation measurements reported in Chapters 4–7. The measured RF spectrum is shown in Fig. 4.5(a), exhibiting a fundamental frequency peak at 9.78 GHz together with its harmonics. A Lorentzian fit to the fundamental RF spectrum gives a –3 dB linewidth of 40 kHz at a 1 kHz RBW, as presented in Fig. 4.5(b). From Fig. 4.5(a), it can be seen that the fundamental RF signal is more than 50 dB above the noise floor, with no additional self-pulsating frequency components, confirming that the laser operated in a pure ML regime. Under the same bias conditions, the optical spectrum in both free running and injection locking with an –5 dB RF power is presented in Fig. 4.5(c). The free-running central wavelength is 1548.5 nm with a full width at half maximum (FWHM) of 5.1 nm. Following RF injection locking, the central wavelength shifts to 1545.1 nm, while the FWHM remains essentially unchanged.

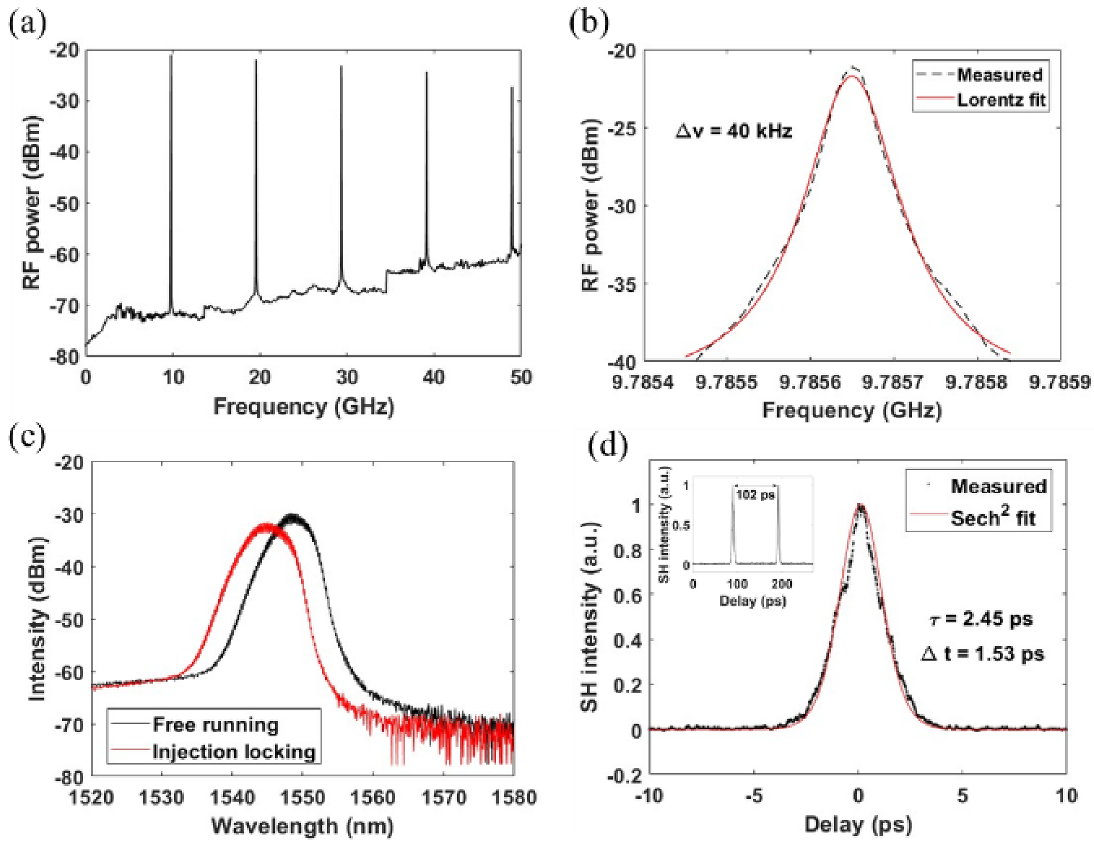


**Fig. 4.5. Measured at 200 mA gain injection current and 1.8 V SA reverse bias: (a) RF spectrum, (b) zoomed-in and Lorentz fitted measured RF frequency, (c) optical spectrum of free running and injection locking at –5 dBm injection power, (d) AC of an isolated pulse and extended AC trace (inset).**

The blue shift observed after RF injection locking is attributed to changes in carrier density and refractive index inside the laser cavity induced by the external RF signal. The increased carrier density alters the refractive index through the plasma effect, leading to a shift toward shorter wavelengths [93]. This wavelength shift was found to remain the same for all injection RF powers. The measured AC traces are shown in Fig. 4.5(d). The single AC pulse width was measured to be 2.45 ps; assuming a sech$^2$ pulse shape, this deconvolves to a pulse duration of 1.53 ps, giving a time-bandwidth product (TBP) of 0.97, which is larger than the transform-limited value ($\approx$0.315). This is most likely due to SPM in the long gain section (>4 mm) [92]. The pulse separation in the AC traces was 102 ps (inset of Fig. 4.5(d)), which matches exactly the reciprocal of the ML frequency of 9.78 GHz in Fig. 4.5(a). After injection locking, the optical pulse showed no discernible change in pulse shape, indicating that injection locking did not introduce noticeable distortion or noise and therefore preserved the stability and quality of the pulses [138]. Injection locking was obtained by injecting an RF electrical signal at 9.78 GHz from a 20 GHz synthesiser into the SA through the on-chip CPW, using the GSG probe and a bias-T, while keeping the device under the free-running ML operating condition. Fundamental hybrid ML effects were observed for RF powers as low as –20 dBm (Fig. 4.6(a)). At first, the passive ML peak linewidth of 40 kHz was reduced to sub-Hertz levels at an injection power of –5 dBm, measured with a 1 Hz RBW, as shown in the inset of Fig. 4.6(a). The single sideband (SSB) noise versus frequency offset is presented in Fig. 4.6(b). The phase noise was measured using the method described in [87]. A strong reduction in phase noise was observed as the injected RF power increased from –20 dBm to –5 dBm. At a 10 kHz offset, the phase noise under passive ML operation was –43 dBc/Hz, improving to –70, –75, –80, and –85 dBc/Hz for injected RF powers of –20, –15, –10, and –5 dBm, respectively. The phase-noise plateau seen in Fig. 4.6(b) between 10 kHz and 1 MHz is attributed to HML effects, which synchronise the laser modes and suppress noise arising from thermal and carrier dynamics [86]. With an injected RF power of –5 dBm, the timing jitter was reduced from 7.2 ps in passive ML operation to 80 fs (100 Hz – 100 MHz) for the fundamental ML case. However, further increasing the RF power from –5 dBm to 0 dBm and above did not lead to a noticeable additional reduction in phase noise.

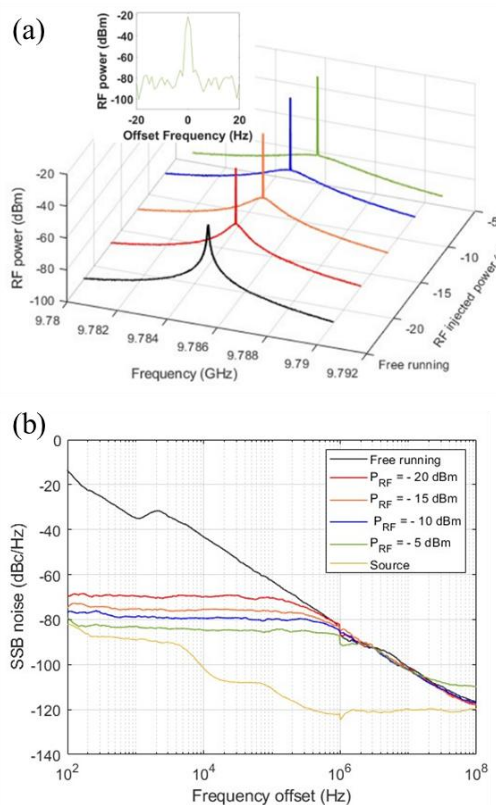


**Fig. 4.6. Free running and fundamental RF injection at different injection powers for (a) RF signal (inset: measured linewidth with an RBW of 1 Hz at –5 dBm injection), and (b) SSB phase noise measured at 200 mA gain injection current and -1.8 V $V_{SA}$.**

Subharmonic injection locking was realised by injecting RF signals at subharmonic frequencies into the SA. This approach synchronises the modes at fractions of the fundamental frequency, which can reduce system complexity and cost. The device showed subharmonic HML effects at different power levels, leading to clear improvements in spectral purity and reduced phase noise. Fig. 4.7(a) presents the RF spectra of the ML round-trip frequency and its subharmonics at 9.78 GHz, 4.89 GHz, 3.26 GHz, and 2.44 GHz, corresponding to the fundamental and subharmonic numbers n = 1, 2, 3, and 4, respectively. The injected RF powers were –5 dBm for the fundamental, 10 dBm for the second subharmonic, 12 dBm for the third subharmonic, and 13 dBm for the fourth subharmonic. Subharmonic injection locking is generally less effective at higher subharmonic numbers because higher powers are required and the harmonic components become weaker as the subharmonic number increases [17,139].

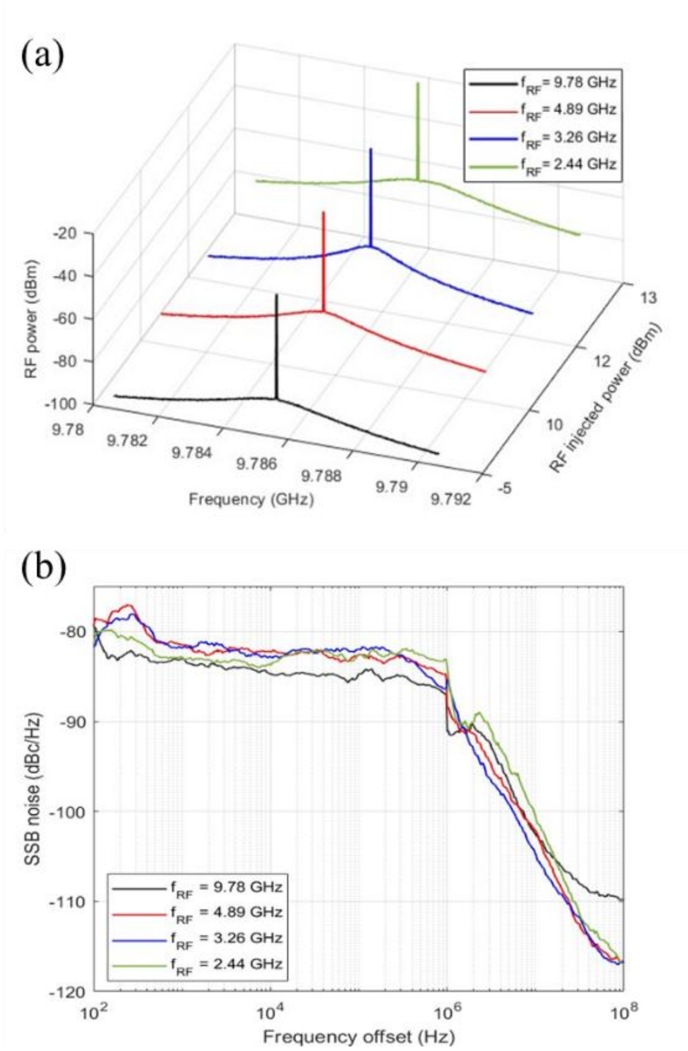


**Fig. 4.7. Measured fundamental and different subharmonic injection locking for (a) RF signal, and (b) SSB phase noise under 200 mA gain injection current and 1.8 V SA reverse bias.**

Compared with the free-running state, all subharmonic frequencies showed a linewidth reduced to sub-Hertz levels. The single sideband phase noise at a 10 kHz offset was between –83 and –85 dBc/Hz for the different subharmonics, with higher subharmonics needing higher injected power to reach these noise levels (Fig. 4.7(b)). The timing jitter was approximately 80 fs (100 Hz–100 MHz) for all subharmonic injections, which is the same as for the fundamental injection case. These results show that subharmonic injection locking can simplify the overall system by using lower-frequency signals, while still improving spectral purity, reducing phase noise, and minimising timing jitter, particularly when combined with an SI substrate. The lower parasitic capacitance associated with the SI substrate improves synchronisation efficiency, making subharmonic injection locking a promising approach for high-performance optical clock generation. The achieved sub-Hertz spectral purity and the observed linewidth narrowing further highlight the effectiveness of injection locking in producing a highly stabilised and precise laser output, suitable for optical clock applications. Table 4.1 compares the injection-locking performance of this work with representative state-of-the-art SMLLDs.

**Table 4.1. State-of-the-art literature comparison of RF injection-locking performance in semiconductor mode-locked lasers.**

| Ref. | Platform | Repetition rate | Locking scheme | Injected RF power |
|---|---|---|---|---|
| Lee *et al.* [12] | SI-InP CPMLL | 36 GHz | Fundamental HML | 0 dBm |
| Ji *et al.* [14] | InGaAsP/InP CPMLL | 28 GHz | Second-subharmonic HML | 26 dBm |
| Hoshida *et al.* [15] | InP DBR SMLLD | 33 GHz | Second- and third-subharmonic HML | 20 dBm |
| Wang *et al.* [16] | III–V-on-Si SMLLD | 1.009 GHz | Fundamental HML | 8 dBm |
| This work | SI-InP SMLLD | 9.78 GHz | Fundamental and second–fourth subharmonic HML | −5 dBm; 10–13 dBm |

## 4.3 Stabilisation through Optical injection locking

Optical injection locking was used to synchronise the modes of the passive SMLLD (slave laser) to those of a master actively MLL (master laser, Pritel), as illustrated in the experimental configuration in Fig. 4.8. Pulses from the master laser, driven by an RF source and operating at a repetition frequency of 10 GHz, were injected into the 10 GHz slave laser. After passing through a variable optical attenuator (VOA) and a polarisation controller (PC), the master signal was injected into the slave laser from the gain-section side using an optical fibre circulator with a lensed-fibre terminal. The injection-locked output was then sent to the OSA and the ESA through an EDFA.

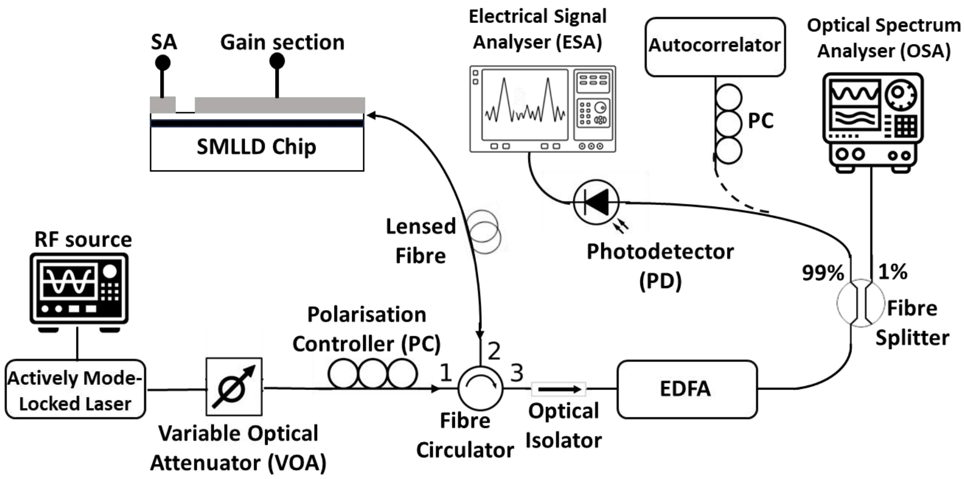


**Fig. 4.8. Experimental configuration of the optical injection locking.**

With an $I_{gain}$ of 150 mA and $V_{SA}$ set to –1.8 V, the optical spectra in both free-running and injection-locked operation are shown in Fig. 4.9(a). Notably, no clear change in the optical spectrum is observed when moving from free running to injection locking. In addition, the pulse width was measured to be 1.8 ps during free running, which remains similar under injection locking when assuming a sech$^2$ pulse shape, as shown in Fig. 4.9(b). The optical power launched into the slave laser was approximately 1.5 mW, while the free-running SMLLD output power was approximately 2.4 mW at $I_{gain}$ = 150 mA and $V_{SA}$ = −1.8 V. This corresponds to an injection ratio of approximately −2 dB.

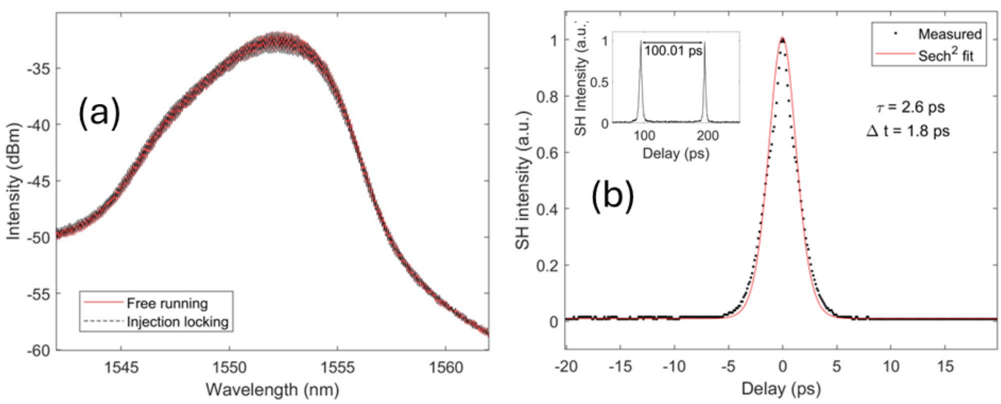


**Fig. 4.9. (a) Optical spectrum of free running and injection locking. (b) AC of an isolated pulse and extended AC trace (inset).**

The device exhibited a free-running RF linewidth of 46.5 kHz. Notably, when optical injection locking was applied, the RF linewidth was dramatically reduced to sub-Hertz levels, as shown in Fig. 4.10(a).

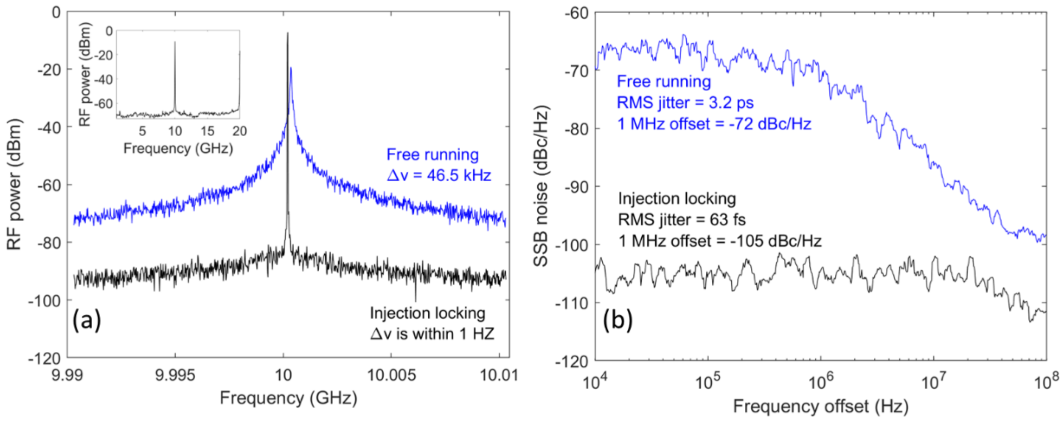


**Fig. 4.10. (a) RF signal for free-running and injection locking operation. (b) SSB phase noise for free-running and injection locking operation.**

This strong linewidth narrowing highlights the effectiveness of optical injection locking in enhancing the spectral purity of the laser. In addition, the SSB phase noise was measured in both the free-running state and after injection locking, as presented in Fig. 4.10(b). The RMS timing jitter of the free-running device, obtained by integrating the SSB phase-noise spectrum over an offset-frequency range of 10 kHz to 100 MHz, was 3.2 ps. With injection locking and an injected RF power of –11.4 dBm, the timing jitter was reduced significantly to 63 fs.

## 4.4 Summary

We developed a 10-GHz passive SMLLD on an SI InP substrate for optical clock applications. With fundamental RF injection locking applied through the SA, the RF linewidth narrowed from the free-running kHz level to sub-Hertz, with a great phase-noise improvement and timing-jitter reduction down to ~80 fs. Importantly, we also achieved subharmonic RF injection locking, which is a key practical selling point because it enables synchronisation using lower-frequency RF signals (simpler electronics), while the SI substrate helps the locking efficiency by reducing RF parasitics, so the required RF power remains relatively low (although a higher subharmonic order still needs higher RF power). A small blue shift in the optical spectrum under RF injection is consistent with carrier-density-induced refractive-index change in the cavity under RF drive. We also demonstrated optical injection locking, achieving RF linewidth reduction from 46.5 kHz to sub-Hertz and timing jitter improvement from 3.2 ps to 63 fs without noticeable pulse/spectrum distortion. However, subharmonic optical injection locking was not observed, because subharmonic optical forcing is intrinsically weaker: it does not provide a strong direct 10-GHz timing component to the slave, so locking would require a much higher injected optical power at the chip (and in practice, this becomes difficult once coupling/circulator/VOA losses are included).

# Chapter 5: Multi-Wavelength Mode-Locked DFB Laser Using Chirped Conventional and Four-Phase-Shifted Sampled Bragg Gratings

This chapter presents the experimental demonstration of a monolithic multi-wavelength passively mode locked DFB laser that generates multiple wavelength channels within the same cavity. The core idea is to use chirped sampled Bragg gratings and distributed π-phase shifts along the DFB cavity so the channel number and spacing are mainly set by design, rather than by using separate DFB elements or external combining. Two grating implementations are studied, the chirped C-SBG and the chirped 4PS- SBG, and the chapter follows a consistent experimental flow, so the comparison is clear. A monolithically integrated saturable absorber is used to enable synchronised passive mode locking across the generated channels. The chapter is therefore structured around the measured optical and time domain characterisation that confirms multi-channel operation, tracks channel behaviour under different bias conditions, and evaluates practical stability[2]. This chapter builds directly on the theoretical background presented in Section 2.4 on DFB lasers based on sampled Bragg gratings, particularly the chirped C-SBG and chirped 4PS-SBG structures discussed in subsections 2.4.3 and 2.4.4, respectively.

## Chirped C-SBG Mode-locked DFB laser

A schematic of the chirped C-SBG-based mode-locked DFB laser is presented in Fig. 5.1. The device comprises a 30 μm SA section, a 1600 μm DFB section, and a 900 μm SOA bent by 10°. Fabrication follows the procedure described in Chapter 3 and can also be referenced in the fabrication procedures reported in [109] on AlGaInAs/InP material with five 6-nm quantum wells as described in Section 2.4.1, with the bandgap structure shown in Fig. 2.14. The ridge waveguide has a width of 2.5 μm and a height of 1.92 μm, with 0.6 nm etched grating recesses, a seed grating period $\Lambda_0$ of 257 nm, and a 50% duty cycle. The sampling periods along the DFB cavity are linearly varied, resulting in a chirp rate of 300 nm/mm, defined by the difference between the initial sampling period ($P_1$ = 4.42 μm) and the final sampling period ($P_n$) over the DFB cavity length. To realise four-wavelength lasing, the DFB cavity incorporates four π-phase shifts located at 1/5, 2/5, 3/5, and 4/5 of its length. By design, each π-phase shift is aligned with the n-th seed grating period ($n\Lambda_0$), so that the placement tolerance is limited to within one seed grating period ($\Lambda_0$). The π-phase shifts, sidewall grating, and ridge waveguide are all defined in a single 100 keV EBPG5200

[2] Part of this chapter have been published previously in: M. Al-Rubaiee *et al.*, *IEEE Journal of Quantum Electronics, **61**, 1-10 (2025).*

electron-beam lithography (EBL) step, where the placement accuracy is typically on the order of a few nanometres, much smaller than $\Lambda_0$.

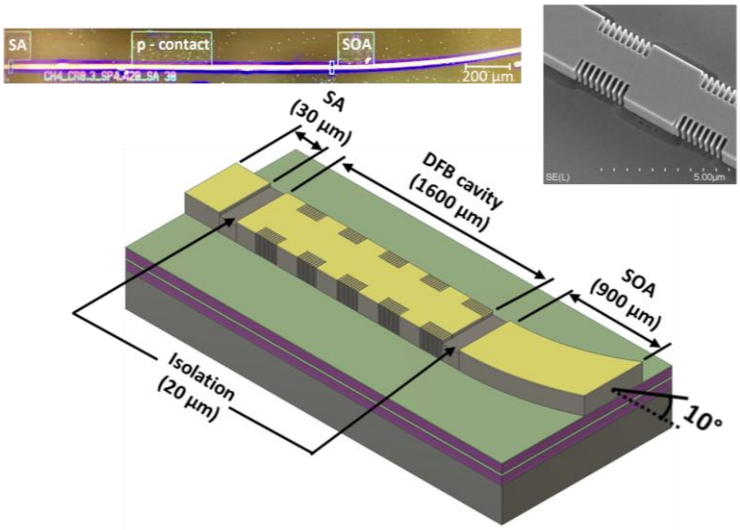


**Fig. 5.1. Schematic of the chirped C-SBG-based multi-wavelength ML-DFB laser, optical micrograph of the fabricated device (left inset), and SEM image of the sidewall grating and ridge waveguide (right inset).**

The left inset of Fig. 5.1 presents a microscope image of the fabricated device, while the right inset shows a scanning electron microscope (SEM) image of the etched sidewall grating and ridge waveguide. The experimental setup is shown in Fig. 5.2. Following fabrication, the devices were cleaved with uncoated facets, and the laser chips were mounted on a thermoelectric cooler (TEC) maintained at 20°C. A CW laser current source was used to forward-bias the DFB gain section, while a separate current source was applied to drive the SOA section. A DC voltage supply was used to reverse-bias the SA section. The optical output from the SOA-facet of the laser was coupled into a lensed SMF, passed through an optical isolator, and then into a 90:10 fibre splitter. From the splitter, 10% of the optical power was directed to an OSA with a RBW of 0.06 nm for high-resolution spectral measurements. At the same time, the remaining 90% was sent through a PC and an EDFA before being delivered to an autocorrelator for recording the AC traces. Fig. 5.3(a) shows the output power collected from the SA-side facet as a function of the DFB current ($I_{DFB}$, 0–300 mA) for different SA reverse voltages ($V_{SA}$, 0 to −3 V), with the SOA section left floating. Increasing the reverse voltage leads to a reduction in the output power ($P$), as the enhanced absorption in the SA section introduces higher intracavity losses. Representative $P$–$I_{DFB}$ and $V_{DFB}$–$I_{DFB}$ curves are presented in the inset of Fig. 5.3(a), with both the SA and SOA sections floating.

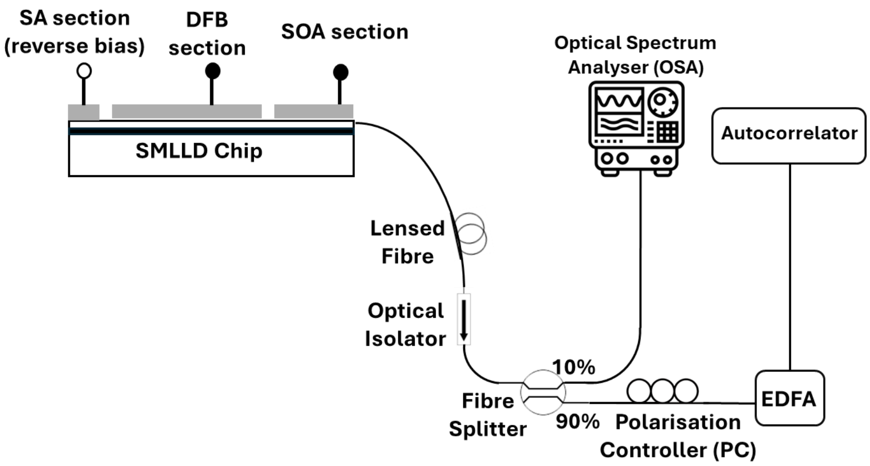


**Fig. 5.2. Experimental measurement configuration.**

Under these conditions, the measured threshold current $I_{th}$ is 60 mA. At $I_{DFB}$ = 300 mA, the output power reaches 9 mW with $V_{SA}$ = -2 V. Fig. 5.3(b) shows the *P–I* characteristics measured from the SOA side, which is used as the output facet for all subsequent measurements. The DFB injection current is swept from 0 to 300 mA, while the SOA current ($I_{SOA}$) is set to 0, 50, 100, 150, 200, and 250 mA with the SA section floating.

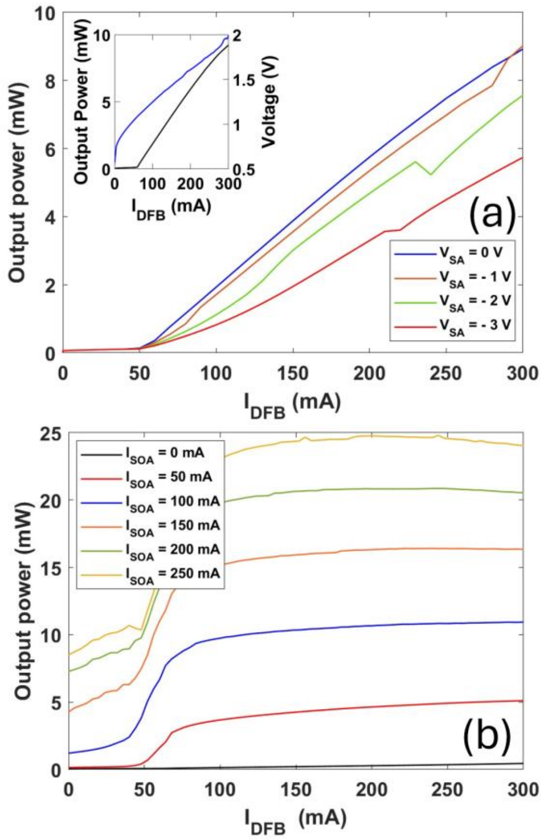


**Fig. 5.3. (a) Output power measured from the SA side as a function of $I_{DFB}$ for different $V_{SA}$ values. The inset shows the voltage–current ($V_{DFB}$–$I_{DFB}$) characteristics with the SA section floating. (b) *P–I* characteristics measured from the SOA side for various $I_{SOA}$ values with the SA section left floating.**

The optical output power increases markedly once the SOA current exceeds 150 mA, reaching a maximum of 25 mW at $I_{SOA}$ = 250 mA. The non-zero output power observed at $I_{DFB}$ for higher SOA currents is attributed to residual electrical crosstalk between the SOA and DFB sections due to incomplete isolation. Current leakage or spreading from the SOA partially pumps the adjacent DFB section, producing measurable output even without direct DFB injection. The corresponding optical spectrum of the device, measured at $I_{DFB}$ = 320 mA, $I_{SOA}$ = 100 mA and $V_{SA}$ = −3 V, is shown in Fig. 5.4(a). Under these conditions, the ML-DFB laser emits four lasing wavelengths at 1564.78, 1565.74, 1566.70, and 1567.65 nm, corresponding to channels CH1–CH4, respectively.

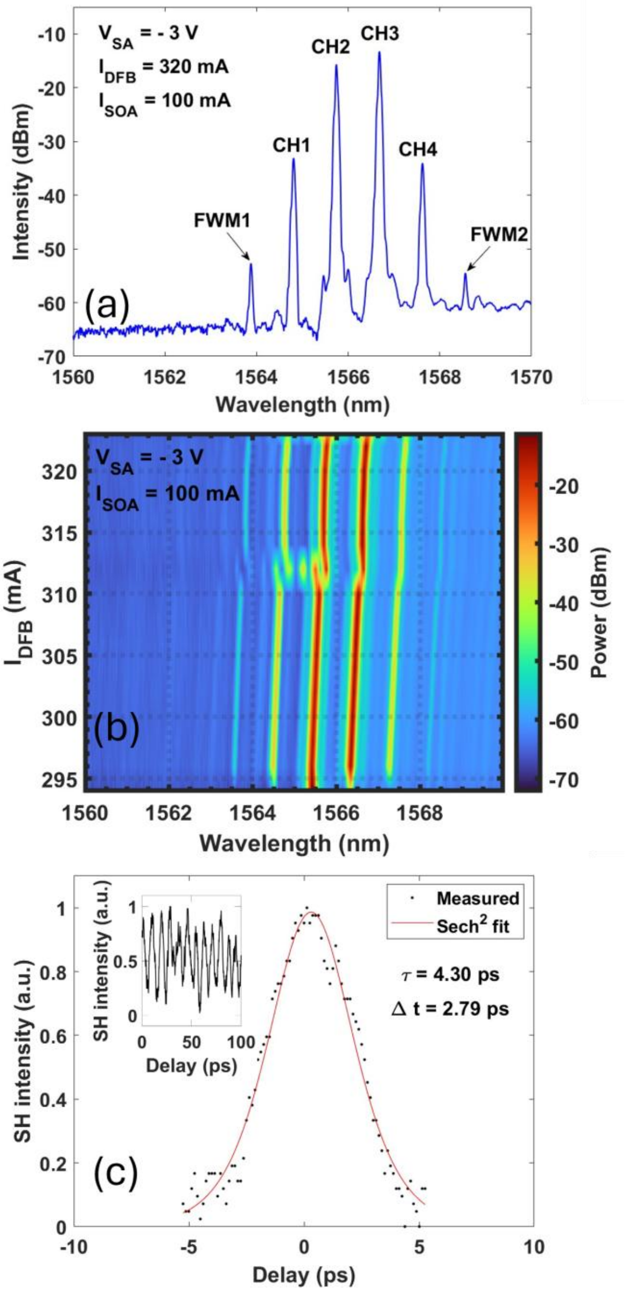


**Fig. 5.4. (a) Measured optical spectrum of the four-wavelength ML-DFB laser. (b) Measured two-dimensional optical spectrum at $V_{SA}$ = −3.0 V and $I_{SOA}$ = 100 mA. (c) Measured AC trace (inset) together with an isolated AC pulse.**

The channel spacing is 0.96 nm, with an SMSR greater than 22 dB. The coupling coefficient is calculated to be $\kappa$ = 15.95 $cm^{-1}$. Clear four-wave mixing (FWM) sidebands appear at 1563.83 nm (FWM1) and 1568.60 nm (FWM2), indicating a good phase relationship between the lasing modes. For $V_{SA}$ = −3.0 V and $I_{SOA}$ = 100 mA, the 2D optical spectrum in Fig. 5.4(b) shows stable four-wavelength operation across an $I_{DFB}$ range of 295–323 mA, with the lasing wavelengths redshifting at approximately 0.014 nm/mA per channel. The single AC pulse width is measured to be 4.30 ps; assuming a $sech^2$ pulse shape, this deconvolves to a pulse width of 2.79 ps, as illustrated in Fig. 5.4(c). The measured optical spectrum has a FWHM of 0.98 nm, giving a TBP of 0.334, which is close to the transform-limited value ($\approx$0.315). The AC traces shown in the inset of Fig. 5.4(c) exhibit a pulse period of 8.33 ps, corresponding to a 120 GHz repetition rate. The non-zero pedestal in the long-span autocorrelation trace shown in the inset of Fig. 5.4(c) was observed mainly for devices incorporating an SOA in our work, suggesting that it is predominantly associated with amplified spontaneous emission from the SOA. For the isolated-pulse trace shown in Fig. 5.4(c), a single peak was extracted and independently normalised to its maximum; no background subtraction was originally applied. The influence of the pedestal was subsequently assessed by estimating its level from the low-signal regions, subtracting this constant background from the raw trace, renormalising the corrected trace, and recalculating the pulse width. The pedestal introduces an underestimation of around 3% in the reported pulse-width estimate, representing only a minor effect on the extracted pulse duration. The same treatment applies to the relevant autocorrelation measurements in Chapters 5 and 6.

Fig. 5.5(a) shows the linear fitting of the lasing wavelengths for the four channels at different $I_{DFB}$ values, with the corresponding fitting parameters listed in Table 5.1. The extracted wavelength tuning slopes give an average value of 0.96 nm with a standard deviation of 0.0034 nm. Fig. 5.5(b) displays the SMSR as a function of $I_{DFB}$, confirming that all channels maintain an SMSR above 20 dB over the 298–322 mA current range.

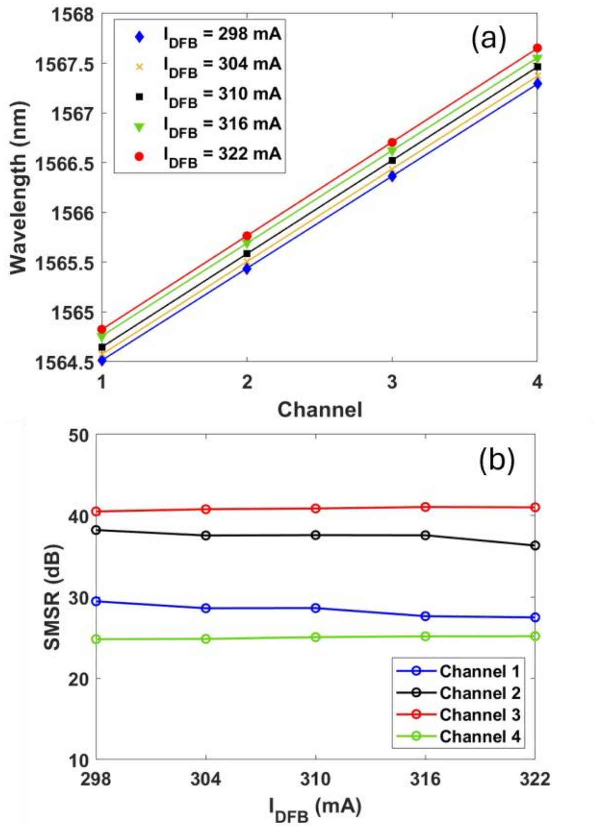


**Fig. 5.5. (a) Measured lasing wavelengths for the four channels together with their linear fits at $I_{DFB}$ = 298, 304, 310, 316, and 322 mA. (b) SMSRs of all four channels plotted as a function of $I_{DFB}$.**

**Table 5.1. Linear-fit results for the chirped C-SBG lasing wavelengths of the four channels at different $I_{DFB}$ values.**

| $I_{DFB}$ | Wavelength slope | Standard deviation |
|---|---|---|
| 298 mA | 0.9560 nm | 0.0031 nm |
| 304 mA | 0.9620 nm | 0.0031nm |
| 310 mA | 0.9690 nm | 0.0049 nm |
| 316 mA | 0.9620 nm | 0.0031 nm |
| 322 mA | 0.9720 nm | 0.0031 nm |
| Average | 0.9642 nm | 0.0034 nm |

The FWM efficiencies, referenced to their carrier tones, are −20.58 dBc for FWM1/CH1 and −21.52 dBc for FWM2/CH4, as obtained from the optical spectrum in Fig. 5.4(a). Fig. 5.6 shows the FWM output powers and the corresponding carrier-referenced suppression ratios as functions of $I_{DFB}$. Over the full current range of 298–322 mA, both FWM1 and FWM2 remain highly stable, with variations of less than 1 dB. The associated suppression ratios, FWM1/CH1 and FWM2/CH4, follow the same trend and stay within a <1 dB variation, confirming stable FWM across the operating range.

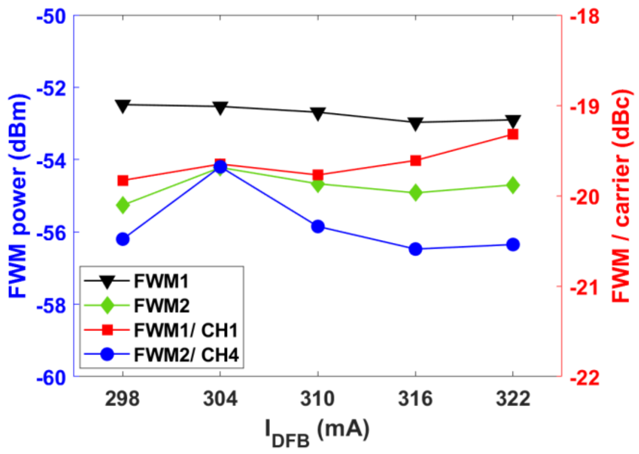


**Fig. 5.6. FWM output power and FWM-to-carrier power ratio as a function of $I_{DFB}$.**

Before detailed characterisation, $I_{DFB}$, $I_{SOA}$, and $V_{SA}$ were varied systematically to identify suitable operating conditions. The DFB current was varied over a range of values, as shown in the two-dimensional optical spectrum in Fig. 5.4(b), and the values were selected from current windows in which all designed wavelength channels operated simultaneously with stable spacing and high SMSR. The reported operating points provided stable simultaneous multi-wavelength mode locking, clear pulse formation, and sufficient output power. The SA voltage was selected from the measured autocorrelation traces as the condition providing the shortest stable pulses. The SOA current was chosen to provide sufficient amplification. The same selection procedure was applied to the subsequent 4PS-SBG devices discussed in Section 5.2.

## 5.2 Chirped 4PS-SBG Mode-locked DFB laser

Fig. 5.7 shows the schematic of the 4PS-SBG-based device, which operates at 1.55 µm and is realised on the same AlGaInAs/InP material platform as the C-SBG laser in Section 5.1, following an identical fabrication process. The structure comprises a 30 µm SA section, a 1500 µm DFB section, and a 650 µm SOA with a 10° bend. The ridge waveguide geometry—including its dimensions, grating recess depth, and duty cycle—is kept consistent with the C-SBG design. The main structural differences are the use of a fully periodic grating (no non-grating regions) and the implementation of four π/2 phase-shift sections per sampling period. The chirp rate is 80 nm/mm, with an initial sampling period of $P_1$ = 4.46 µm. The left inset of Fig. 5.7 shows a microscope image of the fabricated device, while the right inset presents an SEM image of the etched sidewall grating.

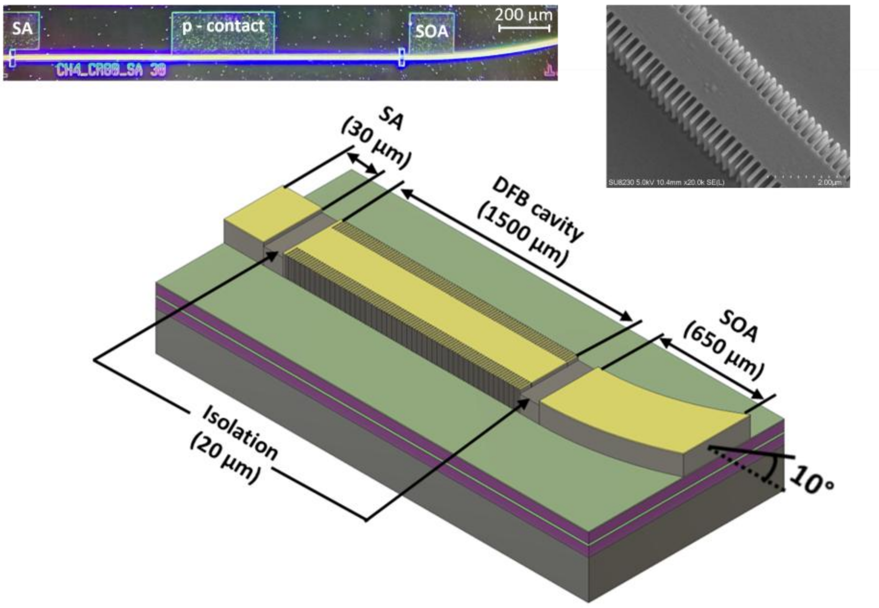


**Fig. 5.7. Schematic of the chirped 4PS-SBG-based multi-wavelength mode-locked DFB laser, along with an optical micrograph of the fabricated device (left inset) and an SEM image of the sidewall gratings (right inset).**

The experimental and measurement setup was similar to what is shown in Fig. 5.2. The output power was initially measured from the SA-side facet as a function of $I_{DFB}$ (0–300 mA) for different SA reverse biases ($V_{SA}$, 0 to −3 V) with the SOA left floating, as shown in Fig. 5.8(a). As $V_{SA}$ becomes more negative, the output power decreases due to increased absorption losses in the SA. The inset of Fig. 5.8(a) displays the typical $P$–$I_{DFB}$–$V_{DFB}$ characteristics, where the threshold current $I_{th}$ is 52 mA with both the SA and SOA sections floating. At $I_{DFB}$ = 300 mA, the device delivers 13.8 mW with $V_{SA}$ = -2.5 V. Fig. 5.8(b) presents the power–current ($P$–$I$) characteristics measured from the SOA side with the SA floating, which is the configuration used for all subsequent measurements. Here, the DFB injection current is swept from 0 to 300 mA, while $I_{SOA}$ is set to 0, 50, 100, 150, and 200 mA with the SA section floating. Compared with the C-SBG device, the 4PS-SBG laser exhibits higher output power and increased slope efficiency, attributed to the stronger grating coupling. The optical output reaches 24.2 mW at $I_{SOA}$ = 200 mA.

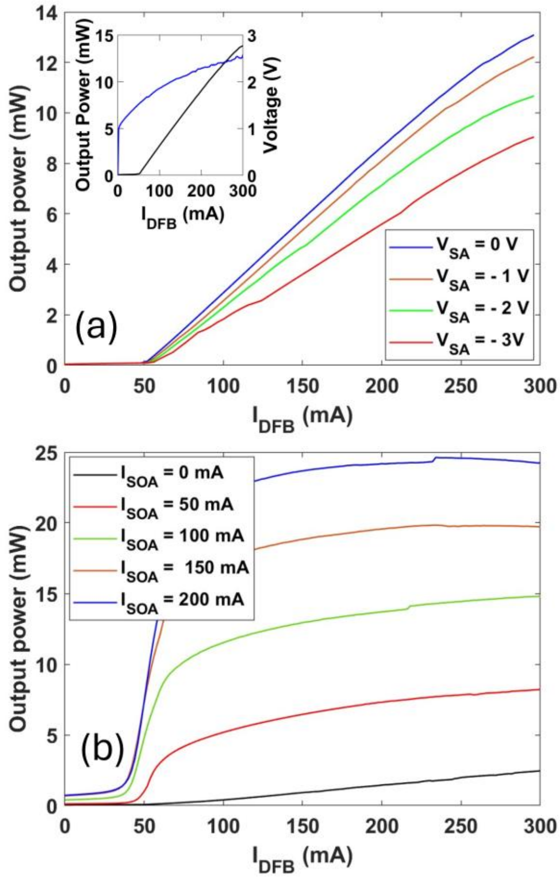


**Fig. 5.8. (a) Output power measured from the SA side as a function of $I_{\mathrm{DFB}}$ for different $V_{SA}$ values. The inset shows the voltage–current ($V_{DFB}$–$I_{DFB}$) characteristics with the SA section floating. (b) P–I characteristics measured from the SOA side for various $I_{SOA}$ values with the SA section left floating.**

Fig. 5.9(a) presents the optical spectrum recorded at $I_{DFB}$ = 272 mA, $I_{SOA}$ = 60 mA, and $V_{SA}$ = −1.1 V. Under these conditions, the ML-DFB laser emits four lasing wavelengths at 1562.35, 1563.31, 1564.27, and 1565.23 nm, corresponding to channels CH1–CH4, respectively. FWM sidebands are also observed at 1561.38 nm (FWM1) and 1566.20 nm (FWM2), with suppression levels of −21.28 dBc and −22.97 dBc relative to the nearest lasing channels, respectively. The channel spacing is 0.96 nm, with an SMSR exceeding 20 dB. The coupling coefficient is calculated to be κ = 23.14 $cm^{-1}$. For $V_{SA}$ = −1.1 V and $I_{SOA}$ = 60 mA, the two-dimensional optical spectrum in Fig. 5.9(b) shows four distinct emission wavelengths across the DFB current range of 100–288 mA. This broader current range of multi-wavelength operation in the 4PS-SBG device, compared with the C-SBG device, is attributed to its higher κ, which provides stronger feedback and improved mode discrimination, allowing stable lasing at the target wavelengths over a wider $I_{DFB}$ window. The lasing wavelengths redshift with current at approximately 0.012 nm/mA per channel. The single AC pulse width is measured to be 4.38 ps; assuming a $sech^2$ pulse shape, this corresponds to a deconvolved pulse width of 2.84 ps, as shown in Fig. 5.9(c). The measured AC trace, shown in the inset of Fig. 5.9(c), reveals a pulse period of 8.33 ps, corresponding to a 120 GHz repetition rate. The measured optical spectrum exhibits a FWHM bandwidth of 0.97 nm. The corresponding TBP is 0.337, indicating that the pulses are nearly transform-limited.

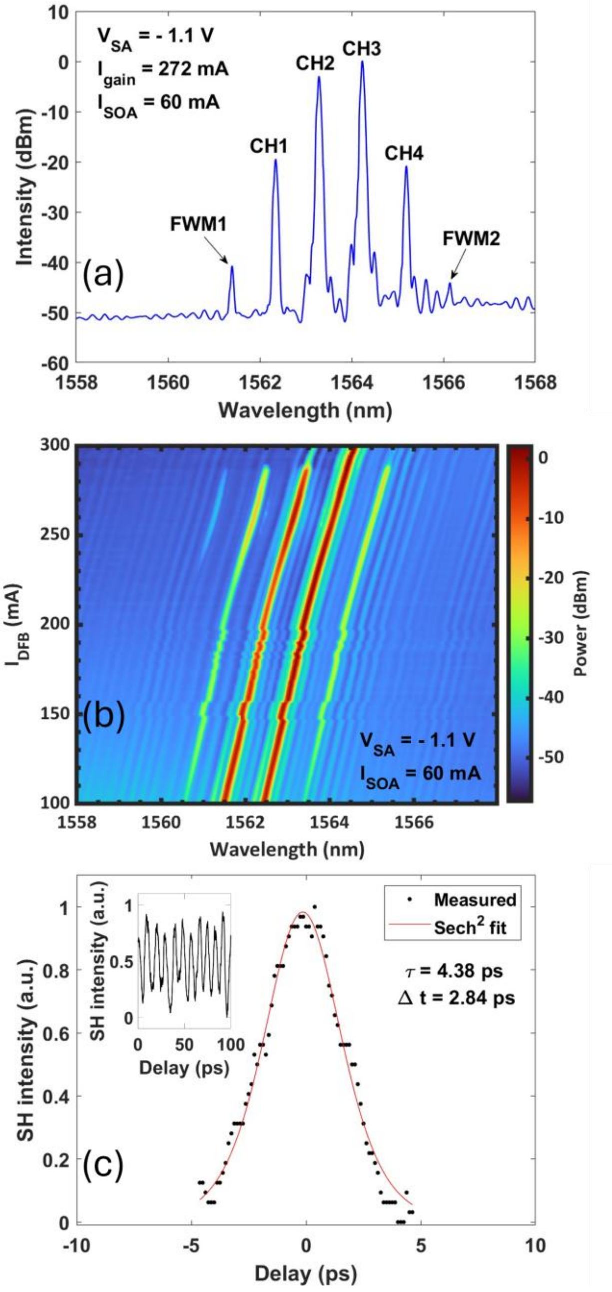


**Fig. 5.9. (a) Measured optical spectrum of the four-wavelength ML-DFB laser. (b) Measured two-dimensional optical spectrum at $V_{SA} = -1.1$ V and $I_{SOA} = 60$ mA. (c) Measured AC trace of the four-wavelength ML-DFB laser (inset) together with an isolated AC pulse.**

Fig. 5.10(a) shows the linear fits of the lasing wavelengths for the four channels at different $I_{DFB}$ values, with the corresponding fitting results listed in Table 5.2. The extracted wavelength tuning slopes give an average value of 0.96 nm with a standard deviation of

0.0043 nm. Fig. 5.10(b) plots the SMSR as a function of $I_{DFB}$, confirming SMSR values above 20 dB for all channels over the 200–280 mA range.

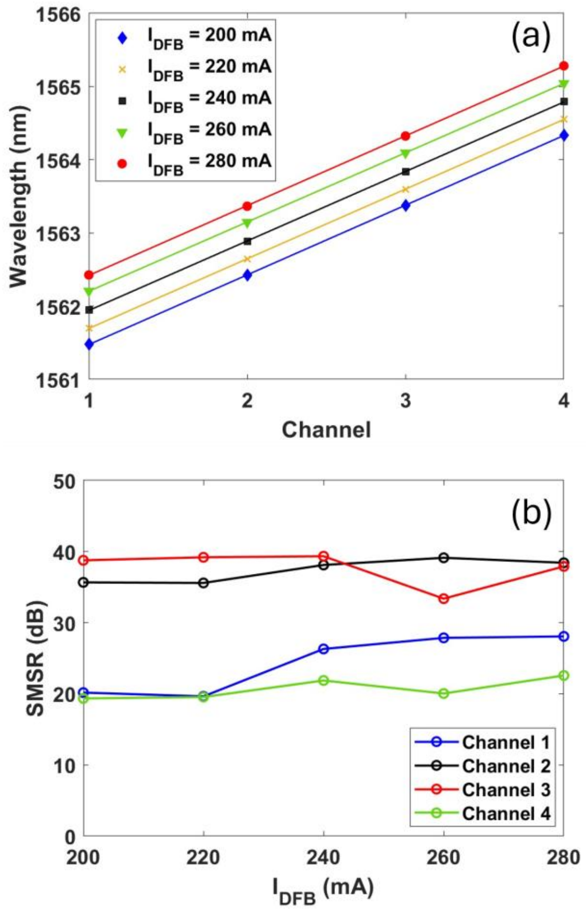


**Fig. 5.10. (a) Measured lasing wavelengths for the four channels together with their linear fits at $I_{DFB}$ = 200, 220, 240, 260, and 280 mA. (b) SMSRs of the four channels plotted versus $I_{DFB}$.**

**Table 5.2. Linear-fit results for the chirped 4PS-SBG lasing wavelengths of the four channels at different IDFB values.**

| $I_{DFB}$ | Wavelength slope | Standard deviation |
|---|---|---|
| 200 mA | 0.9620 nm | 0.0031 nm |
| 220 mA | 0.9620 nm | 0.0031nm |
| 240 mA | 0.9590 nm | 0.0057 nm |
| 260 mA | 0.9560 nm | 0.0031 nm |
| 280 mA | 0.9630 nm | 0.0063 nm |
| Average | 0.9604 nm | 0.0043 nm |

The thermal sensitivity was evaluated by measuring the central wavelengths and channel spacings at TEC temperatures of 10, 20, 30, and 40 °C. These measurements were carried out under fixed bias conditions of $I_{DFB}$ = 280 mA, $V_{SA}$ = −1.1 V, and $I_{SOA}$ = 100 mA. Fig. 5.11(a) shows the central wavelength shift over the 10–40 °C range, revealing a monotonic redshift with an average rate of 0.074 nm/°C, in line with the expected behaviour for 1.55 μm DFB lasers [140,141]. Fig. 5.11(b) presents the average channel spacing, obtained from linear fits of the four lasing wavelengths versus channel index at each temperature. The spacing exhibits a nonlinear temperature dependence, increasing from 10 to 20 °C and then gradually decreasing from 20 to 40 °C. The maximum change in channel spacing is 0.018 nm, between the peak value at 20 °C and the minimum at 40 °C. This overall drift corresponds to an average slope of −0.00010 nm/K, yielding a net thermal coefficient of −104 ppm/K.

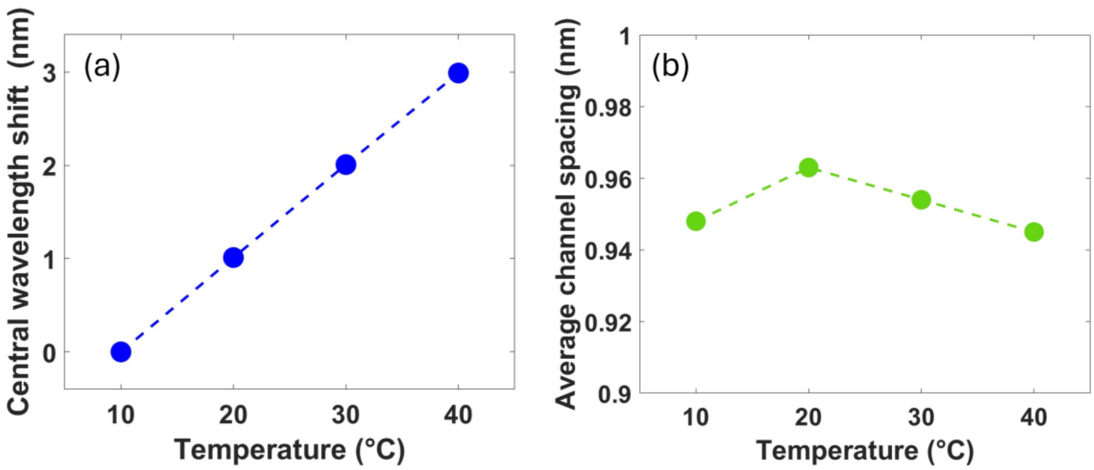


**Fig.5.11. (a) Central wavelength shift with temperature, (b) channel spacing variation with temperature.**

To evaluate device yield and reproducibility, we characterised three dies. As shown in Fig. 5.12, Die 1 exhibits a channel spacing of 0.96 nm with an SMSR of 22.4 dB, Die 2 shows a spacing of 0.94 nm with the highest SMSR of 23.4 dB, and Die 3 has a spacing of 0.95 nm with an SMSR of 20.3 dB. All three devices maintained stable four-wavelength lasing, with channel spacing variations confined within 0.02 nm and SMSR consistently above 20 dB (quoted for the lowest-intensity channel). The optimal bias conditions differed across the dies—Die 1: $I_{DFB}$ = 272 mA, $V_{SA}$ = −1.1 V; Die 2: $I_{DFB}$ = 360 mA, $V_{SA}$ = 2.1 V; Die 3: $I_{DFB}$ = 290 mA, $V_{SA}$ = −3.0 V—while $I_{SOA}$ was fixed at 60 mA in all cases. These variations mainly arise from small fabrication-induced differences between devices, including slight deviations in the DFB grating coupling coefficient, ridge waveguide dimensions, and facet reflectivity. Such variations modify the internal optical feedback, carrier distribution, and effective gain–absorption balance between the DFB, SA, and SOA sections, leading to different bias conditions for optimal operation. Nevertheless, the devices exhibit highly reproducible performance in terms of channel spacing and SMSR.

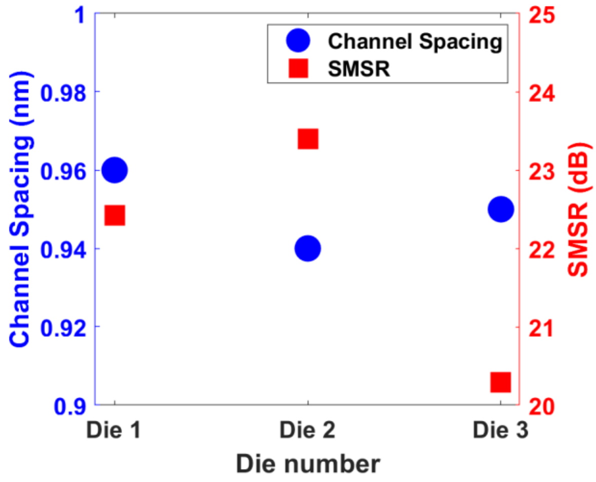


**Fig. 5.12. Channel spacing and SMSR for three dies of the 4-channel 4PS-SBG ML-DFB laser.**

To further highlight the flexibility and scalability of the 4PS-SBG design, an additional device incorporating six π-phase shifts evenly distributed along the cavity was fabricated. This device shares the same cavity length, chirp rate, sampling period, SA section, and SOA section as the previous 4PS-SBG laser, differing only in the number of π-phase shifts. The optical spectrum measured at $I_{DFB}$ = 414 mA, $I_{SOA}$ = 100 mA, and $V_{SA}$ = −2 V is shown in Fig. 5.13(a), revealing mode-locked lasing at six wavelengths: 1562.92, 1563.43, 1563.93, 1564.44, 1564.93, and 1565.44 nm. FWM sidebands are also visible at 1562.40 nm (FWM1) and 1565.96 nm (FWM2), with suppression levels of −15.49 dBc and −10.1 dBc, respectively. These relatively higher dBc values mainly arise from the lower output powers of the outer lasing modes (CH1 and CH6), which act as the carrier references for FWM1 and FWM2. The channel spacing is approximately 0.51 nm, corresponding to 63.75 GHz. The two-dimensional optical spectrum in Fig. 5.13(b) confirms stable six-channel operation over the $I_{DFB}$ range of 408–418 mA. In this case, longitudinal mode competition is more significant than in the four-channel devices because the effective grating cavity length per longitudinal mode ($L_{DFB}$/6) is shorter than that for the four-channel lasers ($L_{DFB}$/4), reducing κL for each mode. Attempts to realise six-wavelength lasing using the C-SBG structure were unsuccessful due to its lower κ, which leads to weaker mode selectivity and stronger mode competition. By contrast, the higher κ of the 4PS-SBG structure enhances feedback and mode discrimination, enabling robust multi-channel lasing. It is also worth noting that applying AR coatings to the DFB facet and optimising device packaging could further improve power stability and channel intensity uniformity.

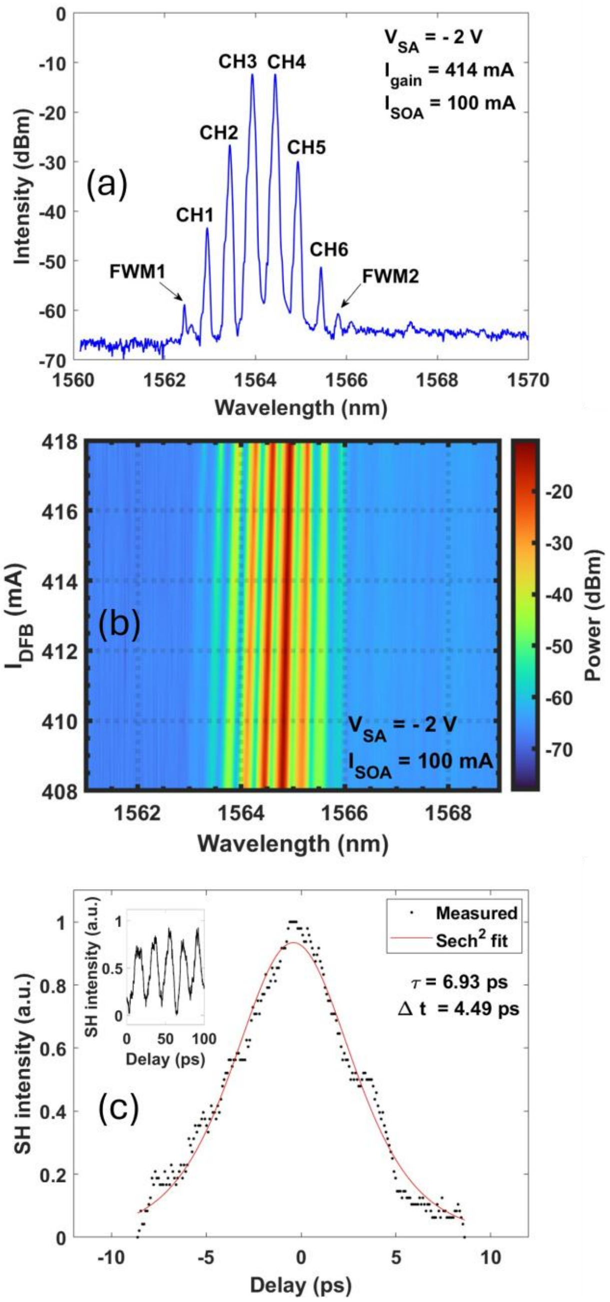


**Fig. 5.13. (a) Measured optical spectrum of the six-wavelength ML-DFB laser. (b) Measured two-dimensional optical spectrum at $V_{SA} = -2.0$ V and $I_{SOA} = 100$ mA. (c) Measured AC trace of the six-wavelength ML-DFB laser (inset) together with an isolated AC pulse.**

The isolated pulses have a measured width of 4.49 ps, as shown in Fig. 5.13(c). The corresponding AC traces, presented in the inset of Fig. 5.13(c), show a pulse separation of 15.7 ps, equivalent to a 63.75 GHz repetition rate. The optical spectrum exhibits a FWHM bandwidth of 0.65 nm, and the calculated TBP is 0.342. These results confirm the versatility of the design and demonstrate the clear advantage of the 4PS-SBG approach for scalable multi-wavelength mode-locking. The radio-frequency (RF) output was measured using a high-speed PD in combination with an external mixer-based frequency-extension scheme, implemented following [142]. This setup extends the usable frequency range beyond the 50

GHz bandwidth limit of the ESA, enabling measurements up to 75 GHz. Fig. 5.14 presents the RF spectrum recorded at $I_{DFB}$ = 414 mA, $V_{SA}$ = −2 V, and $I_{SOA}$ = 100 mA, together with a Lorentzian fit. From this fit, a repetition frequency of 63.75 GHz and a −3 dB linewidth of 2.95 MHz are obtained. The inset of Fig. 5.14 shows the corresponding unfitted, zoomed-out RF trace. The integrated RMS timing jitter was then inferred from the measured RF linewidth using the standard Lorentzian expression [143]. For the six-channel device, this yields a timing jitter of 16.02 ps when integrated over the 10 kHz–100 MHz range.

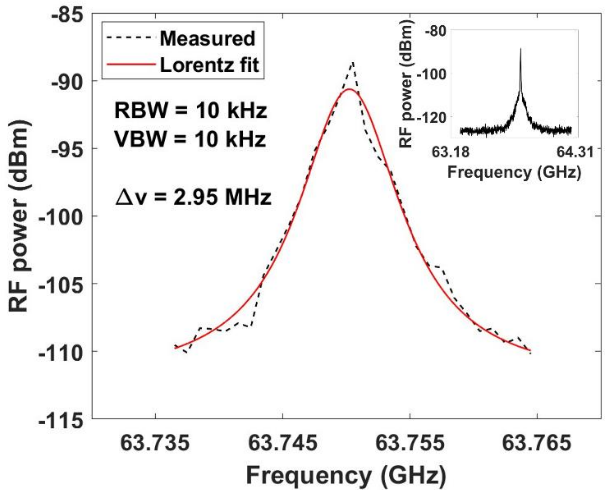


**Fig. 5.14. Lorentzian-fitted RF spectrum measured from the six-channel device at $I_{DFB}$ = 414 mA, $V_{SA}$ = −2 V, and $I_{SOA}$ = 100 mA, with the corresponding unfitted, zoomed-out RF signal shown in the inset.**

Across all three demonstrated devices, the measured optical combs exhibit some variation in line intensities, which is attributed to gain non-uniformity, dispersion, and facet reflectivity effects. Further improvement of comb flatness in future designs could be achieved by: (1) band-structure engineering, for example by adjusting quantum-well thicknesses or adding additional wells to smooth the modal gain profile; (2) facet-coating optimisation using wavelength-selective reflectors to reduce reflectivity-induced power variations; and (3) intracavity spectral shaping through passive elements such as distributed Bragg gratings or spectral equalisation sections to suppress overly dominant lines. The 4PS-SBG devices and their basic channel characteristics are summarised in Table 5.3.

**Table 5.3. Summary of the 4PS- SBG multi-wavelength ML DFB devices.**

| Device | $L_{DFB}$ (μm) | No. of lasing modes | FSR (nm) |
|---|---|---|---|
| 4 channel 4PS-SBG | 1500 | 4 | 0.96 |
| 6 channel 4PS-SBG | 1500 | 6 | 0.51 |

## 5.3 Summary

In this work, we have presented, to the best of our knowledge, the first compact monolithic multi-wavelength passively mode-locked DFB laser based on chirped SBG, achieving simultaneous mode-locking at four wavelengths around 1.55 μm. In contrast to conventional schemes employing parallel DFB arrays or cascaded cavities, the proposed design ensures that all longitudinal modes are generated within a single cavity, so the frequency spacing is inherently stabilised against temperature variations, as thermal drift shifts all wavelengths by the same amount. Multi-wavelength generation is precisely controlled by introducing distributed π-phase shifts along the cavity, which determine the number of supported longitudinal modes. Two grating configurations were investigated: chirped C-SBG and chirped 4PS-SBG. Both devices provide uniform wavelength spacing of 0.96 nm and are synchronised by a monolithically integrated SA. Compared with the C-SBG structure, the 4PS-SBG design offers a higher κ, wider operating current ranges, and improved scalability, as evidenced by the realisation of six-channel operation. Both lasers exhibit high spectral purity (SMSR > 20 dB) and strong phase coherence, generating near–transform-limited pulses of 2.79 ps (TBP = 0.334) for the C-SBG device and 2.84 ps (TBP = 0.337) for the 4PS-SBG device, confirming stable, synchronised mode-locking. The fabrication sequence is also greatly simplified, requiring only a single MOVPE growth and one etching step. This compact, straightforward, and cost-effective platform is well-suited for next-generation DWDM systems, coherent optical communications, and photonic sensing applications where multi-wavelength mode-locking is a key requirement.

# Chapter 6: Multi-Wavelength Mode-Locked DFB Laser Based on Waveguide Bragg Grating Microcavities

This chapter presents a WBG microcavity platform for compact monolithic multi-wavelength DFB lasers with intrinsically stable wavelength spacing, since all longitudinal modes originate from the same cavity and therefore drift together with temperature. The chapter first demonstrates a multi-wavelength mode-locked DFB laser that achieves stable tri-wavelength passive mode-locking within a single monolithic cavity by integrating a DFB section with an SA, and then explores scalability by modifying the central cavity length and phase configuration to realise four- and six-wavelength operation, as well as dual-wavelength emission for monolithic mmWave generation. Building on the same device platform and design principle, the second part of the chapter extends the approach to a dedicated dual-wavelength DFB laser set, where different central cavity lengths are used to engineer different FSRs and hence different mmWave beat frequencies, while maintaining clean dual-mode operation and high SMSR[3]. This chapter builds directly on the theoretical background presented in Section 2.5 on DFB lasers based on WBG microcavities, particularly the multi-wavelength and dual-wavelength WBG microcavity structures discussed in subsections 2.5.1 and 2.5.2, respectively.

## 6.1 Multi-wavelength DFB laser

Fig. 6.1 shows a schematic of the device, consisting of a 20 µm-long SA section, a 15 µm-long electrically isolated section, and a 1000 µm-long DFB section. The DFB section contains a 412.36 µm-long central cavity located between two uniform gratings, each 293.82 µm in length, defined by a seed Bragg grating period ($\Lambda_0$) of 244 nm with a 50% duty cycle. The central microcavity length is chosen to be an integer multiple of $\Lambda_0$, and a π phase shift is placed at the interface between the left grating and the microcavity. The ridge waveguide is 2.5 µm wide and 1.92 µm high, with 0.6 nm etched grating recesses (*d*). The epilayer employs asymmetric quantum wells, comprising three 6-nm wells and three 7-nm wells, as shown in the former section 2.61 with the bandgap structure shown in Fig. 2.25. The device is fabricated using a process that follows the procedure described in Chapter 3 aThe left inset of Fig. 6.1 shows a microscope image of the fabricated device, while the right inset presents a scanning electron microscopy (SEM) image of the etched sidewall grating and ridge waveguide.

[3] Part of this chapter have been published previously in: M. Al-Rubaiee *et al.*, *Optics Express,* **33**, 22222-22234 (2025).; and M. Al-Rubaiee *et al.*, *Optics Letters, **50**, 7219-7222 (2025).*

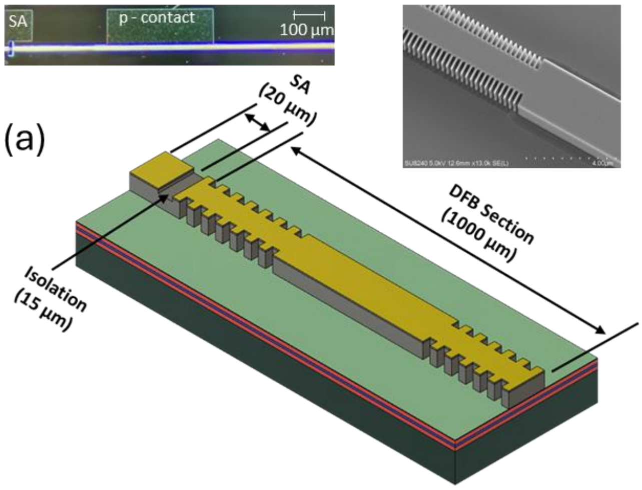


**Fig. 6.1. Schematic of the tri-wavelength ML-DFB laser, with an optical micrograph of the fabricated device (left inset) and an SEM image of the sidewall grating and ridge waveguide (right inset).**

The characterisation setup is shown in Fig. 6.2. After fabrication, the devices were cleaved with uncoated facets, and the laser chips were mounted on a TEC set to 20 °C. A CW laser current source was used to forward bias the DFB laser section, while a DC voltage supply was applied to reverse bias the SA section. The output optical signal emitted from the SA-section facet was coupled into a lensed SMF, followed by an optical isolator and a 90:10 fibre splitter. A 10% portion of the light was sent to an OSA with an RBW of 0.06 nm for detailed spectral analysis. Meanwhile, the remaining 90% was routed through a PC and an EDFA, and then directed either to an autocorrelator for AC trace measurements or to a 50 GHz InGaAs PD and a 40 GHz ESA for comprehensive RF analysis.

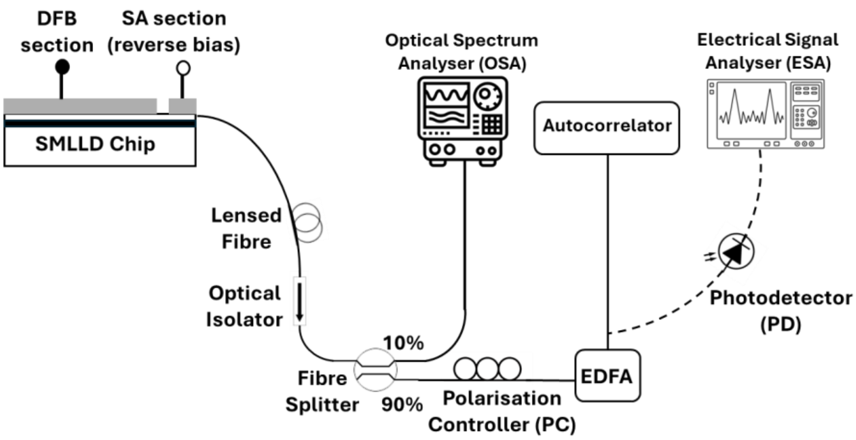


**Fig. 6.2. Experimental measurement setup.**

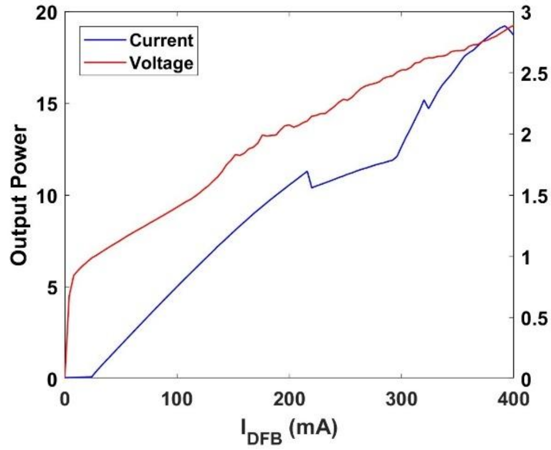


**Fig. 6.3. Measured typical I-P and I-V curves of the fabricated device when the SA section is left floating.**

Fig. 6.3 presents the measured power and voltage characteristics as a function of the DFB current ($I_{DFB}$) using a 2 mA scanning step. The measured threshold current ($I_{th}$) is 24 mA when the SA section is left floating. The kinks observed in the I–P curve are attributed to the main lasing mode hopping between different lasing modes [52].

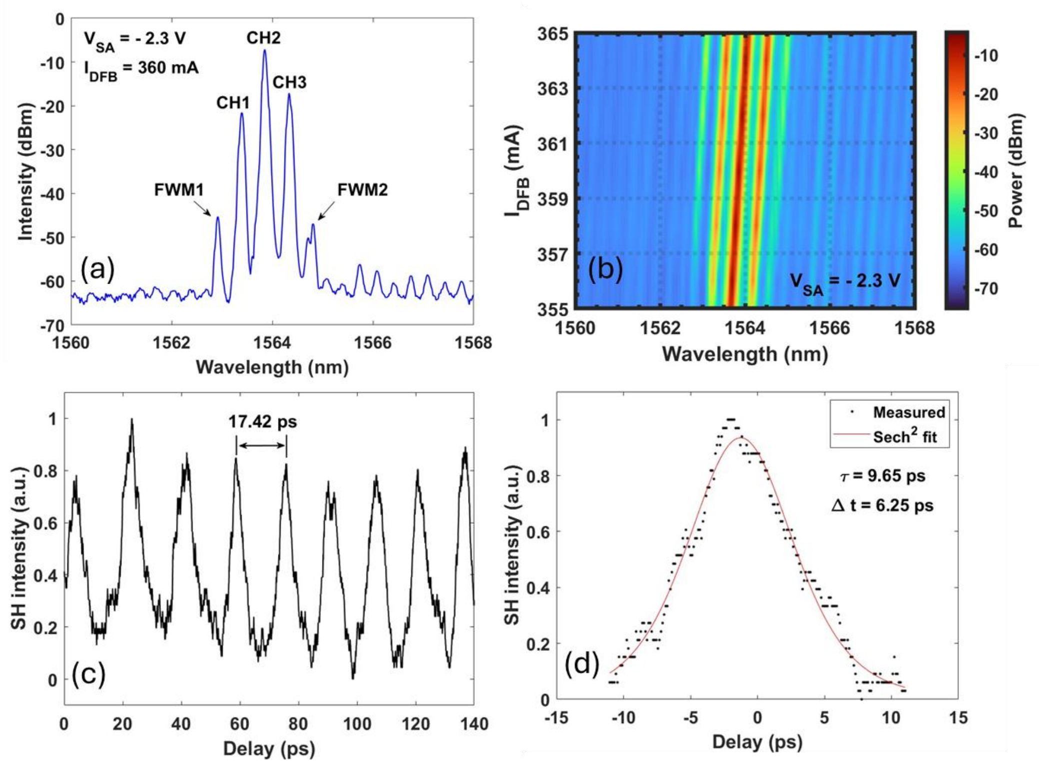


**Fig. 6.4. (a) Measured optical spectrum of the tri-wavelength ML-DFB laser, (b) corresponding 2D optical spectrum, (c) measured AC trace of the tri-wavelength ML-DFB laser, and (d) an isolated AC pulse.**

This behaviour can be mitigated by applying an anti-reflection (AR) coating to the DFB laser facet. The optical spectrum measured at a DFB injection current ($I_{DFB}$) of 360 mA and a reverse SA voltage ($V_{SA}$) of −2.3 V is shown in Fig. 6.4(a). The ML-DFB laser generated three lasing wavelengths at 1563.39 nm, 1563.85 nm, and 1564.31 nm, corresponding to channels CH1, CH2, and CH3, respectively. The channel spacing was measured as 0.46 nm, equivalent to 57.4 GHz, with an SMSR exceeding 30 dB. The appearance of FWM signals indicates a good phase relationship between the lasing modes. Under the same $V_{SA}$ conditions, the 2D optical spectrum in Fig. 6.4(b) shows that the laser maintains stable three-wavelength emission for $I_{DFB}$ between 355 mA and 365 mA. The wavelength redshift with increasing current is approximately 0.035 nm/mA for each wavelength. The measured AC traces in Fig. 6.4(c) show a pulse separation of 17.42 ps, corresponding to a repetition rate of 57.4 GHz. The measured single AC pulse width is 9.65 ps. Assuming a $sech^2$ pulse shape, this deconvolves to a pulse width of 6.25 ps, as shown in Fig. 6.4(d). The calculated TBP is 0.359, indicating that the pulses are nearly transform-limited ($\approx$0.315). The corresponding pulse energy is approximately 157 fJ. The slight irregularities in the AC trace are attributed to weak Fabry–Perot interference arising from partial reflections at interfaces within the SA, isolation, and DFB regions. These effects can be reduced by applying an AR coating to the DFB facet. The effective cavity length of the tri-wavelength ML-DFB laser, estimated from the measured frequency spacing of 57.4 GHz, is approximately 764 μm, comprising the 412.36 μm physical cavity length and the field penetration into the Bragg gratings. The corresponding grating coupling coefficient ($\kappa$) is approximately 28.4 $cm^{-1}$. This strong optical feedback from the Bragg gratings sustains the targeted longitudinal modes while suppressing others outside the effective reflection range. Fig. 6.5(a) shows the linear fit of the lasing wavelengths across the three channels at different $I_{DFB}$ values, with the corresponding fit results summarised in Table 6.1. The wavelength tuning slopes give an average spacing of 0.460 nm with a standard deviation of 0.0075 nm. Fig. 6.5(b) plots the SMSR as a function of $I_{DFB}$, showing that the SMSR remains above 30 dB for each channel over the 356 mA to 366 mA range.

**Table 6.1. Linear fit results for the lasing wavelengths of the three channels with 0.46 nm spacing at different $I_{DFB}$ values.**

| $I_{DFB}$ | Wavelength slope | Standard deviation |
|---|---|---|
| 356 mA | 0.4620 nm | 0.0129 nm |
| 358 mA | 0.4620 nm | 0.0043 nm |
| 360 mA | 0.4620 nm | 0.0043 nm |
| 362 mA | 0.4545 nm | 0.0086 nm |
| 364 mA | 0.4620 nm | 0.0129 nm |
| Average | 0.4608 nm | 0.0075 nm |

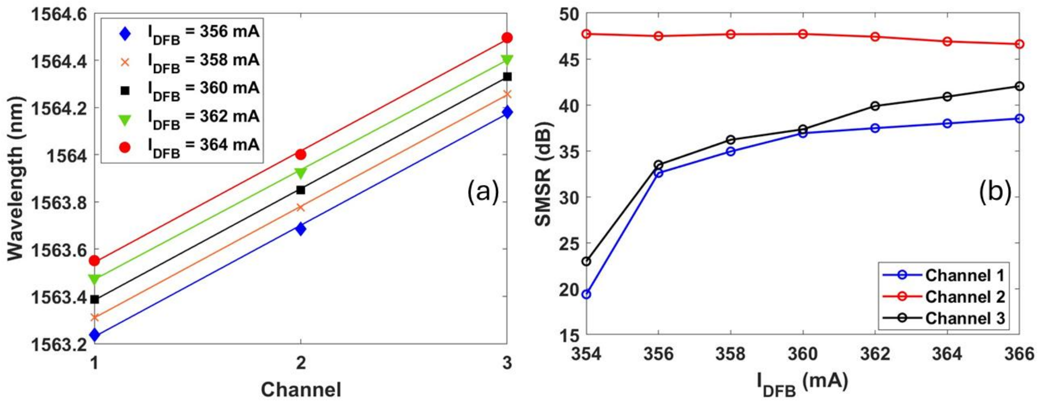


**Fig. 6.5. (a) Lasing wavelengths and corresponding linear fits for the three channels at $I_{DFB}$ = 356 mA, 358 mA, 360 mA, 362 mA, and 364 mA, and (b) SMSRs of the three channels as a function of $I_{DFB}$.**

A second device was fabricated with the same 412.36 μm central cavity length as the first device. Unlike the first device, which incorporated a π phase shift at the left grating interface, this version was designed without a π phase shift, maintaining symmetric gratings on both sides. The 20 μm SA section and all grating parameters, including period, duty cycle, and etch depth, remained unchanged. The measured threshold current ($I_{th}$) was 24 mA with the SA section left floating. At $I_{DFB}$ = 442 mA and $V_{SA}$ = −2.0 V, the laser generated four distinct lasing wavelengths at 1565.54 nm, 1565.99 nm, 1566.45 nm, and 1566.96 nm, corresponding to CH1–CH4 (Fig. 6.6(a)). The measured average channel spacing was 0.46 nm (57.4 GHz), identical to that of the tri-wavelength device. As shown in Fig. 6.6(b), the 2D optical spectrum confirms stable four-wavelength operation over the 340–448 mA bias range.

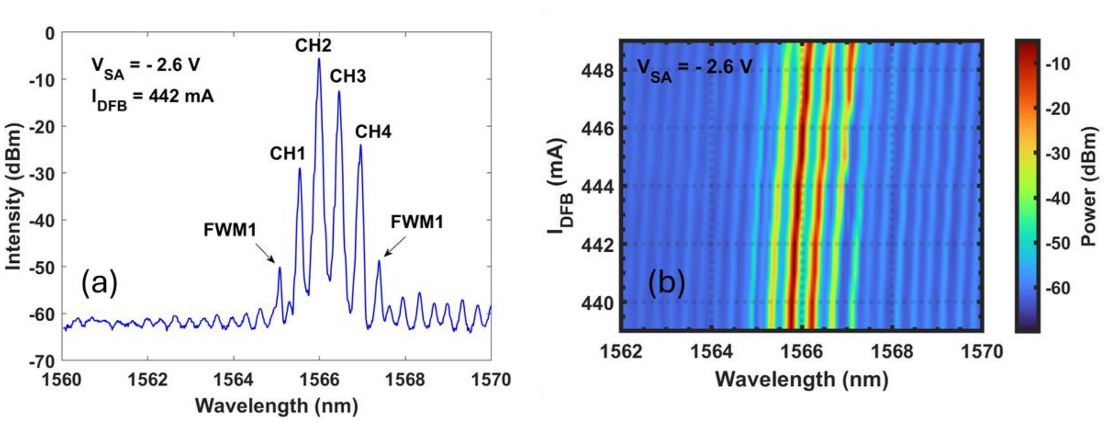


**Fig. 6.6. (a) Measured optical spectrum of the four-wavelength ML-DFB laser, (b) corresponding 2D optical spectrum.**

A third device was fabricated with a central cavity twice the length of that in the first device. The central cavity length of the third device is 824.82 μm, and the SA section length is 30 μm, while all other grating parameters remain unchanged. In contrast to the first device, which included a π phase shift at the interface between the left grating and the microcavity, this third device was designed without a phase shift, preserving fully symmetric gratings on both sides of the cavity. The measured threshold current ($I_{th}$) is 42 mA when the SA section is left floating, and the output power reaches 10.1 mW at $I_{DFB}$ = 300 mA. As shown in Fig. 6.7(a), this ML-DFB laser generated lasing wavelengths at 1559.40 nm, 1559.67 nm, 1559.94 nm, 1560.21 nm, 1560.48 nm, and 1560.75 nm, corresponding to channels CH1 to CH6, respectively. The channel spacing was measured to be 0.27 nm, equivalent to 33.7 GHz. Under the same $V_{SA}$ conditions, the corresponding 2D optical spectrum is shown in Fig. 6.7(b). The calculated effective cavity length for this device is approximately 1309.13 μm, which includes the physical central cavity length and the additional field penetration into the uniform Bragg gratings on both sides. The calculated grating coupling coefficient ($\kappa$) is 20.6 cm$^{-1}$, which is lower than that of the first device, as the longer cavity spreads the current over a larger volume and reduces the current density. This reduces the carrier-induced index modulation, weakens the grating strength, and increases the optical penetration depth, shifting the effective mirror position and lowering κ. The increased penetration depth into each grating extends the optical path, resulting in a denser mode structure and a reduced FSR, which enables six distinct modes to oscillate within the gain bandwidth.

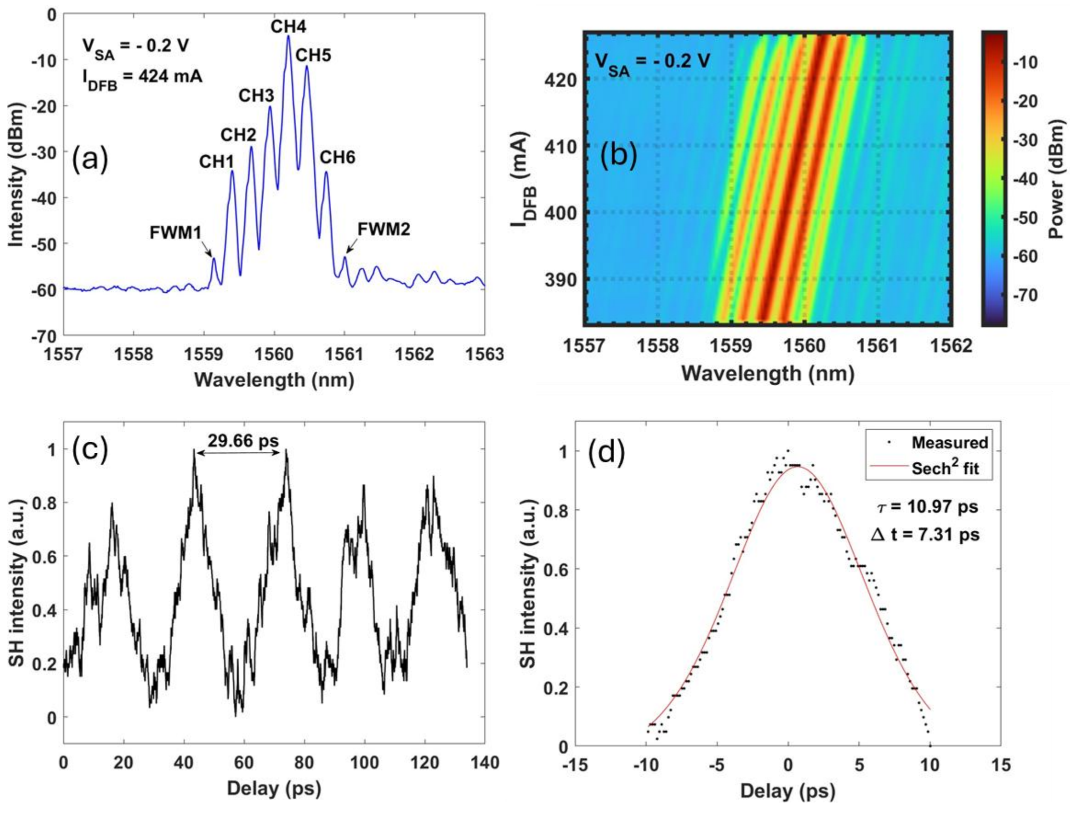


**Fig. 6.7. (a) Measured optical spectrum of six-wavelength ML-DFB laser, (b) 2D optical spectrum, (c) Measured AC trace of the six-wavelength ML-DFB laser, (d) an isolated AC pulse.**

As discussed above, increasing the cavity length reduces the spacing between resonances, allowing more longitudinal modes to reach threshold. However, this introduces trade-offs, as the available gain and total power are shared among more modes, weakening the intensity of individual channels and reducing spectral uniformity. As a result, the FWM sidebands become less pronounced because the optical power associated with each pair of modes is lower. Fig. 6.7(c) shows the measured AC traces, revealing a pulse separation of 29.66 ps, which agrees well with the expected value based on the device FSR of 0.27 nm. The measured single AC pulse width is 10.97 ps. Assuming a sech² pulse shape, this deconvolves to a pulse width of 7.31 ps, as shown in Fig. 6.7(d).

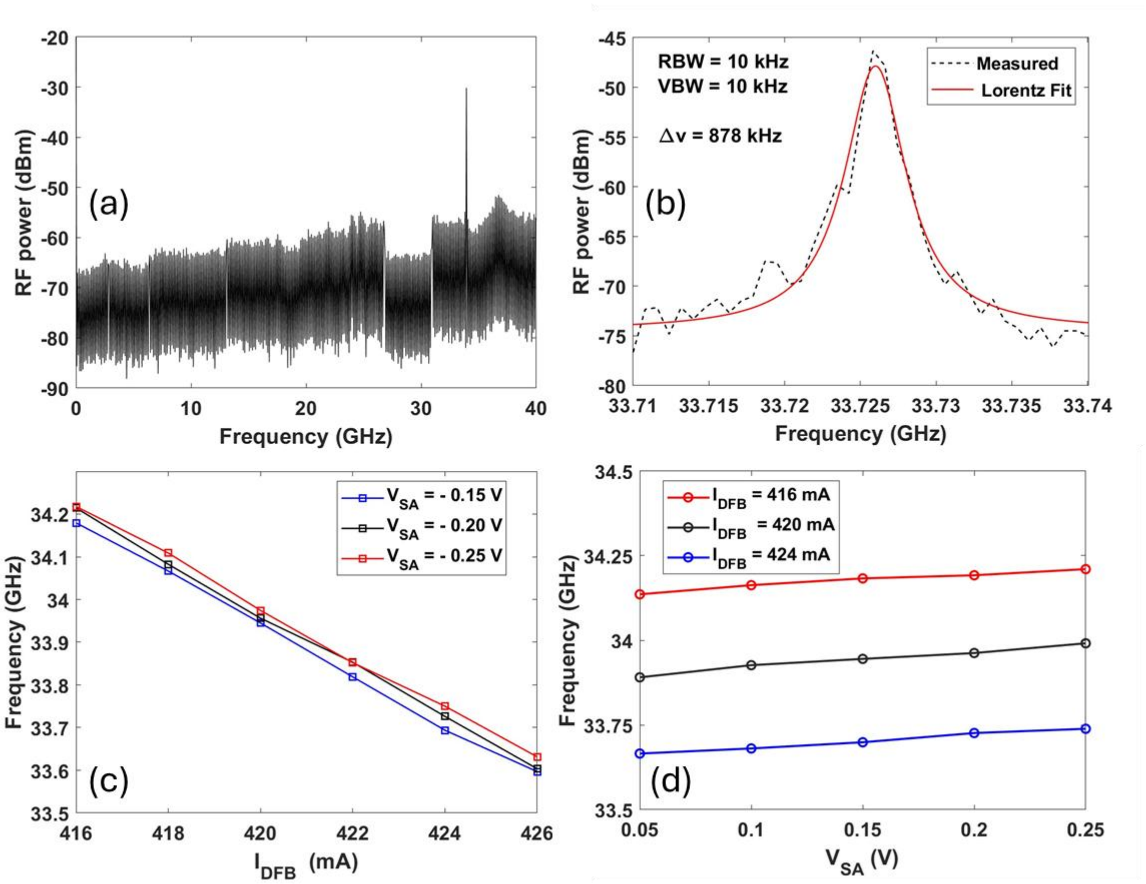


**Fig. 6.8. (a) Measured full RF spectrum of the six-wavelength ML-DFB laser, (b) zoomed RF signal near 33.7 GHz with a Lorentzian fitted profile at $I_{DFB}$ = 424 mA and $V_{SA}$ = −0.2 V, (c) mode-locking frequency dependence on $I_{DFB}$ at $V_{SA}$ = −0.15 V, −0.20 V, and −0.25 V, and (d) mode-locking frequency dependence on $V_{SA}$ at $I_{DFB}$ = 416 mA, 420 mA, and 424 mA.**

The calculated TBP is 0.552, indicating that the pulses are slightly chirped. The corresponding pulse energy is approximately 178 fJ. The irregularities are more pronounced in the six-wavelength AC trace than in the tri-wavelength case, mainly due to the lower per-channel optical power, which increases sensitivity to residual interference and detection noise. As noted above, applying an AR coating to the DFB facet can help suppress these effects. This, together with optimised device packaging, can also improve channel intensity uniformity. The broader pulse width and higher TBP compared to the shorter-cavity device (Device 1) are consistent with the denser mode spacing and reduced per-mode gain, which can lead to increased phase noise and reduced temporal compression. In addition, the observed power imbalance between channels, along with the lower SMSR in six-wavelength operation, is attributed to a reduced grating coupling coefficient ($\kappa$), likely caused by the reactive ion etching (RIE) lag effect during the sidewall grating dry etch process. Future improvements may include optimising the etching conditions or adopting buried grating structures to enhance κ and overall spectral performance. Fig. 6.8(a) shows the full RF spectrum measured at $I_{DFB}$ = 424 mA and $V_{SA}$ = −0.2 V. A strong fundamental peak is observed at the device repetition rate of 33.7 GHz, consistent with the optical spectrum and AC trace results. A Lorentzian fit to the RF peak yields a −3 dB linewidth of 878 kHz, measured using a 10 kHz RBW and video bandwidth (VBW) on the ESA, as shown in Fig. 6.8(b). The measured time-domain jitter is 1.76 ps (1 kHz to 10 MHz).

In addition, the longer effective cavity length in this design contributes to increased phase-noise accumulation over the extended optical path. Fig. 6.8(c) shows the dependence of the mode-locking frequency on $I_{DFB}$ for different values of $V_{SA}$. A decrease in the mode-locking frequency is observed as the injection current increases. This frequency reduction is attributed to an increase in the effective cavity length associated with lower absorption loss. The same trend is observed for all applied $V_{SA}$, with higher $V_{SA}$ values producing slightly higher repetition frequencies. Fig. 6.8(d) shows the dependence of the repetition frequency on $V_{SA}$ for fixed values of $I_{DFB}$. The results indicate that increasing $V_{SA}$ leads to a small but noticeable increase in the mode-locking frequency. This frequency increase is attributed to reduced pulse energy, which causes the pulses to shift earlier and shortens the effective cavity round-trip time. A fourth device was fabricated by halving the central waveguide cavity length relative to the first device while keeping the total DFB cavity length unchanged. To achieve this, the grating sections on both sides of the central cavity were proportionally extended, preserving the overall DFB length at 1000 μm. This design does not include a π phase shift, maintaining fully symmetric gratings on both sides of the cavity. The SA section length was kept at 20 μm, and the remaining grating parameters were identical to those of the three-channel device design. The measured threshold current ($I_{th}$) is 34 mA when the SA section is left floating, and the output power reaches 16.4 mW at $I_{DFB}$ = 300 mA. The optical spectrum in Fig. 6.9(a) shows dual-wavelength emission with lasing peaks at 1559.87 nm and 1560.62 nm.

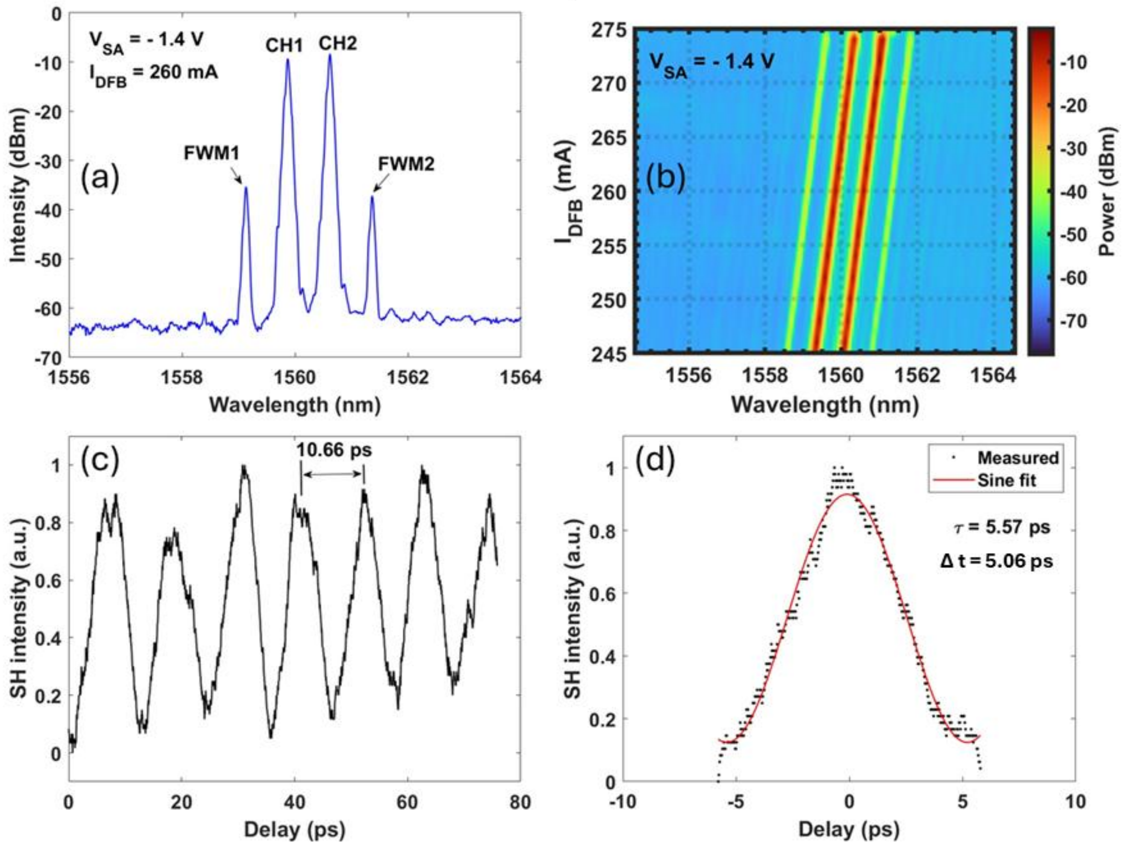


**Fig. 6.9. (a) Measured optical spectrum of the dual-wavelength DFB laser at $I_{DFB}$ = 260 mA and $V_{SA}$ = −1.4 V, (b) corresponding 2D optical spectrum as a function of $I_{DFB}$ at $V_{SA}$ = −1.4 V, (c) measured AC trace of the dual-wavelength DFB laser, and (d) an isolated AC pulse.**

The corresponding 2D optical spectrum in Fig. 6.9(b) further confirms that only two distinct lasing modes are present. The calculated effective cavity length for this device is approximately 482.44 μm, accounting for the shortened physical central cavity and the additional field penetration into the uniform Bragg gratings. This corresponds to a measured FSR of 0.75 nm, which is larger than that of the three-channel device due to the reduced cavity length. The calculated grating coupling coefficient ($\kappa$) is 36.2 cm$^{-1}$, higher than in the first device, as the shorter cavity confines the current to a smaller volume and increases the current density. This strengthens the carrier-induced index modulation, enhances grating strength, and reduces the optical penetration depth, shifting the effective mirror position and increasing κ. The reduced penetration depth shortens the effective cavity length, leading to a sparser mode structure and a larger FSR, such that only two dominant modes lase within the gain bandwidth. The reduced number of lasing modes also increases the per-mode optical power and results in stronger FWM sidebands, as observed in the spectrum. Owing to the dual-mode operation, this device does not satisfy the criteria for mode-locking. Nevertheless, it provides a new approach for monolithic millimetre-wave (mmWave) generation, where the beating between the two optical modes produces a stable high-frequency output. Compared with conventional schemes that require two separate SLM lasers for heterodyne generation, this monolithic dual-wavelength approach removes the need for precise external Stabilisation, hybrid integration, or additional Polarisation control. Since both optical modes originate from the same cavity, the frequency difference between them is intrinsically stable against environmental variations such as temperature fluctuations. This makes the device a compact, cost-effective, and fully integrated alternative for radio-over-fibre (RoF), broadband wireless access networks, and high-frequency photonic signal processing [144]. Although the device is not mode-locked, as at least three modes are generally required, the presence of the SA section introduces nonlinear effects that influence the temporal output. The AC traces in Fig. 6.9(c) show a clear pulse separation of 10.66 ps, corresponding to a measured repetition rate of 93.75 GHz. The measured single AC pulse width is 5.57 ps. Assuming a sinusoidal intensity modulation characteristic of dual-wavelength beating, the AC trace was fitted with a sine function, giving a pulse width of 5.06 ps, as shown in Fig. 6.9(d). The observed pulse formation in the dual-mode device is governed by coherent beating between the two lasing modes, while the SA introduces a more complex dynamic. In particular, the SA's intensity-dependent loss enhances phase coupling between the modes, promoting pulse-like behaviour that is sharper and more defined than the smoother sinusoidal modulation expected from dual-mode beating alone. This nonlinear response amplifies intensity fluctuations and favours the formation of distinct pulses. A summary of the four devices' key dimensions and performance is provided in Table 6.2.

**Table 6.2. Summary of the four WBG microcavity devices**

| Device | *Lcc (μm)* | No. of lasing wavelengths | FSR (nm) | $I_{th}$ (mA) |
|---|---|---|---|---|
| Device 1 | 412.36 | 3 | 0.46 | 24 |
| Device 2 | 412.36 | 4 | 0.46 | 24 |
| Device 3 | 824.82 | 6 | 0.27 | 42 |
| Device 4 | 206.18 | 2 | 0.75 | 34 |

## 6.2 Dual-wavelength DFB laser

It should be noted that this section differs in purpose from Section 6.1. There, the WBG microcavity design was mainly used to control the number of lasing channels. Here, the number of channels is kept fixed at two, and the focus is instead placed on controlling the FSR by varying the central cavity length, thereby enabling different dual-wavelength beat frequencies. As shown in Section 6.1, building on the same device platform and operating principle, the structure can also be engineered to support dual-wavelength emission with different frequency spacing by tailoring the effective cavity length, and hence the FSR. In the following, we used a DFB cavity with an adjusted different central cavity length to realise dual-wavelength DFB lasers operating at different FSRs. The device features a 1000 µm long DFB cavity ($L_{DFB}$). The complete dual-wavelength DFB laser structure is shown in Fig. 6.10. Three different central cavity lengths ($L_{cc}$) were implemented: 366 µm, 244 µm, and 122 µm, referred to as DFB1, DFB2, and DFB3, respectively. Each cavity is designed as an integer multiple of $\Lambda_0$ ($\Lambda_0$ = 244 nm). The corresponding grating lengths ($L_g$) are 317 µm, 378 µm, and 439 µm on each side. The gratings are first-order with a 50% duty cycle. The ridge waveguide is 2.5 µm wide and 1.92 µm high, with etched grating recesses (d) of 0.6 µm depth. The devices were fabricated using the method described in [22,109] and shown in Chapter 3, and are realised on the AlGaInAs/InP material with five 6-nm quantum wells, as reported in [109], following an identical fabrication process. The device uses a single-contact design. Fig. 6.10 includes an SEM image of the sidewall grating and ridge waveguide in the upper-right inset, and an optical micrograph of the fabricated DFB1–3 devices in the lower-left inset.

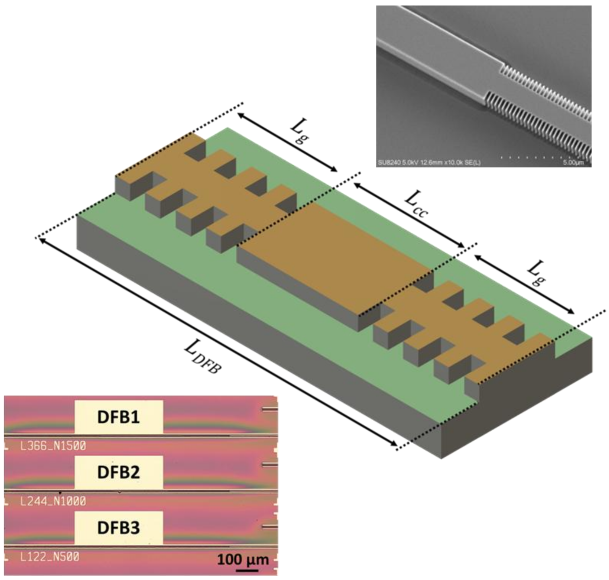


**Fig.6.10. Schematic structure of the WBG microcavity, SEM image of the sidewall grating and ridge waveguide (upper-right inset), and optical micrograph of the fabricated devices (lower-left inset).**

Measured optical spectra of the three fabricated devices are shown in Fig. 6.11. All structures exhibit stable dual-wavelength lasing, with the mode spacing increasing as the cavity length decreases. The measured FSR is approximately 0.41 nm (54.4 GHz) for DFB1, 0.51 nm (67.6 GHz) for DFB2, and 0.65 nm (86.2 GHz) for DFB3. A small discrepancy between the measured and simulated FSRs is observed, which is attributed to the limited 0.06 nm RBW of the OSA used in the measurements. Clean dual-mode operation is maintained for all devices, with SMSRs exceeding 30 dB for both lasing peaks. The key parameters and lasing wavelengths are summarised in Table 6.3. As the central cavity length increases and the FSR drops below 0.37 nm, additional modes appear, disrupting stable dual-mode operation. Fig. 6.12(a–c) shows the 2D optical spectra of the three DFB devices over the current ranges where dual-mode lasing is observed. All spectra exhibit well-defined dual-wavelength peaks with no evidence of mode hopping.

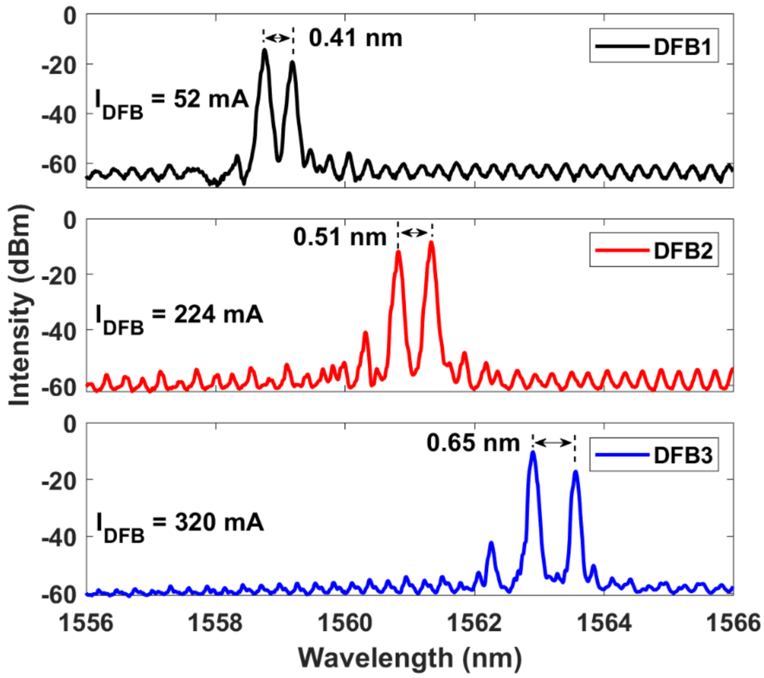


**Fig. 6.11. Measured optical spectra of DFB1, DFB2, and DFB3, demonstrating dual-wavelength lasing.**

**Table 6.3. Cavity parameters and lasing wavelengths of DFB1–DFB3.**

| Device | $L_{cc}$ | FSR | $L_{eff}$ | CH1 | CH2 |
|---|---|---|---|---|---|
| DFB1 | 366 μm | 0.41 nm | 856 μm | 1558.90 nm | 1559.31 nm |
| DFB2 | 244 μm | 0.51 nm | 688 μm | 1560.82 nm | 1561.33 nm |
| DFB3 | 122 μm | 0.65 nm | 540 μm | 1562.91 nm | 1563.56 nm |

The required DFB current increases across the devices due to variations in the central cavity length. DFB1, with the longest cavity, achieves dual-mode operation at the lowest current range (52–70 mA), followed by DFB2 (220–290 mA), and DFB3, with the shortest cavity, at the highest current range (310–350 mA). Shorter cavities reduce the effective gain volume and increase distributed-feedback losses, requiring higher injection currents for stable dual-wavelength lasing. All three devices show similar wavelength shifts of ~0.0165 nm/mA. Weak spectral peaks originate from FWM and residual facet reflections, while the slight power imbalance between the two main modes is attributed to their alignment with the gain peak and the absence of an AR coating. These effects can be mitigated by applying an AR coating and optimising the grating length. Fig. 6.13(a) shows the measured power difference between modes (PDM) and SMSR of DFB1 as a function of $I_{DFB}$. As $I_{DFB}$ increases from 50 mA to 54 mA, the PDM decreases markedly from 26.3 dB to 0.6 dB, while the SMSR improves from 24.5 dB to 42 dB. This is attributed to stronger gain competition, which equalises the power of the two lasing modes and suppresses unwanted side modes. For $I_{DFB}$ above 54 mA, as the current increases to 70 mA, the PDM gradually rises to 6 dB and the SMSR decreases slightly to 36.2 dB, while remaining high. This behaviour indicates a small imbalance in modal gain at higher currents, possibly arising from differential thermal effects or carrier-induced index changes.

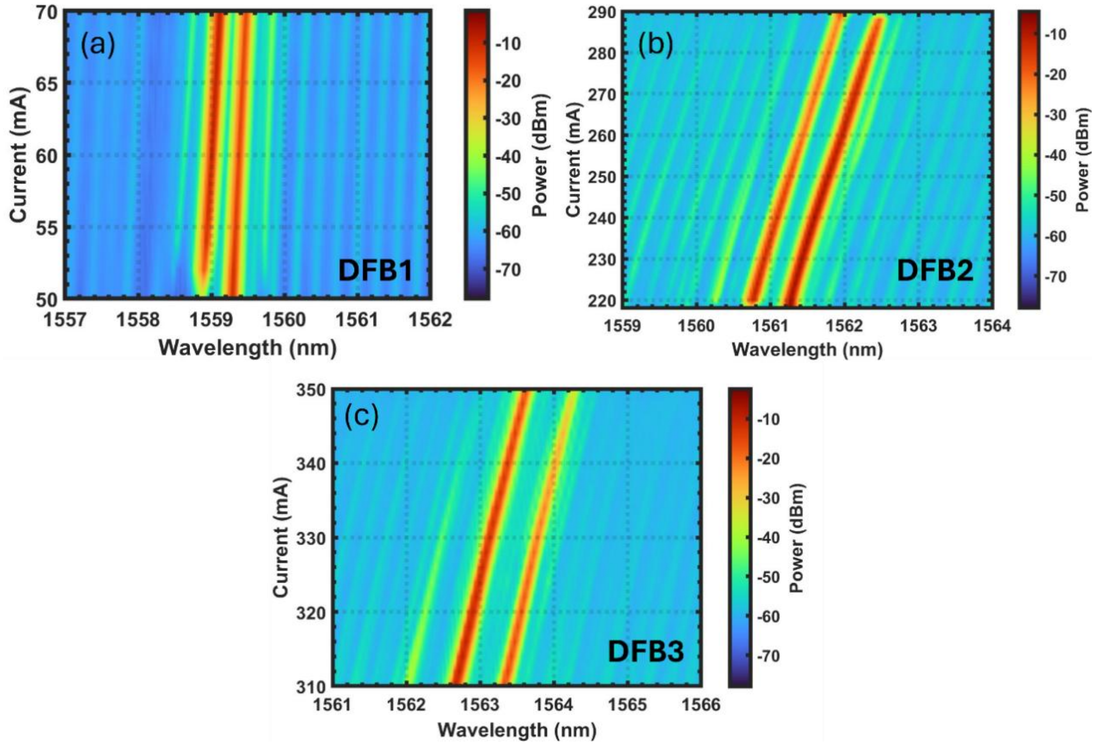


**Fig. 6.12. 2D optical spectra of (a) DFB1, (b) DFB2, and (c) DFB3.**

The PDM performance could be further improved by integrating an electroabsorption modulator (EAM) section, which enables dynamic adjustment of the feedback cavity length through an applied bias voltage. This modifies the optical feedback phase experienced by the two lasing modes. By tuning the feedback phase, the relative gain and loss of the modes can be effectively controlled, allowing the output powers of the two modes to be equalised and stabilised [145,146]. Fig. 6.13(b) shows the linear fit of the lasing wavelengths across the two channels at different $I_{DFB}$ values. As $I_{DFB}$ increases from 52 mA to 68 mA, both wavelengths redshift at a rate of 0.011 nm/mA, while the wavelength spacing between the two modes remains constant at 0.41 nm.

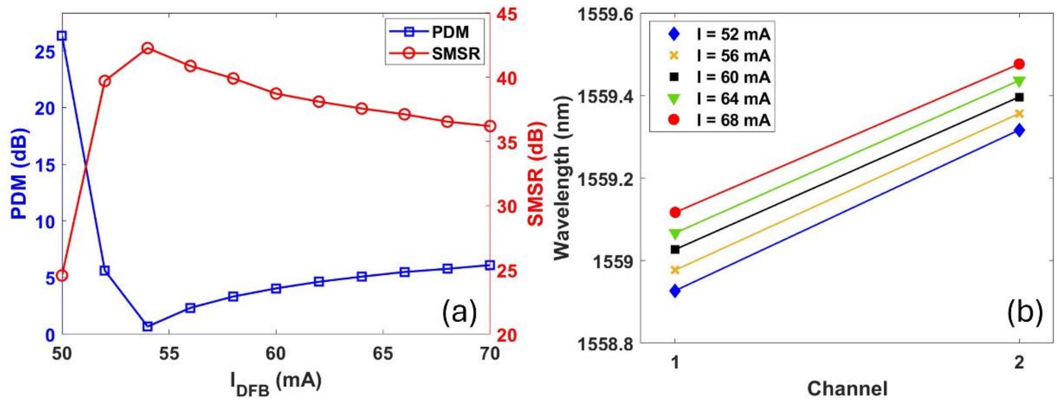


**Fig. 6.13. (a) PDM and SMSR as a function of the $I_{DFB}$ for the DFB1 device, (b) Dual-channel lasing wavelengths of DFB1 at different $I_{DFB}$, along with their linear fits.**

The RF signal was measured using a high-speed PD connected to an ESA, as shown in Fig. 6.14(a). To enable detection of beat frequencies above 50 GHz, the optical output was collected using a lensed fibre, passed through an optical isolator and a PC, and amplified by an EDFA. The amplified signal was converted to the electrical domain by the PD and routed to the ESA through an external mixer and diplexer for frequency downconversion and signal analysis. Fig. 6.14(b) shows the measured RF beat note at $I_{DFB}$ = 52 mA, fitted with a Lorentzian profile. The −3 dB linewidth is 1.15 MHz. The integrated RMS timing jitter of the RF beat note was estimated from the measured linewidth using the Lorentzian method [143], giving 17.10 ps (10 kHz–100 MHz) for DFB1. Fig. 6.14(c) shows the RF frequency shift as a function of $I_{DFB}$. A clear monotonic decrease in RF frequency is observed as the current increases, mainly due to thermal effects, which redshift both lasing wavelengths while maintaining their spectral spacing, thereby reducing the mode-beating frequency. The small deviations from a straight-line trend in the RF frequency can be attributed to factors such as noise from the DC source and external environmental variables, including temperature fluctuations in the device and mechanical vibrations.

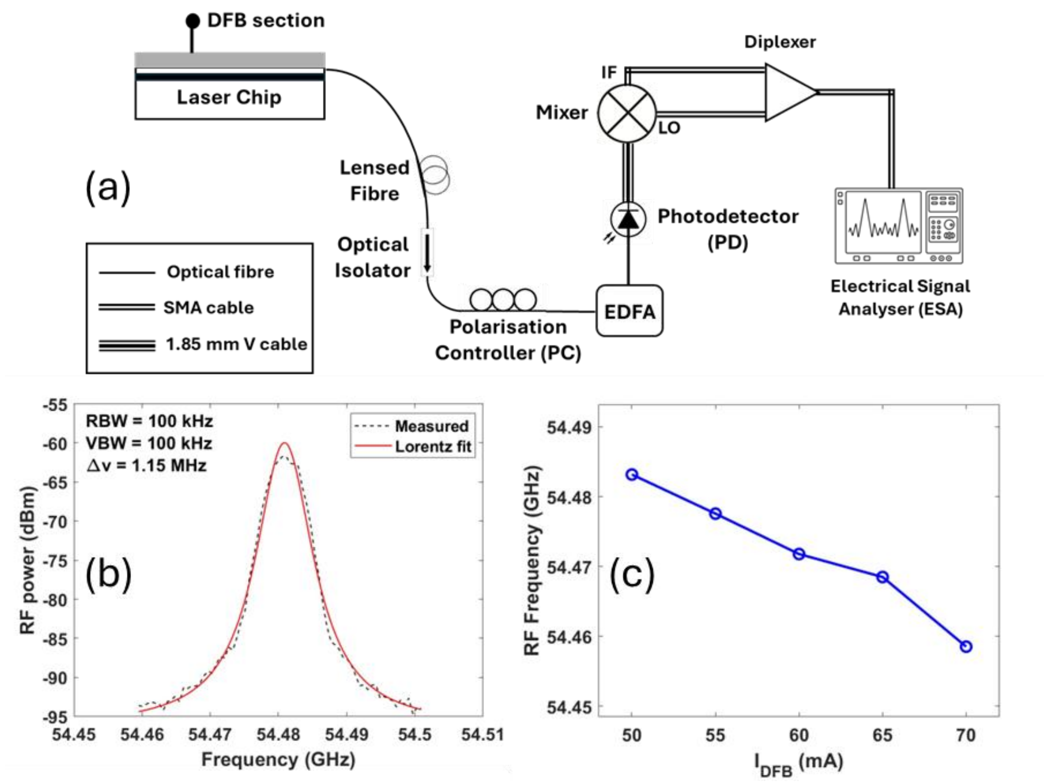


**Fig. 6.14. (a) Schematic of the RF signal measurement system, (b) measured RF beat signal of DFB1 at $I_{DFB}$ = 52 mA, and (c) RF frequency shift as a function of $I_{DFB}$ for DFB1.**

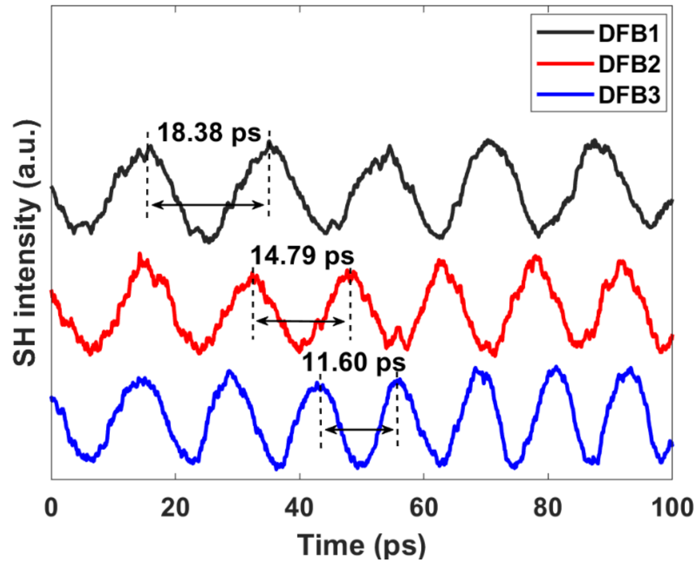


**Fig.6.15. Normalised AC trace measured for each dual DFB device: at $I_{DFB}$ = 52 mA for DFB1, 224 mA for DFB2, and 320 mA for DFB3.**

Fig. 6.15 shows the measured AC traces of the three DFB devices under the same injection current conditions as in Fig. 6.11. The dual-wavelength outputs were amplified using an EDFA and directed to the autocorrelator for time-domain analysis. The extracted beating oscillation periods are 18.38 ps, 14.79 ps, and 11.60 ps for DFB1, DFB2, and DFB3, respectively. These values agree well with the optical mode spacings observed in Fig. 6.11, confirming a good phase relationship between the two lasing modes.

## 6.3 Summary

In this chapter, we have presented a WBG microcavity platform to realise compact monolithic multi-wavelength DFB lasers with intrinsically stable wavelength spacing, since all longitudinal modes are generated within the same cavity and therefore experience the same temperature-induced shifts. The primary contribution is the first, to our knowledge, multi-wavelength ML-DFB laser achieving simultaneous three-wavelength passive mode-locking in a single monolithic cavity. The device is enabled by a fabrication-friendly design requiring only a single MOVPE growth and one III–V dry-etch step, improving simplicity and reproducibility. By tailoring the central cavity length and/or introducing a π phase shift, the platform provides direct control over the number of supported longitudinal modes and the mode-locking frequency. The tri-wavelength device exhibits an effective cavity length of ~764 μm (including field penetration into the gratings), producing a uniform FSR of 0.46 nm (57.4 GHz), an SMSR exceeding 30 dB, and near-transform-limited pulses with a deconvolved pulse width of 6.25 ps and a TBP of 0.359, representing an optimal balance between mode competition, pulse quality, and spectral purity. Device-level scalability was demonstrated by doubling and halving the central cavity length, yielding six-wavelength operation (FSR = 0.27 nm) and dual-wavelength emission (FSR = 0.75 nm), respectively, where the dual-mode case also introduces a monolithic route to stable mmWave generation via two-mode beating.

Using the same WBG microcavity principle, we further demonstrate a complementary dual-wavelength DFB laser platform based on uniform sidewall gratings, where adjusting the central cavity length enables stable dual-mode operation across a broad range of frequency spacings. With central cavity lengths of 366 μm, 244 μm, and 122 μm, FSRs of 0.41 nm, 0.51 nm, and 0.65 nm were obtained, respectively, while maintaining SMSRs above 30 dB. Overall, these results establish a simple, compact, and scalable single-cavity technology for multi-wavelength mode-locked sources and dual-wavelength mmWave photonic generation, with strong potential for DWDM, coherent optical communications, photonic sensing, and future integrated photonic systems.

# Chapter 7: Broadband 100 GHz frequency comb from an asymmetric MQW passively mode-locked laser

This chapter presents the experimental characterisation of the fabricated AMQW passively mode-locked laser, with emphasis on its operation as a broadband 100 GHz frequency-comb source. The device is investigated through electrical, optical, and time-domain measurements to assess the practical suitability of the asymmetric MQW structure for compact high-repetition-rate comb generation.[4]. This chapter builds directly on the theoretical background presented in Section 2.6 on the AMQW passively mode-locked laser, particularly Section 2.6.2, which covers Two-section passive mode-locking with AMQW gain.

## 7.1 Device characterisation and broadband comb performance

Fig. 7.1 shows the schematic of the SMLLD device. The epilayer employs asymmetric quantum wells, comprising three 6-nm wells and three 7-nm wells, as discussed in the former section 2.61 with the bandgap structure shown in Fig. 2.25. The cavity has a total length of 432 µm and consists of a 10 µm SA section, a 412 µm gain section, and a 10 µm isolation groove between the two. The ridge waveguide is 2.5 µm wide and 1.92 µm high.

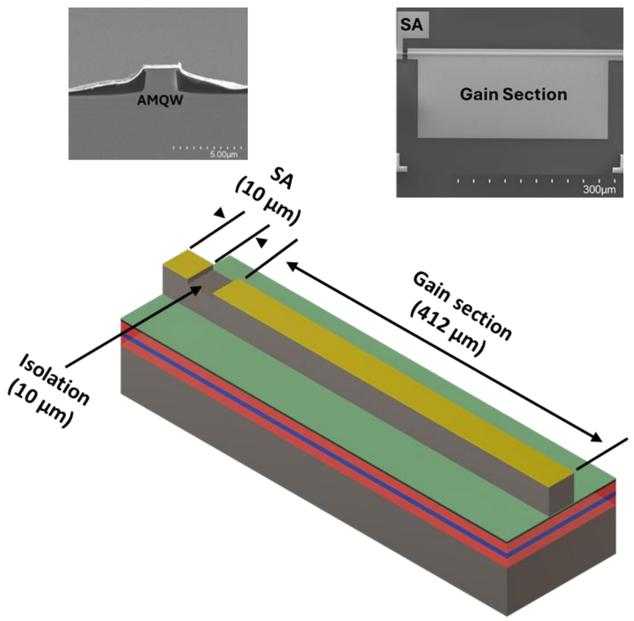


**Fig. 7.1. Schematic of the passive SMLLD, micrograph of the fabricated device (left inset), and SEM image of the ridge waveguide (right inset).**

[4] Part of this chapter have been published previously in: M. Al-Rubaiee *et al.*, *IEEE Photonics Technology Letters*, **37**, 1365-1368, (2025).

The left inset in Fig. 7.1 presents an image of the fabricated device, while the right inset shows a scanning electron microscopy (SEM) cross-sectional image of the ridge waveguide in the gain section. The fabrication follows the SMLLD process described in [109]. After fabrication, the devices were cleaved to form uncoated facets and mounted with indium (In) solder onto a copper heat sink for CW testing at 20 °C. Fig. 7.2 plots the output power from the SA side versus the gain current ( $I_{gain}$), while the SA reverse voltage ( $V_{SA}$) is swept from 0 to −3 V in −1 V steps. The threshold current is 24 mA, and the slope efficiency is 15.35% W/A at $V_{SA} = 0\text{V}$. A maximum output power of 19.2 mW is obtained at $I_{\text{gain}} = 150\text{mA}$ and $V_{\text{SA}} = 0\text{V}$, whereas 1.6 mW is measured at $I_{gain} = 34\text{mA}$ and $V_{SA} = -3\text{V}$. Passive mode-locking is achieved by forward-biasing the gain section and reverse-biasing the SA section. Mode-locking is observed for $I_{gain}$between 30 mA and 42 mA, with $V_{SA}$ between −2.2 V and −3.0 V. Fig. 7.3(a) shows the optical spectrum, measured with a 0.06 nm RBW, at $I_{gain} = 34\text{mA}$ and $V_{SA} = -3.0\text{V}$.

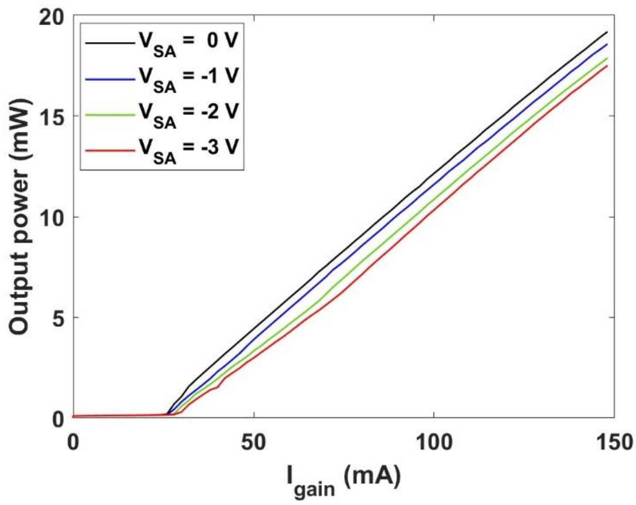


**Fig. 7.2. Output power versus $I_{gain}$ under different $V_{SA}$.**

The central wavelength is 1525 nm, with a −3 dB bandwidth of 10.14 nm, spanning 14 optical lines with a spacing of 0.78 nm (≈100 GHz). Although the simulated gain spectrum is relatively broad, the measured −3 dB bandwidth is constrained by factors including cavity dispersion, wavelength-dependent losses, and variations in modal gain across the lasing spectrum. The measured lasing spectrum shows a peak wavelength near 1530 nm, which is shorter than the 1540 nm design target. This offset is attributed to growth variations in the 6 nm and 7 nm QWs. To shift the emission toward the C-band (around 1550 nm), the material composition can be further fine-tuned, for instance, by slightly reducing the Al content in the InGaAlAs QWs while keeping the QW thickness unchanged. Fig. 7.3(b) shows the relative intensities of the 14 comb lines, with a power variation of about 3 dB across the −3 dB bandwidth. To improve the comb flatness further, several approaches can be considered: (1) band-structure engineering, by fine-tuning the QW thicknesses or introducing additional QWs to better equalise the modal gain; (2) facet-coating optimisation, using wavelength-selective reflection coatings to reduce reflectivity-induced power variations; and (3) intracavity spectral shaping, by integrating passive elements such as Bragg gratings to suppress the dominant modes. Sub-picosecond pulse widths were obtained, as demonstrated by the following measurements. To the best of our knowledge, this spectral width is among the widest reported for a directly electrically pumped QW SMLLD, and it is comparable to the 11.62 nm optical spectrum width reported for a single-section 1.55 μm InAs/InP quantum-dot SMLLD operating at 92 GHz [147].

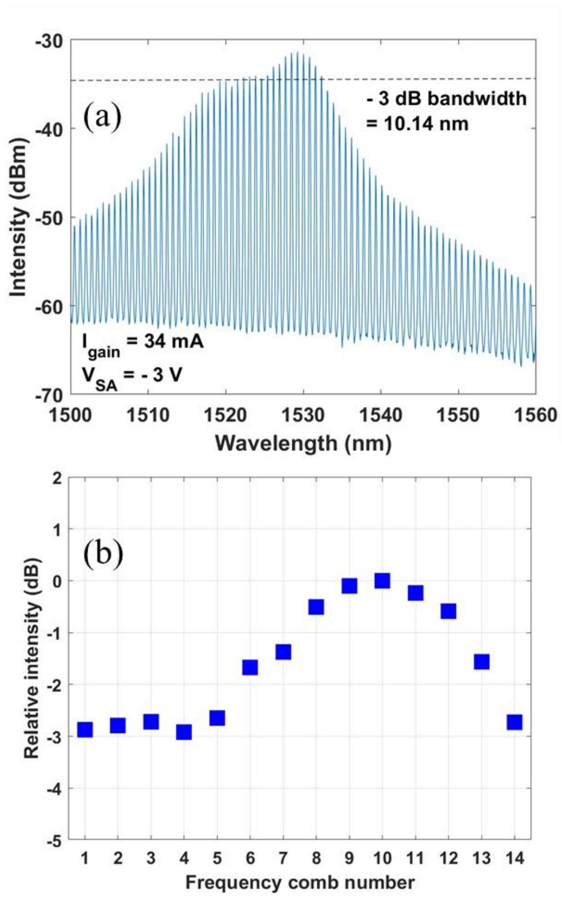


**Fig. 7.3. (a) Measured optical spectrum at $I_{gain} = 34$ mA and $V_{SA} = -3.0$V, (b) Relative intensities of the 14 comb lines within the −3 dB bandwidth.**

The measured frequency comb contains 14 optical lines separated by approximately 100 GHz. The modulation bandwidth per channel was not measured experimentally owing to the unavailability of the required high-speed communication test equipment for eye-diagram and bit-error-rate measurements. Assuming a spectral efficiency of 1 bit/s/Hz, the 100 GHz spacing gives a theoretical upper estimate of 100 Gbps per channel and 1.4 Tbps across the 14 channels. In practice, the usable modulation bandwidth would be lower owing to spectral roll-off, filtering, guard-band requirements, and transmitter/receiver bandwidth limitations. A conservative practical estimate of approximately 50 Gbps per channel therefore corresponds to an aggregate capacity of approximately 700 Gbps. The simulated AC traces and a single AC pulse were presented in Section 2.2 in Fig. 2.27(a) and (b), respectively. The simulated pulse width is 0.68 ps, corresponding to a deconvolved pulse duration of 0.46 ps assuming a sech² pulse shape. At $I_{gain} = 34$ mA and $V_{SA} = -3.0$V, the measured AC trace is presented in Fig. 7.4(a), showing a pulse separation of 10 ps. This corresponds to a 100 GHz repetition rate, consistent with the 0.78 nm spectral line spacing observed in Fig. 7.3. The measured single AC pulse is shown in Fig. 7.4(b), with a width of 0.8 ps. Assuming a $\text{sech}^2$ pulse shape, this deconvolves to a pulse duration of 0.52 ps. The measured time-bandwidth product (TBP) is 0.657, which is higher than the transform-limited value (~0.315), indicating that the pulses still have some chirp. This chirp could potentially be reduced further using external pulse-compression techniques. The chirp is likely introduced by SPM in the gain section. The estimated pulse energy is 17 fJ. Table 7.1 compares the broadband comb performance of this work with representative state-of-the-art MQW SMLLDs.

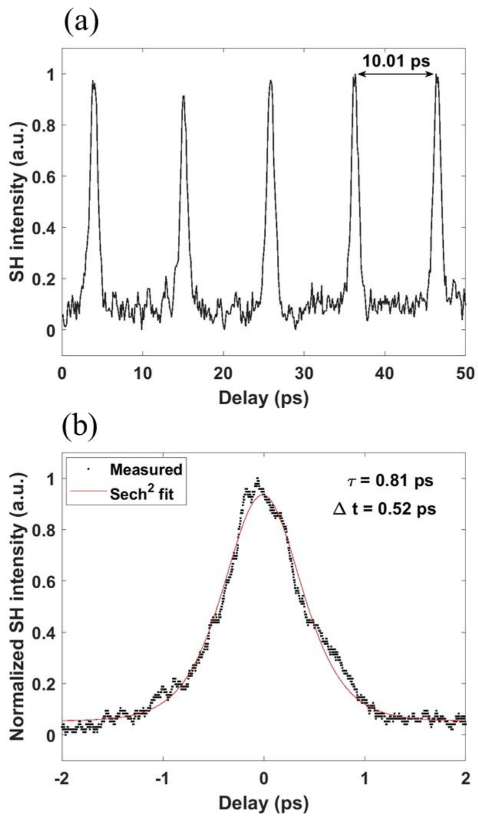


**Fig. 7.5. (a) measured full AC trace, (b) measured isolated pulse fitted with a sech² profile at $I_{gain}$= 34 mA and $V_{SA}$= −3.0 V.**

**Table 7.1. State-of-the-art literature comparison of broadband MQW semiconductor mode-locked laser frequency combs.**

| Ref. | Platform | λ | Rep. rate | −3 dB BW | Pulse width | Key point |
|---|---|---|---|---|---|---|
| Guzmán et al. [62] | MQW ring + MZI | 1.55 µm | 10.16 GHz | ~6.4 nm | >20 ps | Spectral shaping, low power |
| Moskalenko et al. [63] | MQW ring laser | 1.55 µm | ~12 GHz | ~6 nm | ~2 ps | 42 nm at −20 dB, poor flatness |
| Hou et al. [65] | AMQW SMLLD | 1610 nm | 100 GHz | 8.05 nm | 0.44 ps | Previous AMQW design |
| This work | AMQW SMLLD | 1525 nm | 100 GHz | 10.14 nm | 0.52 ps | Widest MQW −3 dB BW |

## 7.2 Summary

We demonstrated a monolithic passively mode-locked AlGaInAs/InP laser diode based on an AMQW design, generating 14 comb lines with 100 GHz spacing and a −3 dB optical bandwidth of 10.14 nm centred at 1525 nm. To the best of our knowledge, this is the widest optical bandwidth reported to date for a directly electrically pumped MQW-based SMLLD. The device also delivers pulse widths down to 0.52 ps. These results highlight AMQW structures as a practical route toward compact, high-repetition-rate frequency-comb sources for integrated photonic systems.

# Chapter 8: Future discussion

The entire thesis investigates the design, modelling, and experimental realisation of semiconductor mode-locked laser platforms for compact microwave and mmWave photonic signal generation and optical frequency combs. It spans from a 10-GHz passively mode-locked laser on a SI InP substrate with RF and optical injection locking, to multi-wavelength DFB lasers based on chirped SBGs and WBG microcavities, and finally to a broadband 100-GHz comb source using an asymmetric MQW design. Owing to their chip-scale footprint and compatibility with fibre-based and integrated microwave photonic links, the devices developed in this work have strong research and practical application potential. In the future, these mode-locked laser platforms could be explored and extended in the following areas:

1. **Comb flatness and multi-wavelength performance.** As explained previously in Chapter 5, Sections 5.1 and 5.2 (chirped C-SBG / 4PS-SBG multi-wavelength devices), Chapter 6, Section 5.1 (WBG microcavity devices), and Chapter 7, Section 7.1 (AMQW comb device), across the multi-wavelength DFB and AMQW comb devices, the measured spectra show some line-to-line power variation, mainly due to gain non-uniformity, dispersion, and facet reflectivity. To further enhance comb flatness, several strategies can be pursued: (1) band-structure engineering, by fine-tuning quantum-well thicknesses or introducing additional QWs to equalise the modal gain; (2) facet-coating optimisation, applying wavelength-selective reflection coatings to minimise reflectivity-induced power variation; and (3) intracavity spectral shaping, integrating passive structures such as distributed Bragg gratings or spectral equalisation sections to suppress dominant modes. In addition, exploring non-linear chirp profiles and alternative chirp/apodisation functions in the sampled-grating designs could provide extra flexibility to manipulate the per-channel intensities and move towards flatter multi-wavelength outputs.

2. **Emission wavelength and active-region engineering.** As explained previously in Chapter 7, Section 7.1, for the 100-GHz AMQW comb source, the measured lasing spectrum peaks around 1530 nm, slightly below the C-band target. A natural extension is to shift the emission toward ~1550 nm by fine-tuning the material composition, for example, by reducing the Al content in the InGaAlAs QWs while keeping the QW thickness unchanged, and by further adjusting the relative thicknesses and number of QWs to maintain a wide and balanced gain spectrum. Similar active-region engineering concepts could also be explored in future multi-wavelength DFB platforms, with the aim

of co-designing the gain profile and grating structure for specific wavelength grids used in WDM and integrated microwave-photonic systems.

3. **Advanced grating design and new cavity concepts.** The chirped C-SBG / 4PS-SBG and WBG microcavity devices explained in Chapters 5 and 6 demonstrate that careful grating and cavity engineering can control the number of wavelengths and spacing within a single cavity. Future work can extend this in two directions. First, different chirp functions (for example, non-linear chirp or segmented chirp profiles) can be investigated to tailor both the spectral positions and the power distribution of the lines. Second, more advanced grating concepts such as superstructure gratings or other multi-period structures could be used to increase the number of channels or realise more complex spectral patterns, which is challenging for the current gratings. These ideas can be combined with buried or higher-κ grating implementations to support a larger number of stable, high-SMSR lines in a compact footprint.

Although the proposed directions are promising, they also come with practical challenges. Achieving tighter control over epitaxial growth, fabricating higher-κ and more complex grating structures without degrading loss, and maintaining stable operation once more channels and wider combs are introduced will all require careful optimisation of both design and processing. Nevertheless, the results demonstrated in this thesis indicate that these challenges are realistic and that the proposed extensions are within reach of current semiconductor laser and integrated photonics technology.

# References


[1] G. P. Agrawal, *Fiber-Optic Communication Systems*, 4th ed. 2011. doi:10.1002/9780470918524.

[2] J. Yao, "Microwave photonics," *Journal of Lightwave Technology*, vol. 27, no. 3, pp. 314–335, 2009.

[3] T. Fortier and E. Baumann, "20 years of developments in optical frequency comb technology and applications," *Communications Physics*, vol. 2, 2019. doi: 10.1038/s42005-019-0249-y.

[4] L. Chang, S. Liu, and J. E. Bowers, "Integrated optical frequency comb technologies," *Nature Photonics*, vol. 16, no. 2, pp. 95–108, 2022. doi: 10.1038/s41566-021-00945-1.

[5] J. H. Marsh and L. Hou, "Mode-locked laser diodes and their monolithic integration," *IEEE Journal of Selected Topics in Quantum Electronics*, vol. 23, 2017. doi: 10.1109/JSTQE.2017.2693020.

[6] W. Wei, J. Chen, J. Huang, Z. Wang, J. Zhang, and T. Wang, "Advances of semiconductor mode-locked laser for optical frequency comb generation," *National Science Open*, vol. 1, Art. no. 20220026, 2022. doi: 10.1360/NSO/20220026.

[7] M. Virte and P. Marin-Palomo, "Integrated multi-wavelength lasers for all-optical processing of ultra-high frequency signals," *Applied Physics Letters*, vol. 123, 2023. doi: 10.1063/5.0170499.

[8] E. H. Bernhardi, M. R. H. Khan, C. G. H. Roeloffzen, H. A. G. M. van Wolferen, K. Wörhoff, R. M. de Ridder, *et al*., "Photonic generation of stable microwave signals from a dual-wavelength $Al_2O_3$:$Yb_{3+}$ distributed-feedback waveguide laser," *Optics Letters*, vol. 37, no. 2, pp. 181–183, 2012. doi: 10.1364/OL.37.000181.

[9] L. Zhang, Y. Zhang, Z. Shang, Y. Su, F. Yan, and Z. Wu, "A generation and distribution system of clock signal source for signal acquisition system," *Engineering Reports*, vol. 4, Art. no. e12494, 2022. doi: 10.1002/eng2.12494.

[10] H. A. Haus, "Mode-locking of lasers," *IEEE Journal on Selected Topics in Quantum Electronics*, vol. 6, pp. 1173–1185, 2000. doi: 10.1109/2944.902165.

[11] U. Keller, "Semiconductor nonlinearities for solid-state laser modelocking and Q-switching," *Semiconductors and Semimetals*, vol. 59, pp. 211–286, 1998. doi: 10.1016/S0080-8784(08)62733-7.

[12] H. K. Lee, V. Loyo-Maldonado, B. C. Qiu, K. L. Lee, C. Shu, S. Pinches, *et al*., "Efficient direct locking of colliding pulse mode-locked lasers on semi-insulating substrate at 1.5 μm," *IEEE Photonics Technology Letters*, vol. 14, no. 8, pp. 1049–1051, 2002. doi: 10.1109/LPT.2002.1021965.

[13] T. Hoshlda, M. R. H. Daza, H. F. Liu, H. F. Liu, M. Tsuchiya, T. Kamiya, *et al*., "Subharmonic hybrid mode-locking of a 33-GHz multisection semiconductor laser," in *Conference on Lasers and Electro-Optics*, 1996, paper CMB7.

[14] C. Ji, N. Chubun, R. G. Broeke, J. Cao, Y. Du, P. Bjeletich, *et al*., "Electrical subharmonic hybrid mode locking of a colliding pulse mode-locked laser at 28 GHz," *IEEE Photonics Technology Letters*, vol. 17, no. 7, pp. 1381–1383, 2005. doi: 10.1109/LPT.2005.848555.

[15] T. Hoshida, H. F. Liu, M. Tsuchiya, Y. Ogawa, and T. Kamiya, "Extremely low-amplitude modulation in a subharmonically hybrid mode-locked monolithic semiconductor laser," *IEEE Photonics Technology Letters*, vol. 8, no. 9, pp. 1160–1162, 1996. doi: 10.1109/68.531822.

[16] Z. Wang, K. Van Gasse, V. Moskalenko, S. Latkowski, E. Bente, B. Kuyken, *et al*., "A III-V-on-Si ultra-dense comb laser," *Light: Science & Applications*, vol. 6, Art. no. e16260, 2017. doi: 10.1038/lsa.2016.260.

[17] A. Nirmalathas, H. F. Liu, Z. Ahmed, D. Novak, and Y. Ogawa, "Subharmonic synchronous mode-locking of a monolithic semiconductor laser operating at millimeter-wave frequencies," *IEEE Journal on Selected Topics in Quantum Electronics*, vol. 3, no. 2, pp. 261–268, 1997. doi: 10.1109/2944.605667.

[18] S. Arahira, S. Kutsuzawa, and Y. Ogawa, "Extreme timing jitter reduction of a passively mode-locked laser diode by optical pulse injection," *IEEE Journal of Quantum Electronics*, vol. 35, no. 12, pp. 1805–1811, 1999. doi: 10.1109/3.806587.

[19] D. J. Klotzkin, *Introduction to Semiconductor Lasers for Optical Communications: An Applied Approach*. 2020. doi: 10.1007/978-3-030-24501-6.

[20] M. M. H. Adib, M. M. H. Adib, C. Füllner, C. Füllner, H. Peng, C. Koos, *et al.*, "Coherent time- and wavelength-division multiplexed point-to-multipoint optical access network using low-cost DFB lasers enabled by a frequency comb," *Optics Express*, vol. 32, no. 22, pp. 38516–38530, 2024. doi: 10.1364/OE.531344.

[21] C. Gilfert and J. P. Reithmaier, "Semiconductor lasers for sensor applications," *NATO Science for Peace and Security Series B: Physics and Biophysics*, pp. 333–353, 2011. doi: 10.1007/978-94-007-0903-4_36.

[22] Z. Li, X. Sun, Y. Fan, A. E. Kelly, S. J. Sweeney, L. Hou, *et al.*, "Multi-wavelength DFB laser based on a sidewall third-order four phase-shifted sampled Bragg grating with uniform wavelength spacing," *Optics Letters*, vol. 50, no. 3, pp. 714–717, 2025. doi: 10.1364/OL.542734.

[23] J. Zhao, Z. Sun, Y. Zhang, Z. Wang, R. Xiao, Z. Yang, *et al.*, "Multi-wavelength DFB laser with high mode stability and uniform spacing for optical I/O technology," *Journal of Lightwave Technology*, vol. 42, pp. 4874–4881, 2024. doi: 10.1109/JLT.2024.3384357.

[24] L. Hou, J. H. Marsh, S. Tang, and X. Chen, "Multiple-wavelength distributed-feedback laser arrays with high coupling coefficients and precise channel spacing," *Optics Letters*, vol. 42, no. 9, pp. 1800–1803, 2017. doi: 10.1364/OL.42.001800.

[25] Y. Yokoyama, M. Yamaguchi, K. Kudo, K. Yashiki, T. Morimoto, T. Sasaki, *et al.*, "1.55-μm wavelength-selectable microarray DFB-LD's with integrated MMI combiner, SOA, and EA-modulator," in *Optical Fiber Communication Conference*, 2000, paper TuL5.

[26] H. Ishii, K. Kasaya, H. Oohashi, Y. Shibata, H. Yasaka, and K. Okamoto, "Widely wavelength-tunable DFB laser array integrated with funnel combiner," *IEEE Journal on Selected Topics in Quantum Electronics*, vol. 13, no. 5, pp. 1089–1094, 2007. doi: 10.1109/JSTQE.2007.903594.

[27] Y. Wang, J. van Engelen, R. van Veldhoven, T. de Vries, V. Dolores-Cazadilla, V. Dolores-Cazadilla, *et al.*, "Versatile butt-joint regrowth for dense photonic integration," *Optical Materials Express*, vol. 11, no. 8, pp. 2478–2487, 2021. doi: 10.1364/OME.431963.

[28] G. Binet, J. Decobert, N. Lagay, A. D. B. Maia, P. Y. Lagrée, and F. Rinaldi, "Selective area grown AlGaInAs multi-quantum wells characterization and modeling for photonic integrated devices," in *2016 Compound Semiconductor Week (CSW), including the 28th International Conference on Indium Phosphide and Related Materials (IPRM) and the 43rd International Symposium on Compound Semiconductors (ISCS)*, 2016. doi: 10.1109/ICIPRM.2016.7528579.

[29] D. Hofstetter, B. Maisenhölder, and H. P. Zappe, "Quantum-well intermixing for fabrication of lasers and photonic integrated circuits," *IEEE Journal on Selected Topics in Quantum Electronics*, vol. 4, no. 4, pp. 794–802, 1998. doi: 10.1109/2944.720492.

[30] Z. Sun, R. Xiao, Z. Su, K. Liu, G. Lv, K. Xu, *et al.*, "Experimental demonstration of wavelength-tunable in-series DFB laser array with 100-GHz spacing," *IEEE Journal of Selected Topics in Quantum Electronics*, vol. 28, 2022. doi: 10.1109/JSTQE.2021.3078636.

[31] Z. Gao, J.-J. He, and L. Wang, "Mode competition analysis in dual-wavelength coupled-cavity semiconductor laser," *Journal of the Optical Society of America B*, vol. 27, no. 3, pp. 432–441, 2010. doi: 10.1364/JOSAB.27.000432.

[32] J. He and K. T. Chan, "Multiple wavelength and wavelength switchable actively mode-locked laser based on semiconductor optical amplifier," in *CLEO/Pacific Rim Conference*, p. 444, 2004. doi: 10.1109/CLEOPR.2003.1276996.

[33] J.-J. Chen, J.-J. Chen, J.-J. Chen, W.-Q. Wei, W.-Q. Wei, J.-L. Qin, *et al.*, "Multi-wavelength injection locked semiconductor comb laser," *Photonics Research*, vol. 10, no. 8, pp. 1840–1847, 2022. doi: 10.1364/PRJ.455165.

[34] S. Liu, Q. Ke, M. Sun, D. Lu, R. Zhang, and C. Ji, "Arrayed waveguide grating based monolithic multi-wavelength mode-locked semiconductor laser," in *CLEO: 2015*, 2015, paper JTh2A.4. doi: 10.1364/CLEO_AT.2015.JTH2A.4.

[35] M. Mielke, G. A. Alphonse, and P. J. Delfyett, "Multiwavelength modelocked semiconductor lasers for photonic access network applications," *IEEE Journal on Selected Areas in Communications*, vol. 25, no. 1, pp. 120–128, 2007. doi: 10.1109/JSAC-OCN.2007.004803.

[36] Z. Yao, C. Jiang, X. Wang, H. Chen, H. Wang, L. Qin, *et al.*, "Recent developments of quantum dot materials for high speed and ultrafast lasers," *Nanomaterials*, vol. 12, Art. no. 1058, 2022. doi: 10.3390/nano12071058.

[37] M. J. Heck, E. A. J. M. Bente, B. Smalbrugge, Y.-S. Oei, M. K. Smit, S. Anantathanasarn, *et al.*, "Observation of Q-switching and mode-locking in two-section InAs/InP (100) quantum dot lasers around 1.55 µm," *Optics Express*, vol. 15, no. 25, pp. 16292–16301, 2007. doi: 10.1364/OE.15.016292.

[38] S. Liu, M. J. Kennedy, H. K. Tsang, J. E. Bowers, D. Jung, J. C. Norman, *et al.*, "High-channel-count 20 GHz passively mode-locked quantum dot laser directly grown on Si with 4.1 Tbit/s transmission capacity," *Optica*, vol. 6, no. 2, pp. 128–134, 2019. doi: 10.1364/OPTICA.6.000128.

[39] S. Hisatake, J. Y. Kim, K. Ajito, and T. Nagatsuma, "Self-heterodyne spectrometer using uni-traveling-carrier photodiodes for terahertz-wave generators and optoelectronic mixers," *Journal of Lightwave Technology*, vol. 32, no. 20, pp. 3683–3689, 2014. doi: 10.1109/JLT.2014.2321004.

[40] K. Kudo, K. Yashiki, T. Sasaki, Y. Yokoyama, K. Hamamoto, T. Morimoto, *et al.*, "1.55-µm wavelength-selectable microarray DFB-LD's with monolithically integrated MMI combiner, SOA, and EA-modulator," *IEEE Photonics Technology Letters*, vol. 12, no. 3, pp. 242–244, 2000. doi: 10.1109/68.826901.

[41] G. Qi, J. Yao, J. Seregelyi, S. Paquet, and C. Bélisle, "Optical generation and distribution of continuously tunable millimeter-wave signals using an optical phase modulator," *Journal of Lightwave Technology*, vol. 23, no. 9, pp. 2687–2695, 2005. doi: 10.1109/JLT.2005.854067.

[42] J. Liu, H. C. Chien, S. H. Fan, B. Chen, J. Yu, S. He, *et al.*, "Efficient optical millimeter-wave generation using a frequency-tripling Fabry-Pérot laser with sideband injection and synchronization," *IEEE Photonics Technology Letters*, vol. 23, no. 18, pp. 1325–1327, 2011. doi: 10.1109/LPT.2011.2159834.

[43] J. Sun, Y. Dai, X. Chen, Y. Zhang, and S. Xie, "Stable dual-wavelength DFB fiber laser with separate resonant cavities and its application in tunable microwave generation," *IEEE Photonics Technology Letters*, vol. 18, no. 24, pp. 2587–2589, 2006. doi: 10.1109/LPT.2006.887336.

[44] Y. Zhang, B. Yuan, J. Shi, W. Qi, L. Li, L. Wang, *et al.*, "A stable dual-wavelength DFB semiconductor laser with equivalent chirped sampled grating," *IEEE Journal of Quantum Electronics*, vol. 58, 2022. doi: 10.1109/JQE.2021.3126447.

[45] Y. Fan, B. Yuan, M. Al-Rubaiee, Y. Sun, S. Zhu, J. Akbar, *et al.*, "Millimeter-wave generation based on four phase-shifted sampled moiré grating dual-wavelength DFB

laser," *IEEE Photonics Technology Letters*, vol. 36, pp. 282–285, 2024. doi: 10.1109/LPT.2024.3351531.

[46] L. Hou, M. Haji, I. Eddie, H. Zhu, and J. H. Marsh, "Laterally coupled dual-grating distributed feedback lasers for generating mode-beat terahertz signals," *Optics Letters*, vol. 40, no. 2, pp. 182–185, 2015. doi: 10.1364/OL.40.000182.

[47] F. Pozzi, R. M. De La Rue, and M. Sorel, "Dual-wavelength InAlGaAs-InP laterally coupled distributed feedback laser," *IEEE Photonics Technology Letters*, vol. 18, no. 24, pp. 2563–2565, 2006. doi: 10.1109/LPT.2006.887205.

[48] S. D. Roh, T. S. Yeoh, R. B. Swint, A. E. Huber, C. Y. Woo, J. S. Hughes, *et al.*, "Dual-wavelength InGaAs-GaAs ridge waveguide distributed Bragg reflector lasers with tunable mode separation," *IEEE Photonics Technology Letters*, vol. 12, no. 10, pp. 1307–1309, 2000. doi: 10.1109/68.883812.

[49] S. Osborne, S. O'Brien, K. Buckley, R. Fehse, A. Amann, J. Patchell, *et al.*, "Design of single-mode and two-color Fabry-Pérot lasers with patterned refractive index," *IEEE Journal on Selected Topics in Quantum Electronics*, vol. 13, no. 5, pp. 1157–1163, 2007. doi: 10.1109/JSTQE.2007.903851.

[50] A. G. Vladimirov and D. Turaev, "Model for passive mode locking in semiconductor lasers," *Physical Review A*, vol. 72, Art. no. 033808, 2005. doi: 10.1103/PhysRevA.72.033808.

[51] R. P. Green, M. Haji, L. Hou, G. Mezosi, R. Dylewicz, A. E. Kelly, *et al.*, "Fast saturable absorption and 10 GHz wavelength conversion in Al-quaternary multiple quantum wells," *Optics Express*, vol. 19, no. 10, pp. 9737–9743, 2011. doi: 10.1364/OE.19.009737.

[52] B. Yuan, Y. Fan, S. Ye, Y. Zhang, Y. Sun, X. Sun, *et al.*, "Dual-wavelength DFB laser array based on sidewall grating and lateral modulation of the grating coupling coefficient," *Journal of Lightwave Technology*, vol. 41, pp. 2775–2784, 2023. doi: 10.1109/JLT.2023.3237601.

[53] K. Yvind, *Semiconductor Mode-Locked Lasers for Optical Communication Systems*. 2003.

[54] S. Zhu, B. Yuan, M. Al-Rubaiee, Y. Sun, Y. Fan, A. S. Hezarfen, *et al.*, "Widely tunable photonic filter based on equivalent chirped four-phase-shifted sampled Bragg gratings," *ACS Photonics*, vol. 12, pp. 899–907, 2025. doi: 10.1021/acsphotonics.4c01899.

[55] J. C. Cartledge and M. O'Sullivan, "Time- and frequency-domain characterization of the relative intensity noise of a quantum-dot frequency comb source laser," *IEEE Journal of Selected Topics in Quantum Electronics*, vol. 25, pp. 1–9, 2019. doi: 10.1109/JSTQE.2019.2926204.

[56] L. Lundberg, M. Karlsson, A. Lorences-Riesgo, M. Mazur, V. Torres-Company, J. Schröder, *et al.*, "Frequency comb-based WDM transmission systems enabling joint signal processing," *Applied Sciences*, vol. 8, Art. no. 718, 2018. doi: 10.3390/app8050718.

[57] R. Rosales, S. G. Murdoch, R. Watts, K. Merghem, A. Martinez, F. Lelarge, *et al.*, "High performance mode locking characteristics of single section quantum dash lasers," *Optics Express*, vol. 20, no. 8, pp. 8649–8657, 2012. doi: 10.1364/OE.20.008649.

[58] J.-Z. Huang, J.-Z. Huang, Z.-T. Ji, J.-J. Chen, J.-J. Chen, W.-Q. Wei, *et al.*, "Ultra-broadband flat-top quantum dot comb lasers," *Photonics Research*, vol. 10, no. 5, pp. 1308–1316, 2022. doi: 10.1364/PRJ.446349.

[59] M. J. R. Heck, A. Renault, E. A. J. M. Bente, Y. S. Oei, M. K. Smit, K. S. E. Eikema, *et al.*, "Passively mode-locked 4.6 and 10.5 GHz quantum dot laser diodes around 1.55 μm with large operating regime," *IEEE Journal on Selected Topics in Quantum Electronics*, vol. 15, pp. 634–643, 2009. doi: 10.1109/JSTQE.2009.2016760.

[60] Z. Lu, J. Liu, P. J. Poole, Y. Mao, J. Weber, G. Liu, *et al.*, "InAs/InP quantum dash semiconductor coherent comb lasers and their applications in optical networks," *Journal of Lightwave Technology*, vol. 39, pp. 3751–3760, 2021. doi: 10.1109/JLT.2020.3043284.

[61] L. Hou, A. C. Bryce, J. H. Marsh, and M. Haji, "490 fs pulse generation from a passive C-band AlGaInAs/InP quantum well mode-locked laser," *Optics Letters*, vol. 37, no. 5, pp. 773–775, 2012. doi: 10.1364/OL.37.000773.

[62] R. Guzmán, G. Carpintero, X. J. M. Leijtens, V. Corral, and C. Gordón, "Optical frequency comb generator based on a monolithically integrated passive mode-locked ring laser with a Mach–Zehnder interferometer," *Optics Letters*, vol. 41, no. 9, pp. 1937–1940, 2016. doi: 10.1364/OL.41.001937.

[63] V. Moskalenko, K. Williams, J. Koelemeij, and E. Bente, "42 nm wide coherent frequency comb generated by a QW based integrated passively mode-locked laser," in *International Semiconductor Laser Conference (ISLC)*, Kobe, Japan, 2016.

[64] M. J. Hamp and D. T. Cassidy, "Critical design parameters for engineering broadly tunable asymmetric multiple-quantum-well lasers," *IEEE Journal of Quantum Electronics*, vol. 36, no. 8, pp. 978–983, 2000. doi: 10.1109/3.853559.

[65] L. Hou, Y. Huang, Y. Huang, Y. Huang, Y. Liu, Y. Liu, *et al.*, "Frequency comb with 100 GHz spacing generated by an asymmetric MQW passively mode-locked laser," *Optics Letters*, vol. 45, no. 10, pp. 2760–2763, 2020. doi: 10.1364/OL.392191.

[66] E. A. Avrutin, J. H. Marsh, and E. L. Portnoi, "Monolithic and multi-GigaHertz mode-locked semiconductor lasers: Constructions, experiments, models and applications," *IEE Proceedings - Optoelectronics*, vol. 147, pp. 251–278, 2000. doi: 10.1049/IP-OPT:20000282.

[67] P. J. Delfyett, S. Gee, M. T. Choi, H. Izadpanah, W. Lee, S. Ozharar, *et al.*, "Optical frequency combs from semiconductor lasers and applications in ultrawideband signal processing and communications," *Journal of Lightwave Technology*, vol. 24, pp. 2701–2719, 2006. doi: 10.1109/JLT.2006.875948.

[68] J. Ye, H. Schnatz, and L. W. Hollberg, "Optical frequency combs: From frequency metrology to optical phase control," *IEEE Journal on Selected Topics in Quantum Electronics*, vol. 9, pp. 1041–1058, 2003. doi: 10.1109/JSTQE.2003.819109.

[69] U. Keller, "Recent developments in compact ultrafast lasers," *Nature*, vol. 424, pp. 831–838, 2003. doi: 10.1038/nature01938.

[70] H. A. Haus, "Theory of mode locking with a fast saturable absorber," *Journal of Applied Physics*, vol. 46, pp. 3049–3058, 1975. doi: 10.1063/1.321997.

[71] W. Wei, J. Chen, J. Huang, Z. Wang, J. Zhang, and T. Wang, "Advances of semiconductor mode-locked laser for optical frequency comb generation," *National Science Open*, vol. 1, Art. no. 20220026, 2022. doi: 10.1360/NSO/20220026.

[72] E. A. Avrutin and E. U. Rafailov, "Advances in mode-locked semiconductor lasers," *Semiconductors and Semimetals*, vol. 86, pp. 93–147, 2012. doi: 10.1016/B978-0-12-391066-0.00003-4.

[73] M. Haji, L. Hou, A. E. Kelly, R. Green, G. Mezosi, J. Javaloyes, *et al.*, "Sub-picosecond pulse generation using fast saturable absorption in AlGaInAs/InP quantum wells," in *2010 23rd Annual Meeting of the IEEE Photonics Society*, 2010, pp. 299–300. doi: 10.1109/PHOTONICS.2010.5698878.

[74] G. Fiol, D. Arsenijević, D. Bimberg, A. G. Vladimirov, M. Wolfrum, E. A. Viktorov, *et al.*, "Hybrid mode-locking in a 40 GHz monolithic quantum dot laser," *Applied Physics Letters*, vol. 96, Art. no. 011104, 2010. doi: 10.1063/1.3279136.

[75] K. Van Gasse, S. Uvin, V. Moskalenko, S. Latkowski, G. Roelkens, E. Bente, *et al.*, "Recent advances in the photonic integration of mode-locked laser diodes," *IEEE Photonics Technology Letters*, vol. 31, pp. 1870–1873, 2019. doi: 10.1109/LPT.2019.2945973.

[76] A. Hermans, K. Van Gasse, and B. Kuyken, “On-chip optical comb sources,” *APL Photonics*, vol. 7, Art. no. 100901, 2022. doi: 10.1063/5.0105164.

[77] K. Yvind, D. Larsson, L. K. Oxenløwe, J. Mørk, and J. M. Hvam, “Mode-locked semiconductor lasers for optical communication systems,” in *Proceedings of the 7th International Conference on Transparent Optical Networks (ICTON 2005)*, vol. 2, 2005, pp. 209–212. doi: 10.1109/ICTON.2005.1506135.

[78] H. Kogelnik and C. V. Shank, “Coupled-wave theory of distributed feedback lasers,” *Journal of Applied Physics*, vol. 43, pp. 2327–2335, 1972. doi: 10.1063/1.1661499.

[79] A. Yariv, “Coupled-mode theory for guided-wave optics,” *IEEE Journal of Quantum Electronics*, vol. 9, pp. 919–933, 1973. doi: 10.1109/JQE.1973.1077767.

[80] T. Erdogan, “Fiber grating spectra,” *Journal of Lightwave Technology*, vol. 15, pp. 1277–1294, 1997. doi: 10.1109/50.618322.

[81] J. Javaloyes and S. Balle, *Freetwm: A Simulation Tool for Semiconductor Lasers*. 2012.

[82] S. Balle, “Simple analytical approximations for the gain and refractive index spectra in quantum-well lasers,” *Physical Review A*, vol. 57, p. 1304, 1998. doi: 10.1103/PhysRevA.57.1304.

[83] P. M. Stolarz, J. Javaloyes, G. Mezosi, L. Hou, C. N. Ironside, M. Sorel, *et al.*, “Spectral dynamical behavior in passively mode-locked semiconductor lasers,” *IEEE Photonics Journal*, vol. 3, pp. 1067–1082, 2011. doi: 10.1109/JPHOT.2011.2172403.

[84] M. Hyun, H. Chung, W. Na, and J. Kim, “Femtosecond-precision electronic clock distribution in CMOS chips by injecting frequency comb-extracted photocurrent pulses,” *Nature Communications*, vol. 14, Art. no. 2345, 2023. doi: 10.1038/s41467-023-38122-3.

[85] H. A. Haus and A. Mecozzi, “Noise of mode-locked lasers,” *IEEE Journal of Quantum Electronics*, vol. 29, pp. 983–996, 1993. doi: 10.1109/3.206583.

[86] L. A. Jiang, M. E. Grein, H. A. Haus, and E. P. Ippen, “Noise of mode-locked semiconductor lasers,” *IEEE Journal on Selected Topics in Quantum Electronics*, vol. 7, pp. 159–167, 2001. doi: 10.1109/2944.954125.

[87] D. von der Linde, “Characterization of the noise in continuously operating mode-locked lasers,” *Applied Physics B: Photophysics and Laser Chemistry*, vol. 39, pp. 201–217, 1986. doi: 10.1007/BF00697487.

[88] F. Ö. Ilday, J. R. Buckley, W. G. Clark, and F. W. Wise, “Timing jitter and phase noise of mode-locked fiber lasers,” *Optics Express*, vol. 18, no. 5, pp. 5041–5054, 2010. doi: 10.1364/OE.18.005041.

[89] L. Hou, A. C. Bryce, J. Akbar, B. Qiu, and M. Haji, “Low divergence angle and low jitter 40 GHz AlGaInAs/InP 1.55 μm mode-locked lasers,” *Optics Letters*, vol. 36, no. 6, pp. 966–968, 2011. doi: 10.1364/OL.36.000966.

[90] L. Hou, M. Haji, J. H. Marsh, A. C. Bryce, D. K. Yvind, L. J. Larsson, *et al.*, “10 GHz AlGaInAs/InP 1.55 μm passively mode-locked laser with low divergence angle and timing jitter,” *Optics Express*, vol. 19, no. 26, pp. B75–B80, 2011. doi: 10.1364/OE.19.000B75.

[91] F. Camacho, E. A. Avrutin, P. Cusumano, A. Saher Helmy, A. C. Bryce, and J. H. Marsh, “Improvements in mode-locked semiconductor diode lasers using monolithically integrated passive waveguides made by quantum-well intermixing,” *IEEE Photonics Technology Letters*, vol. 9, pp. 1208–1210, 1997. doi: 10.1109/68.618479.

[92] G. P. Agrawal and N. A. Olsson, “Self-phase modulation and spectral broadening of optical pulses in semiconductor laser amplifiers,” *IEEE Journal of Quantum Electronics*, vol. 25, pp. 2297–2306, 1989. doi: 10.1109/3.42059.

[93] H. C. Huang, S. Yee, and M. Soma, “The carrier effects on the change of refractive index for n-type GaAs at $\lambda = 1.06, 1.3$, and 1.55 μm,” *Journal of Applied Physics*, vol. 67, pp. 1497–1503, 1990. doi: 10.1063/1.345658.

[94] B. E. A. Saleh and M. C. Teich, *Fundamentals of Photonics*. 1991. doi: 10.1002/0471213748.
[95] J. Buus, “Analytical approximation for the reflectivity of DH lasers,” *IEEE Journal of Quantum Electronics*, vol. QE-17, pp. 2256–2257, 1981. doi: 10.1109/JQE.1981.1070735.
[96] J. S. Jeong, H. K. Lee, and C. H. Lee, “Measurement of facet reflectivity through reflection gain in Fabry–Pérot laser diode,” *IEEE Photonics Technology Letters*, vol. 20, pp. 1225–1227, 2008. doi: 10.1109/LPT.2008.925508.
[97] R. Adler, “A study of locking phenomena in oscillators,” *Proceedings of the IRE*, vol. 34, pp. 351–357, 1946. doi: 10.1109/JRPROC.1946.229930.
[98] P. J. Delfyett, D. H. Hartman, and S. Z. Ahmad, “Optical clock distribution using a mode-locked semiconductor laser diode system,” *Journal of Lightwave Technology*, vol. 9, pp. 1646–1649, 1991. doi: 10.1109/50.108709.
[99] Z. Liu and R. Slavík, “Optical injection locking: From principle to applications,” *Journal of Lightwave Technology*, vol. 38, pp. 43–59, 2020. doi: 10.1109/JLT.2019.2945718.
[100] J.-J. Chen, J.-J. Chen, J.-J. Chen, W.-Q. Wei, W.-Q. Wei, J.-L. Qin, *et al*., “Multi-wavelength injection locked semiconductor comb laser,” *Photonics Research*, vol. 10, no. 8, pp. 1840–1847, 2022. doi: 10.1364/PRJ.455165.
[101] B. Yuan, X. Sun, Y. Huang, R. Zhang, Y. Fan, L. Hou, *et al*., “DFB laser array based on four phase-shifted sampled Bragg gratings with precise wavelength control,” *Optics Letters*, vol. 47, no. 23, pp. 6237–6240, 2022. doi: 10.1364/OL.475909.
[102] S. Tang, *InP-Based Semiconductor Lasers with Novel Sampled Bragg Gratings and Applications*. University of Glasgow, 2019.
[103] B. S. K. Lo and H. Ghafouri-Shiraz, “Spectral characteristics of distributed feedback laser diodes with distributed coupling coefficient,” *Journal of Lightwave Technology*, vol. 13, pp. 200–212, 1995. doi: 10.1109/50.365207.
[104] L. A. Coldren, S. W. Corzine, and M. L. Mašanović, *Diode Lasers and Photonic Integrated Circuits*. 2012. doi: 10.1002/9781118148167.
[105] C. Ferreira Fernandes, *Single Phase-Shifted DFB Laser Diodes*, vol. 17. John Wiley & Sons, Inc., 1998.
[106] M. Al-Rubaiee, X. Sun, B. Yuan, Y. Fan, *et al*., “Simultaneous multi-wavelength mode-locked DFB laser based on waveguide Bragg grating microcavities,” *Optics Express*, vol. 33, no. 11, pp. 22222–22234, 2025. doi: 10.1364/OE.563242.
[107] M. J. Al-Rubaiee, X. Sun, J. Wang, A. Hezarfen, *et al*., “Dual-wavelength distributed feedback laser based on waveguide Bragg grating microcavities,” *Optics Letters*, vol. 50, no. 23, pp. 7219–7222, 2025. doi: 10.1364/OL.575610.
[108] F. Comis, M. Shevchenko, M. Shevchenko, M.-C. Lo, M.-C. Lo, and A. Ruocco, “Experimental analysis and modeling of the penetration depth of uniform and apodized integrated Bragg reflectors,” *Optics Express*, vol. 32, no. 26, pp. 47447–47457, 2024. doi: 10.1364/OE.534778.
[109] L. Hou, P. Stolarz, J. Javaloyes, R. P. Green, C. N. Ironside, M. Sorel, *et al*., “Subpicosecond pulse generation at quasi-40-GHz using a passively mode-locked AlGaInAs-InP 1.55-µm strained quantum-well laser,” *IEEE Photonics Technology Letters*, vol. 21, pp. 1731–1733, 2009. doi: 10.1109/LPT.2009.2031088.
[110] J. M. Luttinger and W. Kohn, “Motion of electrons and holes in perturbed periodic fields,” *Physical Review*, vol. 97, p. 869, 1955. doi: 10.1103/PhysRev.97.869.
[111] D. Ahn, “Theory of non-Markovian optical gain in quantum-well lasers,” *Progress in Quantum Electronics*, vol. 21, pp. 249–287, 1997. doi: 10.1016/S0079-6727(97)00003-7.
[112] M. Al-Rubaiee, B. Qiu, S. Zhu, X. Sun, A. S. Hezarfen, Z. Wang, *et al*., “Broadband 100 GHz frequency comb from an asymmetric MQW passively mode-locked laser,”

*IEEE Photonics Technology Letters*, vol. 37, pp. 1365–1368, 2025. doi: 10.1109/LPT.2025.3604691.

[113] D. R. Medeiros, A. Aviram, C. R. Guarnieri, W. S. Huang, R. Kwong, C. K. Magg, *et al.*, "Recent progress in electron-beam resists for advanced mask-making," *IBM Journal of Research and Development*, vol. 45, pp. 639–650, 2001. doi: 10.1147/rd.455.0639.

[114] N. Vella, E. A. El Joumha, and A. Toureille, "Space charge measurement by the Thermal Step method and TSDC in PMMA," in *8th International Symposium on Electrets (ISE 1994) Proceedings*, 1994, pp. 230–235. doi: 10.1109/ISE.1994.514773.

[115] S. Park, S. S. Kim, L. Wang, and S. T. Ho, "InGaAsP-InP nanoscale waveguide-coupled microring lasers with submilliampere threshold current using $Cl_2$-$N_2$-based high-density plasma etching," *IEEE Journal of Quantum Electronics*, vol. 41, pp. 351–356, 2005. doi: 10.1109/JQE.2004.842311.

[116] K. Inoshita and T. Baba, "Fabrication of GaInAsP/InP photonic crystal lasers by ICP etching and control of resonant mode in point and line composite defects," *IEEE Journal on Selected Topics in Quantum Electronics*, vol. 9, pp. 1347–1354, 2003. doi: 10.1109/JSTQE.2003.819466.

[117] U. Sökmen, A. Stranz, S. Fündling, H. H. Wehmann, V. Bandalo, A. Bora, *et al.*, "Capabilities of ICP-RIE cryogenic dry etching of silicon: Review of exemplary microstructures," *Journal of Micromechanics and Microengineering*, vol. 19, Art. no. 105005, 2009. doi: 10.1088/0960-1317/19/10/105005.

[118] L. Zhao, X. Wang, N. Jiang, K. Nishimura, J. Yi, and S. Fang, "Experimental study of inductively coupled plasma etching of patterned single crystal diamonds," *Scientific Reports*, vol. 15, Art. no. 21062, 2025. doi: 10.1038/s41598-025-08066-3.

[119] N. Furuhata, H. Miyamoto, A. Okamoto, and K. Ohata, "Chemical dry etching of GaAs and InP by $Cl_2$ using a new ultrahigh-vacuum dry-etching molecular-beam-epitaxy system," *Journal of Applied Physics*, vol. 65, pp. 168–171, 1989. doi: 10.1063/1.342564.

[120] U. K. Chakrabarti, S. J. Pearton, and F. Ren, "Sidewall roughness during dry etching of InP," *Semiconductor Science and Technology*, vol. 6, p. 408, 1991. doi: 10.1088/0268-1242/6/5/018.

[121] C. Chen, D. G. Yu, E. L. Hu, and P. M. Petroff, "Photoluminescence studies on radiation enhanced diffusion of dry-etch damage in GaAs and InP materials," *Journal of Vacuum Science & Technology B: Microelectronics and Nanometer Structures Processing, Measurement, and Phenomena*, vol. 14, pp. 3684–3687, 1996. doi: 10.1116/1.588750.

[122] S. J. Choi, K. Djordjev, S. J. Choi, and P. D. Dapkus, "$CH_4$-based dry etching of high Q InP microdisks," *Journal of Vacuum Science & Technology B: Microelectronics and Nanometer Structures Processing, Measurement, and Phenomena*, vol. 20, pp. 301–305, 2002. doi: 10.1116/1.1445164.

[123] K. Nakahara, Y. Wakayama, T. Kitatani, T. Taniguchi, T. Fukamachi, Y. Sakuma, *et al.*, "Direct modulation at 56 and 50 Gb/s of 1.3-μm InGaAlAs ridge-shaped-BH DFB lasers," *IEEE Photonics Technology Letters*, vol. 27, pp. 534–536, 2015. doi: 10.1109/LPT.2014.2384520.

[124] J. Li, S. Tang, J. Wang, Y. Liu, X. Chen, and J. Cheng, "An eight-wavelength BH DFB laser array with equivalent phase shifts for WDM systems," *IEEE Photonics Technology Letters*, vol. 26, pp. 1593–1596, 2014. doi: 10.1109/LPT.2014.2327113.

[125] T. Okamoto, N. Nunoya, Y. Onodera, T. Yamazaki, S. Tamura, and S. Arai, "Optically pumped membrane BH-DFB lasers for low-threshold and single-mode operation," *IEEE Journal on Selected Topics in Quantum Electronics*, vol. 9, pp. 1361–1366, 2003. doi: 10.1109/JSTQE.2003.819495.

[126] N. W. Carlson, S. K. Liew, R. Amantea, D. P. Bour, G. A. Evans, and E. A. Vangieson, "Mode discrimination in distributed feedback grating surface emitting lasers containing a buried second-order grating," *IEEE Journal of Quantum Electronics*, vol. 27, pp. 1746–1752, 1991. doi: 10.1109/3.90000.

[127] S. Sakamoto, T. Okamoto, T. Yamazaki, S. Tamura, and S. Arai, "Multiple-wavelength membrane BH-DFB laser arrays," *IEEE Journal on Selected Topics in Quantum Electronics*, vol. 11, pp. 1174–1179, 2005. doi: 10.1109/JSTQE.2005.853839.

[128] R. Schatz, T. Klinga, J. Wallin, and K. Streubel, "DFB laser with nonuniform coupling coefficient realized by double-layer buried grating," *IEEE Photonics Technology Letters*, vol. 5, pp. 1128–1131, 1993. doi: 10.1109/68.248403.

[129] R. Yu, S. Das, R. Hobbs, Y. Georgiev, I. Ferain, P. Razavi, *et al.*, "Top-down process of germanium nanowires using EBL exposure of hydrogen silsesquioxane resist," in *2012 13th International Conference on Ultimate Integration on Silicon (ULIS)*, 2012, pp. 145–147. doi: 10.1109/ULIS.2012.6193378.

[130] M. Yasui, Y. Sugiyama, M. Takahashi, S. Kaneko, J.-I. Uegaki, Y. Hirabayashi, *et al.*, "Fabrication of glassy carbon molds using hydrogen silsequioxane patterned by electron beam lithography as $O_2$ dry etching mask," *Japanese Journal of Applied Physics*, vol. 47, p. 5167, 2008. doi: 10.1143/JJAP.47.5167.

[131] M. I. Alayo, I. Pereyra, and M. N. P. Carreño, "Thick $SiO_xN_y$ and $SiO_2$ films obtained by PECVD technique at low temperatures," *Thin Solid Films*, vol. 332, pp. 40–45, 1998. doi: 10.1016/S0040-6090(98)01021-9.

[132] J. Hnilica, J. Schäfer, R. Foest, L. Zajíčková, and V. Kudrle, "PECVD of nanostructured $SiO_2$ in a modulated microwave plasma jet at atmospheric pressure," *Journal of Physics D: Applied Physics*, vol. 46, Art. no. 335202, 2013. doi: 10.1088/0022-3727/46/33/335202.

[133] M. W. Geis, G. A. Lincoln, N. Efremow, and W. J. Piacentini, "A novel anisotropic dry etching technique," *Journal of Vacuum Science and Technology*, vol. 19, pp. 1390–1393, 1981. doi: 10.1116/1.571216.

[134] H. A. Hoff, G. L. Waytena, C. L. Vold, J. S. Suehle, I. P. Isaacson, M. L. Rebbert, *et al.*, "Ohmic contacts to semiconducting diamond using a Ti/Pt/Au trilayer metallization scheme," *Diamond and Related Materials*, vol. 5, pp. 1450–1456, 1996. doi: 10.1016/S0925-9635(96)00566-3.

[135] S. Kim, I. Adesida, and H. Hwang, "Measurements of thermally induced nanometer-scale diffusion depth of Pt/Ti/Pt/Au gate metallization on InAlAs/InGaAs high-electron-mobility transistors," *Applied Physics Letters*, vol. 87, pp. 1–3, 2005. doi: 10.1063/1.2137687.

[136] J. Narayan and O. W. Holland, "Rapid thermal annealing of ion-implanted semiconductors," *Journal of Applied Physics*, vol. 56, pp. 2913–2921, 1984. doi: 10.1063/1.333831.

[137] K. Huet, F. Mazzamuto, T. Tabata, I. Toqué-Tresonne, and Y. Mori, "Doping of semiconductor devices by laser thermal annealing," *Materials Science in Semiconductor Processing*, vol. 62, pp. 92–102, 2017. doi: 10.1016/j.mssp.2016.11.008.

[138] T. Hoshlda, M. R. H. Daza, H. F. Liu, H. F. Liu, M. Tsuchiya, T. Kamiya, *et al.*, "Subharmonic hybrid mode-locking of a 33-GHz multisection semiconductor laser," in *Conference on Lasers and Electro-Optics*, 1996, paper CMB7.

[139] M. Wollitzer, J. Buechler, and E. Biebl, "Subharmonic injection locking slot oscillators," *Electronics Letters*, vol. 29, pp. 1958–1959, 1993. doi: 10.1049/EL:19931303.

[140] Y. P. Varshni, "Temperature dependence of the energy gap in semiconductors," *Physica*, vol. 34, pp. 149–154, 1967. doi: 10.1016/0031-8914(67)90062-6.

[141] K. P. O'Donnell and X. Chen, "Temperature dependence of semiconductor band gaps," *Applied Physics Letters*, vol. 58, pp. 2924–2926, 1991. doi: 10.1063/1.104723.
[142] B. Yuan, M. Al-Rubaiee, Y. Fan, L. Hou, J. H. Marsh, Y. Sun, *et al*., "Dual-wavelength distributed feedback laser array based on four-phase-shifted sampled Bragg grating for terahertz generation," *Optics Letters*, vol. 49, no. 12, pp. 3472–3475, 2024. doi: 10.1364/OL.524107.
[143] F. Kéfélian, S. O'Donoghue, M. T. Todaro, J. G. McInerney, and G. Huyet, "RF linewidth in monolithic passively mode-locked semiconductor laser," *IEEE Photonics Technology Letters*, vol. 20, pp. 1405–1407, 2008. doi: 10.1109/LPT.2008.926834.
[144] Y. Fan, Y. Huang, R. Zhang, S. Liang, X. Chen, W. Cheng, *et al*., "Millimeter-wave generation based on a monolithic dual-wavelength DFB laser with four phase-shifted sampled gratings and equivalent chirp technology," *Optics Letters*, vol. 48, no. 19, pp. 5093–5096, 2023. doi: 10.1364/OL.504585.
[145] R. Pawlus, S. Breuer, and M. Virte, "Control of dual-wavelength laser emission via optical feedback phase tuning," *Optics Continuum*, vol. 2, no. 10, pp. 2186–2199, 2023. doi: 10.1364/OPTCON.502550.
[146] L. Hou, B. Yuan, Y. Fan, X. Sun, Y. Sun, S. Zhu, *et al*., "Monolithic dual wavelength DFB lasers based on sidewall gratings for THz/MMW signal generation," *IEEE Journal of Selected Topics in Quantum Electronics*, vol. 31, 2025. doi: 10.1109/JSTQE.2024.3427770.
[147] Z. Lu, J. Liu, S. Raymond, P. Poole, P. Barrios, D. Poitras, *et al*., "312-fs pulse generation from a passive C-band InAs/InP quantum dot mode-locked laser," *Optics Express*, vol. 16, no. 14, pp. 10835–10840, 2008. doi: 10.1364/OE.16.010835.

# Appendix

**Fabrication Workflow**

| Step No. | Process Name | Description / Recipe |
|---|---|---|
| 1 | Sample cleaning | Solvent cleaning using acetone, IPA, and RO water with 3-minute ultrasonic steps each. |
| 2 | Aligned marker definition | Resist: PMMA 15% (4000 rpm, 180°C bake 2 min) + PMMA 4% (4000 rpm, 180°C bake 4 min). Development: MIBK: IPA (1:2.5), 23°C, 30 s. IPA 30 s and RO water 60 s. $O_2$ plasma clean: 110 W, 2 min. Metal deposition: NiCr/Au = 33/100 nm. Lift-off: Acetone, 50°C water bath, 1 h. |
| 3 | Electrical isolation etch | Resist: PMMA 15% / PMMA 15%. Development: MIBK: IPA (1:2.5). Dry etch: $Cl_2/CH_4/H_2/Ar$ = 10/15/10/10 sccm, 60°C, ICP/RF = 750/100 W, 5 mTorr. Mask removal: Acetone, 50°C water bath. |
| 4 | Ridge waveguide and sidewall grating definition | Pre-clean: UV-ozone 5 min. HSQ 2000 rpm, 90°C bake 3 min (~600 nm). Development: 25% TMAH, 23°C, 30 s. Dry etch: $Cl_2/H_2/CH_4/Ar$ = 10/15/10/10 sccm, 60°C, ICP/RF = 750/100 W. |
| 5a | HSQ removal (conductive substrate only) | 6:1 HF for 3 min, room temperature. |
| 5b | Buffer etch for SI substrate (only for SI substrates) | Second HSQ coating (same as Step 4). E-beam patterning to define a 14 µm protected region. Extended ICP etch (~680 nm). HSQ removal after etch. |

| | | |
|---|---|---|
| 6 | Insulating layer deposition | UV-ozone 5 min. PECVD $SiO_2$ 200 nm. HSQ planarisation 4000 rpm, bake 180°C 1 h. PECVD $SiO_2$ 100 nm. |
| 7 | Contact window opening | Resist: PMMA 15% / PMMA 15%. RIE etch $CHF_3$/Ar = 25/15 sccm, 150 W, 30 mTorr. Window widths: p = 1.3 µm, n (SI) ≈ 140 µm. Mask removal: $O_2$ plasma. |
| 8 | P-contact metal deposition (top-side) | Resist: PMMA 15% / PMMA 15% / PMMA 4%. Surface clean: $O_2$ plasma + HCl: $H_2O$ (1:5). Metal: Ti/Pt/Au = 30/30/240 nm. Lift-off: Acetone. |
| 9 | N-contact metal deposition (top-side, SI only) | Same process and metal stack as Step 8, using an n-contact window. |
| 10 | Sample thinning (conductive substrate only) | Mechanical thinning using 9 µm then 3 µm $Al_2O_3$ slurry (370 µm → ~200 µm). |
| 11 | Backside contact deposition (conductive substrate only) | Uniform backside metal deposition, same Au-based stack as top contact. |
| 12 | Annealing | Rapid thermal annealing at 380°C for 60 s. |
| 13 | Cleaving | Cleaving along crystallographic planes to form laser bars |